Seafloor gravity currents: flow dynamics in overspilling and sinuous channels

Robert William Kelly

The University of Leeds

School of Computing

EPSRC Centre for Doctoral Training in Fluid Dynamics

Submitted in accordance with the requirements for the degree of Doctor of Philosophy.

October 2018

The candidate confirms that the work submitted is his/her/their own, except where work which has formed part of jointly authored publications has been included. The contribution of the candidate and the other authors to this work has been explicitly indicated below. The candidate confirms that appropriate credit has been given within the thesis where reference has been made to the work of others.

A version of Chapter 5 has been accepted for publication in Journal of Geophysical Research: Oceans:

"The structure and entrainment characteristics of partially-confined gravity currents". Robert Kelly, Robert Dorrell, Alan Burns and William McCaffrey. Journal of Geophysical Research: Oceans. Under review.

In this manuscript the work is the candidate's own, with the other authors having acted in a supervisory role, providing feedback and suggestions.

"In every outthrust headland, in every curving beach, in every grain of sand there is the story of the earth." – Rachel Carson

Acknowledgements

It feels a bit bizarre to finally be writing this, as it means my time as a PhD student must be drawing to a close. Firstly, I would like to thank my team of supervisors, Bill McCaffrey, Robert Dorrell and Alan Burns, who gave me their utmost support throughout this project. Thank you to Bill, for imparting a smidge of his vast geological knowledge upon this physicist and whose keen insights and ideas were, and continue to be, invaluable. Thank you to Rob, for being my first port of call for any technical query and whose unique and unparalleled skillset were a vital resource to tap into. And thank you to Alan, a total authority on CFD, who taught me almost everything I know on the subject and whose expertise undoubtedly prevented many a futile endeavour on my part.

Next, I would like to thank the CDT management, for providing me with the opportunity to study for a PhD in the first place. I am especially grateful to Peter Jimack, who always made time, and to Claire Savy, who bore the brunt of my unwillingness to deal with paperwork and bureaucracy. Thank you to my fellow students, who worked, laughed, travelled and drank with me. My CDT cohort is a group of immensely talented individuals and they have made the past 4 years unforgettable. A special thanks to Sam Williams, who took me climbing and, in doing so, introduced me to a whole new world.

I would also like to thank the Sorby team of Gareth Keevil, Robert Thomas and Helena Brown. Gareth in particular is thanked for his time, effort, dry wit and for still allowing me access to the lab after the minor flooding incident of 2018.

I am forever indebted to Mum and Dad, both for their constant support and for allowing me the total freedom to make my own choices and mistakes. It doesn't seem to have gone too badly so far.

Finally, I would like to thank Dev. This could very well be the only page of the thesis she will ever read. Somehow, you have been completely supportive while simultaneously showing a total indifference to fluid dynamics or turbidity currents. Frankly, this has been a welcome relief and perhaps ensured I am still sane? I'll let you decide on that one.

Abstract

Turbidity currents are the largest agent of global sediment transport and their deposits, submarine fans, are the largest sedimentary structures on Earth. Submarine fans consist of networks of seafloor channels, which are vital pathways for sediment and nutrient transport to the deep ocean. This work focusses on flow dynamics within these channels, with the aim of understanding the role of the channel form on flow development and identifying implications for the development of channels and, ultimately, for submarine fans.

Laboratory experiments have been conducted of continuous saline gravity currents traversing fixed-form channel models with a range of planform geometries. Both velocity and density data were gathered to investigate the effect of a channel on the flow field. Numerical simulations have also been conducted, using a Reynolds-averaged Navier-Stokes model and a shear stress transport turbulence closure. These allow an extension of the laboratory analysis, both in terms of physical domain size, data resolution and measured variables.

Velocity data reveal how partial confinement exerts a first order control on the vertical variation in flow structure. The channel half-depth acts to limit the height of the velocity maximum, resulting in the development of a confined, high-velocity flow core. The channel form also constrains the lateral and three-dimensional flow structure. Secondary flow rotation, characterised by a local reversal in the radial pressure gradient, is shown here to be inhibited by low channel sinuosity and large levels of overbank fluid losses. A change in cross-sectional channel profile is capable of switching the dominant cross-stream basal flow direction of these structures. Furthermore, channels are shown to cause flow tuning, whereby flows of differing magnitudes entering a channel reach are rapidly modified to show a much restricted magnitude range, that remains quasi-stable thereafter. For the cases studied, this quasi-equilibrium state is characterised by a symmetrical cross-channel basal stress profile. The existence of such a state could explain how seafloor channels can achieve a degree of planform stability.

Contents

List of figures

Chapter 1

Chapter 2

Chapter 3

Chapter 4

Chapter 5

Chapter 6

Chapter 7

Chapter 8

List of tables

Chapter 1

Introduction

1.1 Research background and thesis aims

Gravity currents are a diverse and widespread natural phenomenon. Also referred to as density currents, these flows propagate due to a density difference between the current and its ambient surroundings. They have important applications in industry, aircraft safety, atmospheric pollution and sediment transport [Simpson, 1999]. A number of different causes can provide the required density difference. In a geophysical setting, these could be temperature differences (e.g. atmospheric cold-fronts), salinity differences (e.g. hypopycnal and saline-exchange flows) or the presence of suspended particulate matter entrained within a current (e.g. dust storms, pyroclastic flow, powder snow avalanches and seafloor turbidity currents).

Turbidity currents are the main process through which sediment is transported to the deep ocean. An individual current is capable of transporting 100s of cubic kilometres of sediment, more than the 10 times the annual global fluvial flux [Holeman, 1968; Masson et al., 1996; Talling et al., 2007]. Over timescales of 10^4 to 10^6 years, these currents can form some of the largest geomorphological features on Earth, with volumes of up to millions of cubic kilometres [Meiburg and Kneller, 2010]. Known as submarine fans (e.g. Figure 1.1), these deposits may host environmental archives, and can also form the reservoirs for economically significant accumulations of hydrocarbons. In addition, turbidity currents pose a significant geohazard; capable of reaching speeds of up to 20 m/s [Piper et al., 1999] they may damage or destroy seafloor infrastructure, such as conventional and fibreoptic cables and oil and gas wellheads, pipelines and risers.

Turbidity currents usually traverse the sea bed fully-confined, or more commonly partially-confined, within seafloor channels (e.g. Figure 1.2). Submarine fans comprise

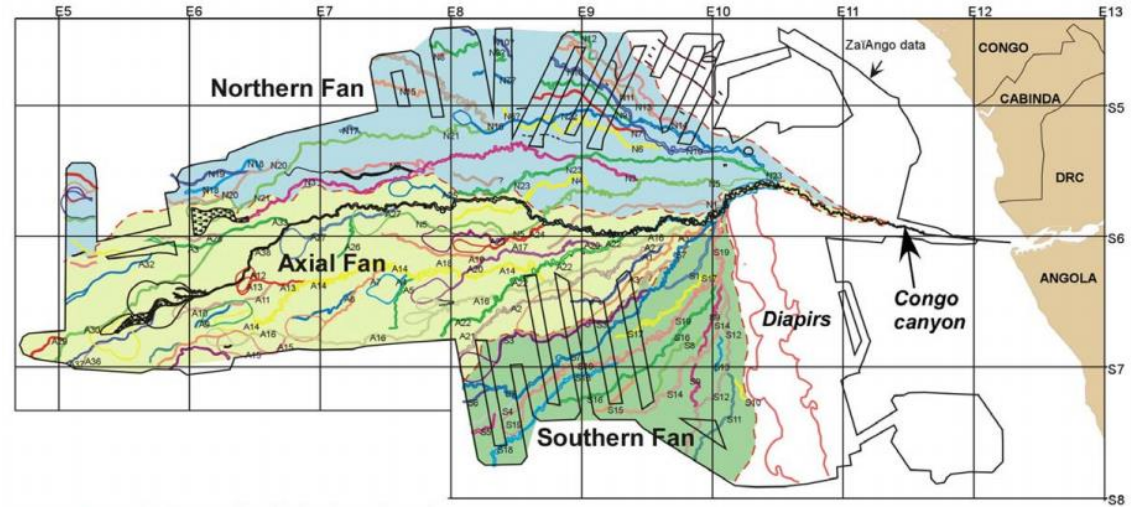

Figure 1.1 Map of the Congo fan off the coast of West Africa [Savoye et al., 2009]. The fan is comprised of a series of sinuous seafloor channels. The channels are fed by a feeder canyon emanating from the mouth of the Congo river.

systems of these channels; formed by the deposits of successive currents, seafloor channels can extend for 1000s of kilometres [Klaucke et al., 1998]. They are often flanked by large levee systems, which can be orders of magnitude wider than the channel itself and are a result of deposition from currents overspilling the channel confines [Birman et al., 2009; Nakajima and Kneller, 2013]. The patterns of morphological evolution of seafloor channels have fundamental differences to those of fluvial channels [Peakall et al., 2000]; for example, seafloor channels appear capable of achieving a degree of planform equilibrium.

Despite the ubiquity and importance of seafloor channels, the mechanisms and processes governing their development are not well understood [Talling et al., 2015]. In particular the complex system of feedback that underlies the interaction between partially-confined turbidity currents and their containing channels is not well characterised. This feedback operates at two timescales: at the scale of individual flows, the flow field is modulated due to flow through the channel form; over longer timescales, the combined depositional and erosional impact of large numbers of successive flows modulates the channel morphology. The immediate focus of the work detailed here is to better characterise the

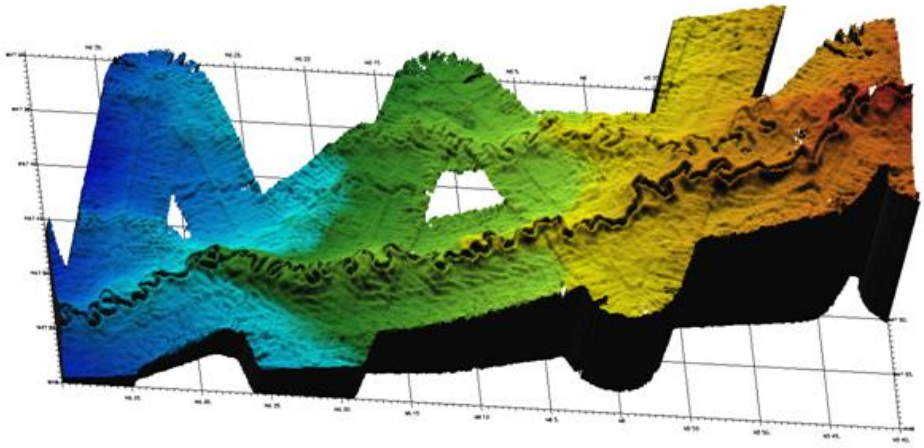

Figure 1.2 Bathymetry data, with vertical exaggeration, shows a seafloor channel which is part of the Amazon fan [Amos and Peakall, 2006]. This particular channel is highly sinuous and flanked by large levees. An old, abandoned channel can also be observed.

control of the submarine channel form on the flow field of turbidity currents, with focus on the development of intrachannel flow structure and on downstream flow evolution. Such information is necessary to understand the evolution of channel morphology, and in turn the turbidite fan systems they build.

1.2 Methodological approaches

A major hurdle in the study of turbidity currents and seafloor channels is their deep-water location. Gathering in-situ flow data is challenging, and so models and theories of channel development have commonly been built using channel morphology data, be that bathymetric, seismic or from ancient systems exposed at outcrop [e.g. Peakall et al., 2000; Jobe et al., 2015]. In recent years, the availability of data from direct observations has become more widespread. Data from natural gravity and turbidity currents have been recorded at a number of locations around the world [e.g. Xu et al., 2004, 2013, 2014; Vangriesheim et al., 2009; Sumner and Paull, 2014; Azpiroz-Zabala et al., 2017]. Although it is becoming increasingly detailed [Sumner et al., 2013, 2014; Dorrell et al., 2014], whole flow field measurement data remain elusive.

Currently, data with the highest resolution come from laboratory and numerical modelling of smaller-scale flows. Laboratory experiments have revealed details of gravity currents' internal structure [e.g. Ellison and Turner, 1959; Middleton 1966; Parker et al., 1986, 1987; Kneller et al., 1997, 1999; Islam and Imran 2010; Sequeiros et al., 2010] and intrachannel dynamics [e.g. Keevil et al., 2006; Imran et al., 2007; Islam and Imran, 2008; Abad et al., 2011; Dorrell et al., 2018a]. They have also been used to study depositional behaviour [e.g. Kane et al., 2008; Ezz et al., 2013] and the morphological evolution of channels [e.g. Mohrig and Buttles 2007; Straub et al., 2008; De Leeuw et al., 2016].

Numerical modelling has provided further insight into the dynamics of channelised gravity currents [e.g. Kassem and Imran 2004; Imran et al., 2007; Giorgio Serchi et al., 2011; Dorrell et al., 2013; Ezz and Imran, 2014], generally achieving good agreement with the laboratory data. Numerical modelling has the potential to expand the scope and parameter spaces of laboratory studies, however this has yet to be truly addressed. To date, models have replicated simplified laboratory setups and scales, giving whole-flow field datasets which are not realistic or practical to record in the laboratory.

In this study, a combined laboratory and numerical approach is applied to the study of gravity currents in submarine channels. The experiments observe and record saline flows traversing channel-levee systems with geometry more representative of field morphology than those used in previous studies. The numerical simulations, conducted using the same channel geometry, complement these experiments by both exploring flow magnitudes and delivering data densities not possible in the laboratory. This approach represents an advance in the field of turbidity current dynamics and allows for the development of more sophisticated process models. Moreover, the development of a reliable and validated numerical model for channelised gravity currents could provide the basis for fully-predictive channel evolution simulations in the future.

1.3 Thesis outline

Chapter 2 offers an overview of the literature and relevant background research. The dynamics and structure of gravity currents are described, as are the classifications and morphology of seafloor channels. Previous field studies, laboratory experiments and numerical and theoretical models are discussed with the main findings summarised.

Chapter 3 gives details on the laboratory experiments and outlines the various methodologies and techniques used in this study.

Chapter 4 provides a full description of the numerical model used to simulate channelised gravity currents. The Reynolds-averaged Navier-Stokes (RANS) equations are explained, followed by details of the shear stress transport (SST) turbulence model, the multiphase mixture model and finally the domains and meshes used throughout the simulations.

Chapter 5 examines the structure and entrainment characteristics of partially-confined gravity currents. The effect of a confining channel on the primary dynamics of a current is investigated, as are the effects on flow entrainment in comparison to a fully-confined environment. The consequences for both flow and channel development are discussed.

Chapter 6 focusses on the cross-stream dynamics of flows in a sinuous channel. The conditions required for the onset of helical structure are analysed. This structure is then explored further, with the underlying mechanisms studied along with its downstream evolution. Furthermore, consideration is given to the control that channel morphology can have on cross-stream flow.

Chapter 7 uses numerical simulations to inspect downstream evolution patterns of partially-confined gravity currents across a range of flow parameters. Maps of basal stress are developed as a tool to analyse the interaction between a current and its containing channel. The concepts of flow tuning and equilibrium states are further developed.

Finally, Chapter 8 summarises the main findings of this thesis. The limitations of this study are also discussed, with ideas given for the possible direction of any future research.

Chapter 2

Gravity current dynamics and submarine channel morphology

2.1 Gravity and turbidity currents

The study of gravity currents presents an incredibly active area of research. The term encompasses a wide range of phenomena including dust storms in the desert [e.g. Aoki et al., 2005], advancing cold fronts in the atmosphere [e.g. Charba, 1974; Simpson and Britter, 1980], thermohaline currents in the ocean [Arneborg et al., 2007; Legg et al., 2009], pyroclastic flows from volcanoes [e.g. Breard et al., 2016; Dufek et al., 2016], avalanches in mountainous regions [e.g. Ancey, 2004; Gruber and Bartlet, 2007], exchange flows in estuaries [e.g. Cuthbertson et al., 2014, 2018] and turbidity currents in the deep ocean [e.g. Meiburg and Kneller 2010; Talling et al., 2015]. Gravity currents are driven by a density difference between the current and the ambient fluid. This section outlines the dynamics and structure of these flows.

2.1.1 Definitions of flow classifications

Possibly the most comprehensive definition of a gravity current is provided by Middleton [1993]:

"Gravity (or density) currents are a general class of flows (also known as stratified flows) in which flow takes place because of a relatively small difference in unit weight (or weights) between two fluids: The gravity flow may move below, above, or between ambient fluid of different unit weight. The difference in unit weight may be due to differences in composition, in salinity, or in temperature."

Turbidity currents are a specific class of gravity current, whose conduits are often (but not exclusively) submarine channels. A generalised definition is given by Kuenen and Migliorini [1950], who describe them as “sediment-laden gravity-driven underflows in which the sediment grains are suspended by fluid turbulence”. Kuenen [1938] was the first to carry out laboratory experiments in this area, after Daly [1936] proposed them as a significant factor in the formation of submarine canyons. Three quarters of a century later and the field of research is as rich as ever [Talling et al., 2015]. Turbidity currents pose a significant geohazard risk to sea-floor infrastructure and communication and could cause significant economic damage via the destruction of submarine cables and pipelines [Piper et al., 1999]. The sediment deposits that form the submarine fan systems are also a rich source of hydrocarbon reservoirs [Meiburg and Kneller, 2010].

The definition of a turbidity current is perhaps not as straightforward as above however; classification systems are confused, perhaps due to their inherent importance in different research areas [Mulder and Alexander, 2001]. Although the term usually refers to sediment suspended in water, it has also been used to describe particles suspended in air such as dust storms and snow avalanches [Hopfinger, 1983]. Middleton [1993] proposed that turbidity currents are not in fact gravity-driven, as stated by Kuenen and Migliorini [1950], but instead particle-driven as, although the particles are moved by gravity, it is then the movement of the particles that drives the interstitial (suspending) fluid [Middleton and Hampton, 1973]. This view, however, fails to identify the crucial relationship and feedback system that exists between the turbulent fluid and suspended particles.

At higher sediment concentrations, approaching those of saturated, sediment-laden debris flows such as mud- and land-slides, then the behaviour and dynamics of the particles certainly has a much larger role to play in the evolution of the current. However, at the lower concentrations of turbidity currents this seems unlikely, especially if the Kuenen and Migliorini definition of turbulent suspension is to be considered. Mulder and Alexander [2001] propose using the Bagnold limit as an upper threshold value for

turbidity currents. This theoretical limit, 9% sediment concentration by volume, was proposed as the maximum concentration for fully turbulent support of the sediment [Bagnold, 1962]. The term 'high-density turbidity currents' has been used by several authors for flows above this threshold [Kuenen, 1966; Middleton, 1966; Pierson and Scott, 1985], but Mulder and Alexander argue that the adjectives high-density or high-concentration are not applicable to turbidity currents as they imply flows in which there are other significant factors in keeping particles suspended other than turbulence. The presence of such high concentration flows has even been questioned [Peakall and Sumner, 2015] and indeed their lifetime would be very short to due to the rate of particulate settling; transformation to more dilute turbidity currents is one such possible pathway for these flows [Felix and Peakall, 2006]. An apparent problem with much of the above literature is that flows are characterised by the bulk density when there can be large vertical variation. Therefore, depending on the level of stratification, it is possible for flows with similar bulk densities to be very different in character.

Bagnold [1962] termed the capability of a flow to keep particles suspended via turbulence, and thus the ability to maintain itself indefinitely, autosuspension. Incidentally this definition has to be inferred as, although the term appeared in the title, it never actually appeared in the body of the paper itself. Bagnold derived a criterion for autosuspension by considering a flow's energy budget. It was based upon the 'power' of the flow,

$$P = \left(\rho_p - \rho_f\right) g \Phi U \sin\theta\,, \tag{2.1}$$

which depends upon the densities of the fluid and particulate phases ρ_f and ρ_p, gravity g, the volumetric sediment concentration Φ, the depth-averaged streamwise velocity U and the slope θ.

The autosuspension criterion was that,

$$P \geq P_N + P_I, \tag{2.2}$$

where $P_N = (\rho_p - \rho_f) g \Phi \omega$, is the power required to keep particles suspended (ω is the settling velocity of the particles) and $P_I = \tau_b U$, is the power expended against the basal stress τ_b.

Pantin [1979] later redefined this criterion with the relationships,

$$P \geq P_I, \qquad e_X P_I \geq P_N, \tag{2.3}$$

where e_X is an efficiency factor that indicates the proportion of power expended against basal stress that also contributes to sediment suspension. Although this theoretical treatment of the autosuspension criteria is useful for characterising flows, it is almost certainly an oversimplification of a complex feedback system which relates the turbulence of the fluid to the subsequent movement of particles.

2.1.2 Mean and bulk flow properties

Fluid dynamic properties (mainly dimensionless numbers) can be applied to the case of gravity currents in order to characterise and categorise the flow. This is vital when studying laboratory and field flows as it provides a scaling mechanism via which flows of vastly different sizes can be compared. The first of these properties is the Reynolds number,

$$Re = \frac{Uh}{\nu}, \tag{2.4}$$

the ratio of viscous to inertial forces, where U is the depth-averaged velocity, h is the current height and ν is the kinematic viscosity. It is commonly used as an indicator of turbulence regimes. For gravity currents of $Re > 1000$, the flow patterns are independent of its value [Simpson, 1999] (although this has been disputed [Stagnaro and Pittaluga, 2014]). This has therefore always been an important threshold for currents initiated in the laboratory.

The best method for defining the thickness of a current is a common debate but the most common form taken is that defined by Ellison and Turner [1959],

$$h = \frac{\left(\int_0^\infty u\, dz\right)^2}{\int_0^\infty u^2\, dz}, \tag{2.5}$$

where $u(z)$ is the mean velocity and z is the vertical direction. Although different conventions have been used by various authors, here x, y and z are the streamwise, cross-stream and vertical directions respectively, with corresponding velocities u, v and w. The second dimensionless number often referred to, and arguably the most important for stratified flows, is the Froude number,

$$Fr = \frac{U}{\sqrt{g'h}}, \tag{2.6}$$

where $g' = g(\bar{\rho} - \rho_a)/\rho_a$, is the reduced gravity and $\bar{\rho}$ and ρ_a are the depth-averaged and ambient density respectively. It is the ratio of inertial to buoyancy forces and as such can be an indication of the stability of the flow since the inertial forces (shearing) are destabilising whilst the buoyancy forces (vertical stratification) are stabilising.

Flows can be characterised as subcritical (Fr < 1) or supercritical (Fr > 1) depending on which forces are dominant [Ellison and Turner, 1959]. Whilst this critical Froude value Fr_c = 1 can be obtained analytically for open channel flows [Te Chow, 1959], it may not hold for gravity currents due to differences such as entrainment of ambient fluid and deposition of sediment. Huang et al. [2009] proposed that the critical value could be non-unity or even non-existent. However, flows that pass through the point of Fr_c experience a hydraulic jump. This phenomenon has been observed in currents passing through the Bosphorus Straits [Sumner et al., 2013], evidence that both flow regimes and a critical Froude number must exist.

The final dimensionless number to be defined here is the bulk Richardson number (as opposed to the gradient Richardson number discussed later), which for gravity currents can be written as,

$$Ri = \frac{g'h}{U^2} = \frac{1}{Fr^2}. \tag{2.7}$$

Similar to the Froude number, it is a measure of the dynamic stability of a flow. It has been closely related to the entrainment of ambient fluid and Parker et al. [1987] proposed the empirical relation,

$$e_w = \frac{0.075}{\sqrt{1 + 718Ri^{2.4}}}, \tag{2.8}$$

for the coefficient of entrainment at the ambient interface (the entrainment velocity normalised by mean streamwise velocity).

2.1.3 Anatomy of a gravity current

The general anatomy and structure of turbidity currents are the same as that of the broader gravity current category. Gravity currents are predominantly generated in the laboratory via two methods [Peakall et al., 2001]. One of these is via the opening of a lock gate which releases a finite volume of relatively dense fluid into the ambient fluid. This is analogous to sudden events such as seismogenic slumping which results in surge like currents [Kneller and Buckee, 2000]. The other method is to use a continuous inlet pump which is perhaps more comparative to the longer, quasi steady-state currents observed in many submarine channels [e.g. Khripounoff et al., 2003; Vangriesheim et al., 2009; Sumner et al., 2013; Dorrell et al., 2014; Azpiroz-Zabala et al., 2017].

Regardless of the generation method, the subsequent flows display the characteristically well defined ‘body and head’ regions of a gravity current that are shown in Figure 2.1, with the head usually being thicker than the body. The resulting dynamics may differ

though, with lock release currents proportionally more dominated by the effects of the head [Hacker et al., 1996]. Whereas the force dominating the motion of the head is the pressure gradient downslope, caused by the density difference between the head and ambient fluid, the body is driven by the gravitational force on the fluid [Stacey and Bowen, 1988].

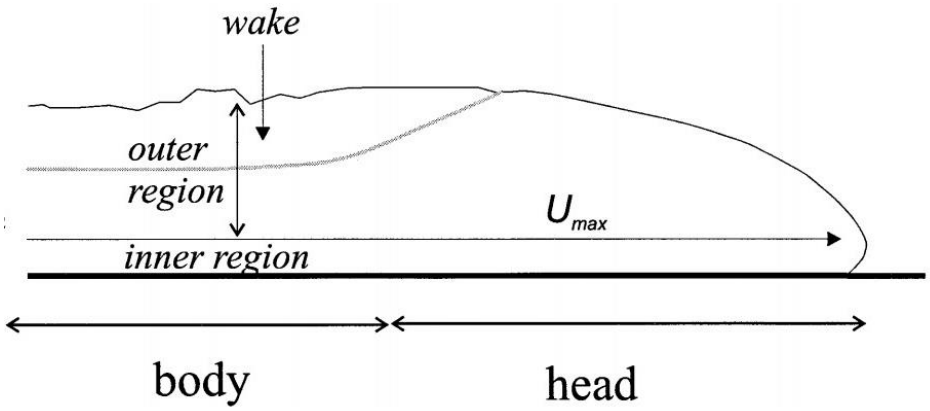

Figure 2.1 Diagram of the structure of a gravity current, modified from Kneller and Buckee [2000]. The highly-transient and turbulent head is followed by a quasi-steady state body.

2.1.4 The head of the current

The head of a gravity current is highly turbulent and, as described above, is driven by the pressure difference caused by the contrasting density of the current and ambient fluid. For a horizontally moving current the head remains quasi-steady, but for flow down a slope the relative size of the head increases with angle [Simpson, 1999]. This is because the front velocity is independent of slope for low angles ($< 3^{\circ}$) and only weakly dependent for steeper slopes due to the dominance of pressure rather than gravitational forces [Keulegan, 1957; Middleton, 1966]. The velocity of the body is slope dependent however and as such can be 30% to 40% faster than the head [Kneller et al., 1997, 1999]. Due to the high levels of turbulence, the head is also a region of intensive mixing. This mixing is contributed to by instabilities between the two fluid phases. These instabilities can come

in the form of billows or lobes and clefts (Figure 2.2). The complex lobe and cleft pattern can also be seen in Figure 2.3 and they are a result of the forces exerted on the current by the floor. The billows occur towards the top of the head and in the wake behind and are a result of the shear between the two fluids. These billows, termed Kelvin-Helmoltz (KH) instabilities, occur in many other sheared flows, e.g. cloud movement in the atmosphere and Jupiter's Red Spot. This intensive mixing leads to high levels of entrainment and as such the head is often twice as thick as the following body [Simpson, 1999]. It has also been suggested that it is a significant factor in erosion by the flow and is therefore an important consideration for sedimentologists [Middleton, 1993; Straub et al., 2008; De Leeuw et al., 2016].

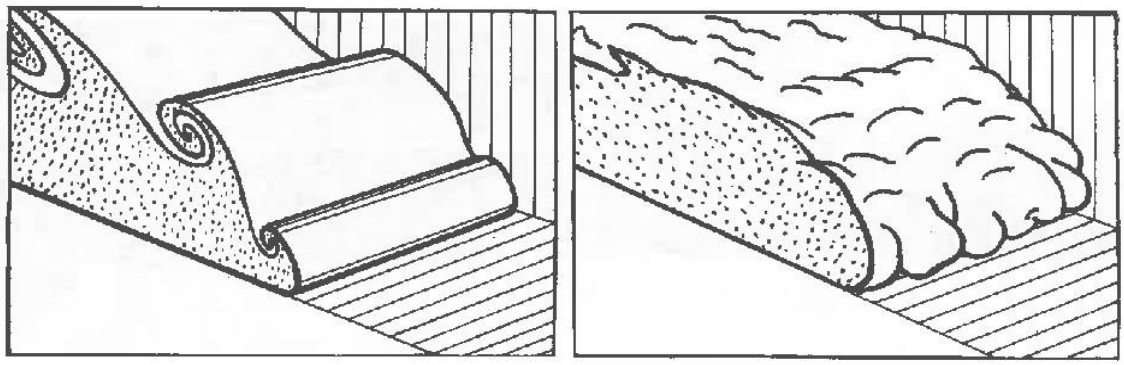

Figure 2.2 Drawing of the different types of instabilities observed at the ambient interface of gravity currents: Kelvin-Helmholtz billows (left) and clefts and lobes (right) [Simpson, 1999].

2.1.5 The body of the current

Whilst the head of the current is highly transient and unstable, the body is, in contrast, quasi steady-state in nature. It is 'quasi' in that it is still subject to fluctuation and instabilities but, when taken as an average over time, it appears to be uniform. KH instabilities are a common feature of the head, however their occurrence rate in the body of the current is less certain.

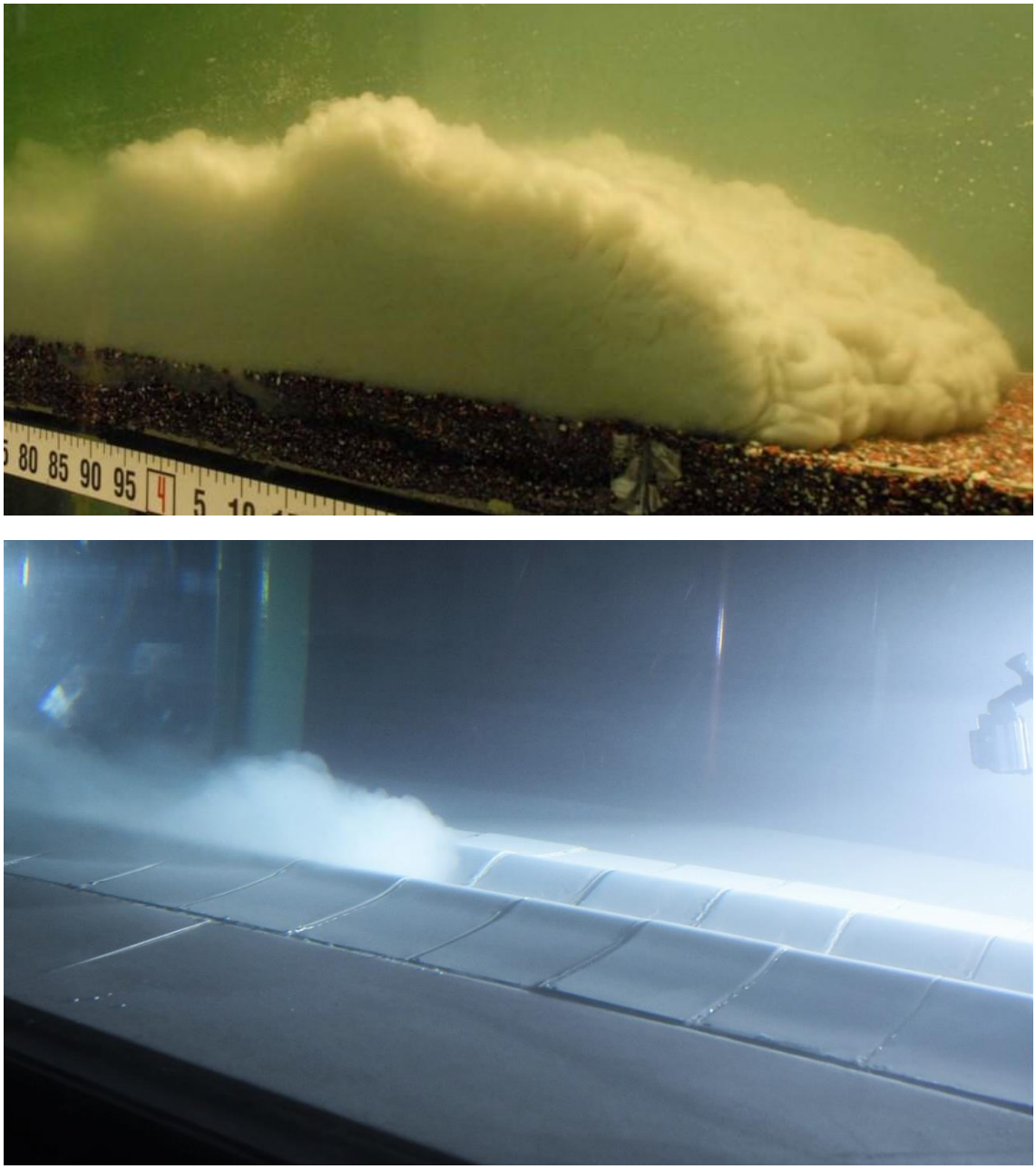

Figure 2.3 Photographs of gravity currents. The top image shows a turbidity current flowing over an erodible bed from experiments by Sequeiros et al. [2010]. The bottom image shows a saline current (with added particulates for visualisation) from experiments conducted as part of this project.

The gradient Richardson number,

$$Ri_g = \frac{-g\frac{d\rho}{dz}}{\rho_a\left(\frac{du}{dz}\right)^2}, \tag{2.9}$$

gives an indication as to the local stability of the stratification of the flow [Kneller and Buckee, 2000]. It is the ratio of buoyancy production and shear production due to turbulence in the vertical direction, where ρ_a is a reference density, here taken as that of the ambient fluid. For regions where $Ri_g < 0.25$ it is often found that the stratification is subject to instability [Turner, 1979]. KH instabilities are the main form of entrainment for turbidity currents and are also a major drag source due to the shear created. Numerical modelling, albeit 2D in nature, has shown that for currents whose upper regions satisfy the criterion $Ri_g > 0.25$ KH instabilities are indeed absent [Kneller et al., 2016]. Kneller et al. suggest that many flows on low gradients fulfil this criterion which could be an explanation as to how currents can travel so far out into the ocean. Sequeiros et al. [2010] present velocity profiles expected for these types of current which challenge the traditional idea of a velocity maximum close to the base (Figure 2.5). However, these experiments were performed over relatively coarse beds which could lead to artificially inflated turbulence levels close to the bed.

2.1.6 Velocity and density structure

The structure of a gravity current is crucial to a further understanding of the dynamics and processes involved, giving clues as to how turbidity currents can travel for such vast distances along the ocean floor. The vertical structure of gravity currents was first investigated in detail by Stacey and Bowen [1988] who conducted a theoretical analysis and drew comparisons with some early experimental data from Ellison and Turner [1959]. A gravity current can largely be characterised by its velocity and density profile features. Typical velocity and density profiles are shown in Figure 2.4. The velocity profile features

the same general shape as that of turbulent wall jets [Launder and Rodi, 1983]. However, defining the characteristic length scale as h/2 does not yield the same satisfactory profile collapses as for wall jets [Gray et al., 2005], showing that there are far more processes involved governing the structure of gravity driven flows. The velocity maximum occurs at a height above the floor determined by the ratio of upper and lower boundary shear and drag forces [Middleton, 1966]. This height is often 0.2-0.3 times the thickness of the current [Kneller et al., 1997].

The height of the velocity maximum also separates what are often termed the inner and outer regions of the flow. The characteristics of the inner region can be compared to those of open channel flow and turbulent boundary layers with a positive velocity gradient and a dominance of near-wall effects. The outer layer is dominated by the effects of shear

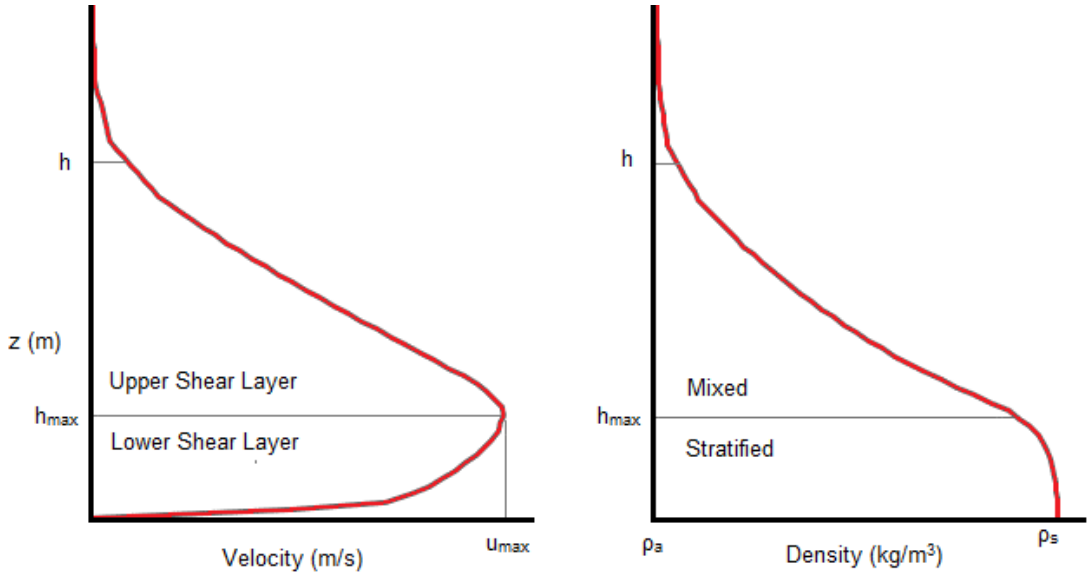

Figure 2.4 Characteristic velocity and density profiles for a saline gravity current. Two shear layers are separated by a velocity maximum. The lower shear layer is generated by basal drag and is stratified in nature, whereas the upper shear layer is a result of drag with the ambient fluid and is subsequently more mixed. h is the height of the current defined by the Ellison and Turner [1959] method (Equation 2.5). ρ_a and ρ_s are the densities of the ambient and initial saline fluid respectively, and h_{max} and u_{max} are the height and magnitude of the velocity maximum.

with the ambient fluid and has a negative velocity gradient. The ubiquity of such velocity profiles, with the maximum close to the base, has been debated. It has been proposed that, if KH instabilities are absent and subsequent drag on the flow is much lower, the velocity maximum could be significantly higher [Kneller et al., 2016]. This has been observed in the laboratory, albeit with the proviso stated above of a rough base not scaled to the current [Sequeiros et al., 2010].

The stratified nature of gravity currents gives rise to the vertical density gradient. For turbidity currents, this density is determined by the levels of sediment present in the flow. These density profiles typically fall into two categories: stepped, two-layer profiles or smooth, continuous profiles (Figure 2.5) [Peakall et al., 2000; Sequeiros et al., 2010; Peakall and Sumner; 2015]. The latter are often characteristic of low-concentration and saline flows observed in the laboratory [e.g. Garcia, 1994; Altinakar et al., 1996]. However, saline currents have been observed entering the Black Sea [Sumner et al., 2014] featuring a very stepped profile.

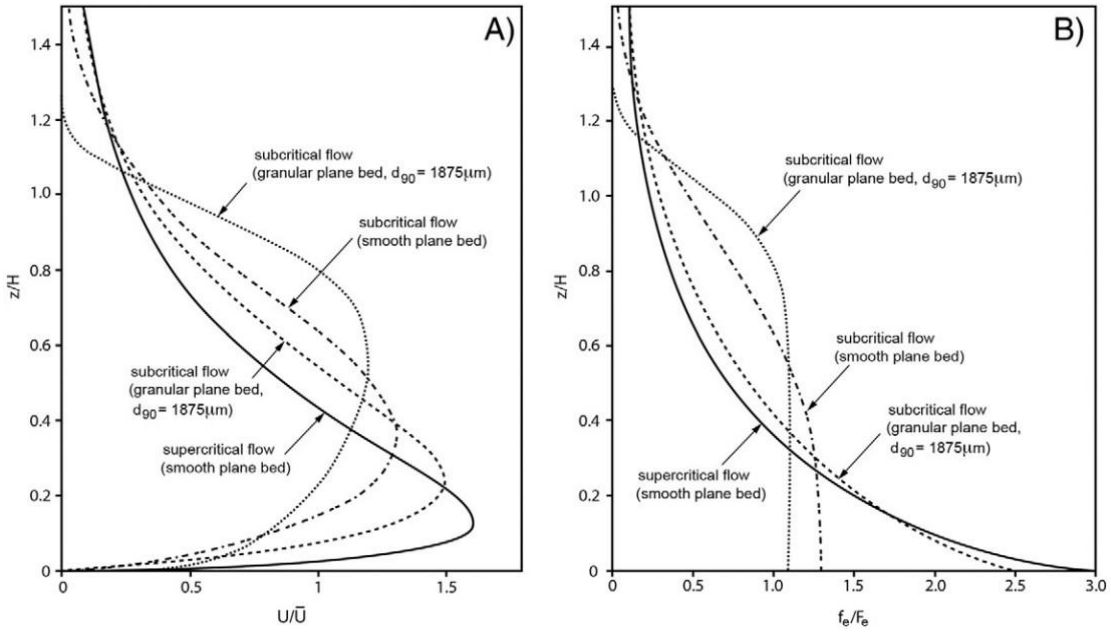

Figure 2.5 Velocity (A) and density (B) profiles of turbidity currents. Various changes in flow condition can change features such as velocity maximum height and stratification. A modified image from Sequeiros et al. [2010].

2.1.7 Turbulence structure

The turbulent structure of gravity currents was first experimentally investigated by Kneller et al. [1997, 1999] using laser Doppler anemometry. This was subsequently built upon by Buckee et al. [2001] and more recently revisited by Islam and Imran [2010] and Cossu and Wells [2012] using modern acoustic Doppler velocimetry. The high measurement frequencies achieved are crucial for identifying the fluctuations from the mean flow field, the magnitude of which determine the turbulence intensity. Both Islam and Imran and Cossu and Wells highlighted that there are no appreciable differences in the turbulent structure of saline and turbidity currents. A key feature observed almost universally is a low level of turbulence close to the velocity maximum, with higher levels of turbulence close to the wall in the inner region and in the shear layer in the outer region. This region of low turbulence has been hypothesised to prevent the transport of mass between the inner and outer region and has been termed the slow diffusion zone (SDZ) [Peakall et al., 2000; Buckee et al., 2001].

This low area of turbulence is not surprising since there are just two methods of turbulence production: that by shear and that by buoyancy. The production due to shear,

$$P_{shear} = -\overline{u_i' u_j'} \frac{du_i}{dx_j}, \tag{2.10}$$

is dependent on the Reynolds stresses and velocity gradient, while the production due to buoyancy,

$$P_{buoy} = -\frac{g}{\rho_a} \overline{\rho' w'}, \tag{2.11}$$

is determined by the so-called buoyancy fluxes. The shear term contributes far more to gravity currents [Buckee et al., 2001; Islam and Imran, 2010] and is low in magnitude at the velocity maximum due to the null velocity gradients at this location. It should be noted that due to the available technology, earlier work such as that by Buckee et al. [2001] only recorded in the vertical plane and neglected cross-stream terms (i.e. the shear production

was calculated using just the $u'w'$ term). The 3D technology used by Islam and Imran showed turbulence intensity to be larger in the cross-stream than vertical direction and therefore should be included in any turbulence calculations.

2.1.8 Field observations

The first evidence of the presence of turbidity currents came as a result of the Grand Banks earthquake in 1929 which shook the continental slope south of Newfoundland. Every telegraph cable that was laid upon the ocean floor south of the epicentre was broken. These breaks occurred in sequence from north to south over a period of 12 hours [Piper et al., 1999]. Several explanations were provided but it was many years before Heezen and Ewing [1952] proposed the idea of a turbidity current. A similar phenomenon occurred in 1966 in the Western New Britain Trench near Papua New Guinea [Krause et al., 1970]. These events serve to highlight only one of the hazards posed by turbidity currents. Incidentally, modern fibre optic cables still lie on the ocean floor in these same hazardous locations.

Observational data from the field used to be scarce, although in recent years various projects have led to a greater range of datasets. However, much of this data is often based upon currents seen in coastal submarine canyons such as the Monterey canyon in California [Paull et al., 2002; Xu et al., 2004; Xu, 2010; Xu et al., 2013, 2014], rather than shallower submarine channels. Using acoustic Doppler technology, Xu [2010] was able to gather velocity profiles for several turbidity currents over the course of a year which largely confirmed the characteristics described above observed in laboratories. The majority of currents were storm-triggered but a later current was believed to be caused by slumping of the canyon wall. Using sediment traps, the make-up of the currents was analysed. Xu concluded that the concentration and grain-sizing of suspended material play a significant role in the development of the turbidity currents, with the currents possibly undergoing an adjustment period of capacity-driven deposition before achieving

the stage of quasi-steady state. It was also observed that finer sediment resulted in thicker flows, due to the lower settling velocity and greater ease of suspension, agreeing with laboratory observations [Garcia, 1994].

Additional canyon flows have been observed off the coast of France [Khripounoff et al., 2009, 2012] and Taiwan [Liu et al., 2012]. The flows recorded in the Gaoping submarine canyon by Liu et al. were due to flooding caused by cyclones, and a possible 'waxing and waning' effect was seen that was non-tidal. Two of the three flows recorded by Khripounoff et al. were also caused by flooding, however the third was believed to be caused by the collapse of part of the canyon wall and as such showed different characteristics. As would be expected, the flooding currents were of a lower sediment concentration and subsequently thicker and slower. More recently, data has been recorded in the Congo canyon [Azpiroz-Zabala et al., 2017]. Flows of varying thicknesses were observed, with significant temporal variation in the secondary flow field.

Although canyon currents provide a good basis for learning more about field scale flows, it is likely they are smaller than their bounding topography and fully-confined, unlike channelised flows which scale with the size of the system and overspill onto the channel levees [Peakall and Sumner, 2015]. The effects of confinement could have a significant effect on flow dynamics [Kassem and Imran, 2004].

There are however some data sets available for partially-confined channel flows. Khripounoff et al. [2003] and Vangriesheim et al. [2009] present data from the Congo submarine channel at a depth of 4000 metres. These provided some insight into the bulk properties and temporal variations in the flows, with mean hourly velocities of the order 1-3 m/s observed. Peak velocities could have been larger. Sediment traps also indicated flow durations of as much as 10 days, although the peaks were closer to 3-9 hours in length. Despite this, the data was purely one dimensional and stationary, so detailed analysis of the currents is limited.

More detailed transect data is available from a saline exchange flow in the Bosphorus Strait [Parsons et al., 2010; Sumner et al., 2013, 2014; Dorrell et al., 2014, 2016]. The Black Sea has a constant salinity deficit to the Mediterranean which results in the gravity current that flows through a curved channel. Flow features include super-elevated flow at the outer bank with significant radial and vertical stratification and reversed helical secondary flow (see Chapter 6). The flow is mostly confined within the channel but does display some overspill. Whilst the vertical stratification featured a very defined stepped profile, this could be attributed to the nature of the flow. Not only is it non-depositional due to the lack of sediment but it also has a low Froude number of 0.41 and thus different to the expected flow properties of larger deep marine systems.

2.1.9 Turbidity currents: initiation and deposition

Volumetrically, turbidity currents are the most important sediment transport process on Earth [Talling et al., 2015]. Up to hundreds of metres deep and reaching speeds of 70 km/h [Piper et al., 1999], a single current can transport over ten times the annual sediment flux from all of the Earth's rivers combined [Talling et al., 2007]. As has been stated above, they have the ability to severe seafloor cables which carry >95% of trans-oceanic data traffic [Carter, 2009], destroy pipelines and are linked to tsunamis [Meiburg and Kneller, 2010].

Piper and Normark [2009] identify three main initiation processes that can trigger turbidity currents:

i) the transformation of slides, slumps and debris flows (often caused by earthquakes) through the entrainment of additional ambient water;

ii) discharge of highly concentrated hyperpycnal flows from the mouths of rivers;

iii) oceanic processes, including storms, tides and internal waves, that provide a means of suspension for coastal and shelf sediment.

Once triggered, the run-out and life of a current is a function of several variables including, but not limited to, sediment load and grain size, slope, channel morphology and surrounding topography, entrainment rate and supply from the source. Normark and Piper [1991] claimed a sufficient slope gradient was required for the flow to be maintained but it has since become clear that the situation is more complex than this. Currents in the North Atlantic Mid Ocean Channel (NAMOC) and the Bengal Fan can stretch for thousands of kilometres out onto the relatively flat abyssal plain (< 0.3º).The presence of subcritical flows [Pirmez and Imran, 2003], exhibiting far more stable stratification levels resulting in a lower entrainment rate and a subsequently lower upper boundary drag, could help explain these vast run-out lengths (Kneller et al., 2016). This, however, contradicts current autosuspension theory and flows of this character are not thought to be capable of being self-sustaining for such long distances [Pantin, 2001].

Turbidity currents are self-channelising, to say that their own sediment deposits form the channels and fan systems that act as their conduits. Knowledge of how and where the currents deposit sediment is of vital importance to both the understanding of system development and also predicting the location of viable hydrocarbon reservoirs. The morphology and characteristics of these channels is discussed in the next section.

2.2 Submarine fans and channels

Submarine fans form the largest sediment accumulations on the planet [Talling et al., 2015]. They also provide vital records of previous tectonic history and climate cycles and are economically important as hydrocarbon reservoirs. The following section describes the different classifications of fans and channels and describes their morphology and evolution.

2.2.1 Classifications

Submarine fans and channels all bear the similarity of being conduits for turbidity currents but they can be very different in nature. Peakall and Sumner [2015] identify six distinct geomorphological types (Figure 2.6). The first of these is the 'arteries and veins' type systems which are the largest subset and form the classic fan-like shape. As such, when reference is made to submarine fans in this review, it is this type of system which is being described and which will be most focussed upon. They are usually directly connected to the mouths of rivers, examples being the Amazon, Congo and Bengal fan, which provide a rich supply of sediment. Due to their size, location, the area they cover and the currents they carry, they are also the best candidate for sources of hydrocarbon reservoir [Mayall et al., 2006; Talling et al., 2015]. Submarine fans, generally stretching from the continental rise to the abyssal plain, are often connected to fluvial systems via submarine canyons or slope valleys running down the continental shelf. Examples of these are the Gaoping and Monterey canyons described previously [Xu, 2010; Liu et al., 2012]. It is possible for successive currents to cause aggradation and channels to form within these structures. This has been observed both at the mouths of the Niger [Deptuck et al., 2007]

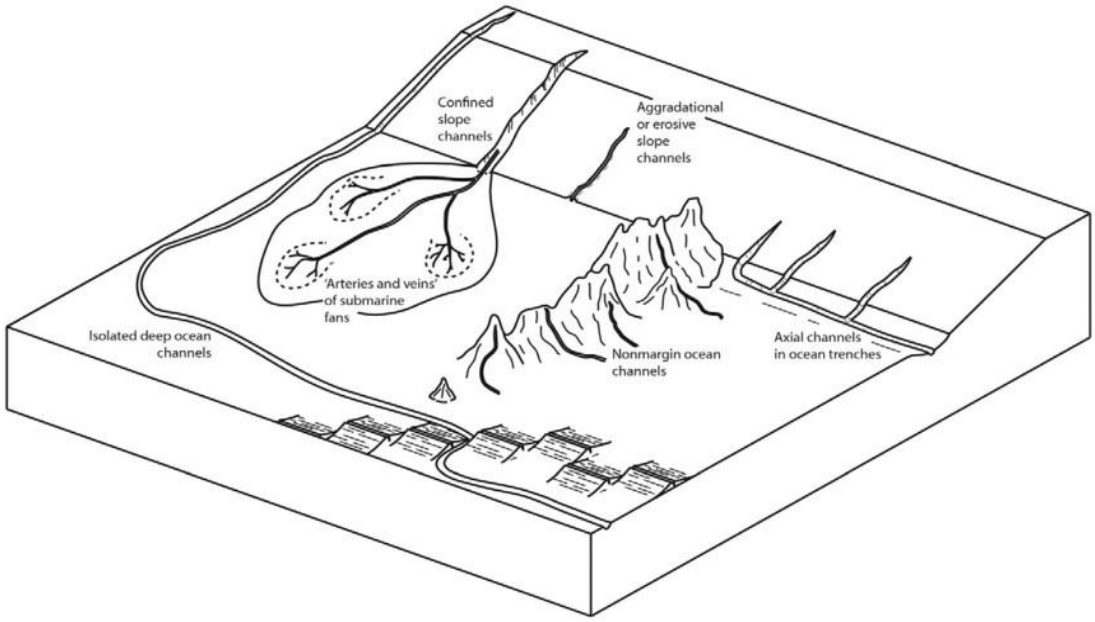

Figure 2.6 Drawing of the different classifications of submarine channels [Peakall and Sumner, 2015].

and the Nile [Samuel et al., 2003]. These ‘confined slope channels’ form the second discrete channel type.

The third classification to be identified are ‘isolated deep ocean channels’. These are individual channels that can achieve vast run out distances, with one example being the 3800 km North Atlantic Mid-Ocean Channel (NAMOC) [Klaucke et al., 1998]. The currents that travel these distances can redistribute not only sediment but also important nutrients and organic material. Depending on the nature of various channel flows on Venus (believed to be formed by lava flows), it is also possible the NAMOC is home to the longest particulate flows in the solar system [Peakall and Sumner, 2015].

The other channel types to be observed are: ‘axial channels in ocean trenches’ (e.g. the Chile Trench [Thornburg and Kulm, 1987]), ‘slope channels’ (similar to confined slope channels but without the surrounding canyon environment) and ‘non-margin ocean channels’ found far out in the basin with non-terrestrial sediment sources such as volcanic seamounts [Gardner, 2010].

2.2.2 Morphology and Geometry

Submarine fans come in all shapes and sizes, from a few kilometres across such as the numerous systems off the coast of California [Shepard and Buffington, 1967], to the giants that stretch for thousands of kilometres out into the deep ocean such as the Bengal Fan [e.g. Galy et al., 2007]. The nature of these fans has numerous controls, including the surrounding topography, sediment sources and even the latitude at which they occur [Cossu et al., 2015]. Whilst the fans do indeed resemble arteries and veins, there is usually only one active channel at a time [Anka et al., 2009]. This continues until avulsion occurs due to successive infilling of the channel [Dorrell et al., 2015], whereby the current breaks out of the confining channel, often at a bend, and begins to form a new active strand. This process is what results in the formation of fans over geological timescales [Amos and Peakall, 2006].

Submarine channels share a lot of geometrical similarities with their fluvial counterparts. Meander wavelength, radius and channel width ratios have all been shown to be comparable to some of the world's largest fluvial systems [Clark et al., 1992]. Despite these similarities, it would appear that correlations between certain parameters, such as slope and channel sinuosity, are weaker for the submarine environment and that crucial differences, such as the far smaller density difference between fluids, mean the controls on channel development are subsequently far more complex [Kolla et al., 2007]. Most of the knowledge of deep-water morphology has been gained through the use of 3D seismic data and bathymetry. Indeed, Kolla et al. found that, despite the general similarities between fluvial and submarine geometry, there are significant differences in both the internal channel architecture and in how the systems evolve. It is common to find submarine channels contained within a larger channel, sometimes referred to as the 'master channel' [Posamentier and Kolla, 2003]. Due to super-elevation and overspill, turbidity currents can have significant interaction with this environment [Straub and Mohrig, 2008]. Fluvial and submarine channels can also migrate in different ways [Kolla et al., 2007]. Whereas fluvial systems shift continuously laterally with a downstream component, submarine channel migration can be far more complex [Peakall et al., 2000]. It can be continuous or discrete, laterally moving or vertically aggrading, with or without a downstream component due to the far greater variety of flows that can occur [Peakall and Sumner, 2015].

These differences are thought to be caused not only by the relatively smaller density difference between fluids, but also by the effect of Coriolis forces, behaviour of secondary flow fields, sediment grain size, the frequency and duration of flows (which for turbidity currents are far more varied) and even changes in sea level. It would also seem that submarine channels tend towards attaining a steady state [Peakall et al., 2000; Wynn et al., 2007]. Rivers will increase their sinuosity due to erosion at the outer bends and deposition at the inner bends. This can continue until the formation of an oxbow lake, whereby the river cuts off an entire meander. This is not generally observed for submarine

channels, which seem to find a state of equilibrium at a certain sinuosity (Figure 2.7) [Peakall et al., 2000]. The channel continues to aggrade to a point at which it becomes unstable and a turbidity current avulses by breaking through the outer levee due to internal forcing (Figure 2.8) [Dorrell et al., 2015]. This achievement of a spatio-temporal stability points to a fundamental difference in the flow dynamics. Whilst inner bend deposits have been observed in both system-types [Klaucke and Hesse, 1996], outer bend deposits (sometimes referred to as 'nested mounds') are believed to be unique to submarine channels [Peakall et al., 2000]. It is these nested mounds that allow the planform equilibrium to be achieved and Kane et al. [2008] experimentally showed this to be directly related to the degree of flow bypass (the amount of flow passing a point that is non-depositional).

Different submarine channels can attain a wide range of sinuosities, from very straight channels such as the NAMOC to highly meandering systems such as the Indus Fan [Clark et al., 1992]. Possible reasons for this have been described above, but Mayall et al. [2006] believe they can be categorised into four causes: an initial erosive base, lateral stacking, lateral accretion and sea-floor topography. Not included in this list however, is the more recent proposition of Peakall et al. [2012] that the Coriolis forces (and thus the latitude) have a large impact on the degree of sinuosity. This challenges the previous view that systems could largely be classified into high-sinuosity, low-gradient, fine-grained, and

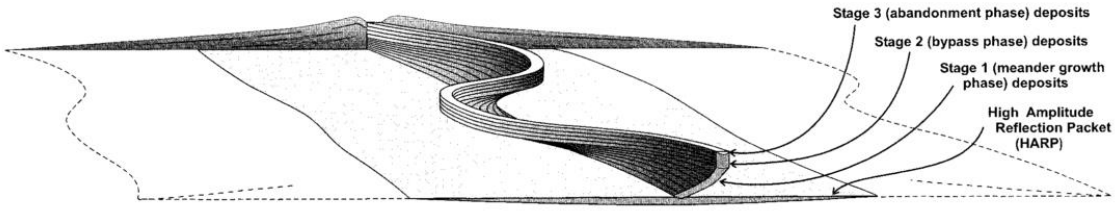

Figure 2.7 A diagram showing the aggradational model proposed by Peakall et al. [2000]. An initial growth phase exists where the channel's sinuosity increases. An equilibrium phase is then reached during which the channel aggrades upwards with no change in planform, before eventually avulsing and being abandoned.

low-sinuosity, high-gradient, coarse-grained categories. The latitude-sinuosity correlation has been contested though [Sylvester et al., 2013] so, whilst the Coriolis effect may be a significant factor, it is likely one of many.

While the intrachannel architecture is the biggest controlling factor on the flow dynamics, it is the levees that make up most of the system volume. They can have widths many times that of the channel, stretching for tens of kilometres, and are constructed via the deposition of current overspill [Birman et al., 2009]. Constituted of many laterally continuous beds, knowledge of their thickness is vital in characterising subsequent hydrocarbon reservoirs [Skene et al., 2002]. Skene et al. proposed that levee thickness decays exponentially away from the channel, while Kane et al. [2007] claimed a power law decay. Field data has shown both of these to be possibilities [Nakajima and Kneller, 2013] and Birman et al. [2009] developed both an analytical and numerical model to show that the amount of entrainment of ambient fluid is the deciding factor. Nakajima and Kneller [2013] conducted a thorough analysis of much of the available topographic data. They found the axial slope of the channel could be used to divide the two regimes (although this is intrinsically linked with entrainment levels), with steeper slopes (> 0.6º) exhibiting power law decay and shallower slopes an exponential or logarithmic decay. This threshold

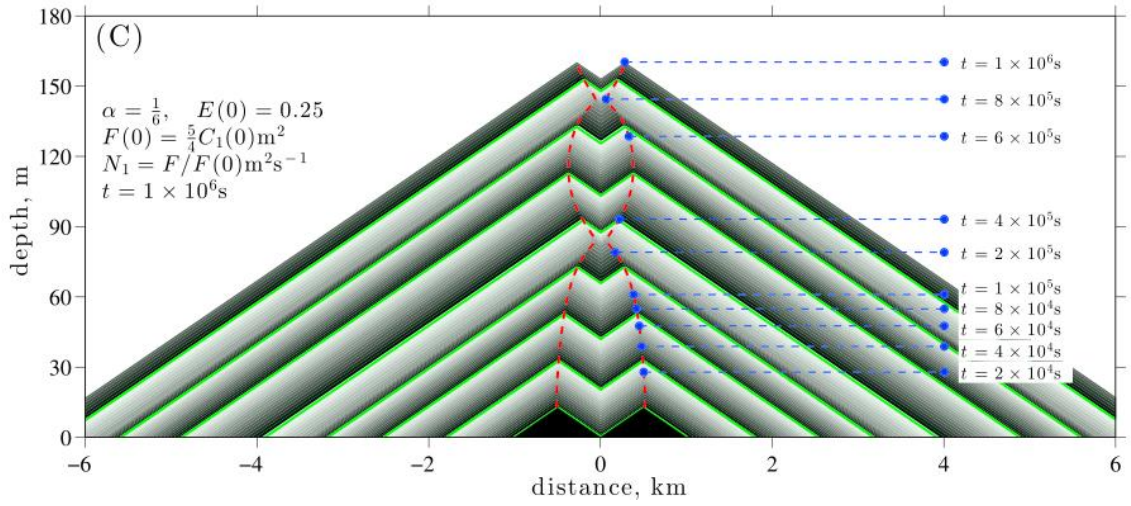

Figure 2.8 A model developed by Dorrell et al. [2015] shows how successive depositional flows can result in channel instability by infilling the channel. This process could lead to eventual channel avulsion.

gradient was shown to vary though and it was proposed this could be due to a grain size effect (which affects settling velocity). Regardless of which decay rule is employed, the fit to the data close to the levee crest (within a channel width) is often unsatisfactory and a different characterisation method is needed here.

2.3 Experimental modelling of gravity currents

The limitations of field data, outlined previously, means experimental modelling is vitally important in the investigation of the dynamics of gravity currents. Kuenen [1938] was the first to undertake laboratory tests. These were simply observational in nature, aimed at identifying bulk flow properties. Since then, aided by advancement in technology and a development in the wider knowledge of the field, experimental work moves on to ever greater heights.

As has been previously described, gravity currents are created in the laboratory via one of two methods: the opening of a lock gate to release a surge of denser fluid or the use of a continuous inlet pump. Respectively, these two methods reflect either surge type currents associated with slumping and slides or longer, quasi steady-state currents often resulting from concentrated hyperpycnal flows at the mouths of rivers. De Rooij and Dalziel [2001] found that lock release currents form a more pronounced head, due to the greater initial internal forcing, and that this is where deposition was most active, in contrast to continuous currents whose deposition is dominated by the body. Peakall et al. [2001] therefore claim that the use of lock gate currents has led to too much focus being placed by researchers on the effect of current heads. They go on to suggest that flows produced via an external input tank are in fact not only the most suitable method for modelling continuous currents, but also surge-type currents.

As well as there being two methods for the release of the current, there are also two main methods for achieving a density difference between the current and ambient fluid. The

first and most straightforward of these is the use of salt to create a saline solution. The second method is the use of sediment to create a particulate solution. Note that these two methods can be mixed to create a hybrid solution. The use of a particulate current enables the study of erosion and deposition. However, the issue of scaling arises and, due to the much lower Reynolds numbers of laboratory scale flows, the currents often never achieve autosuspension. Additionally, the very fine sediments needed for scale are dominated far more by electrostatic forces than an equivalent grain of sand would be. This often results in flocculation and these bigger particles soon drop out of the flow.

2.3.1 Technologies and techniques

Modern-day experimental techniques for the study of gravity current dynamics can predominantly be split into two categories: Doppler shift technologies and particle imaging techniques. The Doppler shift category consists of laser Doppler anemometry (LDA), ultrasonic Doppler velocimetry profiling (UDVP) and acoustic Doppler velocimetry (ADV). The high frequency attainable with LDA allows the calculation of turbulent variables and Buckee et al. [2001] used it to generate vertical turbulence profiles. However, it requires both fluid phases to be of the same refractive index and only measures in two dimensions at a single point. More recently, ADV has been used to capture turbulence characteristics [Islam and Imran, 2010; Cossu and Wells, 2012]. This would appear to be a clear upgrade as it does not require refractive index matching and can measure in 3D at up to 100 Hz. It can also be used both at a point and as a profiler. UDVP, although not as capable of capturing the turbulent characteristics of a flow due to its lower inherent frequency, does allow the production of entire planes of mean flow velocities, thus enabling the visualisation of flow features such as the secondary circulation cells observed by Keevil et al. [2006] (Figure 2.9 and described further in Chapter 6). Whilst it does require a certain flow depth to be effective, it can cover much wider ranges than ADV.

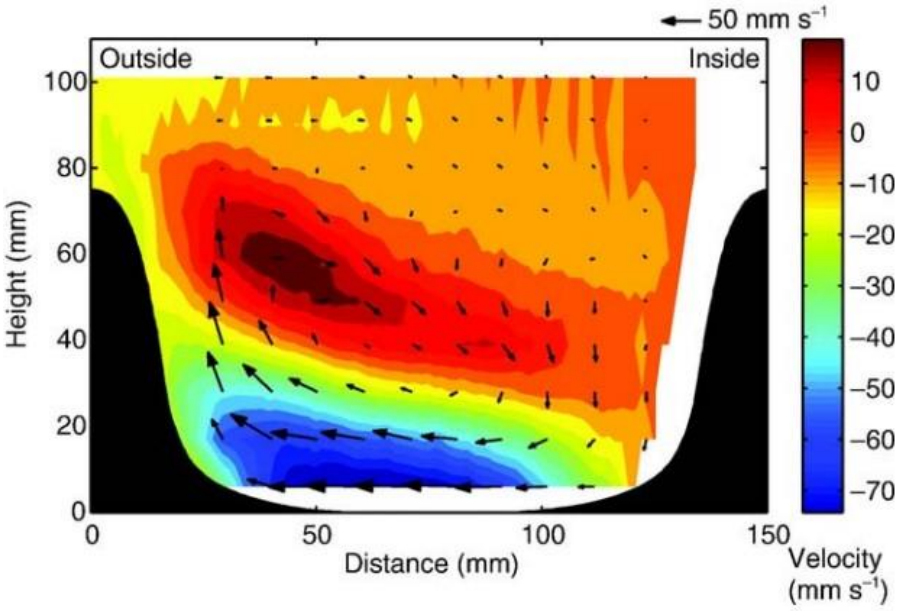

Figure 2.9 A cross-sectional cross-stream velocity contour of a gravity current [Keevil et al., 2006]. An example of the data and flow visualisation that can be achieved using acoustic Doppler technologies.

2.3.2 Straight channel studies

The majority of experimental work has taken place in straight channels. These come in many forms and can either be fixed [e.g. Ellison and Turner, 1959], have erodible beds [e.g. Parker et al., 1987] or be fully erodible [e.g. Straub and Mohrig, 2008; De Leeuw et al., 2016]. Cross-sections have ranged from rectangular to trapezoidal shapes.

Studies have often focussed on the vertical structure of currents, as this can give great insight into the behaviour and transportation abilities of a flow [Sequeiros et al., 2009]. These have ranged from identifying the profiles of mean quantities such as velocity and concentration [e.g. Ellison and Turner, 1959; Middleton, 1966; Garcia, 1993, 1994; Altinakar et al., 1996], to the characterisation of turbulence structure [e.g. Kneller et al., 1997, 1999; Buckee et al., 2001; Islam and Imran, 2010]. Additionally, Sequeiros et al. [2010] examined the effect that bedforms can have on the flow. Although erodible beds

had been used before [Garcia, 1993], their explicit impact had not been identified. It was shown that they could have a significant effect on both sub- and super-critical regimes, with their presence leading to a velocity maximum higher in the channel. Stagnaro and Pittaluga [2014] disputed the findings of Sequeiros et al., finding little variation in flow dynamics when varying Froude number over a smooth bed. They did however observe some dependence on Reynolds number.

Eggenhuisen and Mccaffrey [2012] also observed changes in the flow structure when encountering a basal obstruction. Levels of turbulence within the inner region were significantly increased and this was dissipated upwards as the current travelled downstream. They concluded that this could lead to a "non-equilibrium net-upwards transport of sediment" that could counteract the effects of stratification and the presence of the previously described slow diffusion zone (SDZ). Additional flow phenomena have been investigated in straight channels. Ho et al. [2018] explored the dynamics of pulsed flows which are known to occur during storm flushing episodes in canyons. These were found in most cases to merge to form a single flow with implications for flow signatures found in deposits.

Using erosional channels, Straub and Mohrig [2008] were able to link the vertical density structure to rate of levee growth. The volume of sediment in the outer region, plus the level of confinement of the flow, determined the degree of deposition on the outer banks. De Leeuw et al. [2016] conducted experiments over an initially featureless slope. Channel inception was shown to occur via levee deposition and intrachannel erosion in different areas of the flow.

2.3.3 Sinuous channel studies

Over the past decade, more focus has been placed on the study of sinuous channels. Keevil et al. [2006] presented some of the first experimental data for submarine bends. The main finding was that gravity currents can generate river-reversed secondary flow. Cross-

stream flow at the bend apexes circulated in the opposite direction to that seen in rivers (Figure 2.9), with basal flow directed towards the outer bank. Keevil et al. claimed that this promotes higher levels of turbulence and could help break down the barrier presented to vertical sediment mixing by an SDZ. It was also highlighted as a possible mechanism for forming the outer bank deposits or 'nested mounds' discussed previously, that are unique to submarine channels. This reversed flow phenomenon was subject to much discussion. Imran et al., observed vertically stacked rotational cells rotating in opposite directions. Abad et al. [2011] conducted a similar experiment, albeit with a more sinuous channel. Reversed secondary flow was not observed. Using a combination of experimental results and theory, Abad et al. proposed three regimes based on the stratification of the flow and bed roughness: upper-reversed, middle-normal and lower-reversed. Subsequent analysis applied to field cases predicted flows to be lower-reversed in the Black Sea, middle-normal throughout most of the Amazon fan and upper-reversed in the Monterey Canyon. Indeed, reversed flow field data was observed by Sumner et al. [2014] in the Black Sea data (Section 2.1.8).

Using a singular channel bend, Kane et al. [2008] investigated the depositional character of identical currents whilst varying the aspect ratio and thus the level of flow confinement. Care should be taken when considering a singular channel bend, as the role of previous bends and the nature of changing secondary flow is not included. Less confined flows with a higher rate of flow bypass (non-depositional) tended to deposit at the outer bend, whilst the opposite was true for lower rates of bypass. Straub et al. [2008] conducted experiments with a series of identical flows in an erosional channel. Large levels of super-elevation were observed due to runup of the current on the outer banks. Although thicker, steeper levees grew on the outer bank, there was almost no change in planform because of deposition at both banks. Channel relief decreased though due to a greater rate of deposition at the channel base than the levees. This lack of change in planform supports the theory that submarine channels can, over the course of a few flows, achieve a spatio-temporal stability. Later, Straub et al. [2011] made a preliminary investigation into the

role of sinuosity on deposition patterns. They found a criterion for the containment of flows, in that a current is unlikely to remain confined if its kinetic energy is greater than that of the potential energy gain associated with channel relief. They also added to the view of Keevil et al. [2006] that channel bends are important in increasing the mixing intensity of a flow. It should be noted that, with the possible exception of Straub et al. [2011], all of the above studies employed largely unrealistic channel profiles with either rectangular cross-sections or high aspect ratios and steep levees. This can be attributed to the ease of manufacturing such channels and the limits placed on instrumentation.

Islam et al., [2008] conducted experiments in a channel with a trapezoidal profile and a relatively low aspect ratio of 5. This channel profile was more conducive to allowing overspill and previously observed flow patterns of vertically stacked cells were interrupted, with the upper cell being destroyed. Dorrell et al. [2018a] emphasised the role of temporal variation in the flow, with previous studies all focussing on time-averaged mean flow properties. They showed how, in the laboratory, the orientation of a rotational cell fluctuates over bend vortex-shedding time-scales, much larger than those of characteristic turbulent mixing.

2.4 Numerical modelling of gravity currents

Gravity currents have been studied via numerical methods for the best part of half a century. Daly and Pracht [1968] were amongst the first to apply computational fluid dynamic (CFD) techniques to these flows, using a ‘marker and cell technique’ which has many similarities to modern finite element methods. They recognised the value of the numerical technique in not only aiding the analytic and experimental investigations but also its ability to better examine parametric effects. With modern techniques, numerical analysis also has the potential to investigate field scale flows that are not achievable in a laboratory setting. The insight into governing effects that can be obtained through the creation of a suitable model should also not be underestimated. The validation and

evaluation process of a model can often lead to a greater understanding of the flow dynamics, through the examination of characteristics that are both present and absent in the predictions.

Modern CFD methods can be broadly split into two categories. The use of a Reynolds-averaged Navier-Stokes (RANS) model or large eddy and direct numerical simulation (LES and DNS). The former category involves solving the RANS equations on a discretised grid. To obtain these equations from the Navier-Stokes equations the instantaneous velocity $u = \bar{u} + u'$, is split into a time-averaged and fluctuating component. This introduces additional unknowns: the Reynolds stresses $R_{ij} = -\rho\overline{u_i' u_j'}$. Due to the non-linearity of this turbulent term, a closure system is required that models these and relates them to known variables. Closure is generally obtained in one of two ways, eddy viscosity models (EVMs) [Jones and Launder, 1972] or Reynolds stress models (RSMs) [Launder et al., 1975].

2.4.1 Eddy viscosity models (EVMs)

The EVM category includes the commonly used two-equation k-ϵ and k-ω turbulence models, as well as more complex variations. These have been used to study the dynamics of gravity currents by a range of authors [e.g. Eidsvik and Brørs, 1989; Bournet et al., 1999; Chen and Lee, 1999; Choi and Garcia, 2002; Kassem and Imran, 2004; Huang et al., 2005, 2008; Imran et al., 2007; Paik et al., 2009; Giorgio Serchi et al., 2011; Ezz and Imran, 2014; Arfaie et al., 2018]. All EVMs share a common method in that they employ the Boussinesq hypothesis [Boussinesq, 1877],

$$\frac{R_{ij}}{\rho} = -\overline{u_i' u_j'} = -\frac{2}{3}k\delta_{ij} + \nu_t\left(\frac{\partial \bar{u}_i}{\partial x_j} + \frac{\partial \bar{u}_j}{\partial x_i}\right). \tag{2.12}$$

This relates the eddy viscosity, ν_t (the transport of momentum due to turbulent eddies), to the Reynolds stresses via the corresponding velocity gradients. The eddy viscosity is

usually calculated from other known variables such as turbulent kinetic energy, k, and turbulent dissipation, ϵ, which are found via the use of transport equations. A common problem, encountered by Eidsvik and Brørs [1989] and investigated by Stacey and Bowen [1988], is that of an over prediction of the stratification levels which results in a highly stepped flow. This is attributed to a lack of diffusion of mass through the velocity maximum due to a low eddy viscosity magnitude at this point (corresponding to the low velocity gradient) and as such would appear to be a weakness of all EVMs.

Despite this, good agreement with experimental data has still been achieved in a variety of ways. Choi and Garcia [2002] managed to get closely match vertical profiles using a k-ϵ model, although the tuning of an empirical constant found in the *transport* equation which is responsible for the amount of turbulence production due to buoyancy was required. Alternatively, Huang et al. [2005] investigated the effect of altering the turbulent Schmidt number, $Sc_t = \nu_t/K_t$, where K_t is the eddy diffusivity (the transport of mass due to turbulent diffusion). This is usually assumed to have a value of 1 but a value of 1.3 appeared to improve predictions. Tominaga and Stathopoulos [2007] commented on this in a review of the effect of Sc_t on a range of flow types and interpreted it as "a decrease in the turbulent diffusivity in order to take into account the decay of turbulence due to density stratification". What neither Huang et al. nor Tominaga and Stathopoulos noted though was that there is no requirement for Sc_t to remain constant and that indeed it is likely to vary throughout the flow.

Paik et al. [2009] adopt a slightly different approach to others in that they use a low-Reynolds number version of the k-ϵ model, which they claim is more suitable for simulating laboratory scale flows. Indeed, this resolved three dimensional characteristics such as Kelvin-Helmholtz instabilities. These are generally not seen in other RANS simulations which generally predict more diffused patterns at the ambient interface. Previously, these have only been modelled using more complex and expensive techniques such as LES and DNS [Hartel et al., 2000a,b; Necker et al., 2002, 2005]. However, it is

debatable how realistic these results are, with these flow features rarely reported in the laboratory.

Kassem and Imran [2004] used the standard k-ϵ model to study the effects of confinement and levee steepness on the evolution of a gravity current. The unconfined cases saw a lesser degree of flow thickening due to entrainment because of lateral spreading and overspill. The vast majority of the numerical literature cited above considers straight channels. Whilst this means easy validation of the model against experimental data and simplifies the meshing and set up process, it is arguably not as relatable to many submarine systems.

Some studies have been conducted using numerical models in sinuous channels to study the effect of a channel's curvature on current dynamics and evolution. Kassem and Imran [2004] were the first to do so and chose to use the k-ϵ model, whilst Das et al. [2004] used a simpler depth averaged model. Imran et al. [2007] ran some simulations in conjunction with experiments and reproduced the vertically stacked cells observed in the laboratory. Giorgio Serchi et al. [2011] also focused on the secondary circulation debate showing how both rotational directions can occur. A persistent problem throughout the literature is the use of unrealistic channel profiles, presumably due to the greater ease of simulation setup. All the literature cited above utilise rectangular cross-sections. Ezz and Imran [2014] make use of the same trapezoidal profile as that used by Islam et al. [2008] in the laboratory. The slope of the intra channel bank was found to have a large impact on flow dynamics, highlighting the need for further investigation of the role of channel morphology.

2.4.2 Reynolds stress models (RSMs)

The RSM option is the less common choice due to an increased computation time and a higher level of difficult in achieving convergence. This is because, rather than using an eddy viscosity concept to find the Reynolds stresses, each stress is computed using a

separate transport equation. Despite the increased complexity, it is a little surprising at the small amount of literature available relating to gravity currents. Brørs and Eidsvik [1992] followed up their EVM analysis with the use of an RSM and claim significantly better results. Comparisons with experimental observations however is limited to early data [Ellison and Turner, 1959] and no direct contrast with the EVM predictions is presented so it is hard to explicitly see the differences. Other than this, few other authors appear to have carried out numerical analysis via this method.

2.4.3 Large eddy simulation (LES) and direct numerical simulation (DNS)

Recent computational work has often focussed on the use of more advanced solvers such as LES and DNS. The increased computational expense is the limiting factor for these simulations. DNS numerically solves the Navier-Stokes without the use of any turbulence models such as those described in the previous sections. This places certain requirements on the mesh since every spatial and temporal scale must be resolved, from the small Kolmogorov dissipative scales, $\eta = (\nu/\epsilon)^{0.25}$, to the large integral scale L, which relates directly to the size of the largest turbulence structures. The mesh requirements are thus,

$$N\delta x > L, \qquad \delta x \leq \eta, \tag{2.13}$$

where N is the number of mesh nodes and δx is the cell size. LES uses similar techniques but there are no such mesh requirements. Scales below that of the grid are filtered out and modelled (often with similar techniques as for RANS models), whilst those captured by the grid are solved 'directly' as with DNS. As such, there is no such as thing as a mesh independent LES.

The first DNS investigations pertaining to gravity currents were conducted by Hartel et al. [2000a,b] who examined the head dynamics of a lock-release current. 3D simulations up to Re = 750 captured the expected lobe and cleft features, previously not observed in a numerical model. Runs up to Re = 30000 had to revert to 2D due to computational

limitations, but cases run on a free slip base agreed closely with the inviscid theory of Benjamin [1968] (Section 2.5). Necker et al. [2002, 2005] and Blanchette et al. [2006] conducted similar studies, again just concerning the initial stages of a lock-release current in a rectangular channel. It was found that, whilst 2D and 3D simulations agreed at early development times in terms of flow advancement, significant differences including large, unnatural billows occurred over longer time-scales. This would appear to be a common issue with 2D simulations [e.g. Cantero et al., 2007; Nasr-Azadani and Meiburg, 2011; Kneller et al., 2016] due to a lack of turbulent dissipation in the lateral direction. The only higher Reynolds number currents to be computed in 3D are by Cantero et al. [2008] who resolved a Re = 15000 flow using a 131 million node mesh. They identified four zones of turbulence:

i) zone 1 - the part of the head close to the interface where the shear layer leads to the production of vortices;

ii) zone 2 - the part of the head close to the wall which resembles a turbulent boundary layer;

iii) zone 3 - upstream (towards the body from the head) from zone 1, where the vortices mature and break up;

iv) zone 4 - upstream of zone 3, where the turbulent structures from zone 2 and 3 begin to interact.

Whilst all of the above studies studied a saline type current, Cantero et al. [2009] extended the approach to particulate currents and studied the effect particle settling velocity can have via altering the stratification of the flow. It was found that particles with a higher settling velocity could stratify a flow to such an extent that the flow relaminarised below the velocity maximum, thus completely preventing any turbulent mass or momentum transfer vertically through the flow. This can be seen as an extreme case of the SDZ.

The only study to apply LES (or DNS) to curved channels is by Mahdinia et al. [2012] (Figure 2.10). The secondary flow topic is addressed as reverse flow is observed, although it is pointed out that the lock exchange current could well have different dynamics to the previous continuous currents of interest in this area [e.g. Keevil et al., 2006; Abad et al., 2011]. Other observed characteristics include intensified turbulence close to the inner wall and an increase in near-bed turbulence and a reduction in secondary flow strength as channel radius is increased. Good agreement with experimental data leads to Mahdinia et al. claiming valid simulations could be run even on medium cell-number meshes. It should be noted that the expense and complication of LES and DNS has limited all studies to finite volume releases with no input or output conditions, in rectangular, fully confined

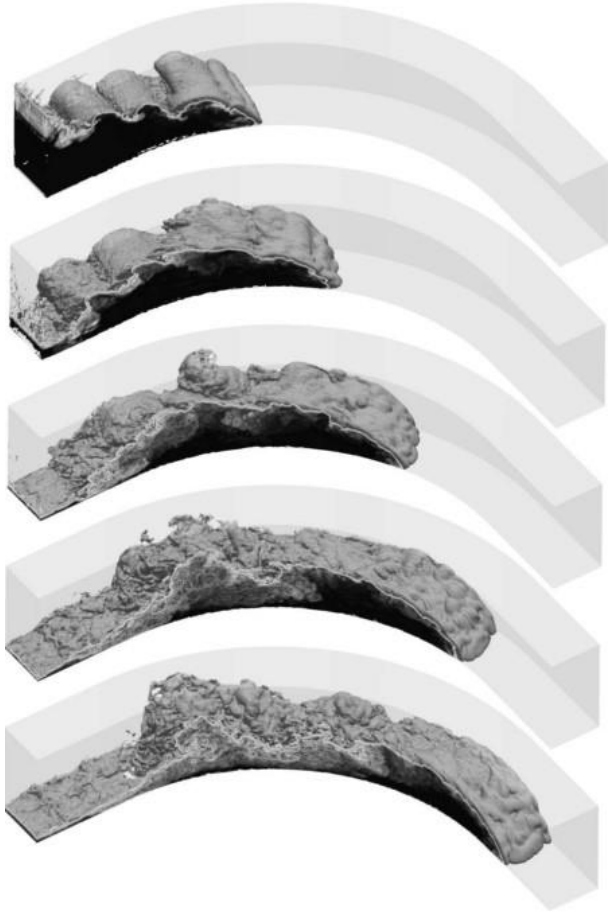

Figure 2.10 The only LES study to date which investigates dynamics in a curved channel [Mahdinia et al., 2012]. A density isosurface visualises the ambient interface as the current traverses the channel. Currently, LES and DNS are too computationally expensive to model complex geometries or larger Reynolds numbers.

channels. Ever-increasing computational resources undoubtedly mean there is the opportunity to extend this to more realistic geometries in the future.

2.5 Theoretical modelling of gravity currents

Theoretical and analytical models have the ability to develop our fundamental understanding of gravity currents by the illuminating the explicit effects of specific variables. They can be used to study all aspects of the field, from the dynamics and development of the currents to the evolution of the containing channels.

Early theoretical work conducted in association with gravity currents focussed on dimensional analysis, including the seminal papers of Benjamin [1968]. His theory was based upon energy conservation and a depth-averaged approach, where one value for a variable is adopted for the entire height of the flow. This laid the groundwork for many subsequent models such as those outlined by Holyer and Huppert [1980] and Shin et al. [2004]. The main derivation of Benjamin was that of the current velocity for an inviscid flow in deep ambient,

$$U = \sqrt{2g'h}, \tag{2.14}$$

where $\sqrt{2}$ is in fact the Froude number. The proportionality relation $U \propto \sqrt{g'h}$, had already been derived by von Karman [1940] by applying the Bernoulli condition along the upper current interface. However, this is invalid in deep water since the interface must be dissipative and as such Bernoulli cannot be applied [Simpson, 1999]. Shin et al. [2004] found an alternative treatment of Fr = 1. Experimental work by Huppert and Simpson [1980] indicated a relationship between the Froude number and the fractional depth h/H, where h is the current height and H is the ambient height.

These dimensional analyses are of course very simplified and idealised. Later models have tried to add increasing levels of complexity. Once method of doing this is via the

use of box models to analyse the development of finite volume releases. These split the flow into several horizontal layers, with each layer being depth-averaged rather than the entire flow height. Whilst the assumption is made that a single variable can represent the flow horizontally, several experimental results have shown this not to be the case and that significant flow development can occur [Garcia, 1993; De Rooij and Dalziel, 2001]. Despite this, several authors [Huppert and Simpson, 1980; Hogg and Huppert, 2001] have had success predicting depositional patterns and flow intrusion using this method. When balancing gravitational and inertial forces (viscous forces can be ignored until the flow is so stretched that $Re < 2.25$ [Bonnecaze et al., 1993]), it is found that the current front evolves as $t^{2/3}$ [Meiburg and Kneller, 2010].

Currently, the highest level of complexity belongs to models based upon the shallow water equations. These start from Navier-Stokes and invoke Boussinesq and hydrostatic approximations. Traditionally they have been depth-averaged [Rottman and Simpson, 1983; Bonnecaze et al., 1993], thus assuming a well-mixed flow with uniform sediment distribution. They also assume zero net entrainment-detrainment at the interface. Both of these assumptions would appear questionable, however shallow water models have the ability to study horizontal variations in the flow. For deep ambient, single layer shallow water equations hold such that conservation of mass can be written as,

$$\frac{\partial h}{\partial t} + \frac{\partial}{\partial x}(Uh) = 0, \tag{2.15}$$

and conservation of momentum as,

$$\frac{\partial}{\partial t}(Uh) + \frac{\partial}{\partial x}(U^2 h + g' h^2) = 0. \tag{2.16}$$

For shallow ambient, a two-layer approach is required in order to capture the dynamics of the upper layer [Bonnecaze et al., 1993]. For most situations though, these equations require numerical solutions. The horizontal variation in the models has allowed authors to identify certain phases in the life of a current. Rottman and Simpson [1983] observed

an initial ‘development’ phase in which the current is travelling at a constant speed. This is followed by a ‘self-similar’ phase once the head effects dissipate and the turbulence of the body overtakes it. In this phase, velocity decreases as $t^{-1/3}$.

Models have also been developed to study the vertical variations in currents. Stacey and Bowen [1988] were the first in this regard. Equations for velocity and concentration profiles were derived from those of momentum and diffusion. Numerical solutions saw a strong dependence on the Richardson number. More recently, both Dorrell et al. [2013] and Bolla Pittaluga and Imran [2014] have developed models with the respective aims of characterising secondary flow and deriving vertical profiles. The model of Dorrell et al. cites radial material transport as a key control on secondary flow orientation and that reversed flow may be far more likely in the field than was previously predicted by Abad et al. [2011]. The model of Bolla Pittaluga and Imran achieves relatively good agreement with experimental data for both straight and sinuous channels. However, both models have been subject to criticism [Peakall et al., 2014; Bolla Pittaluga et al., 2014] for not fully charactering three dimensional effects seen in curved channels. Interestingly, the models of all three sets of authors described above require a profile of eddy viscosity as part of the input. The lack of knowledge in this area highlights a source of error with unknown magnitude.

Finally, a theoretical approach has also been taken in regards to channel evolution by Dorrell et al. [2015] (Figure 2.8). This contradicts an earlier view that channel avulsions can be linked to changes in sea level [Maslin et al., 2006] and instead says the process is driven by internal forcing due to the current infilling the channel. The model does assume that levee steepness remains constant, whereas records show that levee steepness grows as the channel aggrades to higher heights above the sea floor [Peakall and Sumner, 2015].

2.6 Summary

Both the dynamics and structure of gravity currents have been described, followed by an outline of submarine channel morphology and classification. There exists a relatively wide range of studies relating to gravity current dynamics, including laboratory experiments, numerical simulations and theoretical models. Despite this, laboratory experiments remain limited, with highly idealised channel models prevalent throughout. This is also the case for numerical simulations, with an additional limitation placed on complex modelling techniques (LES and DNS) by computational resources. Altogether, this highlights the need for studies utilising channel geometry representative of field observations to fully capture the effect of channel morphology and ascertain the extent to which it controls the flow.

Chapter 3

Laboratory methodology and design

3.1 Introduction

A suite of experiments was conducted in the Sorby Environmental Fluid Dynamics Laboratory to investigate the dynamics of partially-confined turbidity currents. Both velocity and density data were recorded as saline gravity currents traversed fibreglass channel models. The currents were quasi steady-state in nature, maintained by continuous pumping of the saline solution into the laboratory flume for a set duration. This has several advantages over a lock-release style current as has been previously described; most notably, generating a far longer and steadier current body, allowing greater convergence in any time-averaged data. It is also a far better analogue for most natural flows [Peakall and Sumner, 2015; Azpiroz-Zabala et al., 2018]. Such quasi-steady flows are thus commonly employed in many other experimental studies [e.g. Buckee et al., 2001; Keevil et al., 2006; Stagnaro and Pittaluga 2014].

A saline solution, salt mixed with tap water, was used to create the required density difference between the ambient fluid and the current and the subsequent creation of gravity currents. There are both advantages and disadvantages to this approach compared to the use of particulates and the creation of turbidity currents. Although saline gravity currents do not take into account particulate effects, the underlying dynamics have been shown to be very similar to turbidity currents, especially velocity and density profiles, [e.g. Buckee et al., 2001; Felix et al., 2005; Cossu and Wells 2012] and are a well-established proxy [Islam and Imran 2010; Hogg et al., 2016]. Turbulence structure is also very comparable. Islam and Imran [2010] observed the same characteristic turbulent kinetic energy (TKE) profiles in both saline and particulate flows, with a low around the velocity maximum and more pronounced levels in the upper and lower shear layers.

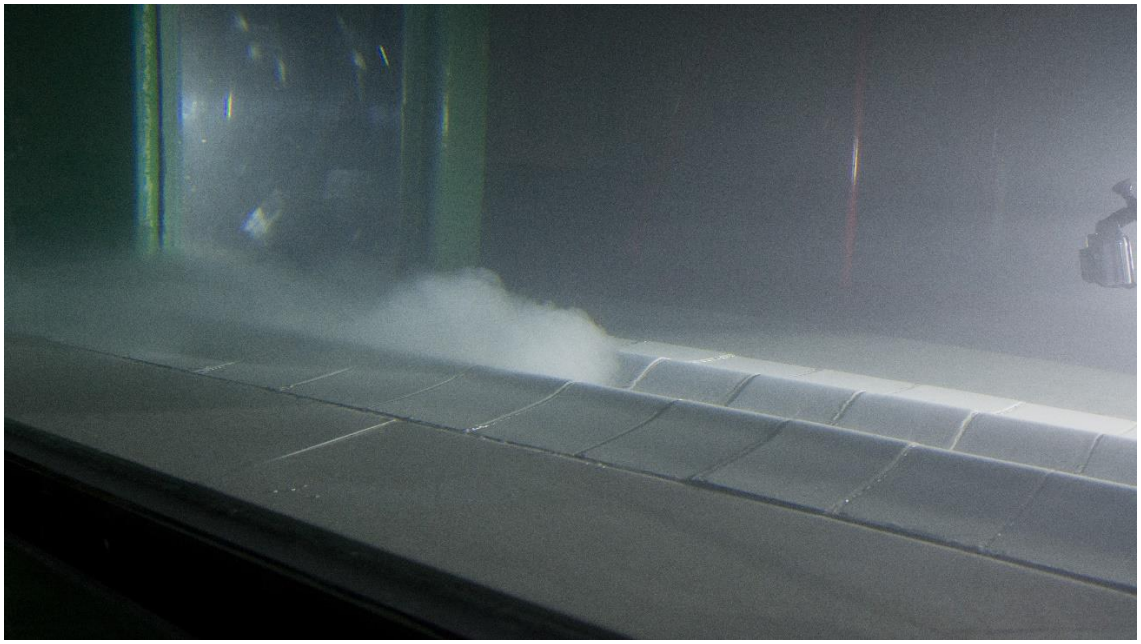

Figure 3.1 Photograph of the head of a current traversing the straight channel. A small amount of clay has been added to the flow for visualisation purposes.

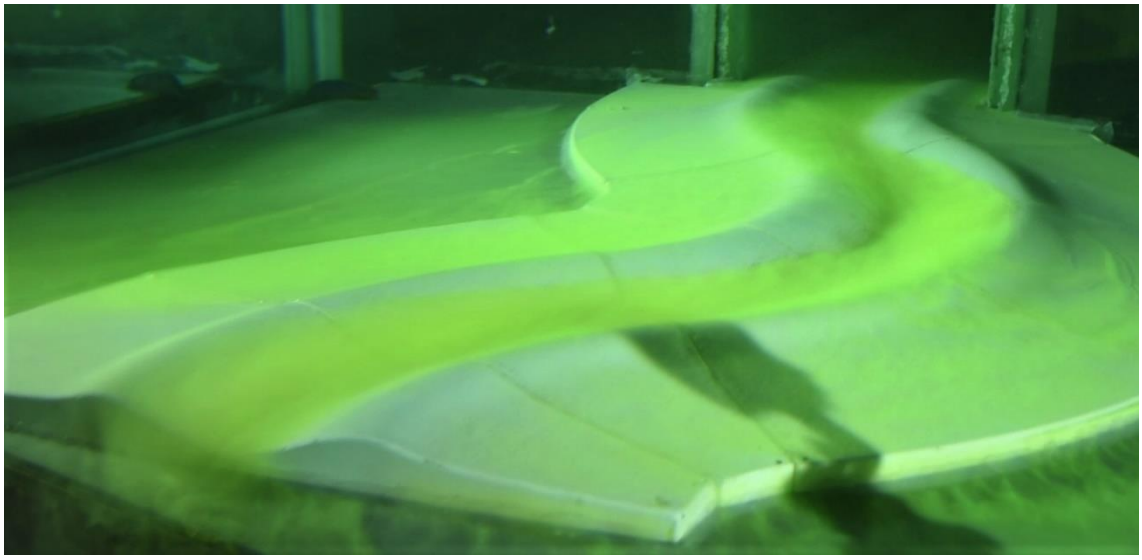

Figure 3.2 Photograph of the body of a current traversing the high sinuosity channel. The majority of the flow is confined within the channel, with overspill present on the levees. Yellow dye has been added to the flow for visualisation purposes.

Cossu and Wells [2012] showed that Reynolds stresses, viscous stresses and TKE were all broadly similar in both flow types. The advantage of a saline current is the lesser scaling issues. At laboratory scales, flows are often not large enough to enable autosuspension, resulting in premature deposition of the sediment. If sediment grain size is scaled down to the size of the flow, intermolecular forces become dominant and leads to the flocculation of grains. The resulting larger particles then drop out of the flow. An additional advantage of saline flows which should not be underestimated is the increased simplicity. A particulate solution is often far more complicated (and thus time consuming) to prepare and keep in suspension. This results in fewer experimental runs in a given time frame (laboratory time is realistically finite and resource dependent) and, subsequently, less data.

Velocities were recorded with acoustic Doppler velocimetry (ADV) which allows the capture of data with both a high spatial and temporal resolution. Ultrasonic Doppler velocity profiling (UDVP) was also briefly used to measure bulk flow properties. Both these technologies use the Doppler shift of a returning sound wave to calculate the speed of a flow. However, UDVP has a lower temporal resolution than ADV (2 Hz compared to 100 Hz) and only records the component of velocity aligned with the probe. ADV captures three-component velocities, allowing the investigation of smaller and shallower flows. Finally, density was recorded by siphoning out small samples throughout the height of the flow via a peristaltic pump. These samples could then be measured with a density meter.

3.2 Experimental facility and flume setup

All experiments were conducted in a flume in the Sorby Environmental Fluid Dynamics Laboratory (SEFDL) at the University of Leeds. The flume used was specifically designed for continuous release gravity current experiments (Figures 3.3-3.5). The main tank area is square, measuring 1.7 m x 1.7 m, and also measures 1.7 m deep. For each

experiment the flume was filled with tap water to a level of 1.5 m, measured on the downstream side of the flume. An additional inlet channel is centred on the upstream side of the tank, along which the gravity currents could develop before entering the main tank area. This measures 0.34 m wide and 1.5 m long. The section of this inlet channel along which the currents could flow (excluding the area taken up by the inlet box described later) was 1 m long. The entire flume could be tilted and, for these experiments, was set at a slope of either 2º or 0.5º. A false floor was suspended on a table 0.4 m above the base of the flume. This extended the entire length of the inlet channel. In the main tank area, there was a 0.1 m gap left to the tank walls on the downstream and side walls, giving an area of 1.6 m x 1.6 m. This gap allowed excess fluid to descend into and collect in the sump underneath the false floor and not affect the flow dynamics, allowing longer experimental durations. Flow measuring instrumentation was mounted to a mechanical traverse on top of the flume. This could be moved over the entire main tank area either manually or electronically.

The saline solution was prepared in a large mixing tank with a maximum capacity of ~1800 litres. The mixing process involved filling the tank with tap water and then adding salt manually. ADV seeding was also added at this stage, described in more detail in Section 3.5.1. The solution was mixed with a motorised impellor, always for a minimum of 15 minutes as the main tank was filled or drained. The density was then recorded using an Anton Paar DMA 35 Ex density meter to an accuracy of 0.1 kg/m^3. For all the experiments in this project, an excess density of 2.5% was used such that the density of the saline solution was $\rho_s = 1.025\rho_a$.

The saline solution was pumped into the upstream end of the inlet channel; this process was controlled by an electromagnetic flow meter to ensure minimal variation in input flow rate. Flow rates of between 0.1 l/s and 4 l/s were possible. Before entering the inlet channel, the fluid passed through a momentum diffuser. This was to ensure a gravity driven flow was produced rather than a pressure induced wall jet. The momentum diffuser was constructed as follows: a cap was placed over the input pipe; holes were drilled

through the walls of the input pipe; a pipe with a larger diameter was places around the input pipe to capture and transport the fluid once it came through the holes; mesh was placed over the end of this larger pipe. The fluid then entered an inlet box which was positioned at the start of the channel and was moulded to the same profile, with the aim of giving a smooth flow transition to the channel. A schematic of this setup can be seen in Figure 3.6. In order to ensure a fixed fluid volume in the tank prolong the possible experimental duration, fluid was pumped out of the tank at a rate equal to the input flow rate. This process was also controlled by an electromagnetic flow meter. The outlet pipe was positioned in the base of the sump to ensure as much as the fluid being pumped out was excess saline. This same pump could be used to speed up the draining the tank after each experiment, increasing the amount of experiments possible in a day.

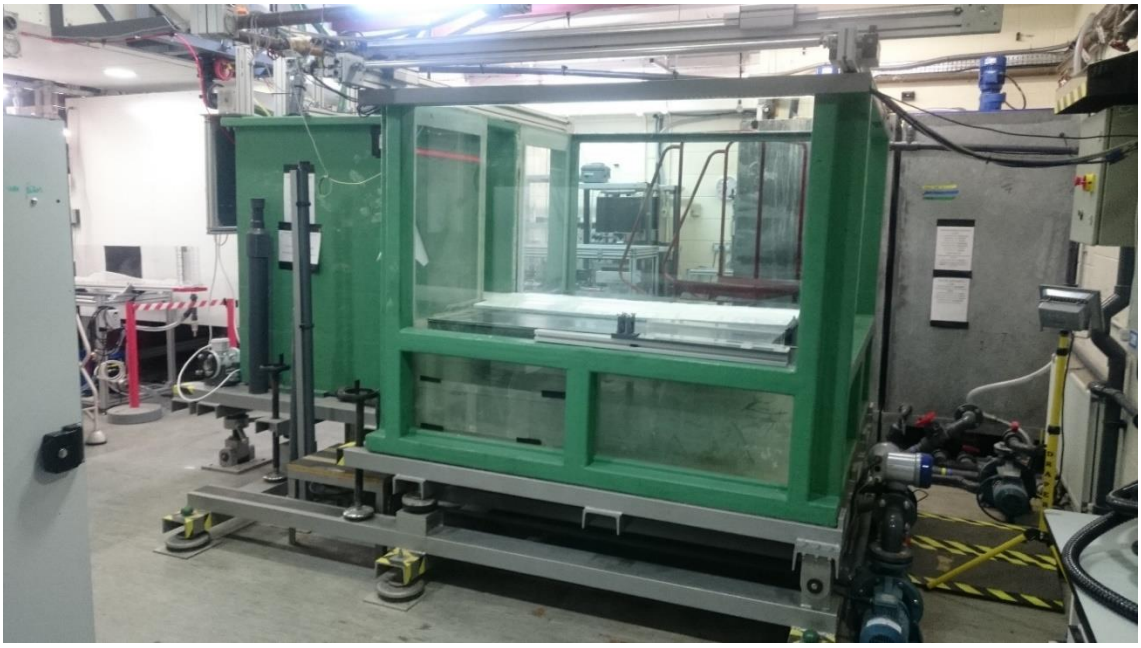

Figure 3.3 Photograph of the flume used for this project. Large mixing tanks can be seen in the background, with the main green flume in the foreground. The straight channel model is in-situ on the false floor of the tank.

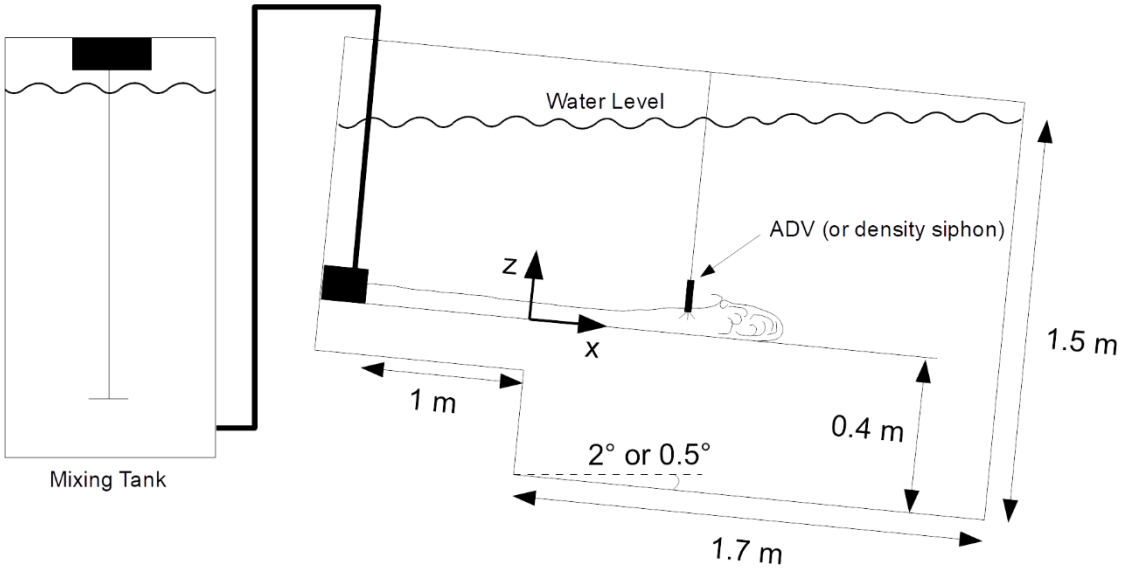

Figure 3.4 A cross-sectional schematic of the laboratory flume setup.

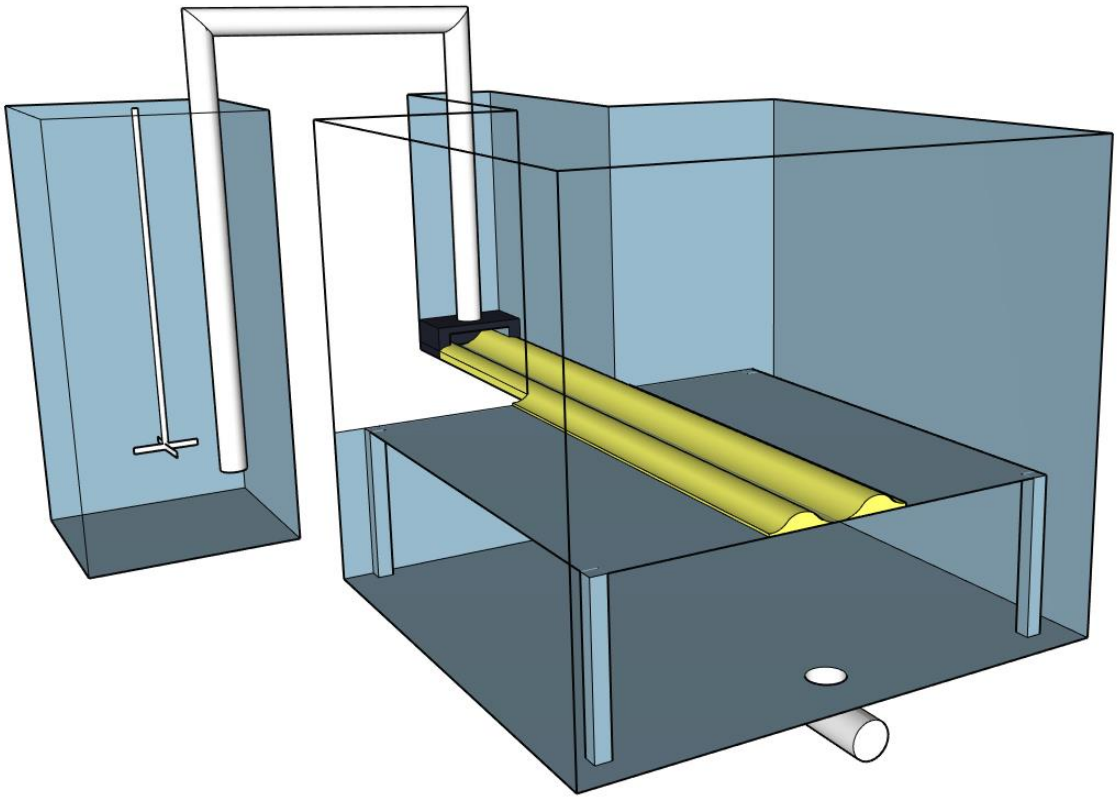

Figure 3.5 A visualisation of the experimental flume setup with a straight channel (yellow) in-situ. Saline fluid is pumped from the mixing tank into the inlet box at the head of the channel via a momentum diffuser. The gravity current then traverses the channel model, with excess dense fluid being collected in the sump beneath. Fluid is pumped out from the base of the sump at the same rate as at the inlet to ensure a constant water level in the flume.

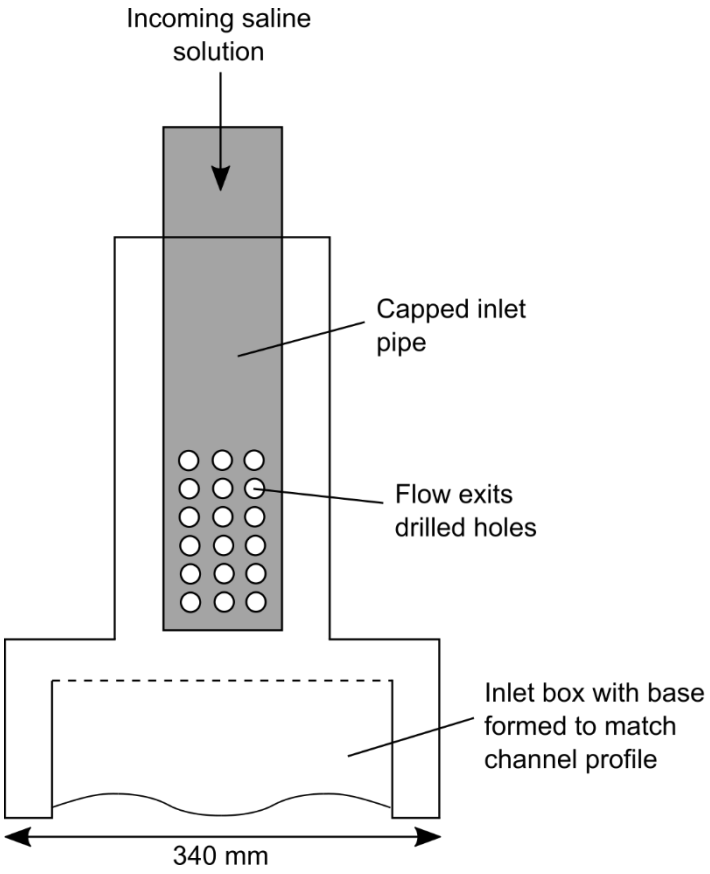

Figure 3.6 Schematic of the apparatus used to deliver the saline solution to the beginning of the inlet channel (channel profile not to scale). In order to diffuse momentum, the inlet pipe is capped. Drilled holes around the sides of the pipe allow the fluid to exit into a larger, surrounding pipe. The fluid then enters an inlet box places at the head of the channel. The base is formed to match the profile of the channel, to allow as smooth a transition as possible.

3.3 Fibreglass channel model – design and development

3.3.1 Channel profile

All experiments were conducted using fibreglass channel models designed specifically for this project. Channels used in gravity current experiments can either be erodible (often made from sand) [e.g. Mohrig and Buttles 2007; Straub et al., 2008; De Leeuw et al., 2016] or fixed [e.g. Keevil et al., 2006; Islam et al., 2008; Abad et al., 2011]. There are

advantages to both setups. Erodible channels allow the study of morphology development and the erosion and deposition processes. Fixed channels allow a systematic investigation of flow dynamics and provide a fixed reference point.

Levels of flow confinement can also vary, from fully-confined with straight side walls (most common) [e.g. Parker et al., 1987; Buckee et al., 2001; Sequeiros et al., 2010; Cossu and Wells 2012], to lower aspect ratio channels with considerable overbank flow [e.g. Mohrig and Buttles 2007; Islam et al., 2008; Kane et al., 2008].

Channel design was identified as a key area that could be improved over previous studies. Due to technological or logistical concessions, such as manufacturing processes or the spatial resolution of velocity data, laboratory channel profiles are often not representative of morphologies found in the field. Previous experiments have used profiles which are often rectangular [e.g. Imran et al., 2007; Kane et al., 2008; Abad et al., 2011] or occasionally trapezoidal in shape [Islam et al., 2008], presumably due to manufacturing restraints. Aspect ratios are also often small (i.e. the channels are relatively deep compared to the flow and channel width). This can be to ensure the flow is deep and confined enough to measure [e.g. Keevil et al., 2006], although recent instrumentation advances (ADV) negate this. In the field, submarine channels have large aspect ratios (width/depth), ranging from 8 for deep channels to 100 for shallower channels [Foreman et al., 2015]. To this author's knowledge, a fixed channel, with a smooth profile and an aspect ratio of less than 2 has not been used before. Considering channel geometry has been identified as a key control on flow dynamics [Islam et al., 2008], this is perhaps surprising.

The overriding aim when designing the channel profile was therefore to create a more physically realistic morphology, while maintaining a viable laboratory scale flow. Using the relationship $U = Fr\sqrt{g'h}$, estimates of the Reynolds number of flows could be made for a given Froude number [Benjamin, 1968]. The dimensions of the flume determined the width of the model by restricting certain planforms (Section 3.3.4). This gave a total model width (including levees) of 0.66 m with the channel occupying the central 0.22 m.

A channel depth of 27.5 mm gave flows both deep enough to measure and sufficiently high estimated Reynolds numbers (> 3000) to be fully turbulent. The resulting aspect ratio of 8 was also just within the range seen in the field. The profile takes the shape of a sine curve. This fulfils two criteria: a smooth profile with no sharp inflection points to adversely affect flow dynamics; a low maximum intrachannel slope of 22º. This is less than the angle of repose of most sediment and therefore future proofing the model for particulate current experiments that study depositional patterns. The final profile is shown in Figure 3.7. While it is an improvement over previous studies, it is still an idealised representation of a submarine channel.

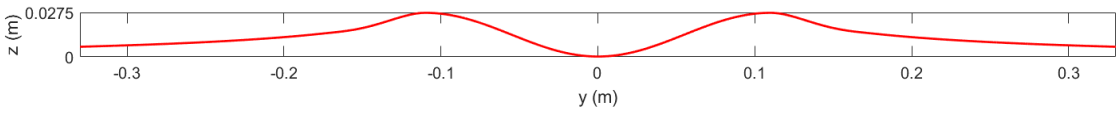

Figure 3.7 Cross-sectional profile of the fibreglass channel model used throughout this project. The channel is 220 mm wide and 27.5 mm deep giving and aspect ratio of 8. Levees exist on either side and stretch for a distance equal to the channel width. These are based on a combination of laboratory [Straub, personal communication] and field data [Nakakima and Kneller, 2013]. Axes are not stretched to show the true profile.

3.3.2 Levee profile

It was equally important that the levee reflected real world morphology. Again, previous studies have neglected this area, either using unrealistically steep slopes [e.g. Keevil et al., 2006; Islam and Imran 2008] or lacking them altogether [e.g. Islam et al., 2008]. Nakajima and Kneller [2013] conducted a comprehensive review of available field levee data and identified several trends. Depending on slope, either a power or exponential law was used to fit the levee shape. For steeper slopes they found the relationship $z = H(L/Y)^{-B}$, gave a good fit to the data, where z is the levee height, H is the channel depth,

L is the distance from the channel thalweg, Y is half the channel width, $B = 0.5535\theta^{0.662}$, and θ is the slope. Although this relationship works well for the far field architecture it fails to capture the morphology near the crest. Therefore, the inner third of the levee profile was determined using data from previous gravity current experiments conducted over an erodible bed by Straub et al. [2008] [Straub, personal communication]. These data points can be seen in Figure 3.8. The profile was then determined by a polynomial matching the gradients of the sine curve at the channel crest and that of the field data. A remaining degree of freedom was used to minimise the error to the laboratory data.

In the field, levees can be up to two orders of magnitude wider than the channel itself [Birman et al., 2009; Nakajima and Kneller 2013]. Therefore, in order to gain this realistic levee profile at the laboratory scale, the levee was cut off prematurely i.e. before it reached the same height as the channel base. It was thought this preferable to artificially imposing a boundary condition on the levee; any effects of this (or lack of) are discussed in the next section.

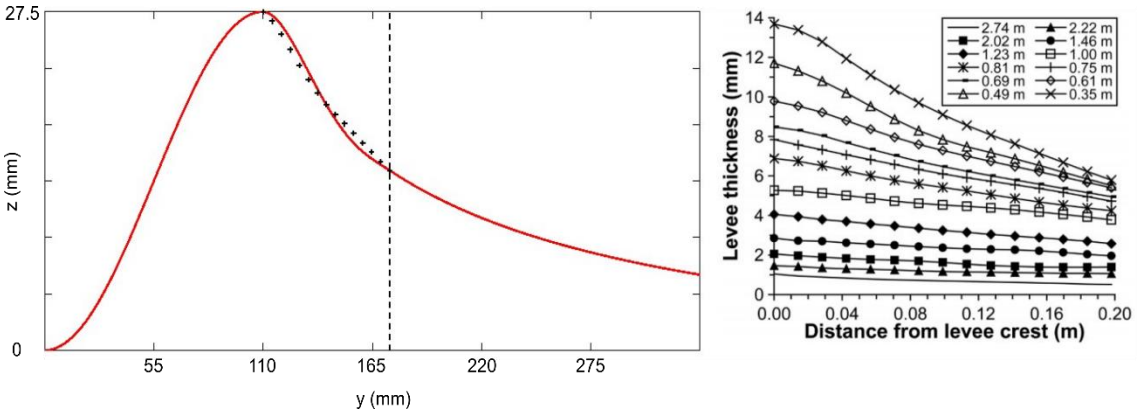

Figure 3.8 The levee profile of the model (left) was determined by a combination of laboratory and field data. The field data was obtained from a review undertaken by Nakajima and Kneller [2013]. The laboratory data was provided by Kyle Straub [personal communication] from a previous erodible channel study (right) [Straub et al., 2008]. The dashed line shows the boundary between where the levee profile is determined by the field and laboratory data.

3.3.3 Utilising numerical modelling in experimental design

One advantage of the combined laboratory and numerical modelling approach of this project is the ability to use preliminary simulations to aid experimental design (details of the numerical model can be found in the next chapter). This optimisation approach is not uncommon in engineering fields but is a relatively unusual methodology in the environmental sciences. Preliminary simulations were used to check several features of the flow including (i) any effect on flow dynamics of the levee 'step' at the edge of the fibreglass model and (ii) bulk flow quantities that had previously been estimated.

i) Two simulations were conducted, one of a current traversing a straight channel with the proposed model geometry and the same current traversing a channel with an extended levee profile (Figure 3.9). The velocity and density structure of the two flows were compared. It was found that there was negligible or no change in the intrachannel flow and only very small differences in the overbank flow on the levee (Figure 3.10).

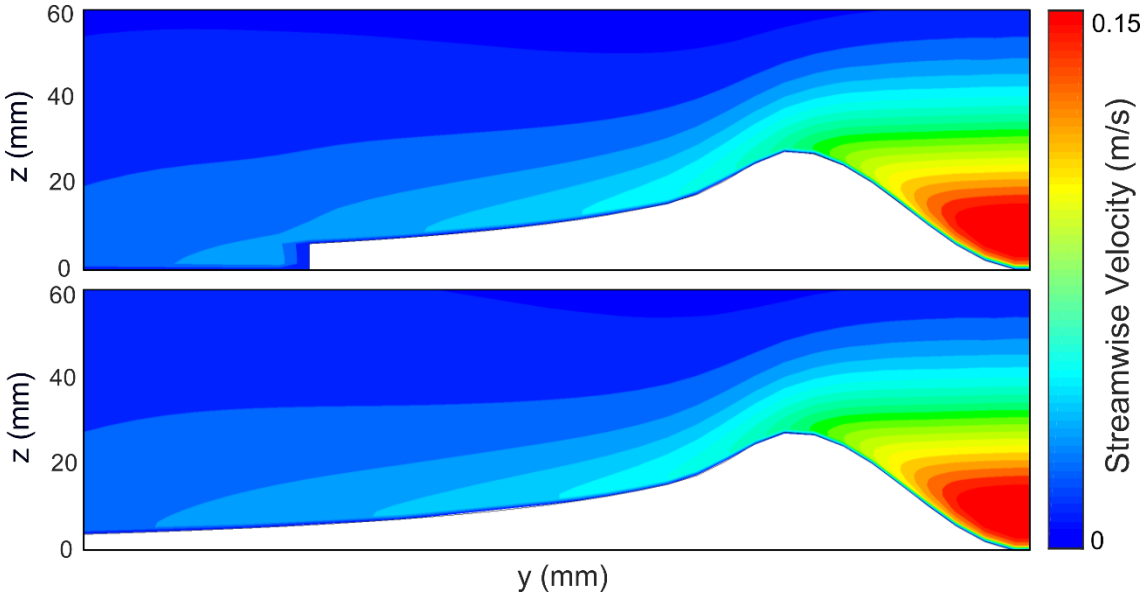

Figure 3.9 Comparison of the streamwise velocity field in two straight channel models (vertical axis exaggerated). The top model features the levee step found on the fibreglass model, while the bottom model has a continuous profile. The only difference occurs at the step itself, with no effects on the levee or intrachannel.

ii) The bulk flow quantities of a range of currents were calculated with input flow rates across the range possible in the laboratory. Even the smallest possible flows which are fully-confined by the channel were found to have $Re > 2500$ and therefore be fully turbulent.

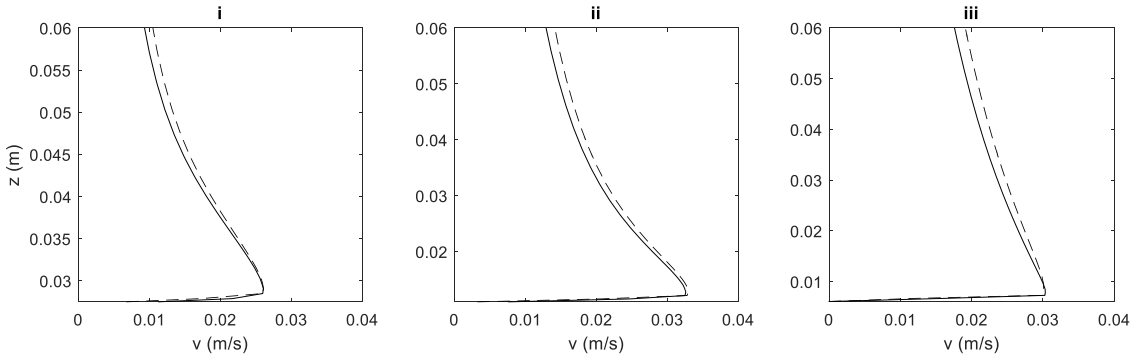

Figure 3.10 Cross-stream profiles at (i) the levee crest (y = 0.11 m), (ii) mid-levee (y = 0.22 m) and (iii) the step (y = 0.33 m), for the simulations in Figure 3.9. There is negligible effect from the levee step on the cross-stream flow field. Solid line – levee step; dashed line – no step.

3.3.4 Channel planforms

A novel, flexible channel model design was developed for this study. In order to allow multiple channel layouts individual curved and straight channel sections were manufactured using fibreglass (Figures 3.11 and 3.12). These tessellating pieces can be combined to create a variety of channel planforms with varying sinuosity (Figures 3.13 and 3.14). An additional 1 m long channel section was manufactured to fit in the inlet channel. This flexibility allows the investigation of the effect of channel sinuosity on the flow. The width and curvature of the pieces were designed so that three channel sinuosities would fit in the flume in SEFDL. Given a larger flume an even greater variety of channel planforms would be possible, including inserting straight sections between bends.

During this study four different channel planforms were utilised: a straight channel and three sinuous channels with 1, 2 and 3 curved channel sections per bend. Throughout the rest of this thesis, these channels will be referred to as the straight, low sinuosity, mid sinuosity and high sinuosity channels respectively. Table 3.1 shows the properties of the different sinuous channels. In order to ensure the axial direction of the channels was parallel to the slope, one curved channel piece was cut in half for the first half bend of the low and mid-sinuosity channels.

In order to ensure the channels did not float due to their hollow nature, each section was filled with epoxy resin. Sections were then glued in the required layout to the false floor with silicon sealant. This was strong enough to keep the channel fixed firmly in place but could be cut away relatively easily when switching channel planforms. The edges of the channel sections were slightly rounded, resulting in small dips at each junction between sections. These were filled with silicon gel and smoothed to create an even surface. The long inlet section remained in the inlet channel, flush with the inlet box, for all experiments.

Table 3.1 Sinuous channel geometry details.

Channel properties	Low-sinuosity	Mid-sinuosity	High-sinuosity
Sinuosity	1.01	1.05	1.11
Angle of curvature	30º	60º	90º
Axial length of single bend (mm)	233	450	637
Thalweg length of single bend (mm)	236	472	708
Total bends	6.5	3	2.17
Total channel sections	6.5	6	6.5

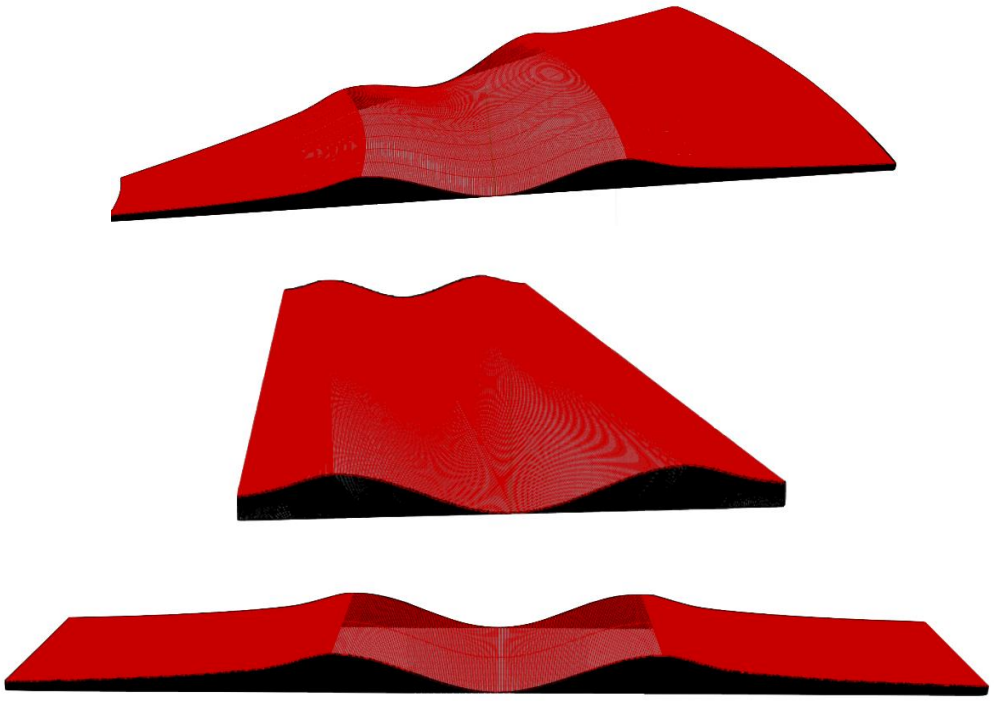

Figure 3.11 CAD images of the three channel pieces used to construct the channel layouts: curved (top), inlet (centre) and straight (bottom).

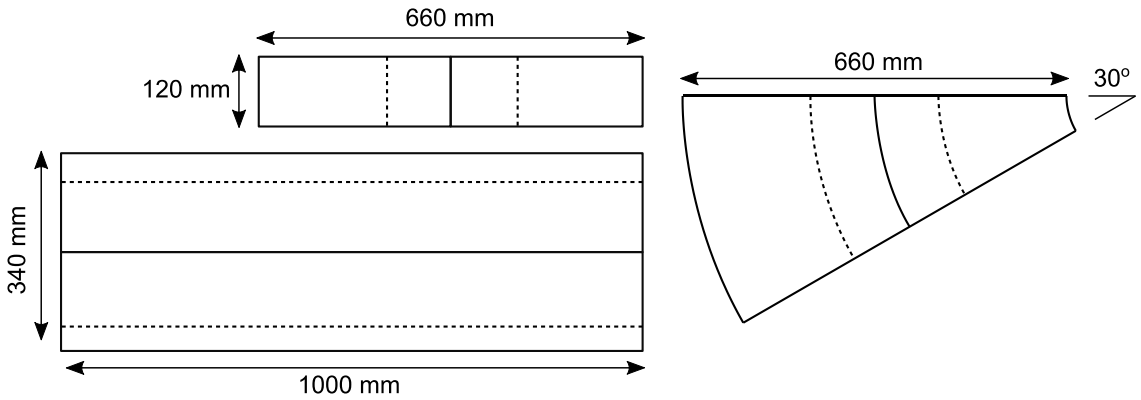

Figure 3.12 Schematic of the straight, curved and inlet channel pieces used to construct the channel layouts.

Figure 3.13 Photographs of the straight channel setup (top) and the high sinuosity channel setup (bottom).

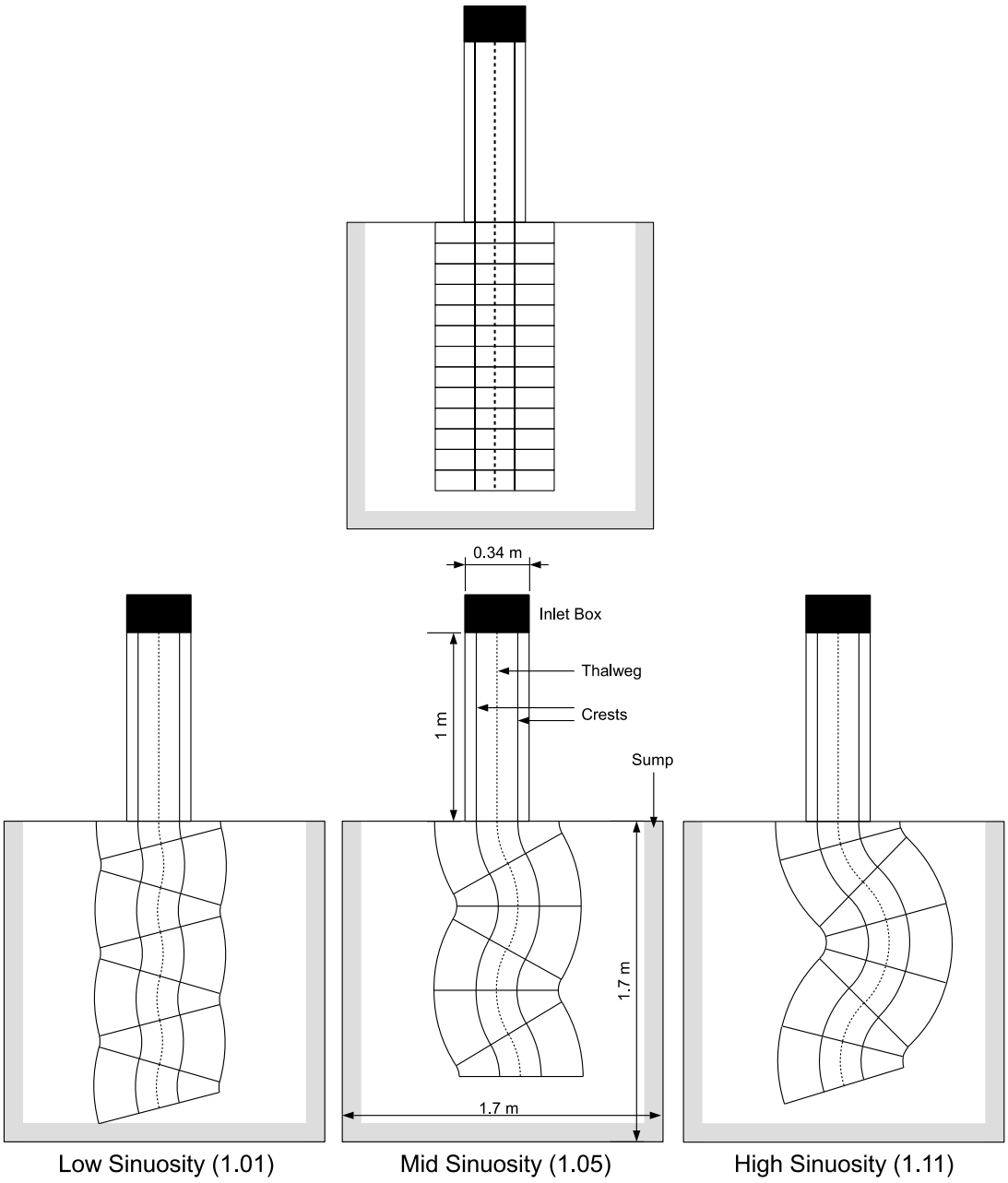

Figure 3.14 The four channel planforms used in this study, shown within the laboratory flume.

3.4 Experimental procedure

Each experimental run broadly followed the same procedure. The slope of the flume was set to either 0.5º or 2º, measured using an inclinometer to an accuracy of 0.1º. The relevant channel layout was positioned on the false floor. The ADV or density siphon were manually positioned at a specified location. The flume was then filled with tap water to a depth of 1.5 m, with the saline solution prepared in the mixing tank as previously described. Saline was then pumped into the flume; the flow rate was controlled manually by an electromagnetic flow meter. Simultaneously, fluid was pumped out from the flume at the same rate via the same mechanism. Each experiment lasted for either approximately 2 or 4 minutes (see Section 3.5.1), measured from the time the head of the current passed the instrumentation. The specific operation of the ADV and density siphon are described in the relevant sections below (3.5.1 and 3.5.3). After each experimental run, the input pump was switched off and the output pump turned up to maximum. Once the tank finished draining, the process could be repeated.

3.5 Instrumentation

Both velocity and density data were recorded for this study. Velocity was measured using acoustic Doppler velocimetry, while density data was gathered with the combination of a bespoke density siphon and a density meter. All instrumentation was suspended from a mechanical traverse that was mounted on the top of the flume, allowing deployment anywhere within the main tank area. The protocols used to operate the instrumentation and the measurement locations are outlined below.

3.5.1 Acoustic Doppler velocimetry (ADV)

Velocity data was gathered using a Nortek Vectrino II acoustic Doppler velocimeter. This allows the recording of three-component velocities at a sampling rate of 100 Hz.

Velocities are recorded in a series of 'bins' spaced 1 mm apart. The velocimeter can measure a maximum of 35 bins, creating a velocity profile 34 mm in height. For reference, the channel depth in this study is 27.5 mm. These bins range between 40 and 74 mm below the head of the transmitting transducer. Therefore, the flow being measured is at least 40 mm beneath the ADV, so flow disturbance is minimised. A schematic of an ADV is shown in Figure 3.15.

ADV uses the Doppler shift of a back-scattered acoustic signal to calculate the velocity of a fluid. This signal is emitted by a central transducer at a fixed frequency. Four receiving transducers, spaced evenly at 90 degree intervals around the central transducer, then record the frequency of the reflected signal. The change in frequency from the original signal can then be used to calculate the velocity of the fluid using,

$$V = -\frac{\mathrm{c}\Delta F}{F_{emitted}},$$

where c is the speed of sound in water, $F_{emitted}$ is the original signal frequency, $\Delta F = F_{received} - F_{emitted}$ is the change in frequency recorded by each receiver and V is the velocity of the fluid relative to the receiver. Crucially, each receiver will record a different change in frequency, allowing the measurement of three-component velocities. Full details of the technology can be found in Nortek documentation and Voulgaris and Trowbridge [1998].

The back-scattering or reflection of the acoustic signal is a result of small particles in the flow; subsequently the quality of ADV is better in 'dirty' fluid. There are in fact lots of small particles in tap water itself and ADV generally works fairly well in such an environment. To improve data quality further, 400 g of seeding particles were added to each tank of saline solution in the mixing stage. It should be noted that it is the velocity of the particles that is recorded, not the fluid itself, and it is therefore assumed the two are identical i.e. no phase slip. This is the same for all acoustic and optical techniques. Various data filtering methods were trialled. However, the data appeared to be of a good enough quality that none were eventually employed, with negligible to no difference seen

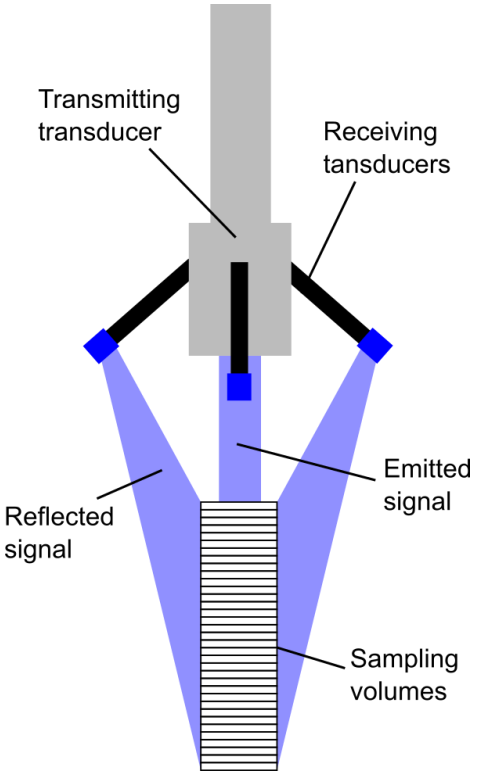

Figure 3.15 Schematic of a Nortek Vectrino II acoustic Doppler velocimeter. A central transducer emits an acoustic signal. The reflected signal is recorded by four receiving transducers. Velocities are recorded in 35 sampling volumes, 40 – 74 mm below the head of the transmitting transducer.

in either the mean or transient flow properties. A sample velocity time series from a single bin can be seen in Figure 3.16.

For each experiment, the ADV was positioned before filling the tank (see Section 3.4). Figure 3.17 shows how the body of the current is steady enough that consecutive time-averaging windows give the same results. Therefore, multiple measurement locations can be recorded at during a single flow. For a single location experiment, data was averaged between 30 and 90 seconds after the head passed the ADV. For two measurement locations, data was averaged between 30-90 and 120-180 seconds after the head passed the ADV. The 30 second gap between averaging windows allows the ADV to be repositioned. The height of the ADV could not be altered during a run, so only positions with the same channel base height could be done during the same run (e.g. opposite levee crests). Measurement locations are specified in the relevant sections of each chapter.

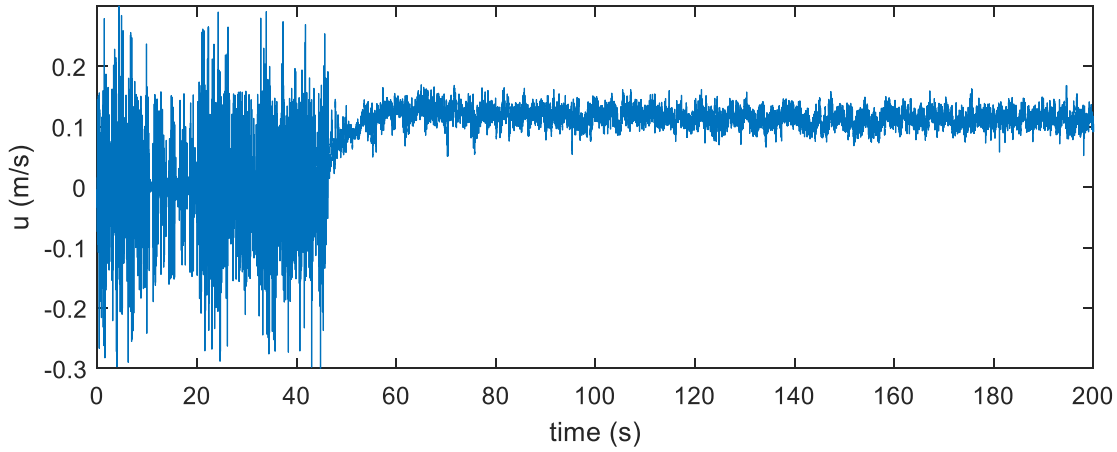

Figure 3.16 A sample time series of the velocity of a single sampling bin. Large amounts of noise are present until the current enters the measurement field at approximately 45 seconds.

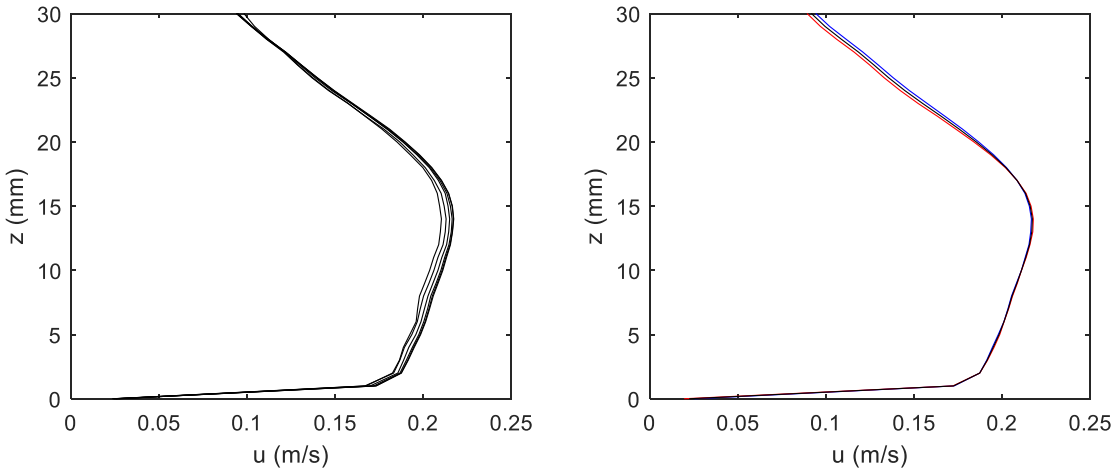

Figure 3.17 Streamwise velocity profiles from a flow traversing the straight channel showing the effects of time averaging. Profiles on the left show data averaged over 10, 20, 30, 40, 50 and 60 seconds. Due to the similarity of the data, a solid black line is used for all profiles for clarity. A 60 second averaging allows a suitable level of convergence. Profiles on the right show data averaged over 30-90 seconds (blue), 90-150 seconds (red) and 30-150 seconds (black) after the head of the current has passed the ADV. There is negligible difference in data averaged over consecutive 60 second windows, showing how multiple locations can be measured during a single run.

3.5.2 Repeatability

In order to assemble datasets illustrating the dynamics of a current across the width of a channel, data from multiple flows must be compiled. These ensemble datasets can then be used to create such as the cross-sectional contours seen in Chapter 6. It is therefore important that a degree of repeatability can be achieved, so that varying flow conditions do not adversely affect the results. It was found that, due to the strict input conditions achieved via the use of an electromagnetic flow meter, the flows in this work were highly repeatable. Figure 3.18 shows streamwise and cross-stream velocity profiles at bend 2 of the mid-sinuosity channel at a slope of 2º, constructed using data from three different components. This example was chosen to illustrate the worst-case scenario: the cross-stream velocity at the end of the sinuous channels showed the greatest degree of variability in any experiment, yet even here the profiles concatenate reasonably well.

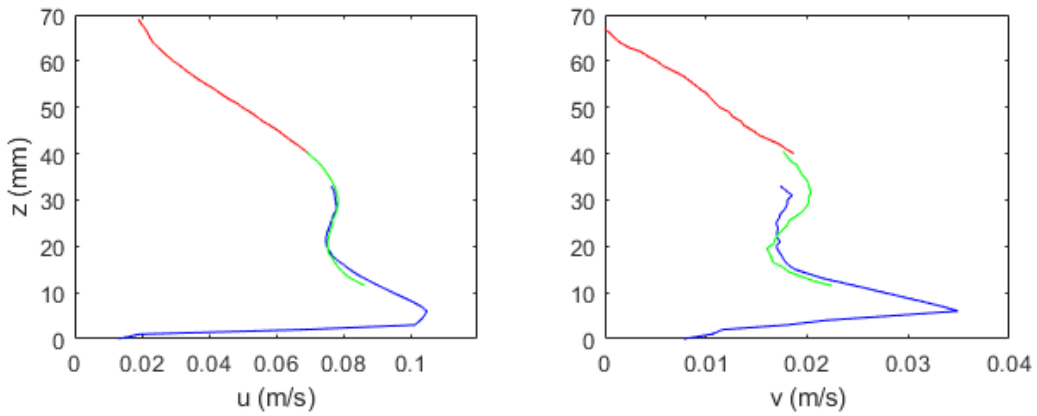

Figure 3.18 Streamwise and cross-stream velocity profiles at bend 2 of the mid-sinuosity channel at a slope of 2º. Red, green and blue profiles represent data taken from different currents with identical input condition. The profiles concatenate well and show how ensemble datasets can be used to generate whole flow-field visualisations.

3.5.3 Density siphoning

Density data was gathered by extracting fluid samples from various heights throughout the flows. These samples were extracted using a bespoke density siphon designed specifically for this study. A crucial aspect of recording good quality density data is to minimise flow disruption, in order to prevent any artificially induced mixing in front of the siphon. Here, very narrow steel tubing was used, with an external diameter of 1.6 mm and an internal diameter of 1 mm. Full details of the siphon rig can be found in the caption of Figure 3.19 which shows a schematic of the design. The steel tubes protruded 15 cm from the front of the PVC mounting rack and flexible plastic tubing was used to connect the steel tubing to the pump outside the flume.

A peristaltic pump was used to extract fluid from each pipeline into separate sampling pots. For each flow, the pump was switched on 30 seconds after the head of the current had passed the siphon rig. 45 seconds of pumping was sufficient in order to get a large enough sample to measure. Both the density and temperature of each of the 12 siphoned samples, plus samples from the mixing tanks (saline) and main flume (tap water), were measured and recorded manually using an Anton Paar DMA 35 Ex density meter to respective accuracies of 0.1 kg/m^3 and $0.1^{\circ C}$. When processing the data, all densities were corrected to a normalising temperature of $15^{\circ C}$ using the volumetric temperature expansion coefficient of water.

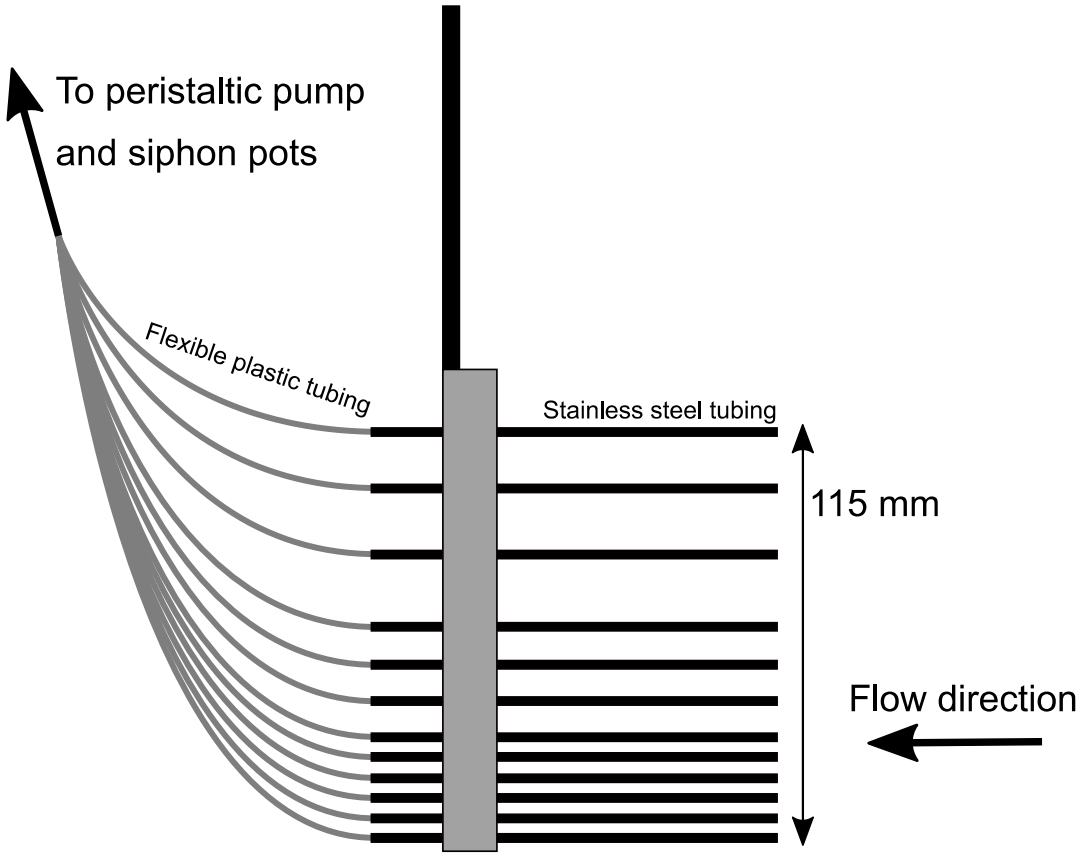

Figure 3.19 Schematic of the density siphon used in this work. It was designed to introduce minimal flow disturbance. Very narrow gauge, hollow steel tubing was used, with an external diameter of 1.6 mm and an internal diameter of 1 mm. These tubes were held by a PVC mounting rack. The siphon had a total vertical range of 115 mm, with increased resolution towards the bottom. Vertical heights of the individual tubes are: 3, 8, 13, 18, 23, 28, 38, 48, 58, 78, 98 and 118 mm. Flexible plastic tubing connected the siphon to a peristaltic pump outside the flume, which extracted fluid samples into separate pots.

Chapter 4

Reynolds-averaged Navier-Stokes modelling of gravity currents

4.1 Introduction

The numerical simulation of fluids, often encompassed under the term computational fluid dynamics (CFD), is a continually evolving field. A variety of modelling techniques exist. The simulation of turbulent flows can generally be broken down into three categories: Reynolds-averaged Navier-Stokes (RANS) models, large eddy simulation (LES) and direct numerical simulation (DNS). The applications of these to the study of gravity currents has been discussed in Chapter 2 (Section 2.4). The level of sophistication and complexity increases from RANS, to LES, to DNS. Respectively, the required computational resources also follow this trend.

A gravity current is a complex flow to model numerically. It is a turbulent, transient, two-phase flow with varying density. Furthermore, interaction with both the basal boundary and ambient fluid dictates a flow's evolution, so accurate modelling of both near-wall dynamics and shear-induced mixing is critical. Here, RANS modelling of a non-Boussinesq flow is carried out with a shear stress transport (SST) turbulence closure. Previous studies using RANS modelling have had varying degrees of success with replicating laboratory results within simple geometries [e.g. Imran et al., 2004; Huang et al., 2005; Giorgio Serchi et al., 2011], while others present numerical results without any laboratory comparison [e.g. Ezz and Imran, 2014]. In this study, flows are simulated within the same channel geometry and environment as the laboratory. The accuracy of the model in terms of predicting laboratory values is as good as any previous RANS simulations, despite the use of a more realistic channel geometry than previously employed.

This chapter gives full details of the numerics and discusses the rationale of using a RANS based model.

4.2 Choice of model

For any fluid dynamical problem, an appropriate choice of numerical model is critical. While DNS may give the best possible results, its computational expense places large restrictions on the Reynolds numbers of flows and the complexity of environments that can be modelled. Likewise, LES suffers from the same issues. DNS and LES have been used to simulate gravity current in previous studies, but these have been limited to short timescales, simple rectangular domains and maximum Reynolds numbers of 15000 [Cantero et al., 2008]. This was a large computational exercise, using a 131 million node mesh. More recent DNS studies have not managed to surpass this in terms of flow magnitude [Nasr-Azadani and Meiburg, 2011, 2015; Hogg et al., 2016].

Therefore, while these more expensive numerical techniques can be hugely valuable in investigating fundamental dynamics, RANS based models are turned to in order to gain insights on a wider scale. Despite ever-increasing computing power, these still appear to offer the best compromise between performance and expense when modelling larger flows over timescales of more than about 30 seconds. Good agreement can be achieved with laboratory observations.

For RANS simulations, a closure system is required when modelling turbulent flows (see Sections 4.3.2 and 4.3.3). Previously, the majority of gravity current studies have employed the popular k-ϵ model [e.g. Kassem and Imran, 2004; Huang et al., 2005, 2008; Giorgio Serchi et al., 2011] and the k-ω model has also been used [Gup et al., 2014]. In this study, the shear stress transport (SST) model [Menter, 1994, 2009] is employed, which has not previously been used in the area of gravity currents. This combines both the previously mentioned models to address weaknesses in both, and in previous work was found to give marginally better performance than the k-ϵ model with similar

computational times [Kelly, 2015]. An additional advantage of developing a RANS model is that, due to the absence of a Reynolds number dependence, there is the possibility of upscaling it to simulate larger scale flows in a field environment.

The details of this RANS SST model are described in the following sections.

4.3 Governing equations

4.3.1 Navier-Stokes equations

The basis of any CFD model are the Navier-Stokes equations which govern then movement of a fluid. Most commonly, these are written as equations for the conservation of mass and momentum. For an unsteady, compressible fluid, the conservation of mass, or continuity equation, can be expressed as,

$$\frac{\partial \rho}{\partial t} + \frac{\partial \rho u_i}{\partial x_i} = 0, \tag{4.1}$$

and the three conservation of momentum equations, one for each component, can be expressed as,

$$\frac{\partial \rho u_i}{\partial t} + \frac{\partial \rho u_j u_i}{\partial x_j} = -\frac{\partial p}{\partial x_i} + \frac{\partial}{\partial x_j}\left(\mu\left(\frac{\partial u_i}{\partial x_j} + \frac{\partial u_j}{\partial x_i}\right) + \lambda \delta_{ij} \frac{\partial u_j}{\partial x_j}\right) + \rho f_i, \tag{4.2}$$

where μ is the dynamic viscosity, λ is the second coefficient of viscosity (often approximated as $-2\mu/3$) and ρf_i are the body forces, where usually $f_x = 0, f_y = 0, f_z = g$. Differentiating by parts and using (4.1), (4.2) can be rewritten as,

$$\rho \frac{\partial u_i}{\partial t} + \rho u_j \frac{\partial u_i}{\partial x_j} = -\frac{\partial p}{\partial x_i} + \frac{\partial}{\partial x_j}\left(\mu\left(\frac{\partial u_i}{\partial x_j} + \frac{\partial u_j}{\partial x_i}\right) + \lambda \delta_{ij} \frac{\partial u_j}{\partial x_j}\right) + \rho f_i. \tag{4.3}$$

Going back to basic principles and Newton's second law, the change in momentum of a fluid should be equal to the net force exerted on it. This can be seen within the Navier-Stokes equations. The left-hand side of (4.3) contains the time derivative and convective

terms, representing the total rate of change of momentum. The right-hand side contains the pressure, viscous and external body forces acting on the fluid.

4.3.2 Reynolds-averaged Navier-Stokes (RANS) equations

Solving the Navier-Stokes equations explicitly requires further manipulation and a high level of computational resources; this is the realm of DNS. A turbulent flow is characterised by its eddies, which form across a range of scales. The largest interact with the mean flow, extracting energy and affecting its motion with their vorticity. Simultaneously, turbulence is maintained by the stretching of the eddies' vortex lines by the mean flow. The smaller eddies are then stretched by and extract energy from the larger eddies, highlighting the idea of an energy cascade. At smallest turbulent scales, known as the Kolmogorov scale [Kolmogorov, 1941], turbulent kinetic energy is dissipated into heat. This length scale,

$$\eta = \left(\frac{\nu^3}{\epsilon}\right)^{\frac{1}{4}}, \tag{4.4}$$

which DNS must resolve, shortens as the Reynolds number increases. Therefore, DNS becomes prohibitively expensive at higher Reynolds numbers. An alternative approach is to Reynolds-average the Navier-Stokes equations which exploits the random nature of turbulence. This is the method which will be employed in this study and is a very common technique, requiring far less computational resources than the LES and DNS equivalents.

Reynolds-averaging refers to the decomposition of a variable into a mean and fluctuating component and the subsequent time-averaging. Taking the pressure variable as an example,

$$p = P + p', \tag{4.5}$$

this has been split into a mean part, P, and a fluctuating part, p'. The timescale of the mean part, T, is far larger than that of the fluctuating part, t', such that $T \gg t'$. If we time-average over a timescale t, such that $t' \ll t \ll T$, then we can write,

$$\overline{p} = P, \qquad \overline{p'} = 0, \tag{4.6}$$

with the bar denoting the time-average. If working with an incompressible form of the Navier-Stokes equations, this approach can be taken for all the variable to obtain the RANS equations. An incompressible flow is one where, given an infinitesimal volume moving with the flow, the density within this volume is constant. For a buoyancy-driven flow, this would mean applying the Boussinesq approximation. This states that the effects of any density difference are negligible in the inertial terms of the Navier-Stokes equations (those on the left-hand side of 4.3) and only applies to the body forces term. Therefore, a constant density is substituted into both the continuity and momentum equations, except in the source term for external forces (ρf_i). This reduces the Navier-Stokes equations to an incompressible form. The Boussinesq approximation can work well for dilute flows with an excess density in the 1-2% range. Above this though, density effects must be considered everywhere [Giorgio Serchi et al, 2011].

If the Reynolds-averaged form of the velocity is substituted into the compressible forms of the Navier-Stokes equations (4.1 and 4.2), things quickly become more complicated. Instead, a Favre-average is employed. This can be written as,

$$u_i = \tilde{u}_i + u_i', \tag{4.7}$$

where $\tilde{u}_i$ is the mean component and u_i' is the fluctuating component. This differs from the Reynolds-average in that it is density weighted and the mean part is defined as,

$$\tilde{u}_i = \frac{\overline{\rho u_i}}{\overline{\rho}}, \tag{4.8}$$

where the density, $\rho = \overline{\rho} + \rho'$, is still Reynolds-averaged. Substituting the Reynolds-averages form of the density and pressure, and the Favre-averaged form of the velocity into (4.1) and (4.2), we get,

$$\frac{\partial \overline{\rho}}{\partial t} + \frac{\partial \overline{\rho}\tilde{u}_i}{\partial x_i} = 0, \tag{4.9}$$

$$\frac{\partial \overline{\rho}\tilde{u}_i}{\partial t} + \frac{\partial \overline{\rho}\tilde{u}_j\tilde{u}_i}{\partial x_j} = -\frac{\partial P}{\partial x_i} + \frac{\partial}{\partial x_j}\left(\mu\left(\frac{\partial \tilde{u}_i}{\partial x_j} + \frac{\partial \tilde{u}_j}{\partial x_i} - \frac{2}{3}\delta_{ij}\frac{\partial \tilde{u}_k}{\partial x_k}\right) - \overline{\rho u_i' u_j'}\right) + \overline{\rho} f_i, \tag{4.10}$$

after time-averaging, which are the RANS equations for a compressible flow. These are then solved for the mean values. However, this process has introduced a new quantity,

$$\frac{R_{ij}}{\rho} = -\overline{u_i' u_j'}, \tag{4.11}$$

which are known as the Reynolds stresses. Each momentum equation now has three new terms, so the system is not closed. To address this, the Boussinesq eddy-viscosity hypothesis is used, not to be confused with the Boussinesq approximation for buoyancy which is described above. The eddy-viscosity hypothesis states that the Reynolds stresses are proportional to the mean strain rates, such that,

$$R_{ij} = -\overline{\rho u_i' u_j'} = \mu_t\left(\frac{\partial \tilde{u}_i}{\partial x_j} + \frac{\partial \tilde{u}_j}{\partial x_i} - \frac{2}{3}\delta_{ij}\frac{\partial \tilde{u}_k}{\partial x_k}\right) - \frac{2}{3}\overline{\rho} k \delta_{ij}, \tag{4.12}$$

where μ_t is the eddy viscosity and,

$$k = \frac{1}{2} u_i' u_i', \tag{4.13}$$

is the turbulent kinetic energy (TKE). In order to solve this system, equations must be formed to calculate values for k and μ_t. The turbulence model used for this is described in the following section.

4.3.3 Shear stress transport (SST) turbulence model

Traditionally, the two most commonly employed RANS turbulence closures are the k-ϵ and k-ω eddy viscosity models. These use two transport equations each to solve for the TKE and then either ϵ, the rate of dissipation of kinetic energy, or ω, the turbulence

frequency. The k-ϵ model is arguably the most widely used turbulence model and it generally handles free-stream turbulence well. However, due to the form of the ϵ equation, it cannot be integrated up to a boundary and instead uses wall functions to automatically define the flow behaviour in near-wall regions. The k-ω can directly resolve the boundary layer of a flow but is sensitive to free-stream variations in k and ω.

In this study, the shear stress transport (SST) model is used [Menter, 1994]. This combines the two aspects of the k-ϵ and k-ω models. Likewise, it uses two transport equations,

$$\frac{\partial \overline{\rho} k}{\partial t} + \frac{\partial \overline{\rho} k \tilde{u}_i}{\partial x_i} = P_k + P_{kb} - \beta^* \overline{\rho} k \omega + \frac{\partial}{\partial x_i}\left((\mu + \sigma_k \mu_t) \frac{\partial k}{\partial x_i} \right), \tag{4.14}$$

$$\frac{\partial \overline{\rho} \omega}{\partial t} + \frac{\partial \overline{\rho} \omega \tilde{u}_i}{\partial x_i} = \frac{\alpha_1}{\nu_t} P_k + P_{\omega b} - \beta \overline{\rho} \omega^2 + \frac{\partial}{\partial x_i}\left((\mu + \sigma_\omega \mu_t) \frac{\partial k}{\partial x_i} \right) + 2(1 - F_1) \overline{\rho} \sigma_{\omega 2} \frac{1}{\omega} \frac{\partial k}{\partial x_i} \frac{\partial \omega}{\partial x_i}, \tag{4.15}$$

where the turbulent production due to shear is,

$$P_k = \min(2\mu_t \frac{\partial \tilde{u}_i}{\partial x_j} S_{ij}, 10\beta^* \overline{\rho} k \omega), \tag{4.16}$$

the turbulent production due to buoyancy is,

$$P_{kb} = -\frac{\mu_t}{\overline{\rho} \sigma_\rho} g_i \frac{\partial \overline{\rho}}{\partial x_i}, \tag{4.17}$$

the buoyancy term in the ω equation is,

$$P_{\omega b} = \frac{\omega}{k}\left((\alpha_1 + 1) C_3 \max(0, P_{kb}) - P_{kb} \right), \tag{4.18}$$

the values for the constants are,

$$\sigma_\rho = 1, \sigma_k = 2, \sigma_\omega = 2, \sigma_{\omega 2} = 1.168, \alpha_1 = \frac{5}{9}, C_3 = 1, \beta^* = 0.09, \beta = 0.075,$$

and the mean strain tensor is

$$S_{ij} = \frac{1}{2}\left(\frac{\partial \tilde{u}_i}{\partial x_j} + \frac{\partial \tilde{u}_j}{\partial x_i}\right). \tag{4.19}$$

Furthermore, the eddy viscosity is defined as,

$$\nu_t = \frac{\alpha_1 k}{\max(\alpha_1 \omega, SF_2)}, \tag{4.20}$$

where $S = \sqrt{2S_{ij}S_{ij}}$. Two blending functions,

$$F_1 = \tanh\left[\left(\min\left(\max\left(\frac{\sqrt{k}}{\beta^* \omega y}, \frac{500\nu}{y^2\omega}\right), \frac{4\rho\sigma_{\omega 2}k}{CD_{k\omega}y^2}\right)\right)^4\right], \tag{4.21}$$

$$F_2 = \tanh\left[\left(\max\left(\frac{2\sqrt{k}}{\beta^* \omega y}, \frac{500\nu}{y^2\omega}\right)\right)^2\right], \tag{4.22}$$

are used to transition the performance of the model between the near-wall and free stream regions, where,

$$CD_{k\omega} = \max\left(2\rho\sigma_{\omega 2}\frac{1}{\omega}\frac{\partial k}{\partial x_i}\frac{\partial \omega}{\partial x_i}, 10^{-10}\right). \tag{4.23}$$

While the underlying equations may appear more complex than the model's original k-ϵ and k-ω counterparts, the computational solving time is relatively similar for all the variants.

4.3.4 Mixture model

The multiphase nature of the flows is resolved with the use of a mixture model. This essentially reduces the model to a single-phase problem. The entire simulation domain is

comprised of one fluid, the 'mixture'. This fluid's density can vary between that of the saline, ρ_s, and that of the ambient water, ρ_w. It is defined as,

$$\frac{1}{\overline{\rho}} = \frac{1-\alpha}{\rho_w} + \frac{\alpha}{\rho_s}, \tag{4.24}$$

where α is the mass fraction of the saline phase and can take any value between 0 and 1. This density is used throughout both the RANS and SST equations. To calculate the value of the mass fraction, an additional transport equation is used,

$$\frac{\partial \alpha\rho}{\partial t} + \frac{\partial \alpha\overline{\rho}\tilde{u}_i}{\partial x_i} = -\frac{\partial \overline{\alpha'\rho u_j'}}{\partial x_j}, \tag{4.25}$$

where the Reynolds flux term is modelled using the Boussinesq hypothesis as,

$$-\overline{\alpha'\rho u_j'} = \frac{\mu_t}{\sigma_t}\frac{\partial \alpha}{\partial x_j}, \tag{4.26}$$

and $\sigma_t = 1$, is the turbulent Schmidt number. For multiphase problems with significant density differences and high density gradients, such as free-surfaces, the mixture model is inadequate and a different approach is required (e.g. volume of fluid or Eulerian methods). However, for flows such as gravity currents, where density differences are generally small, the mixture model performs well.

4.4 Numerical methods

4.4.1 Software and hardware

The simulations in this study were performed using the ANSYS CFX 18.2 software package. This uses a finite volume based method to solve the governing equations outlined above. A mesh is created to discretise the simulation domain into a series of cells. The governing equations are then 'solved' on volumes centred on each cell node by minimising an error function. The solver will go through several iterations before an

acceptable level of error is reached. At this stage, the solver moves forward in time (the amount of time is known as the timestep) and the process begins again. The size of timestep is an important variable to consider. In order to achieve convergence (approach a stable solution), the timestep must be small enough so as not to disrupt the system and invoke large variable gradients, both spatially and temporally. Too small a timestep results in unnecessarily long computation times. The closer a system is to a steady state, the larger a timestep can be. For these simulations, a variable timestep was used. The initial timestep was set at 0.1 seconds, with conditions set such that if too few or too many iterations were required to achieve convergence, the timestep would increase or decrease accordingly. This allowed smaller timesteps while flow was still highly transient (i.e. when the head was traversing the channel) and larger timesteps when the flow approached a steady state (i.e. once the body of the current dominated the channel). Specified model details are shown in Table 4.1.

Simulations were run in parallel on the advanced research cluster 2 (ARC2) at the University of Leeds. This high performance computer is comprised of nodes with 16 x 8-core Intel E5-2670 2.6 Ghz processors with 32GB DDR3 1600Mhz RAM. Straight channel simulations were run on 2 nodes (32 processors) and sinuous simulations were run on 4 nodes (64 processors), with run-times generally in the 6-12 hour range.

Table 4.1 Numerical schemes specified within the ANSYS CFX simulations.

Model Detail	Specification
Initial timestep	0.1 s
Maximum timestep	5 s
Minimum timestep	0.01 s
Advection scheme	High resolution
Transient scheme	2nd order backwards Euler
Turbulence numerics	High resolution
Reference density	1000 kg/m^3

4.4.2 Boundary conditions

Additionally, boundary conditions must be defined at the edges of the simulation domain. For these simulations, the walls and floors of the domain were specified as no-slip walls, where the condition of $u_i = 0$ is imposed. The upper surface of the domain was specified as a free-slip wall. Here, no condition is imposed on the velocity of the flow, but the basal stresses are zero. An inlet was positioned at the head of the inlet channel. Here, the mass flow was specified to match the laboratory flows, e.g. a 1 l/s flow was simulated with a 1 kg/s input condition. The saline mass fraction at the inlet was defined as $\alpha = 1$. The size of the inlet was adjusted for each flow rate so that $Fr = 1$. A pressure outlet was positioned at the end or bottom of the domain (see Section 4.5). This maintains the system pressure, ensuring output flow rate matches the input flow rate. A pressure outlet is more numerically stable than directly specifying an equal output mass flow rate as it allows for small continuity errors. For the straight channel simulations, a symmetry condition was imposed along the channel thalweg. This is similar to a free-slip wall except the additional constraint of imposing normal gradients to the boundary. For a symmetrical simulation like the straight channel setup this cuts the domain size in half and vastly reduces the computational expense.

4.4.3 Post processing

Simulations were run for a simulation time of 2 minutes, with results files outputted every 10 seconds. Data was analysed and post-processed with ANSYS CFD-Post 18.2, with some data being exported to MATLAB for further analysis. In agreement with the laboratory data (Section 3.5.1), once the head had passed through the domain, the system attained close to a steady-state. Due to the time-averaging in the RANS equations, small-scale flow fluctuations are not resolved, hence there is little benefit in time-averaging any results data. Inevitably, the defined boundary conditions mean that, because of the

continual input of saline, the flow slowly thickens. However, in agreement with the laboratory data, this effect is generally negligible over the timescales modelled. All numerical data presented throughout this study is therefore taken at a timestep between 90 and 120 seconds after the simulation start time. This range is used to avoid any unwanted reflection effects. These come about due to domain sidewalls and are enhanced in the numerical simulation due to the absence of a true upper free-surface. In the laboratory, reflections are damped due to energy loss at the upper boundary. In the numerical model there is no such mechanism, so some flexibility must be employed in order to avoid these effects, which do not affect the dynamics of the flow but can provide anomalous results around the flow interface.

4.4.4 Transient flow characteristics

Figure 4.1 explicitly shows the time evolution of a l/s current traversing the straight channel domain (Section 4.5.1). All flows exhibit broadly the same characteristics. Initially, the current traverses the inlet channel. The inlet boundary condition of $Fr = 1$ aims to minimise any initial flow slumping or inflation and mimic the conditions of the laboratory inlet box which allows the flows to regulate their inlet height. Once the current enters the main tank area, the head remains confined within the channel while the upper part of the body overspills onto the surrounding area. The flow then enters the sump which collects excess fluid.

The isosurfaces shown in Figure 4.1 are taken at a density of 1002.5 kg/m^3 (or a saline mass fraction of 10%). This represents the interface of the current and ambient fluid and shows a smooth, uniform surface. In the laboratory, this surface is unsteady and interrupted by occasional Kelvin-Helmholtz billows. The failure to resolve these large scale turbulence structures is a common feature of previous RANS modelling [e.g. Huang et al., 2005, 2008; Giorgio Serchi et al., 2011]. However, Paik et al. [2009] showed how by using a sufficiently fine mesh and directly resolving near wall flow it is possible to

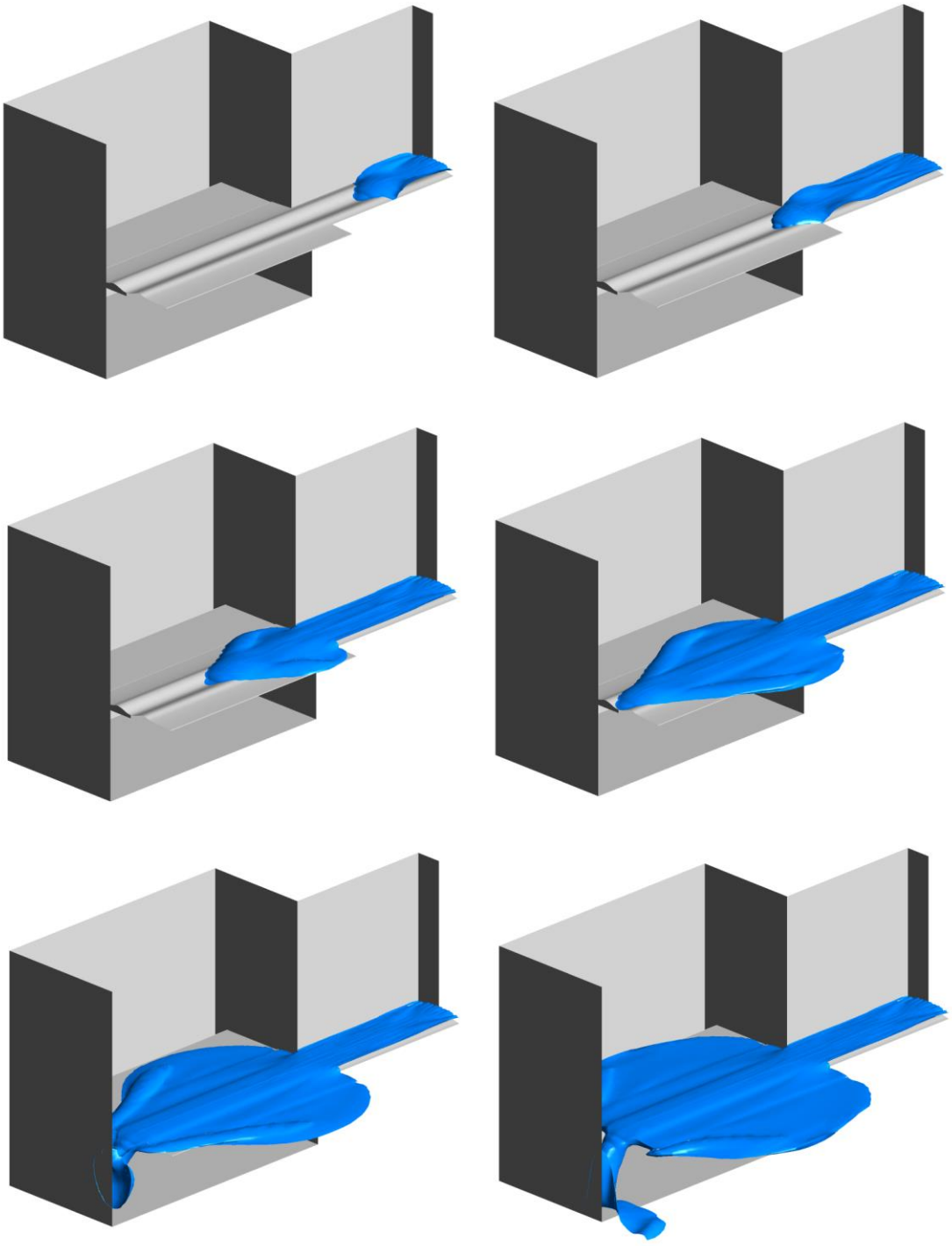

Figure 4.1 Isosurfaces at a density of 1002.5 kg/m^3 represent the ambient interface and show the time evolution of a 1 l/s current traversing the straight channel domain (see Section 4.5.1). Each image is separated by a time of 5 seconds. After traversing the inlet channel, the head of the current remains confined within the channel while overspill spreads over the main tank area before entering the sump.

capture these flow features. Here, with the use of an SST model that does such near wall resolution, a sufficiently high resolution mesh may also be able to pick out these interface instabilities. However, as mesh independence of velocity and density variables was achieved (Section 4.5.3) and this study focussed on mean bulk flow properties, such an approach was not taken.

4.5 Simulation domains

As detailed above, the numerical model is run on a mesh that represents the flow domain. This section provides details on these meshes.

All meshes used in this study are a structured grid. Unstructured, automatically generated grids are often used within areas such as the aerospace industry when modelling very complex geometries where structured grids are impractical. However, the geometries here are, in comparison, relatively simple, so it is possible to achieve a structured grid. The advantages of this approach are improved convergence and stability. Additionally, a higher resolution in critical areas can often be achieved with less total cells.

Critical areas are regions which are of most interest or higher variable gradients are expected. Here, for example, a higher resolution is required around the channel where the currents will flow, whereas away from the channel a lower resolution can be used.

4.5.1 Straight channel mesh

The mesh used for the straight channel simulations is shown in Figure 4.2. This directly replicates the T-Tank flume used for the laboratory experiments. Modelling the whole flume like this has a couple of advantages. Firstly, the design of the flume, with an underlying sump, actively minimises the unwanted reflections mentioned previously. Secondly, the flow is subject to the exact same environmental influences as the laboratory flow, optimising model performance. To simplify the meshing process, a separate mesh

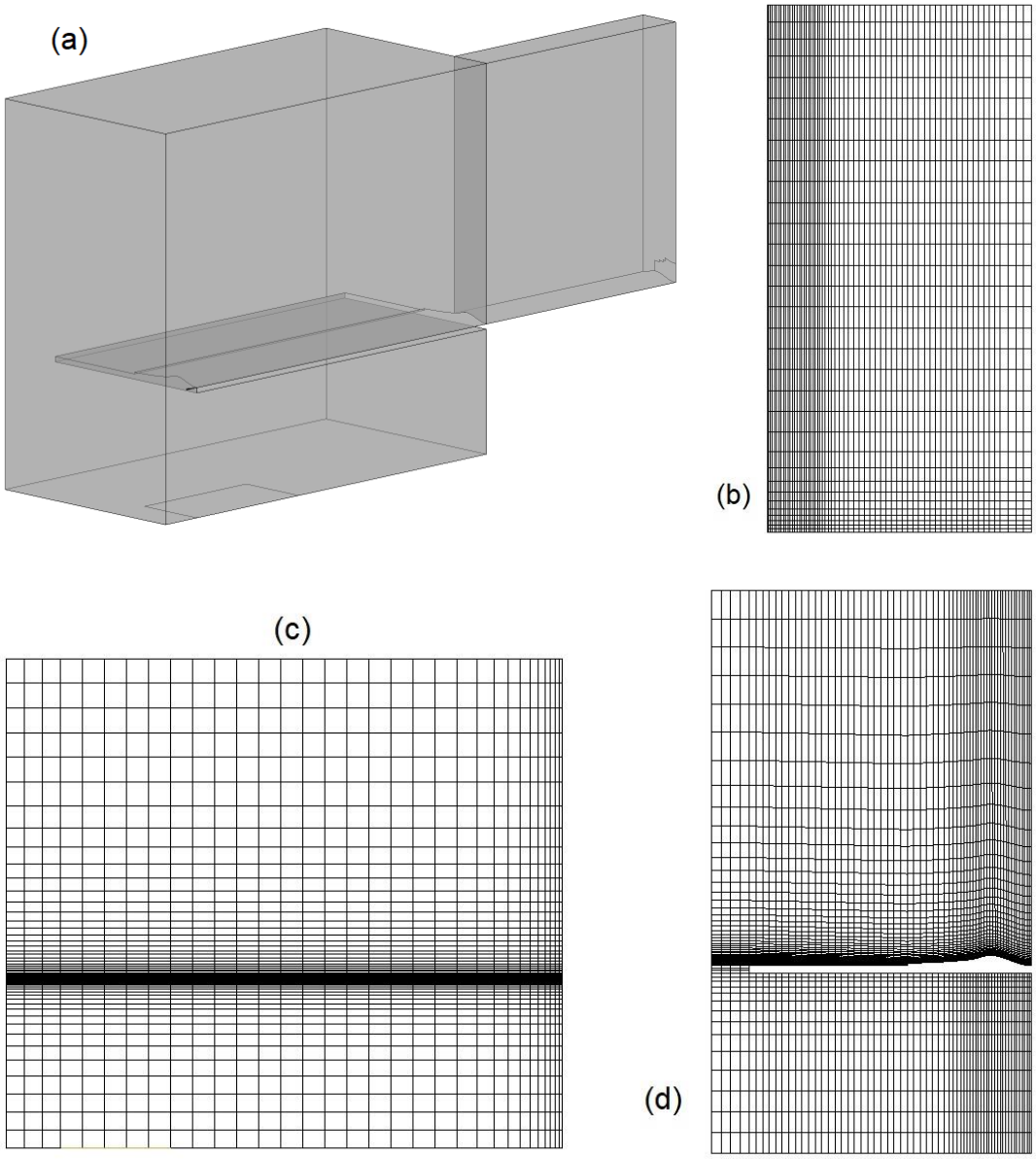

Figure 4.2 The mesh used in the straight channel simulations replicated the flume used in the laboratory: (a) shows a graphical representation of the main tank domain, with an inlet at the start of the input channel and an outlet at the base of the sump; (b) looking down at the top surface of the mesh; (c) looking sideways at the central symmetry surface; (d) looking upstream at the inlet side of the main flume.

was used to model the inlet channel. However, it used identical cell measurements to the main flume mesh to ensure the best possible connection at the interface. The inlet was positioned at the start of this channel and the pressure outlet positioned in the base of the sump as in the laboratory. Channel geometry was identical to the laboratory.

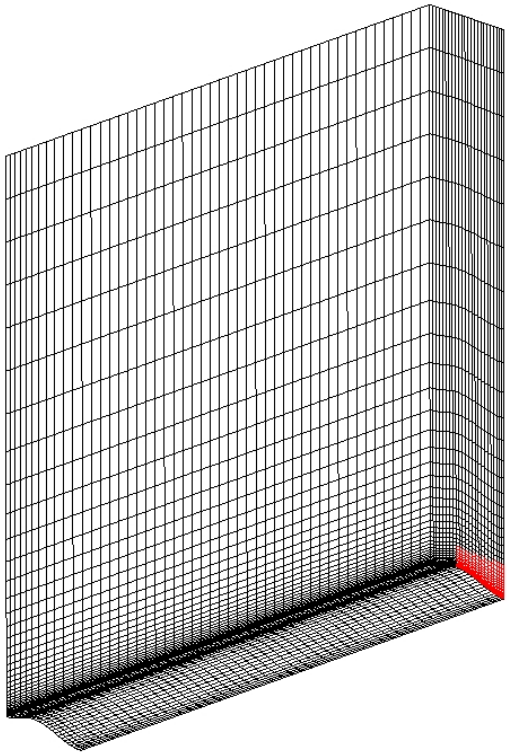

Figure 4.3 The inlet channel mesh which was joined to the main flume mesh in Figure 4.2. The zone of the mesh specified as an inlet is shown in red, the size of this zone varied depending on input flow rate to ensure $Fr = 1$.

4.5.2 Sinuous channel meshes

Due to the increased complexity of the sinuous meshes, a simpler overall geometry was employed. This is shown in Figure 4.4. Side sumps were used to dampen any sidewall reflection; these used a very coarse mesh as no flow resolution was required here. The entire downstream surface was specified as the pressure outlet. This generally worked well, although the last bend of each channel was slightly affected by reflection effects so

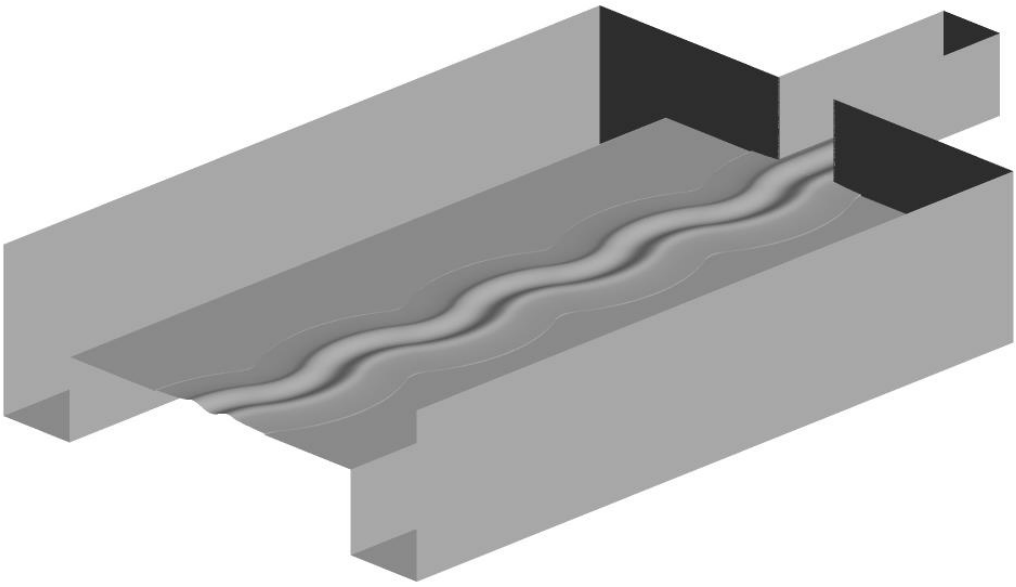

Figure 4.4 A graphical representation of the mid sinuosity mesh, with the surfaces specified as walls shaded. A side sump was used to reduces reflection effects and the entire downstream end surface was specified as a pressure outlet.

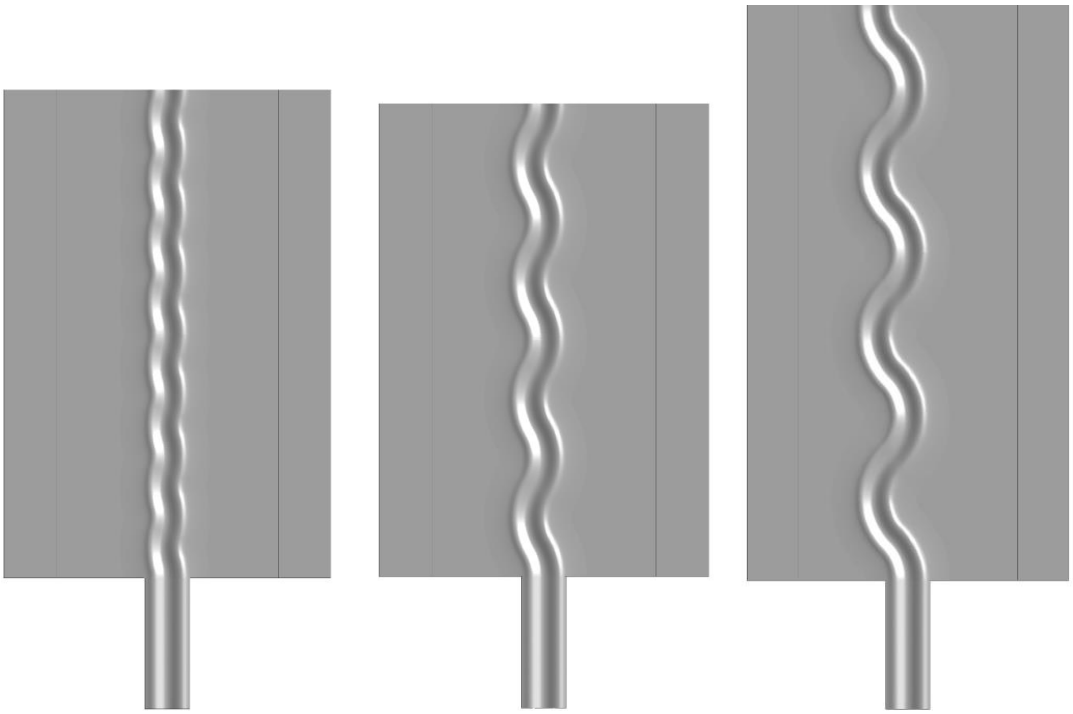

Figure 4.5 Planform views of the channel surface created by the low (left), mid (centre) and high sinuosity (right) meshes.

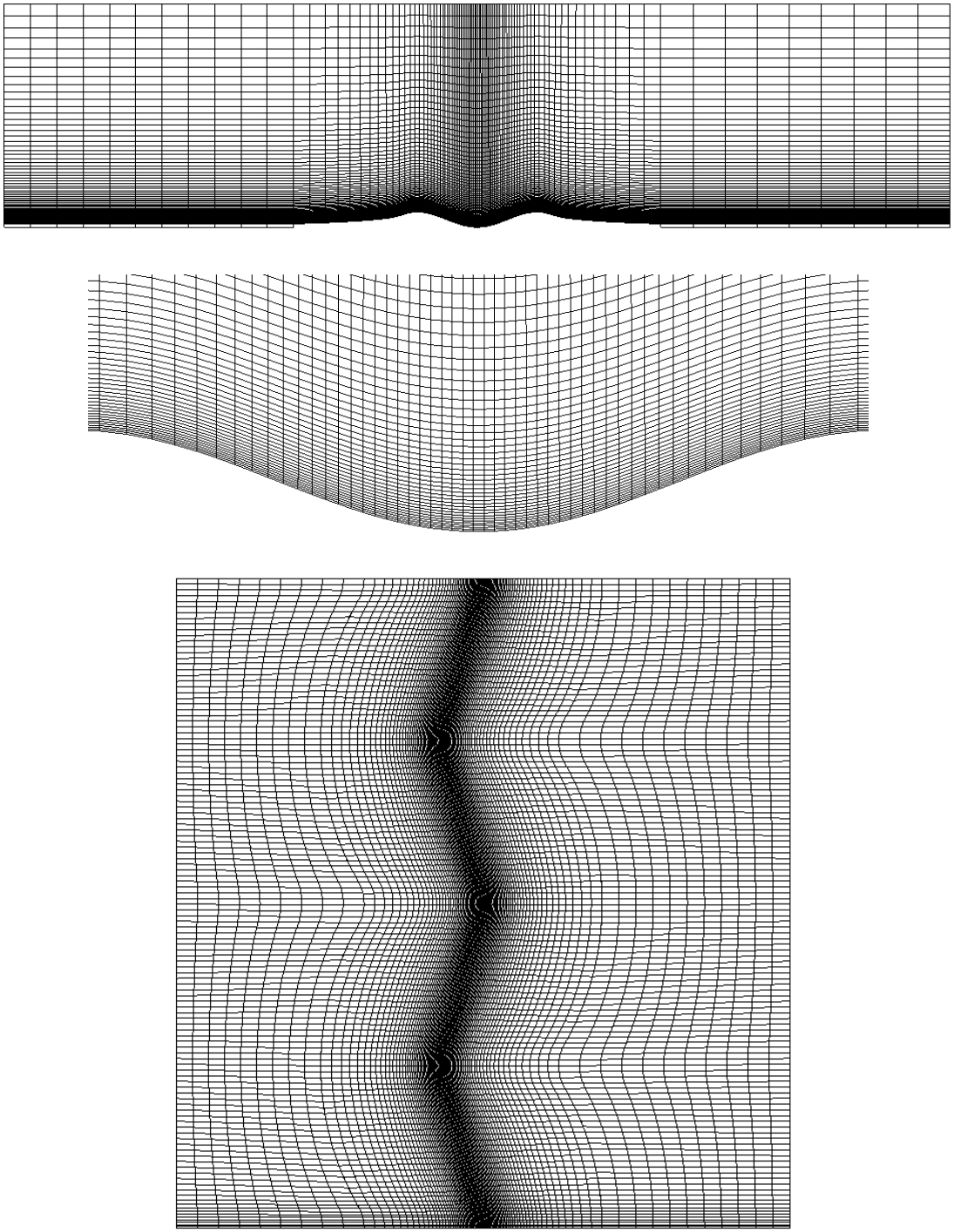

Figure 4.6 (top) Cross-sectional view of the mid sinuosity mesh looking upstream. Coarse additions, which are not shown, were added to either side to create sumps to reduce reflections; (centre) a magnified view of the channel; (centre) the channel surface of half the mid sinuosity mesh, again the side sumps have been excluded. Streamwise resolution is increased towards the inlet where higher variable gradients are found, before a constant resolution is maintained down the length of the channel.

data from these bends were excluded from any analysis. The same 1 m long inlet channel was used as for the straight channel mesh (Figure 4.3). The height of the domain was reduced so that the top free-slip surface was 0.5 m above the channel, this was found to have no effect on the current dynamics but reduced the number of cells required.

The domain width is also larger than for the straight channel setup. This was done to minimise any sidewall effects on the flow. Additionally, the channels were also extended lengthwise beyond what was possible in the laboratory (Figure 4.5). This allowed the investigation of the effects of a series of bends on flow development. Furthermore, one simulation used an even longer channel and this is described in Chapter 7.

4.5.3 Mesh independence

An important concept within CFD is one of mesh independence. This ensures any data are not affected by the resolution of the mesh. It can be tested by continually increasing the mesh resolution until the results become constant. This is usually most critical close to any boundaries. It is also only important in areas of interest, here for example there is no need for mesh independence in the sumps. Details of the meshes used are shown in the mesh independence checks are shown in Table 4.1, with examples of variable comparisons shown in Figures 4.7 and 4.8. In both cases, mesh B is the one used throughout this work.

The y^+ value associated with a mesh is an important variable when considering model performance close to a wall. It is a non-dimensional variable that assesses mesh resolution close to a boundary and is defined as,

$$y^+ = \frac{u^* y}{\nu}, \tag{4.27}$$

where $u^* = \sqrt{\tau_b/\rho}$, is the friction velocity and τ_b is the basal shear stress, defined as,

$$\tau_b = \mu \frac{\partial u}{\partial z}\Big|_{z=0}. \tag{4.28}$$

The k-ϵ and k-ω models that the SST model is based on have different methods of dealing with near-wall flow. The k-ϵ model can not be integrated up to a wall, so it employs wall functions to address this. These are empirical functions that define flow behaviour at a boundary and mean that a mesh can be fairly coarse close to a boundary, with recommended maximum y^+ values of approximately 200. The k-ω model can be integrated right up to a wall, although this subsequently requires a much finer mesh, with recommended maximum y^+ values of 2. The SST model automatically shifts between these two approaches depending on mesh resolution; with a coarse mesh the SST model essentially reverts to a k-ϵ model. Therefore, to take advantage of its capabilities, meshes which are used for SST simulations should have low values for y^+.

Table 4.2 Details of meshes used in the straight channel mesh independence study.

Mesh variant	A	B	C
Number of elements	76,291	186,282	291,464
Max intrachannel y^+	25	2	1

Table 4.3 Details of meshes used in the mid sinuosity channel mesh independence study.

Mesh variant	A	B	C
Number of elements	401,770	1,790,550	3,825,900
Max intrachannel y^+	15	2	1

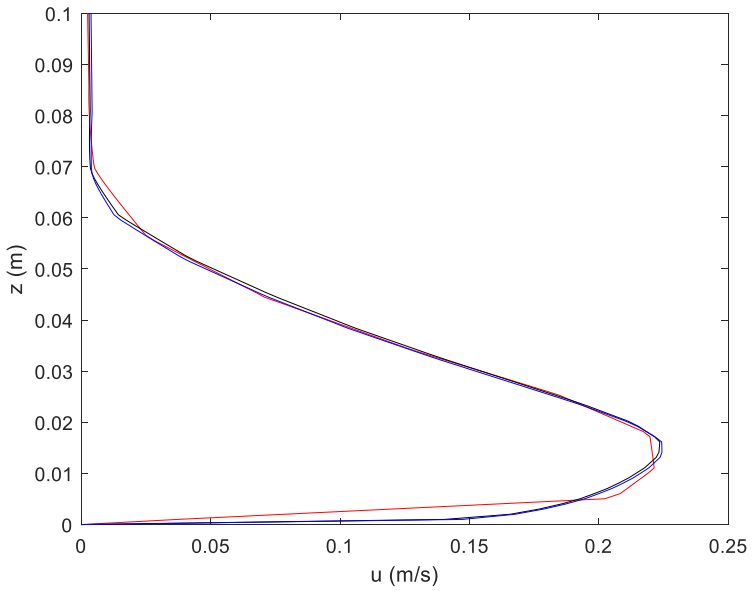

Figure 4.7 Example of a mesh independence comparison for the straight channel. Thalweg velocity profiles 1 m downstream for a 2 l/s current. Mesh A – red; Mesh B – black; Mesh C – blue.

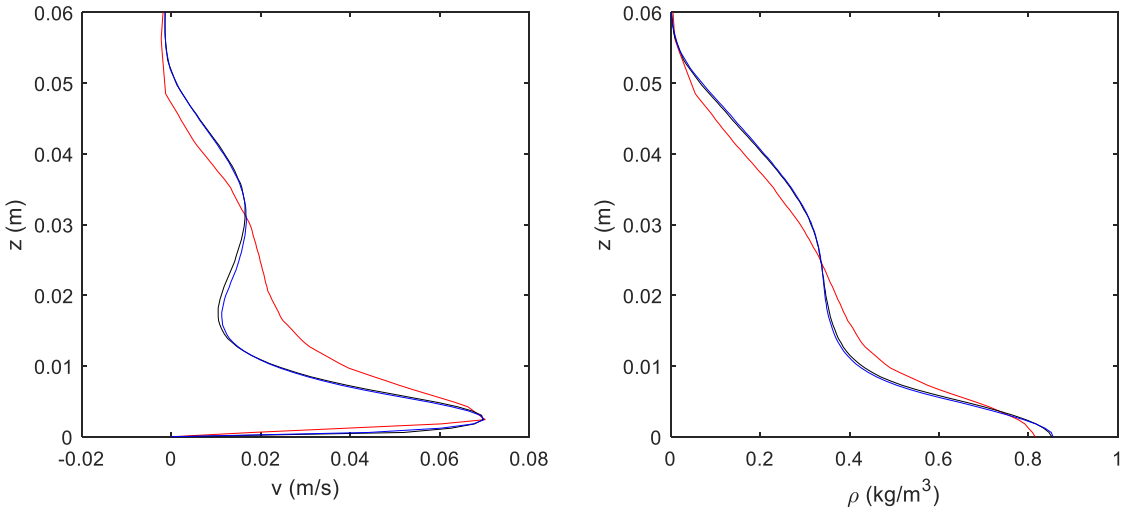

Figure 4.8 Examples of a mesh independence comparison for the mid sinuosity channel. Thalweg velocity and density profiles at the apex of bend 2 for a 1 l/s current. Mesh A – red; Mesh B – black; Mesh C – blue.

Chapter 5

The structure and entrainment characteristics of partially-confined gravity currents

Key points

- In partially-confined settings, channel depth is a key control on the height of a gravity current's velocity maximum.
- Both streamwise and overbank discharge rates can rapidly adjust downstream, with evidence of flow tuning and equilibration.
- The entrainment coefficient of a partially-confined flow is similar to that of a fully-confined flow with the same Richardson number.

Abstract

Seafloor channels are the main conduit for turbidity currents transporting sediment to the deep ocean and they can extend for thousands of kilometres along the ocean floor. Although it is common for channel-traversing turbidity currents to spill onto levees and other out-of-channel areas, the associated flow development and channel-current interaction remain poorly understood; much of our knowledge of turbidity current dynamics comes from studies of fully-confined scenarios. Here, the role that partial lateral confinement may play in affecting turbidity current dynamics is investigated. A report is given on laboratory experiments of partially-confined, dilute saline flows of variable flux rate traversing fixed, straight channels with cross-sectional profiles representative of morphologies found in the field. Complementary numerical experiments, validated

against high-resolution laboratory velocity data, extend the scope of the analysis. The experiments show that partial confinement exerts a first order control on flow structure. Overbank and downstream discharges rapidly adjust over short length-scales, providing a mechanism via which currents of varying sizes can be tuned by a channel and conform to a given channel geometry. Across a wide range of flow magnitudes and states of flow equilibration to the channel, a high-velocity core remains confined within the channel with a constant ratio of velocity maximum height to channel depth. Ongoing overbank flow prevents any flow thickening due to ambient entrainment, allowing stable downstream flow evolution. Despite dynamical differences, the entrainment rates of partially-confined and fully-confined flows remain comparable for a given Richardson number.

5.1 Introduction

Seafloor channels are the main conduits through which turbidity currents transport sediment from the continental shelf to the deep ocean [Meiburg and Kneller, 2010; Peakall and Sumner, 2015]. The submarine fans that they form are some of the largest sedimentary accumulations on Earth [Curray et al., 2002; Talling et al., 2007]. Due to the inherent challenges the deep-water environment poses, only recently have direct field measurements become more widespread [Khripounoff et al., 2003; Xu, 2010; Sumner et al., 2013; 2014; Talling et al., 2013; Dorrell et al., 2014; 2016; Azpiroz-Zabala et al., 2017]. In comparison there has been a long history of model development based on laboratory experiments [e.g. Ellison and Turner, 1957; Middleton, 1966; Garcia and Parker, 1983; Bonnecaze et al., 1993; Buckee et al., 2001; Keevil et al., 2006; Straub et al., 2008; Islam and Imran, 2010; Sequeiros et al., 2010] and numerical simulations [e.g. Eidsvik and Brørs, 1989; Imran et al., 2004; Huang et al., 2005; Cantero et al., 2009; Abd El-Gawad et al., 2011; Giorgio Serchi et al., 2011; Dorrell et al., 2014; Kneller et al., 2016].

The majority of these studies were conducted within fully-confined channels. Yet the partially-confined channel-levee component of natural systems usually extends much further than the fully-confined canyons that feed them [Normark and Damuth, 1997; Klaucke et al., 1998; Meiburg and Kneller, 2010; Nakajima and Kneller, 2013]. Those studies that do consider unconfined/partially-confined settings have been run over erodible beds [Mohrig and Buttles, 2007; Straub et al., 2008; De Leeuw et al., 2016] and tend to focus on morphological evolution and channel inception rather than flow dynamics. While such studies increase knowledge of channel and system development, the evolving channel geometries limit the consistency of flow data measured from successive currents.

The dynamics and behaviour of partially-confined flows, where the current can overspill onto the levees, are arguably far more complex and difficult to predict than for fully confined flows. Differing levels of confinement lead to changes in the ratios of ambient entrainment and overbank losses, but a systematic review of the flow field under a range of confinements is lacking. Mohrig and Buttles [2007] defined channelised, quasi-channelised and unconfined regimes based on the advancement of the flow front, but without presentation of detailed flow velocity or density data.

To date, it is fully-confined studies that have been widely used to explain and predict the structure and properties of gravity currents. Parker et al. [1987] conducted straight channel experiments and reviewed previous experimental data to find a Richardson number dependent expression for the entrainment coefficient of a flow,

$$e_w = \frac{0.075}{\sqrt{1 + 718Ri^{2.4}}}. \tag{5.1}$$

The rate at which a flow entrains ambient fluid is a key factor in both its spatial and temporal development and could help to provide an explanation as to why turbidity currents can travel for thousands of km [Meiburg and Kneller, 2010]. Kneller et al. [2016] used numerical simulations to show that, under certain conditions, turbidity currents can

have a stably stratified upper shear layer (Figure 1) with little mixing and low velocity gradients, resulting in a reduction in ambient entrainment; when predicting flow characteristics the use of bulk variables to approximate local variables was also questioned (such as using the bulk Richardson number as a proxy for the gradient Richardson number, a measure of stratification stability). In another fully-confined experiment, Sequeiros et al. [2010] observed a dependence of the velocity structure of the flow on the Richardson number, attributed to changes in stratification stability. The velocity profiles of subcritical flows ($Ri > 1$) exhibited a velocity maximum close to the top of the flow, although a large bed roughness is likely to have caused this. This is in contrast to previously observed profiles where the outer shear layer is 5-10 times thicker than the inner layer [Meiburg and Kneller, 2010]. Additionally, Sequeiros [2012] suggested that channel morphology can be used to predict Richardson or Froude numbers and subsequently flow conditions. However, this approach has limitations for erosional or bypassing flows as it does not take into account Reynolds-dependent turbulent effects in the lower boundary [Imran et al., 2016]. Also, high velocity maximum heights were not replicated in the simulations of Kneller et al. [2016], despite the stably stratified layer, nor in further experiments of subcritical flows which found limited dependence on Richardson number [Stagnaro and Pittaluga, 2014].

Regardless of the debate over confined-flow structure, the kinematics of a partially-confined flow must be fundamentally different due to the occurrence of overspill. Here, saline flow experiments have been conducted in a straight fixed channel with a channel-levee profile designed to be a realistic representation of morphology found in the field. Velocity data for a range of flow magnitudes has been captured (Table 5.2) with the aim of analysing partially-confined flow dynamics, entrainment characteristics and flow evolution.

Additionally, numerical simulations using a RANS (Reynolds-averaged Navier-Stokes) model have been used both to extend the range of flow conditions that are possible in the laboratory and to produce data for the whole flow field.

Table 5.1 Variable and notation definitions.

Variable	Expression
Flow depth	$h = \frac{\left(\int_0^\infty \lvert u\rvert \, dz\right)^2}{\int_0^\infty \lvert u\rvert^2 \, dz}$, where $\lvert u\rvert = \sqrt{u^2 + v^2}$
Depth-averaged velocity	$U = \frac{\int_0^\infty u \, dz}{h}, V = \frac{\int_0^\infty v \, dz}{h}, \lvert U\rvert = \frac{\int_0^\infty \lvert u\rvert \, dz}{h}$
Reynolds number	$Re = \frac{\lvert U\rvert h}{\nu}$
Froude number	$Fr = \frac{\lvert U\rvert}{\sqrt{g'h}}$
Richardson number	$Ri = \frac{g'h}{\lvert U\rvert^2}$
Reduced gravity	$g' = g\frac{\bar{\rho} - \rho_{ambient}}{\rho_{ambient}}$, where $\bar{\rho} = \frac{\int_0^\infty \rho \, dz}{h}$
Gradient Richardson number	$Ri_g = \frac{-g\frac{\partial \rho}{\partial z}}{\rho\left(\frac{\partial \lvert u\rvert}{\partial z}\right)^2}$

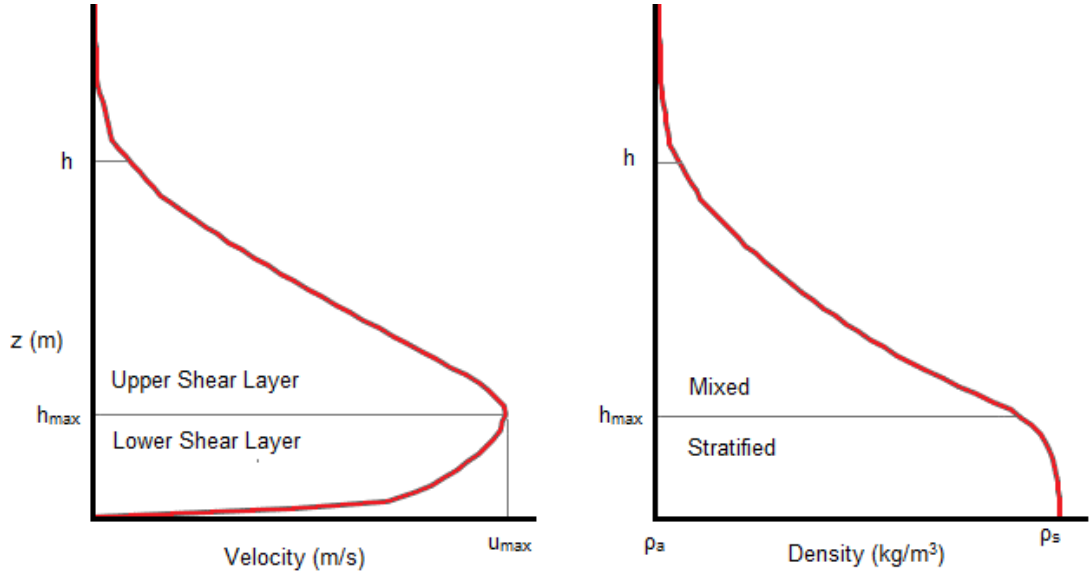

Figure 5.1 Velocity and density profiles for a gravity current generated by the release of a saline solution into an ambient fluid (water), as depicted in Figure 5.2. These are characterised by two shear layers separated by a velocity maximum. The lower shear layer is generated by basal drag and is stratified in nature, whereas the upper shear layer is a result of drag with the ambient fluid and is subsequently more mixed. h is the height of the current defined by the Ellison and Turner [1959] method in Table 5.1, ρ_a and ρ_s are the densities of the ambient and saline fluid respectively, and h_{max} and u_{max} are the height and magnitude of the velocity maximum.

5.2 Methodology

5.2.1 Laboratory setup

A series of continuous release saline gravity current experiments were conducted in the Sorby Environmental Fluid Dynamics Laboratory at the University of Leeds. While saline currents do not allow for the study of particulate settling, they do provide a good dynamical model of turbulent and stratification effects in turbidity currents [Kneller & Buckee, 2000; Islam & Imran, 2010; Cossu & Wells, 2012]. The flume used measured 1.7 m x 1.7 m and had a water depth of 1.5 m. An additional 1 m long inlet channel, along

which the currents developed, was centred on one side wall. The entire flume was inclined at an angle of 2° downstream. A fibreglass channel model was placed on a suspended floor 0.4 m above the tank base, with the area underneath acting as a sump to collect denser than ambient fluid.

The channel model is 0.22 m wide and extended the entire length of the inlet channel and 1.5 m into the main flume. The channel-levee profile was designed specifically to create an environment that might replicate morphology found in the field. The channel itself was 0.0275 m deep, giving an aspect ratio of 8, and the channel profile took the form of a sine curve to give a maximum slope of 22° on the channel sides. Channel size and width/depth ratio were chosen to balance the need for deep enough flows to be fully turbulent, while achieving a low aspect ratio as is often seen in the field [Clark et al., 1992; Kenyon et al., 1995]. The channel is bounded by a 22 cm wide levee on either side. The outer part of the levee profile is determined by the relationship $z = H(L/Y)^{-B}$, where z is the height of the levee, H is the channel depth, L is the distance from the channel thalweg, Y is half the channel width, and $B = 0.5535S^{0.662}$, where S is the slope. This was found to be give the best fit to channel levees on slopes >0.6° by Nakajima and Kneller [2013]. Although this relationship works well for the far field architecture it fails to capture the morphology near the crest. Therefore, the inner third of the levee profile was determined using data from previous gravity current experiments conducted over an erodible bed [Straub et al., 2008].

The gravity currents were created by preparing a saline solution of 1025 kg/m^3 density (2.5% excess density). The solution was pumped into the tank and controlled by an electromagnetic flow meter to minimise variation in the input flow rate. Before entering the tank, the fluid passed through a momentum diffuser, manufactured by capping the input pipe and drilling a series of holes in the pipe wall; this pipe was placed within a further inlet pipe which fed an inlet box modelled to fit the channel profile. This ensured that a buoyancy driven flow developed, rather than a dynamically different wall jet driven by inherited momentum and pressure. Fluid was also pumped out from the base of the

tank at an equal rate to ensure a constant water depth. Three flow rates were investigated: 0.2, 1 and 2 l/s (Table 5.2). The 0.2 l/s flow rate was chosen to give a near bank-full current. The 1 l/s flow rate was chosen to ensure a large enough quantity of overbank spill to measure with the ADVs (see below). The 2 l/s flow rate was chosen as the largest achievable rate for which an appropriate flow duration could be achieved without over-filling the sump. Hereafter, these will be referred to respectively as bank-full, equilibrium, and oversize currents.

Instantaneous three-component velocities were captured with a profiling Nortek Vectrino II acoustic Doppler velocimeter (ADV) sampling at 100 Hz. Vertical resolution of the data is 1 mm with each profile extending 35 mm above the model base. Velocities were recorded both at the channel thalweg and the channel crest.

Ultrasonic Doppler velocity profiling (UDVP) was used at the channel thalweg to capture larger velocity profiles. The ADV velocity profiles were extended with the UDVP data for the purposes of calculating bulk flow properties.

Table 5.2 Bulk flow properties of the three laboratory flows calculated from channel thalweg ADV/UDVP data, 1 m downstream from the main tank inlet.

Input Flow Rate (l/s)	0.2 (bank-full)	1 (equilibrium)	2 (oversize)
h (cm)	3.17	4.75	5.33
U (m/s)	0.111	0.153	0.174
Re	3550	7250	9250
Fr/Ri	1.50/0.44	1.65/0.37	1.77/0.32

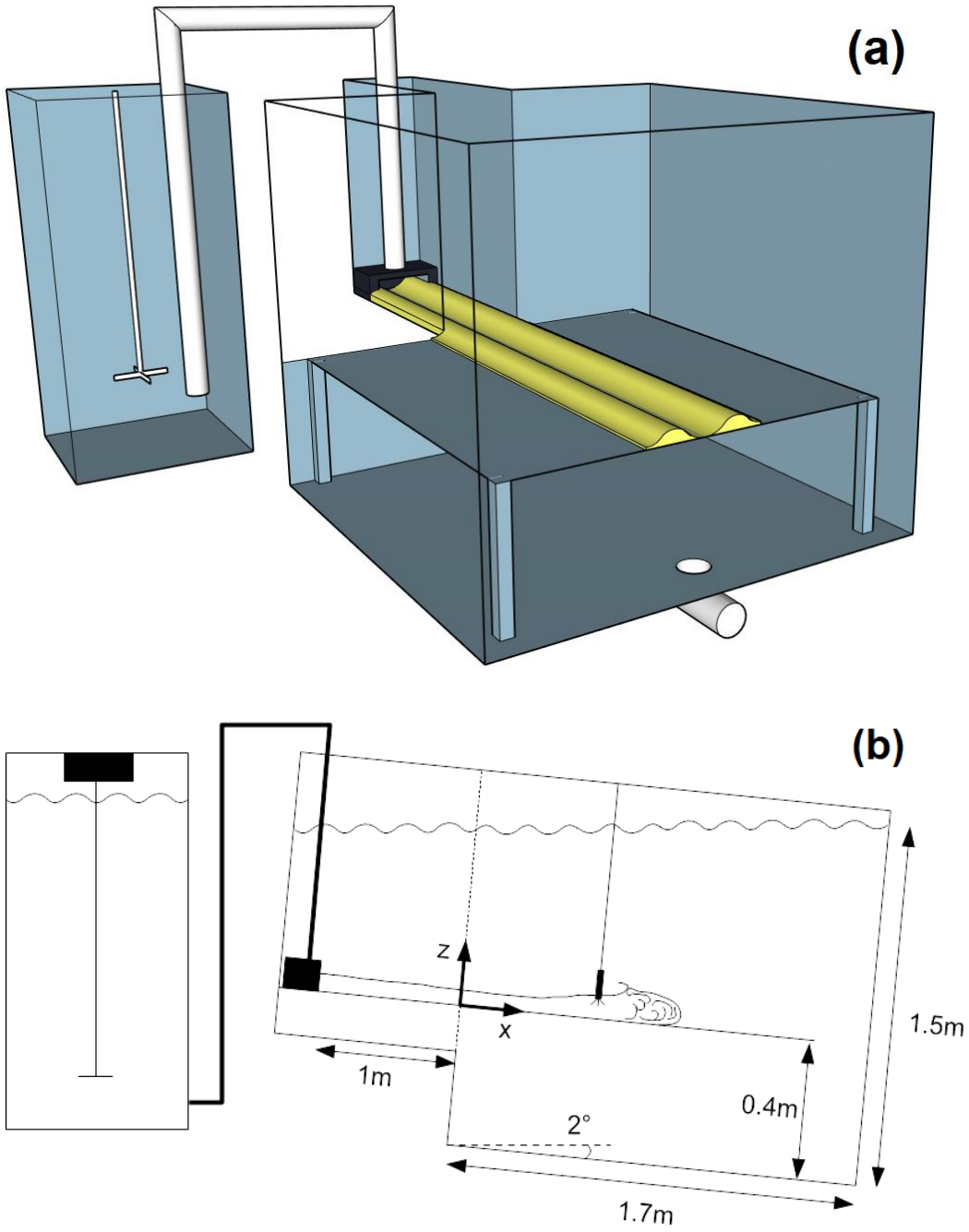

Figure 5.2 (a) A 3D visualisation (channel profile not to scale) and (b) a cross-sectional schematic of the setup employed in the Sorby Laboratory. Saline was pumped from a large mixing tank via a momentum diffuser into the main tank which was inclined at 2°. A 1 m long confined inlet channel allowed the flow to develop. The channel was elevated on a false floor to allow fluid to collect in a sump underneath. The frame of reference is defined relative to the channel, with the origin positioned on the channel thalweg at the entrance to the main tank.

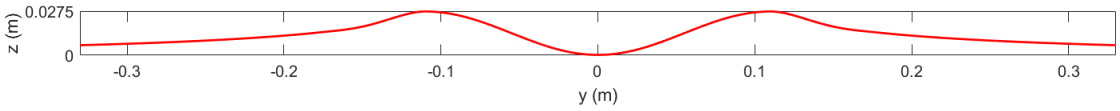

Figure 5.3 Cross-sectional view of the channel model. The channel measures 0.22 m wide and 0.0275 m deep with an aspect ratio of 8. The profile is that of a sine curve which results in a maximum steepness of 22°. The levee profile was determined using a combination of laboratory data [Straub et al., 2008] and field data [Nakajima and Kneller, 2013].

5.2.2 Numerical model

Numerical simulations of the laboratory flows and additional flow conditions were performed with a Reynolds-averaged Navier-Stokes (RANS) model, solved using the software ANSYS CFX 18.2. This is governed by the Reynolds-averaged mass and momentum conservation equations,

$$\frac{\partial \overline{\rho}}{\partial t} + \frac{\partial \overline{\rho}\tilde{u}_i}{\partial x_i} = 0, \tag{5.2}$$

$$\frac{\partial \overline{\rho}\tilde{u}_i}{\partial t} + \frac{\partial \overline{\rho}\tilde{u}_j\tilde{u}_i}{\partial x_j} = -\frac{\partial P}{\partial x_i} + \frac{\partial}{\partial x_j}\left(\mu\left(\frac{\partial \tilde{u}_i}{\partial x_j} + \frac{\partial \tilde{u}_j}{\partial x_i} - \frac{2}{3}\delta_{ij}\frac{\partial \tilde{u}_k}{\partial x_k}\right) - \overline{\rho u_i' u_j'}\right) + \overline{\rho} f_i, \tag{5.3}$$

where the velocity terms have been separated into Favre-averaged components, $\tilde{u}_i$, and fluctuating components, u_i'. Reynolds-averaged density and pressure are denoted by $\overline{\rho}$ and P respectively.

A shear stress transport (SST) turbulence closure has been used to model the Reynolds stresses, $-\overline{\rho u_i' u_j'}$. This combines the free-stream capability of the popular k-ϵ model with the explicit wall resolution of the k-ω model, and was found to perform better when compared with the laboratory data. It is still a two-equation eddy viscosity model, with transport equations for k, the turbulent kinetic energy and ω, the turbulence frequency.

However, blending functions are utilised in order to exploit the near-wall treatment of the k-ω model and the free-stream capability of the k-ϵ model [Menter, 1994].

To model variations in flow density, a mixture model was employed. This requires the solving of one conservation of mass equation (5.2) and one conservation of momentum equation (5.3) for the mixture. In this case, the mixture comprises water and saline with densities $\rho_w = 1000$ kg/m^3 and $\rho_s = 1025$ kg/m^3, respectively. The density of the mixture is defined by $\frac{1}{\overline{\rho}} = \frac{1-\alpha}{\rho_w} + \frac{\alpha}{\rho_s}$, where α is the saline mass fraction. This variable density is used in all terms of the model, including that of gravity. Additionally, a transport equation is solved for the saline mass fraction,

$$\frac{\partial \alpha\rho}{\partial t} + \frac{\partial \alpha\overline{\rho}\tilde{u}_i}{\partial x_i} = -\frac{\partial \overline{\alpha'\rho u_j'}}{\partial x_j}, \tag{5.4}$$

where the Reynolds flux term is modelled using the eddy diffusion hypothesis as,

$$-\overline{\alpha'\rho u_j'} = \frac{\mu_t}{\sigma_t}\frac{\partial \alpha}{\partial x_j}, \tag{5.5}$$

and μ_t, and $\sigma_t = 1$, are the eddy viscosity and turbulent Schmidt number respectively. Flow conditions and channel morphology were kept identical to laboratory values. Two larger flows with flow rates of 3 and 4 l/s, higher than was possible in the laboratory, were also simulated. Moreover, to investigate the role of Reynolds number, a set of flows were simulated in a channel scaled 4 times larger than in the laboratory. Flow rates were scaled upwards by a factor of 16 to ensure the same flow rate per unit area. Tables 5.3 and 5.4 show the bulk quantities of these flows. A more detailed description of the numerical model can be found in Chapter 4.

Use and validation of this modelling approach is extensive both in this field [e.g. Imran et al., 2004, 2007; Giorgio Serchi et al., 2011; Ezz and Imran, 2014] and related fields [e.g. Gauer at al., 2005; Doronzo, 2013]. Additionally, the numerical model has been compared to the experimental data in this study (Section 5.3.1).

Table 5.3 Bulk flow properties of the numerically simulated flows in the laboratory scale channel, calculated from channel thalweg data, 1 m downstream from the main tank inlet.

Input Flow Rate (l/s)	0.2	1	2	3	4
h (cm)	3.05	4.36	5.01	5.43	5.69
U (m/s)	0.111	0.151	0.175	0.194	0.212
Re	3390	6580	8770	10500	12100
Fr	1.64	1.84	1.96	2.03	2.15
Ri	0.372	0.295	0.260	0.243	0.216

Table 5.4 Bulk flow properties of the numerically simulated in flows in the upscaled channel, calculated from channel thalweg data, 4 m downstream from the main tank inlet.

Input Flow Rate (l/s)	3.2	16	32	48	64
h (cm)	11.7	15.1	17.2	18.5	19.4
U (m/s)	0.179	0.294	0.325	0.353	0.377
Re	20900	44300	55900	65100	73300
Fr	1.77	1.89	1.89	1.97	2.06
Ri	0.321	0.251	0.281	0.257	0.235

5.3 Results

5.3.1 Velocity, density and turbulence structure

The velocity profiles of the three laboratory flows are shown in Figure 5.4. These were captured with an ADV 1 m downstream of the main tank inlet to allow the flows to develop. As has been observed in many previous studies [e.g. Ellison and Turner, 1959; Garcia and Parker, 1993; Islam and Imran, 2010] all profiles exhibit a lower shear layer caused by basal drag and an upper shear layer caused by drag and subsequent mixing with the ambient fluid. These are separated by a velocity maximum. Here, the height of the velocity maximum remains almost constant for all flows at a height equal to half the channel depth. This is despite the changes in flow height, discharge, and Richardson number, suggesting that channel depth is a key control on partially-confined flow development.

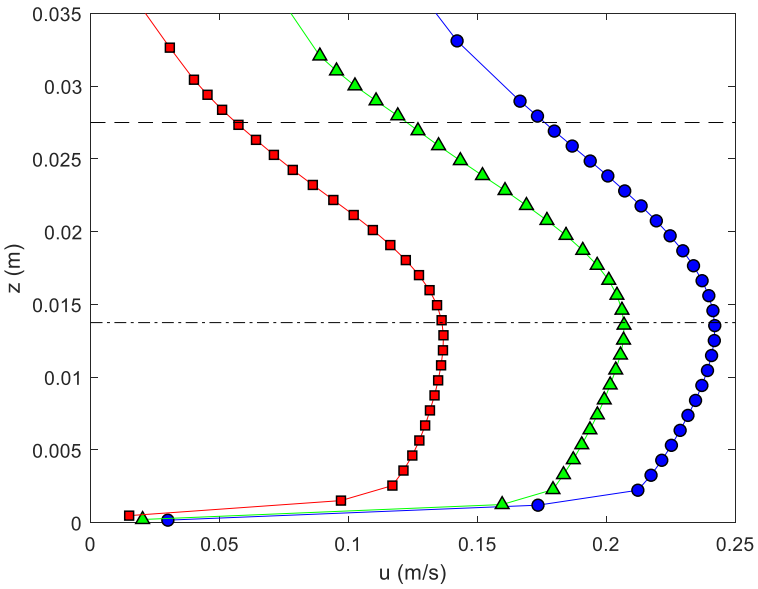

Figure 5.4 Channel thalweg ADV velocity profiles measured 1 m downstream from the main tank inlet, time-averaged over a 1 minute period. Red squares – 0.2 l/s; Green triangles – 1 l/s; Blue circles – 2 l/s. The dashed lines indicate channel depth and half channel depth. The height of the velocity maximum remains almost constant despite changes in flow rate and depth. This is in contrast to confined flows where velocity maximum height scales with flow depth.

The numerical simulations predict velocity profiles that compare well with the laboratory data (Figure 5.5) and model performance is certainly at least comparable to previous gravity current studies [e.g. Huang et al., 2005; Giorgio Serchi et al., 2011]. Except for the bank-full flow, the constant velocity maximum height is replicated (Figure 5.6) and the simulations show it remains constant at flow magnitudes larger than were possible in the laboratory. The upper shear layers are captured well, although the numerical simulations predict slightly different magnitudes for the maximum velocity and lower shear layer. In accordance with previous laboratory [e.g. Sequeiros et al., 2010; Islam and Imran, 2010] and numerical studies [e.g. Imran et al., 2004, 2007; Giorgio Serchi et al., 2011; Kneller et al., 2016], the simulations provide density data that show a stratified region below the velocity maximum with an increasingly mixed region above. The collapse of the simulated profiles in the lower shear layer (Figure 5.6) shows the bank-full flow to be characteristically different to the larger, overspilling flows, suggesting that overspill plays an important role in the development of flow structure.

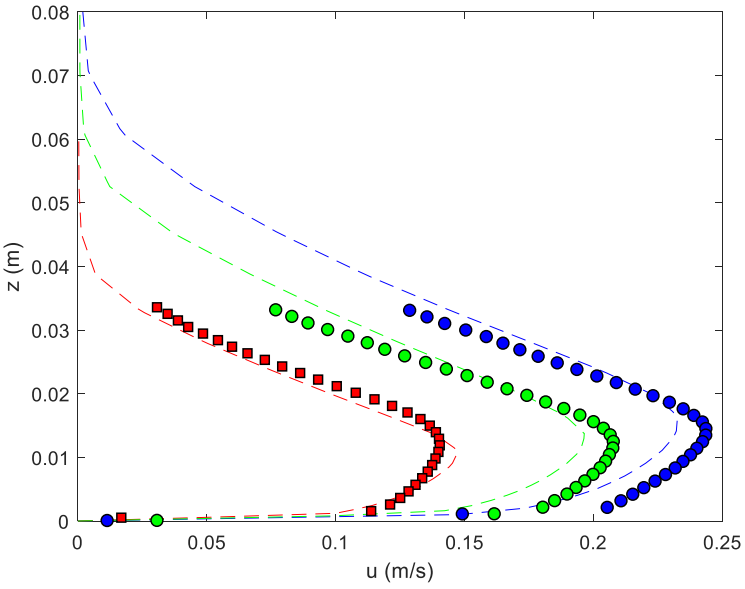

Figure 5.5 Channel thalweg ADV (symbols) and numerical (dashed lines) velocity profiles, measured 1 m downstream from the main tank inlet. Red - 0.2 l/s; Green - 1 l/s; Blue - 2 l/s. Data is not normalised to explicitly show similarities and differences.

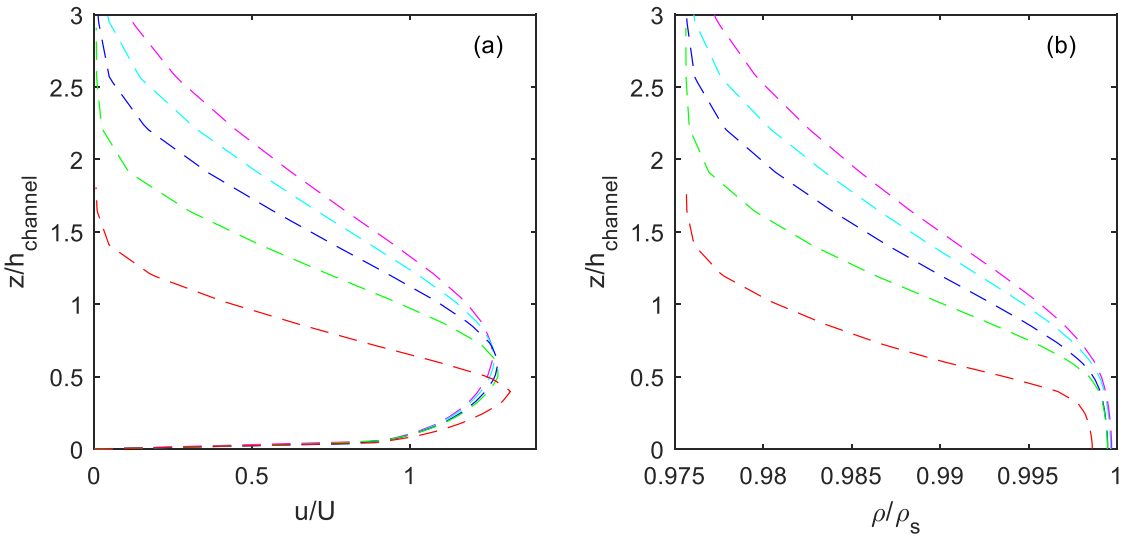

Figure 5.6 Channel thalweg numerical velocity (a) and density (b) profiles, normalised with depth averaged velocity/saline density and channel depth, measured 1 m downstream from the main tank inlet. Red – 0.2 l/s; Green – 1 l/s; Blue 2 l/s; Cyan – 3 l/s; Magenta 4 l/s. Numerical simulations show a constant velocity maximum height for larger flow rates and heights than could be achieved in the laboratory. With the exception of the bank-full flow (red trace), both velocity and density profiles collapse well in the lower shear layer where large levels of stratification are present.

Additionally, turbulent kinetic energy (TKE) profiles from both the laboratory and numerical simulations are shown in Figure 5.7 and can be seen as an additional verification tool for assessing the model's performance. TKE is a measure of the energy carried by turbulent eddies and is calculated as the sum of the mean velocity fluctuations, $k = 0.5\left(\overline{u'^2} + \overline{v'^2} + \overline{w'^2}\right)$. High frequency data collection allows the direct measurement of these fluctuations in the laboratory. TKE profiles for gravity currents are characterised by two local maxima in either shear layer [Buckee et al., 2001; Imran and Islam, 2010]. Both the laboratory and numerical profiles presented here share this shape. While TKE profiles from numerical models have been reported previously [e.g. Giorgio Serchi et al., 2011], a direct comparison to laboratory data has not been made before. As such, the

capability of such models in accurately predicting the turbulence structure of gravity currents is relatively unknown.

Here, the shape and positions of the minima and maxima for the three different flow sizes are predicted well. The relative changes in magnitudes between the flows are also in agreement. There are some differences in absolute magnitudes, especially for the larger flows, which are shown explicitly via not normalising the data. Considering highly fluctuating data the TKE profiles are calculated from, model performance is adjudged to be good.

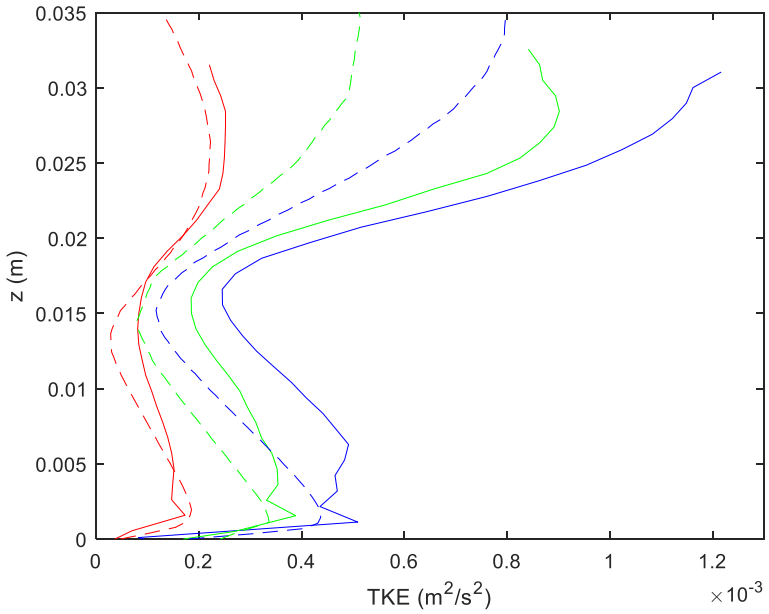

Figure 5.7 Channel thalweg ADV (solid) and numerical (dashed) turbulent kinetic energy profiles measured 1 m downstream from the main tank inlet. Red – 0.2 l/s; Green – 1 l/s; Blue 2 l/s. No data normalisation to show an explicit comparison.

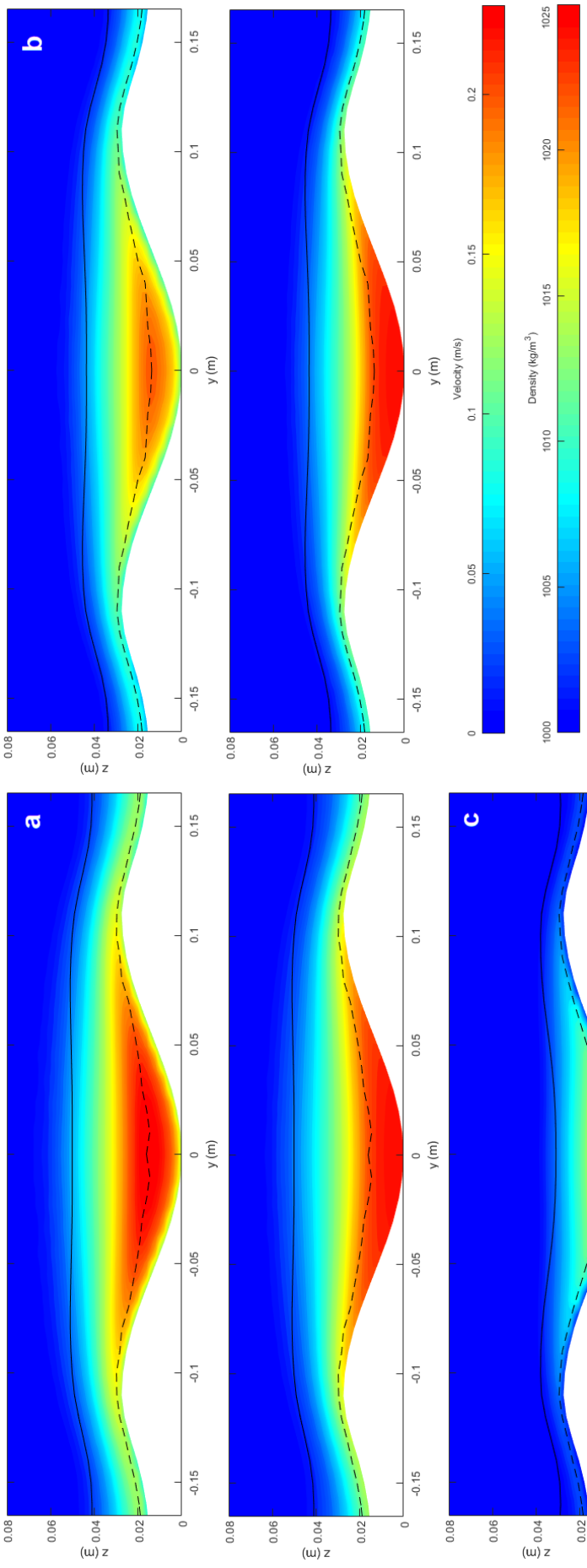

Figure 5.8 a) 2 l/s; b) 1 l/s; c) 0.2 l/s. Numerical velocity and density contours. The solid line shows the flow height and the dashed line shows the velocity maximum height. A non-mixed, stratified region below the velocity maximum height is evident in all flows. The channel also appears to maintain a confined 'high-velocity core'.

5.3.2 High Reynolds number simulations

In order to investigate the effect of Reynolds number, flows were simulated in a channel scaled four times larger than the laboratory geometry. To compare to the laboratory scale flows, flow rates were scaled upwards by a factor of 16 to keep the same flow rates per unit area. The resultant flows had Reynolds numbers between 20,900 and 73,300 (Table 5.4). The thalweg velocity and density profiles are shown in Figure 5.9. Similarly to the laboratory scale flows, the height of the velocity maximum of these larger remains fixed at around half the channel depth. The smallest, bank-full flow shows distinctly different characteristics with a relatively faster, more mixed core.

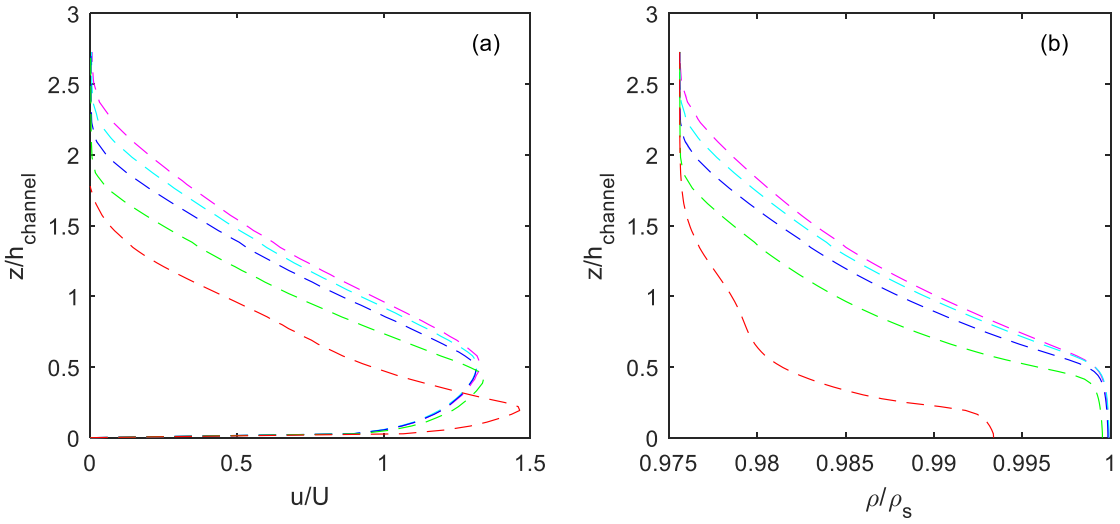

Figure 5.9 Channel thalweg numerical velocity (left) and density (right) profiles for the higher Reynolds number flows traversing the scaled-up channel. Profiles are normalised with depth averaged velocity/saline density and channel depth, measured 4 m downstream from the main tank inlet. Red – 3.2 l/s; Green – 16 l/s; Blue 32 l/s; Cyan – 48 l/s; Magenta 64 l/s.

5.3.3 Flow evolution and overspill

Total streamwise and overbank discharges are shown in Figure 5.10 using both the laboratory and numerical data. The simulations predict the downstream discharge well, showing close agreement with both the magnitudes and the spatial evolution. The downstream evolution of the overbank losses is also predicted well, although magnitudes for the two larger flows were over-predicted by 13-73%.

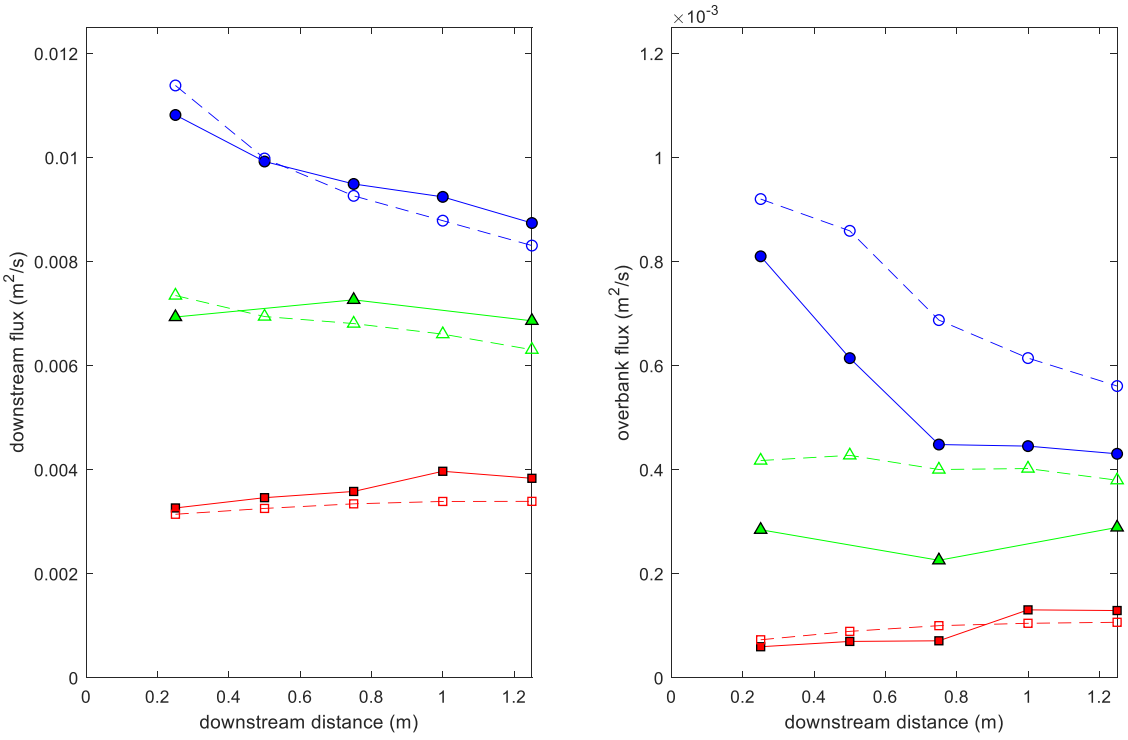

Figure 5.10 Downstream evolution of streamwise and overbank discharges from laboratory data (solid) and numerical simulations (dashed). Red – 0.2 l/s; Green – 1 l/s; Blue 2 l/s. The simulations predict the spatial evolution well, although they overestimate the magnitude of overspill for the two larger flows. Flow tuning is evident in the different ways each flow evolves. Both the streamwise and overbank discharge of the 0.2 l/s flow increase downstream as ambient fluid is entrained and the flow inflates. The discharges of the 1 l/s flow remain relatively constant indicating a close-to-equilibrium balance between overbank losses and ambient entrainment. The discharge of the 2 l/s flow changes rapidly with large initial overbank losses. The streamwise discharge continues to reduce downstream, despite ambient entrainment.

The three currents clearly interact with the channel in different ways. The bank-full current is dominated by ambient entrainment and as a result the streamwise discharge increases downstream. Overbank losses subsequently also increase as the current inflates and overspills the confinement of the channel. Both the streamwise discharge and overbank losses of the equilibrium current remain fairly constant, suggesting a balance between entrainment and overspill. The oversize current exhibits large initial overbank losses which result in a reduction in streamwise discharge. Overspill rates reduce rapidly downstream however as the current size reduces. These are examples of the two main ways – inflation vs. deflation – in which a current can evolve and be 'tuned' to equilibrium by a channel.

5.3.4 Entrainment

The entrainment of a flow can be found by a depth integration of the incompressibility equation,

$$\frac{\partial}{\partial x}\int_0^\infty u\,dz + \frac{\partial}{\partial y}\int_0^\infty v\,dz + w_\infty = 0, \tag{5.6}$$

where $w_\infty = \partial h/\partial t - w_e$ is a product of the shallow-water approximation [Parker, 1986]. Assuming a temporally stable flow, and using definitions in Table 5.1, this becomes,

$$e_W|U| = \frac{\partial Uh}{\partial x} + \frac{\partial Vh}{\partial y}, \tag{5.7}$$

where the entrainment velocity, $w_e = e_W|U|$, has been defined as a product of the entrainment coefficient, e_W, and the depth-averaged velocity magnitude of the flow. The entrainment coefficient describes the ability of a flow to entrain ambient fluid. For fully-confined flows with no cross-stream variation, (5.7) becomes,

$$e_W U = \frac{\partial U h}{\partial x}, \tag{5.8}$$

which is the standard form used for confined laboratory flows [Parker, 1987]. For partially-confined flows in a straight channel, when integrated across the channel from thalweg to crest, (5.5) becomes,

$$\hat{e}_W |\widehat{U}| Y = \frac{\partial \widehat{U} A}{\partial x} + V(Y) h(Y), \tag{5.9}$$

where the cross-sectional area of the current is defined as $A = \int_0^Y h \; dy$, channel average velocities as $|\widehat{U}| = \left(\int_0^Y \int_0^h |u| \, dz \, dy \right) / A$, the channel average entrainment coefficient as $\hat{e}_W = \left(\int_0^Y e_W \, |U| \, dy \right) / |\widehat{U}| Y$, and Y is half the channel width. The values of e_W presented here are all calculated using (5.9). If (5.8) is used for an overspilling, partially-confined flow, negative values will be observed if the current is deflating. Such a current is still clearly entraining ambient fluid and shows how overspill must be taken into account when analysing the entrainment characteristics of such flows. A channel-average Richardson number, defined as the mean of the thalweg and crest Richardson number, is also used in order to account for cross-stream variations.

Both the laboratory and numerical data output entrainment coefficients of the same order of magnitude (Figure 5.11), with the range of simulated values overlapping with the laboratory counterparts. The difference between simulated and laboratory values is largest for the 1 l/s flow which is attributed to the lower longitudinal resolution in the laboratory data for this flow. A clear difference can be seen between the bank-full and the larger, overspilling flows. The dependence of e_W on Richardson number for fully-confined flows, described by Parker et al., [1987] using (5.1), still appears to hold for the partially-confined setting. Figure 5.12 shows how the data presented here fall within the scatter of the previous laboratory data. However, there is also an apparent upper bound on e_W for these partially-confined flows. Neither an increase in flow magnitude, nor a reduction in Richardson number, results in a change in e_W (Figures 5.11 and 5.12),

perhaps suggesting a limit imposed on the entrainment ability of a current by the channel.

Further evidence for the 'tuning' effect of the channel described above is displayed in Figure 5.13. The downstream evolution of the Richardson number shows how each flow approaches an equilibrium. This is particularly evident in the thalweg. Cross-sectional contours of gradient Richardson number in Figure 5.14, produced using numerical simulation data, show how the stability of the stratification varies throughout each of the flows. The vertical structure is typical of a gravity current [Kneller et al., 2016], with values approaching infinity around the velocity maximum due to the reversal of the velocity gradient while a less stable layer above this that helps to drive entrainment. Here, localised low gradient Richardson regions are seen over the levee crests.

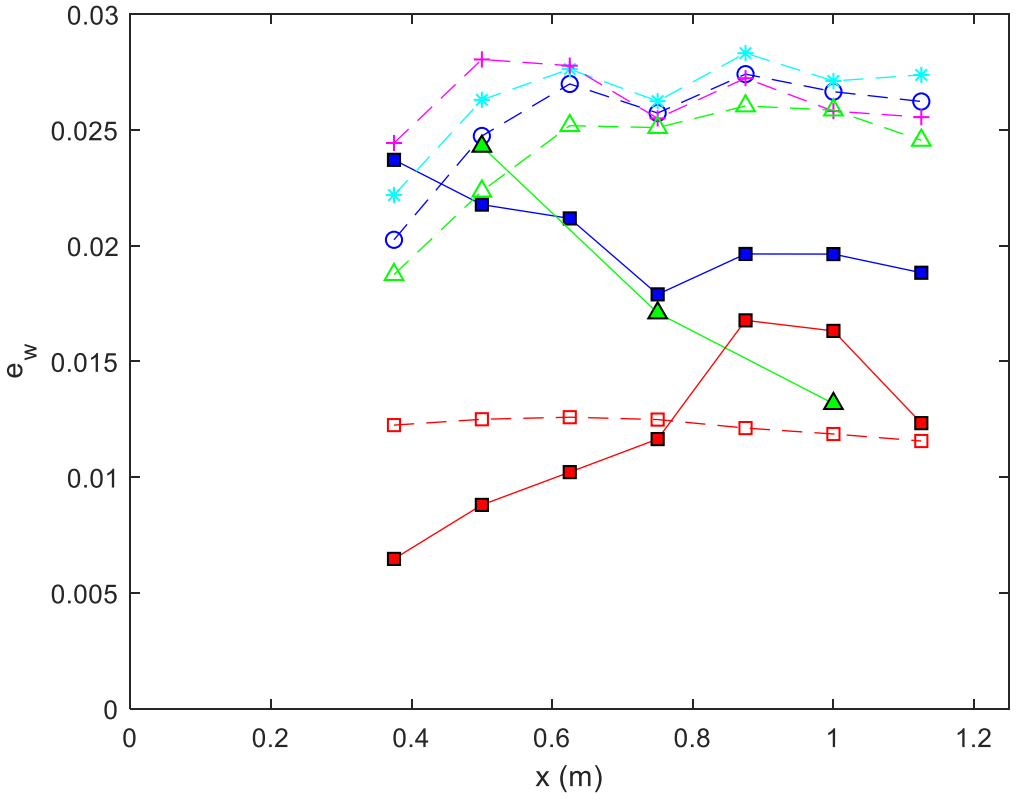

Figure 5.11 Downstream evolution of entrainment coefficient. Laboratory – solid; Numerical – dashed. Red – 0.2 l/s; Green – 1 l/s; Blue 2 l/s; Cyan – 3 l/s; Magenta 4 l/s. The magnitudes of the entrainment coefficient show overlap between the numerical and experimental data, although the simulations largely predict slightly higher values.

A reduction in bulk Richardson number is also seen over the levee crests for all flows. Similar cross-stream variations and magnitudes are found for the gradient Richardson number when depth-averaged over the upper shear layer. The depth-averaging region was defined to be between 0.5 and 2.5 standard deviations above the velocity maximum, found by approximating the upper velocity profile with a Gaussian distribution. This region was chosen to include the entire upper shear layer which is responsible for ambient entrainment while excluding the very high magnitudes found around the velocity maximum. This region also spans above the flow height determined by the Ellison and Turner [1959] definition (Table 5.1) which is used in the calculation of bulk quantities.

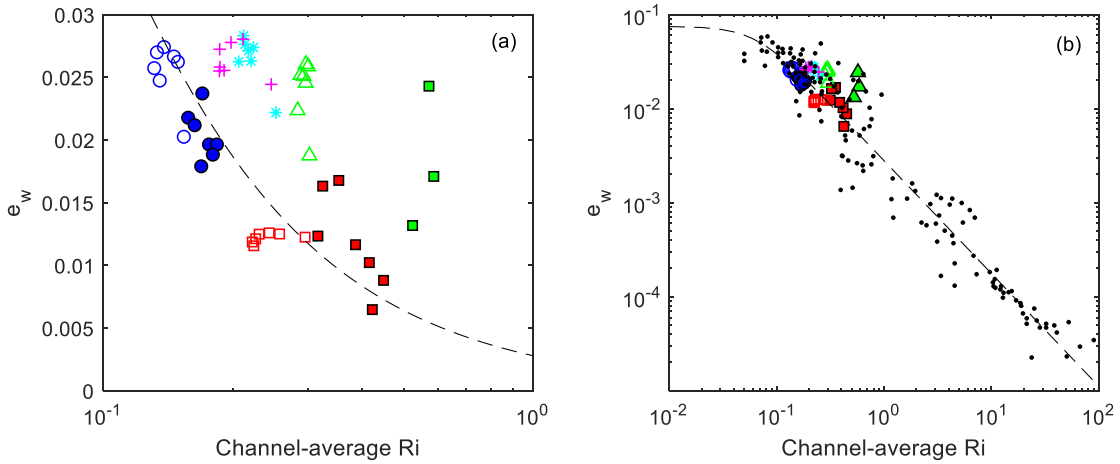

Figure 5.12 Entrainment coefficient is dependent on the (channel-average) Richardson number. Laboratory – filled; Numerical – hollow. Red – 0.2 l/s; Green – 1 l/s; Blue 2 l/s; Cyan – 3 l/s; Magenta 4 l/s. Data shown on linear (a) and logarithmic (b) axes. The dashed line indicates the Parker et al. [1987] relationship (5.1). Previous experimental data from confined flows, collated by Parker et al., are shown in black on the right [Ellison and Turner, 1959; Lofquist, 1960; Ashida and Egashira, 1975]. The standard deviation of the entrainment coefficient from the defined relationship is 0.041 for the previous confined data and 0.015 for the data presented here.

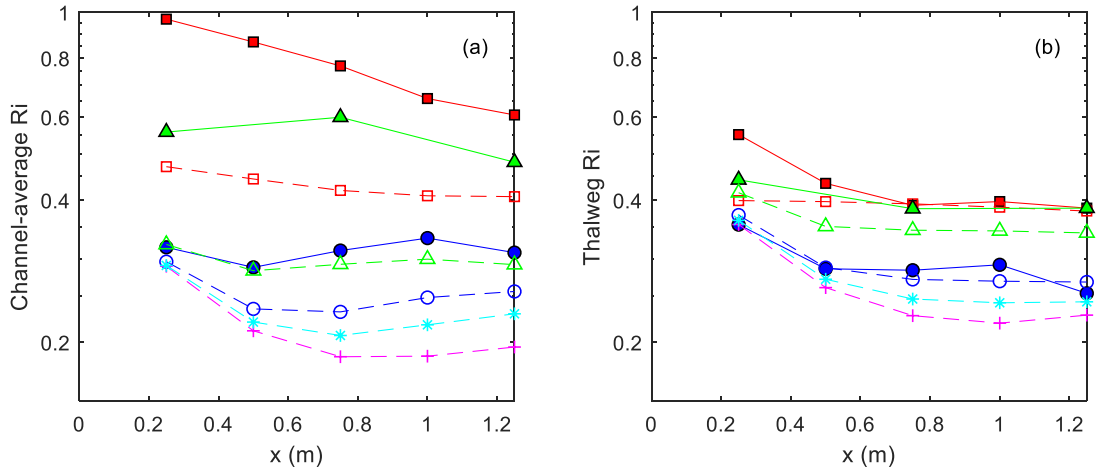

Figure 5.13 Downstream development of channel-average (a) and thalweg (b) Richardson number. Laboratory – solid; CFD – dashed. Red – 0.2 l/s; Green – 1 l/s; Blue 2 l/s; Cyan – 3 l/s; Magenta 4 l/s. CFD density data are used in the calculation of the laboratory values in the absence of laboratory density data. There is an adjustment period before each flow approaches an equilibrium Richardson number, the distance of which is dependent on flow magnitude.

Figure 5.14 (next page) a) 2 l/s; b) 1 l/s; c) 0.2 l/s. Gradient Richardson contours for each flow rate exhibit regions of decreased magnitudes above the levee crests, and indication of decreased stability and increased mixing. Both the cross-stream variations and magnitudes of the bulk Richardson number (solid line) are comparable with the depth-averaged gradient Richardson number (dashed line). The bulk Richardson number would appear to be a good proxy for the gradient Richardson number in the upper shear layer and a good indication of mixing levels. The depth-average was calculated between 0.5 and 2.5 standard deviations (dash-dot lines) above the velocity maximum (dashed line). The flow height is also shown with a solid line.

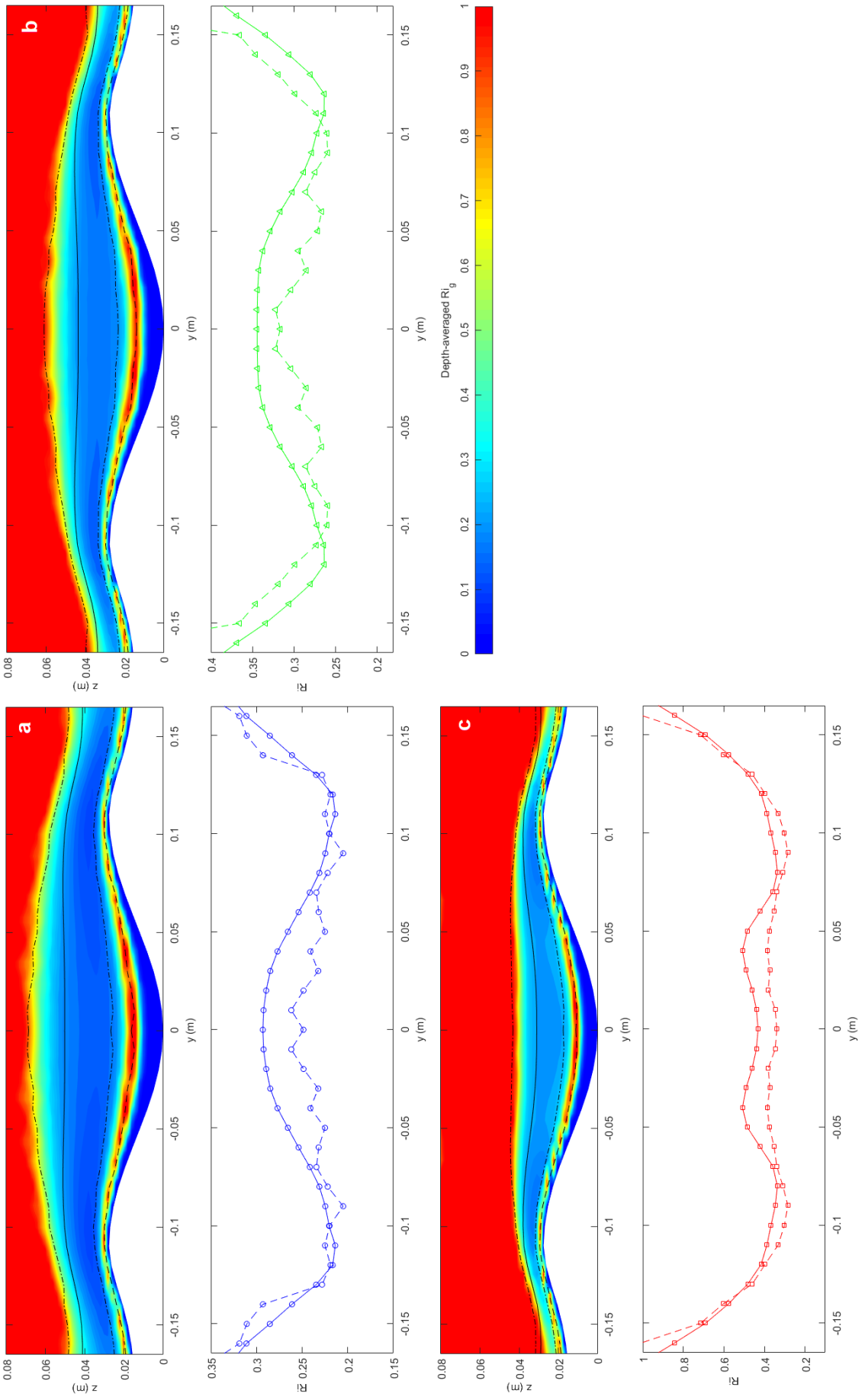
a
b
c
z (m)
y (m)
Depth-averaged Ri$_g$
Ri

5.4 Discussion

5.4.1 Channel forcing

The occurrence of overspill and associated inherent cross-stream variation mean the dynamics of a partially-confined flow are fundamentally different to those of a fully-confined flow. For a fully-confined flow, the velocity maximum height, h_{max}, is determined solely by the balance between basal and ambient drag [Middleton, 1993]; h_{max} scales with height, with values observed between $h_{max}/h = 0.1$ [Buckee et al., 2001] and $h_{max}/h = 0.3$ [Kneller et al., 1999]. Variations are to be expected with differences in basal materials, laboratory conditions and the difficulty in defining a current's height. A dependence of h_{max} on both the flow's Richardson number [Sequeiros et al., 2010] and Reynolds number [Stagnaro and Pittaluga, 2014] has also been observed. For the partially-confined flows analysed here, h_{max} remains nearly constant for all the laboratory-scale flows at a height equal to half the channel depth, regardless of flow height or Richardson number. This could suggest an increase in the ratio of ambient to basal drag for larger flows, perhaps due to the increase in overspill and the surface area of the ambient interface. For the upscaled flows, described in Section 5.3.2, the smaller flows have a relatively lower position of h_{max}. This can be explained by the basal drag remaining constant but ambient drag increasing with Reynolds number. However, half the channel depth remains as an upper limit on h_{max} for the larger flows indicating that, even at large Reynolds numbers, channel depth remains a first-order control on flow structure.

It would appear the channel has the ability to maintain a high velocity 'core' (illustrated in Figure 5.8). A value of h_{max} less than the channel depth allows the current to maintain a highly stratified lower region confined by the base of the channel. This region provides a gravitational driving force that is sustained along the length of the channel and enables the possibility of a stable downstream flow evolution pattern. The forcing on the current exerted by the channel is therefore further confirmed as a key control on the flow

dynamics and can be recognised as an important mechanism in sustaining current run-out.

It is unclear at what point h_{max} could exceed the channel depth, although this would make a rapid dissipation of the current likely, with the lower region no longer fully restricted and nothing to prevent lateral spreading. In a laboratory study with varying levels of flow confinement, Mohrig and Buttles [2007] defined a threshold of $h/H > 5$, where H is the channel depth to differentiate confined vs. effectively unconfined flow. It was proposed that at this threshold the high velocity core exceeds the confines of the channel, resulting in an unconfined flow, although there was no vertical resolution in the velocity data which were acquired from overhead cameras. The laboratory and simulated flows described here have values in h/H ranging from 1.15 to 3. While none of these flows approach the $h/H > 5$ threshold, the constant height of the velocity maximum suggests any transition would not be gradual.

5.4.2 Flow tuning

A channel is clearly capable of 'tuning' oversize flows via overspill, with deflation and flow stripping occurring here for flows with $h/H > 1.9$. Mohrig and Buttles [2007] also observed this tuning effect, reporting flows with $h/H > 1.3$ undergoing deflation until a constant flow height was reached. At the laboratory scale at least, such oversize flows appear to be unable to propagate in a partially-confined setting. While it is therefore unlikely the $h/H > 5$ threshold would be breached via gradual flow evolution, external factors could trigger this scenario. A current emerging from a canyon system could be disproportionally deep before being stripped or thinned by the channel, analogous to the oversize current described here that experienced significant overspill proximally (Figure 5.10). A break in slope, as often seen at a channel-lobe transition zone [Wynn et al., 2002; Dorrell et al., 2016], could also cause a sudden thickening of the flow and a subsequent avulsion or transition to unconfinement. Additionally, increasing channel instability,

caused by continual deposition, could lead to a channel being unable to provide the necessary degree of confinement to contain the high velocity core [Dorrell et al., 2015]. Here, onlythe dynamics of straight channel confinement are considered; channel sinuosity leads to flow elevation at bend apexes [Keevil et al., 2006; Cossu and Wells, 2010; Dorrell et al., 2013], providing an additional mechanism for flow avulsion.

While the size of the flow can be tuned via overspill, ambient entrainment can also lead to the inflation of an undersize flow. This mechanism allows the achievement of an equilibrium whereby a current's overbank losses are balanced with ambient entrainment. In contrast, entrainment is the sole mechanism for fully-confined flow evolution, resulting in continued inflation [Symons et al., 2017]. Here, quasi-equilibrium currents, characterised by $h/H = 1.75$, maintain a steady flow height with both streamwise and overbank discharges remaining constant along the length of the channel (Figure 5.10). Further evidence of tuning can be seen in Figure 5.13. Each flow must propagate for a characteristic length before attaining a constant Richardson number, with the magnitude of this length correlated with the size of the flow. It is unlikely, however, that for a given channel geometry, there exists a unique equilibrium flow condition that all currents evolve towards regardless of input. Rather, a partially-confining channel allows a range of currents to develop a balance between ambient entrainment and overbank losses which allows stable downstream evolution. Figure 5.15 illustrates the different flow evolution possibilities depending on the ratios of the entrainment and overspill mechanisms and the contrast to a fully-confined setting.

If a channel has the capability to modify flows along its length, an impact in the overbank deposit record would be expected. Differing levels of overspill near the channel inlet followed by an approach to an equilibrium value would suggest a transformation from heterogeneous overbank deposits proximally to homogenous deposits distally. This is, however, based on the assumption that all overbank flow is of a similar depositional character. Larger overbank flows may bypass the channel-proximal levee, significantly complicating the depositional record in these locations.

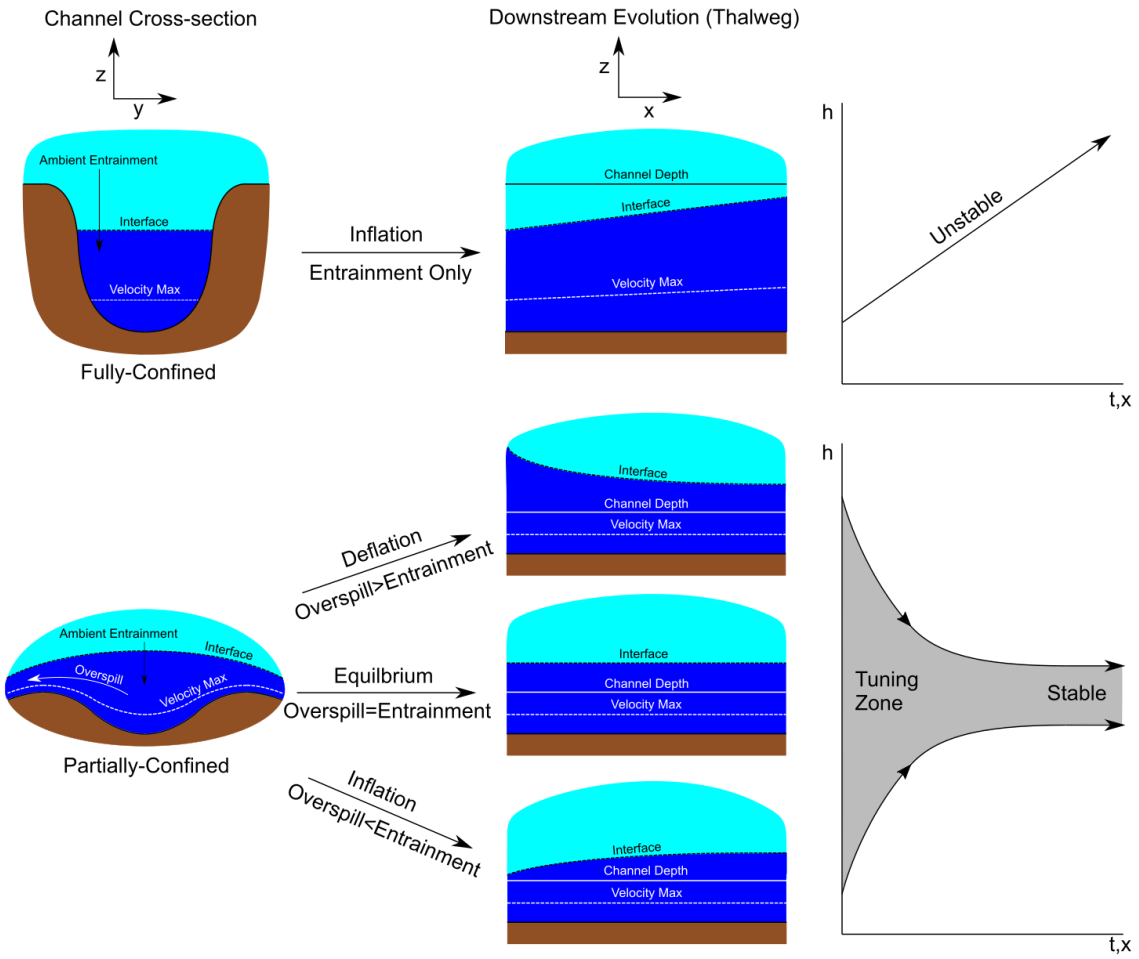

Figure 5.15 Downstream evolution patterns of fully and partially-confined flows. Entraining fully-confined flows can only inflate in an unstable evolution pattern. Partially-confined flows can either inflate or deflate to approach a stable equilibrium where overbank losses are balanced by ambient entrainment.

5.4.3 Entrainment and cross-stream variation

It can be seen from (5.4) that for a partially-confined flow the overspill term, Vh, has a significant impact on the entrainment. This is evident in the markedly lower entrainment coefficient values for the bank-full flow (Figure 5.11). It is also the primary reason for the difference in simulated and laboratory values (Figure 5.10 shows how the numerical model over-predicts overspill levels for the larger flows). It is therefore slightly surprising

that, for a given Richardson number, these partially-confined flows exhibit similar entrainment rates to fully-confined flows (Figure 5.12), despite the differences in flow dynamics described above, such as the occurrence of overspill. It should be noted that the calculation of the Richardson numbers for the laboratory flows is dependent on the numerical density data. Given the relatively low spread of this and previous data, however (see Figure 5.12), it is unlikely any discrepancies would significantly affect the Richardson number calculations or any conclusions drawn.

As is the case with the velocity maximum height, there does appear to be an upper limit on flow entrainment efficiency. Despite an increase in input flow rate and a reduction in thalweg Richardson number (Table 5.3), the larger 3 and 4 l/s laboratory scale flows do not exhibit higher values of entrainment coefficient. This appears to be driven by a lower Richardson number at levee crests resulting in a lower channel average Richardson number and the corresponding associated average entrainment characteristics. Again, the constraints of the channel morphology and the increasing levels of overspill appear to be a key control on flow dynamics.

For all the flows considered it is important to take into account cross-stream variations, as these can be significant, affecting not only calculated entrainment levels but also definitions of Richardson number. The bulk Richardson number is often used as an approximation for the gradient Richardson number (see definitions in Table 5.1), which can be used to identify regions of increased mixing due to buoyant instability. For partially-confined flows, these regions occur above both levee crests (Figure 5.14) highlighting how mixing processes at channel boundaries are key to the entrainment process. Using 2D direct numerical simulation of the Navier-Stokes equations, Kneller et al. [2016] found that the bulk Richardson number was not a good measure of the gradient Richardson number, which served as a good indicator to a flow's entrainment behaviour. Here though, the bulk Richardson number, for all flows, appears to be a good proxy for the gradient Richardson number in the upper shear layer (Figure 5.14). This is the region responsible for ambient entrainment and thus of most interest when examining

mixing rates. Both the magnitudes and the cross-stream variations are captured well in the numerical modelling reported here. It is possible that the 2D nature of the simulations reported by Kneller et al. [2016] may have resulted in the artificial dampening of some of the flow's mixing mechanisms.

5.5 Conclusions

Both laboratory experiments and numerical simulations show that for a partially-confined gravity current the geometry of the containing channel is a first-order control on the flow dynamics. Here, at the laboratory scale, the height of the velocity maximum for a range of flows was not affected by changes in multiple factors including flow height and Richardson number. The velocity maximum remained fixed at a height equal to half the channel depth, which resulted in the development of a high-velocity core and highly stratified lower shear layer, both confined within the channel. Numerical simulations at larger Reynolds numbers confirm the half channel depth upper limit on the velocity maximum height. The channel form plays a key factor in controlling the downstream evolution of the current. The joint mechanisms of overspill and ambient entrainment allow partially-confined flows to either deflate or inflate towards a quasi-equilibrium state. There are significant cross-stream variations in the Richardson and gradient Richardson numbers of partially-confined flow. Low Richardson number regions observed over the levee crests indicate increased levels of mixing and highlight the importance of overspill in the entrainment process. Despite this, the entrainment coefficients for a given Richardson number are similar to those of fully-confined flows in previous studies.

Chapter 6

Density driven flows in sinuous submarine channels: through the 2D plane and the 3D flow structure found there

Key points

- Helical flow can be inhibited both by low channel sinuosity and large overbank losses.
- Secondary rotational cells are characterised by a local reversal in the radial pressure gradient.
- Two horizontally adjacent rotational cells can form at the inflection point between bends.
- A change in cross-sectional channel geometry can switch the dominant basal flow direction.

Abstract

Sinuous submarine channels are significant topographic features on the seafloor, acting as the main conduit for turbidity currents transporting sediment to the deep ocean. A channel's sinuosity is a key control on a current's dynamics and structure, with the onset of rotational cross-stream cells and a helical flow structure a well-known and previously studied phenomenon. However, there has been much discussion, and little consensus, on what determines the orientation of a cell's rotation. Here, a combination of laboratory experiments and numerical simulations of continuous saline gravity currents traversing sinuous channels with a fixed cross-sectional profile, representative of morphologies found in the field are presented. Both the experiments and simulations show how both

large levels of fluid lost overbank and low channel sinuosity can inhibit the formation of rotational cells. When rotational cells do form, the numerical simulations show how they are consistently characterised by a local reversal in the horizontal pressure gradient. An outcome of this helical structure is a switching of rotational direction between bends which can result in laterally adjacent cells of opposing rotation at inflection points. Furthermore, channel morphology is shown to have a first order effect on the lateral flow structure, with a change in cross-sectional profile capable of switching the dominant direction of basal flow.

6.1 Introduction

Turbidity currents are responsible for forming some of the largest sedimentary structures on Earth [Curray et al., 2002]. Individual currents are capable of transporting 100s of cubic kilometres of sediment [Masson et al., 1996; Talling et al., 2007]. Their deposits, submarine fans [Covault et al., 2011; Bouma et al., 2012], are composed of seafloor channel networks, culminating in a series of lobes. Knowledge of the underlying fluid dynamics is crucial in understanding both the behaviour of the currents and the evolution of their containing channels. The ability of a current to be both aggrade and erode a channel, and the effects of channel confinement on a current, results in a complex feedback system.

Key insights have come from both laboratory studies [e.g. Ellison and Turner, 1959; Middleton, 1966; Parker et al., 1986; Buckee et al., 2001; Keevil et al., 2006; Straub et al., 2008; Sequeiros et al., 2010; De Leeuw et al., 2016; Dorrell et al., 2018a] and numerical models [e.g. Eidsvik and Brørs, 1989; Kassem and Imran, 2004; Huang et al., 2005; Giorgio Serchi et al., 2011; Dorrell et al., 2013, 2014, 2015; Luchi et al., 2018]. More recently, direct observations, once considered unfeasible due to the location and discrete nature of these flows, have started to become more common. Datasets of turbidity current events now exist from both the Congo Canyon [Khripounoff et al., 2003; Azpiroz-

Zabala et al.,2017] and Monterey Canyon [Xu et al., 2004; Xu, 2010]. Additionally, a more comprehensive dataset exists of a saline exchange current flowing through a single channel bend into the Black Sea [Sumner et al., 2013, 2014; Dorrell et al., 2014, 2016].

The often sinuous nature of submarine channels has led to suggestions that the changes in flow dynamics induced by channel bends can enhance sediment transport capacity and flow runout distances [Pirmez and Imran, 2003; Straub et al., 2008]. A primary focus of previous work has therefore been on flow structure in channel bends, with helical flow patterns observed in the laboratory [Keevil et al., 2006; Islam and Imran, 2008; Islam et al., 2008; Abad et al., 2011; Dorrell et al., 2018a], numerical simulations [Kassem and Imran, 2004; Imran et al., 2007; Giorgio Serchi et al., 2011; Ezz and Imran, 2014] and the field [Sumner et al., 2014; Azpiroz-Zabala et al., 2017]. Helical flow is a well understood phenomenon in fluvial and open channel flows, with the cross-stream components of the upper flow directed towards the outer bank and lower flow directed towards the inner bank. It is caused by the competing forces of centrifugal acceleration and the resulting lateral pressure gradient due to super-elevation at the outer bank [Rosovskii, 1957].

However, the nature of this helical structure in gravity and turbidity currents is more complex. Rotational secondary flow cells been observed rotating in both a river-reversed [e.g. Keevil et al., 2006] and river-like [e.g. Abad et al., 2011] direction. Two field datasets have captured secondary flow dynamics, both displaying complex behaviour. Sumner et al. [2014] observe large fluctuations in the secondary flow of a partially-confined saline gravity current as it traversed a channel bend. However, at the bend apex, a clear river-reversed cell was recorded. Azpiroz-Zabala et al. [2017] observe two vertically stacked cells with opposing rotational directions, interpreted from a thalweg velocity profile, in a fully-confined turbidity current close to the inflection point between two bends in the Congo Canyon. Vertically and horizontally stacked cells have also been observed in laboratory and numerical studies but only for fully-confined flow [Imran et al., 2007; Islam and Imran, 2008; Islam et al., 2008; Dorrell et al., 2018a].

Several theoretical models exist which attempt to provide an explanation for a cell's rotational direction. Abad et al. [2011] characterise secondary flow orientation by the height of the velocity maximum (an assumed function of Froude number) and bed roughness. Dorrell et al. [2013] theorise that non-zero radial fluxes, which arise from super-elevation, stratification and overspill, control flow orientation. Sumner et al. [2014] use field observations to highlight the importance of varying down- and cross-stream advection terms. Bolla Pittaluga et al. [2014a, b] and Peakall et al. [2014] discuss the importance of stratification in secondary flow. Azpiroz-Zabala et al. [2017] present a field-based model of secondary flow considering the balance of super-elevation and radial stratification. Dorrell et al. [2018a] emphasised the role of temporal flow variations, showing how, in the laboratory, the orientation of a rotational cell fluctuates over bend vortex-shedding time-scales, which are much larger than those of characteristic turbulent mixing.

The importance of channel morphology in determining secondary flow dynamics has been highlighted previously [Islam et al., 2008; Ezz and Imran, 2014]. Despite this, there is a lack of studies that utilise realistic cross-sectional channel profiles, both in terms of aspect ratio and curvature, and resolve secondary flow dynamics. Islam et al. [2008] and Ezz and Imran [2014] both employ the same trapezoidal profile with an aspect ratio of 5 and conclude that the bank slope has a large effect on the flow dynamics.

Here, both laboratory experiments and numerical simulations of partially-confined gravity currents in a shallow channel with a realistic aspect ratio and levee profile are presented. Three channel sinuosities are studied and these are shown to have a first order effect on lateral flow structure and thus meander bend development. It is shown how the level of overbank loss is a key control on rotational cell development, with large levels capable of supressing the mechanism completely. Furthermore, a distinctive radial pressure gradient field, characterised by a localised reversal, is associated with all rotational cells observed in the numerical simulations. Finally, an examination is made of

the switching in direction of a cell between bends and how this can result in the development of complex secondary flow fields.

6.2 Methodology

6.2.1 Laboratory experiments

A set of continuous-release saline gravity current experiments were conducted in the Sorby Environmental Fluid Dynamics Laboratory. The currents, with a fixed input flow rate of 1 l/s, traversed a fibreglass channel model of sinuous planform. Three different sinuosities were investigated via the use of tessellating curved channel sections (Figure 6.1). The cross-sectional channel and levee profile were kept constant (Figure 6.2). The channel was 0.0275 m deep and 0.22 m wide giving an aspect ratio of 8, with the profile taking the form of a cosine curve, $z = 0.01375(\cos(\pi x/0.11) + 1)$. The outer two thirds of the levee profile were determined by the relationship $z = H(L/Y)^{-B}$, where z is the levee height, H is the channel depth, L is the distance from the channel thalweg, Y is half the channel width, and $B = 0.5535S^{0.662}$, where S is the slope. This was found to be give the best fit to channel levees on slopes > 0.6° by Nakajima and Kneller [2013]. Although this relationship works well for the far field levee architecture it fails to capture the morphology near the crest. Therefore, the inner third of the levee profile was determined using data from previous gravity current experiments conducted over an erodible bed by Straub et al. [2008] [Straub, personal communication].

The main area of the flume used was 1.7 m wide and 1.7 m long, with a water depth of 1.5 m. The channel models were fixed to a false floor suspended 0.4 m above the flume base; the area beneath the model acted as a sump to collect excess dense fluid. Additionally, a 1 m long and 0.34 m wide straight inlet centred on the upstream side of this area allowed the currents to develop before entering the main flume area. The channel model extended along this inlet. Saline solution with a 2.5% excess density was prepared in a large mixing tank such that $\rho_s = 1.025\rho_a$, where ρ_a and ρ_s are the densities of the

ambient and saline fluid respectively. The saline was pumped into start of the inlet channel; this process was controlled by an electromagnetic flow meter to ensure minimal variation in the input flow rate. Before entering the inlet channel, the saline passed through a momentum diffuser to ensure a gravity driven flow. The whole flume setup could be tilted and was set at an angle of either 2º or 0.5º sloping downstream. A diagram of this setup can be seen in Figure 6.3.

Both velocity and density data were recorded. Three-component velocities were measured at a sampling rate of 100 Hz by a profiling Nortek Vectrino II acoustic Doppler velocimeter (ADV). Each measured profile had a vertical range of 35 mm with a spatial resolution of 1 mm. Profiles were measured at 0, 20, 55 (mid-channel) and 110 mm (crest) laterally from the thalweg. At the mid-channel location, the slope of the channel floor induced a region of low signal to noise ratio; affected data were excluded from the results. Throughout this study, velocity components are defined relative to the channel; downstream (u) and cross-stream velocities (v) are respectively parallel and perpendicular to the local thalweg.

A 12-channel peristaltic pump was used to siphon samples out of the current at vertical heights above the channel base of 3, 8, 13, 18, 23, 28, 38, 48, 58, 78, 98 and 118 mm. Profiles were measured at 0 (thalweg), 55 (mid-channel) and 110 mm (crest) laterally from the thalweg. Samples were siphoned out using narrow steel tubing (protruding 15 cm upstream from a holding rack) with an outer diameter of 1.6 mm in order to minimise flow disturbance. The densities (ρ) of the samples were then measured with an Anton Paar DMA 35 Ex density meter to an accuracy of 0.1 kg/m^3.

From both the experimental and numerical models, at-a-point and net radial fluid and material fluxes were computed,

$$q_f = \int_0^\infty v\, dz, \qquad Q_f = \int_L^R \int_0^\infty v\, dz dr\,, \tag{6.1}$$

$$q_c = \int_0^\infty vc\, dz, \qquad Q_c = \int_L^R \int_0^\infty vc\, dz dr\,, \tag{6.2}$$

where v is the cross-stream velocity, $c = (\rho - \rho_a)/\rho_a$ is the effective concentration, r is the radial direction and L and R are the levee crests. The non-zero radial fluxes correlate to three-dimensional flow where mass and material constantly move from the inner bank to outer bank, or vice versa [Dorrell et al., 2013]. Non-zero net radial fluxes correlate to non-zero mass and momentum transport through increasing and decreasing super-elevation around a meander-bend [Sumner et al., 2014].

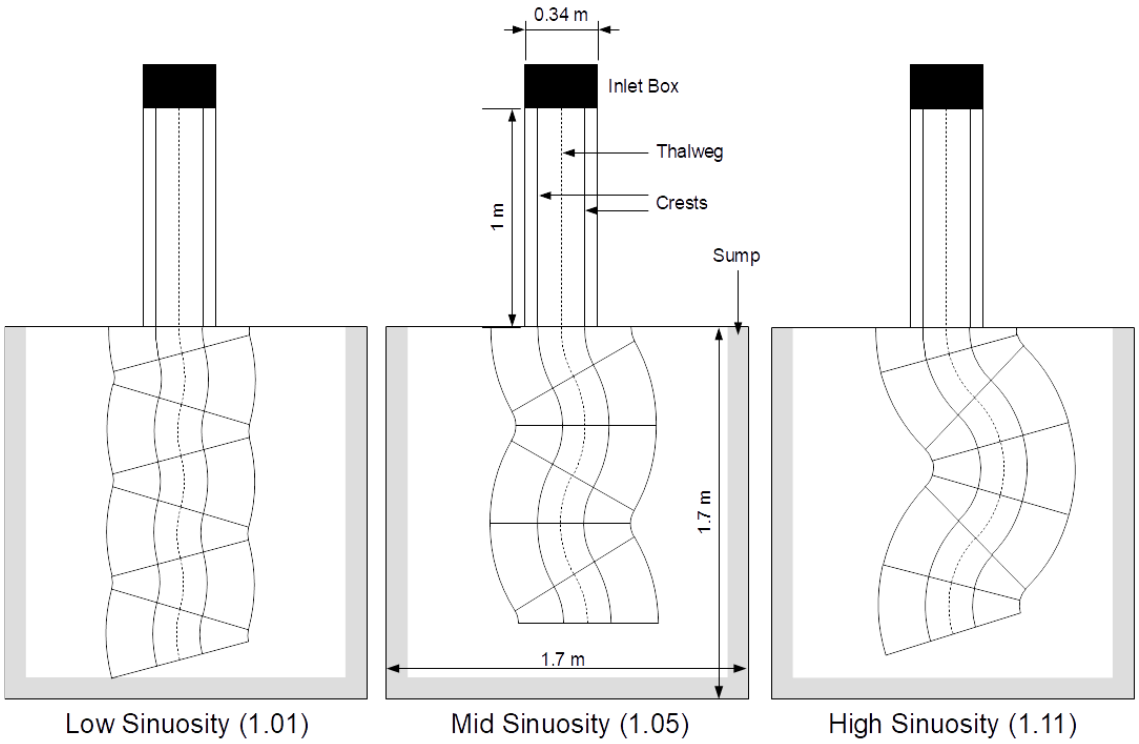

Figure 6.1 Planform schematics of the three channel layouts employed in the laboratory. Tessellating pieces were used to create three different sinuosities.

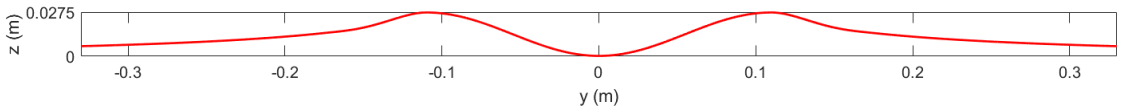

Figure 6.2 Cross-sectional profile of the channel model. The channel measures 0.22 m wide and 0.0275 m deep with an aspect ratio of 8. The profile is that of a cosine curve which results in a maximum steepness of 22°. The levee profile was determined using a combination of laboratory data [Straub et al., 2008] and field data [Nakajima and Kneller, 2013].

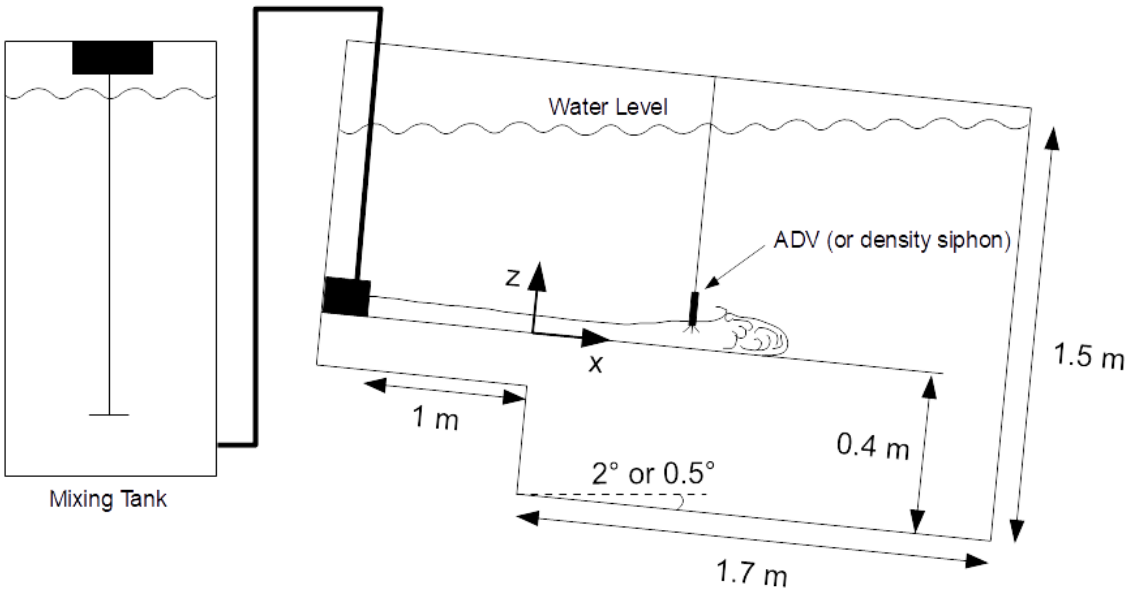

Figure 6.3 A cross-sectional schematic of the experimental setup employed in the Sorby Fluid Dynamics Laboratory.

6.2.2 Numerical simulations

Alongside the laboratory experiments, numerical simulations of saline gravity currents were conducted. A Reynolds-averaged Navier-Stokes (RANS) model was used, solved with ANSYS CFX 18.2. The Reynolds-averaged mass and momentum conservation equations are,

$$\frac{\partial \overline{\rho}}{\partial t} + \frac{\partial \overline{\rho}\tilde{u}_i}{\partial x_i} = 0, \tag{6.3}$$

$$\frac{\partial \overline{\rho}\tilde{u}_i}{\partial t} + \frac{\partial \overline{\rho}\tilde{u}_j\tilde{u}_i}{\partial x_j} = -\frac{\partial P}{\partial x_i} + \frac{\partial}{\partial x_j}\left(\mu\left(\frac{\partial \tilde{u}_i}{\partial x_j} + \frac{\partial \tilde{u}_j}{\partial x_i} - \frac{2}{3}\delta_{ij}\frac{\partial \tilde{u}_k}{\partial x_k}\right) - \overline{\rho u_i' u_j'}\right) + \overline{\rho} f_i, \tag{6.4}$$

where the velocity terms have been separated into Favre-averaged components, $\tilde{u}_i$, and fluctuating components, u_i'. Reynolds-averaged density and pressure are denoted by $\overline{\rho}$ and P respectively.

A shear stress transport (SST) turbulence closure has been used to model the Reynolds stresses, $-\overline{\rho u_i' u_j'}$. This combines the free-stream capability of the popular k-ϵ model with the explicit wall resolution of the k-ω model. It is a two-equation eddy viscosity (μ_t) model, with transport equations for k, the turbulent kinetic energy and ω, the turbulence frequency; blending functions exploit the near-wall treatment of the k-ω model and the free-stream capability of the k-ϵ model [Menter, 1994].

To model variations in flow density, a mixture model was employed. In this case, the mixture comprises water and saline with densities $\rho_a = 1000$ kg/m^3 and $\rho_s = 1025$ kg/m^3, respectively. The density of the mixture is defined by $\frac{1}{\bar{\rho}} = \frac{1-\alpha}{\rho_a} + \frac{\alpha}{\rho_s}$, where α is the saline mass fraction. This variable density is used in all terms of the model, including that of gravity. Additionally, a transport equation is solved for the saline mass fraction,

$$\frac{\partial \alpha \rho}{\partial t} + \frac{\partial \alpha \bar{\rho} \tilde{u}_i}{\partial x_i} = -\frac{\partial \overline{\alpha' \rho u_j'}}{\partial x_j}, \tag{6.5}$$

where the Reynolds flux term is modelled using the eddy diffusion hypothesis as,

$$-\overline{\alpha' \rho u_j'} = \frac{\mu_t}{\sigma_t} \frac{\partial \alpha}{\partial x_j}, \tag{6.6}$$

and $\sigma_t = 1$ is the turbulent Schmidt number. Use and validation of this modelling approach is extensive both in this field [e.g. Imran et al., 2004, 2007; Giorgio Serchi et al., 2011] and related fields [e.g. Gauer at al., 2005; Doronzo, 2013]. Additionally, the numerical model has been compared to the experimental data in this study (Section 6.3.1).

Input flow rate (1 l/s) and channel geometry were kept identical to the laboratory, although the study domain was extended to allow analysis of a greater number of bends downstream. To investigate the effect of channel morphology, additional simulations were conducted using a channel with a flatter cross-sectional profile, $z = 0.01375(\cos(\pi x/0.11) + 1)^{11}$, (Figure 6.4). Aspect ratio and input flow rate remained unchanged. The profile was kept smooth so as to have no adverse flow effects from sharp corners.

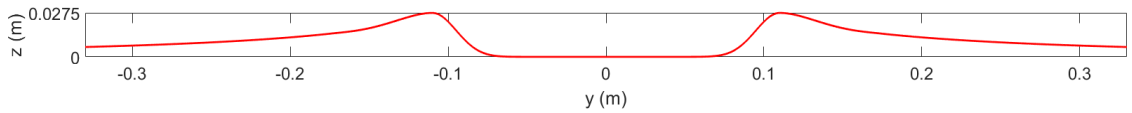

Figure 6.4 Cross-sectional profile of the additional channel used in the numerical simulations. The aspect ratio and levee shape remain unchanged.

6.3 Results

6.3.1 Laboratory data and comparison to numerical simulations

The laboratory velocity and density data were used to create the cross-sectional contour plots shown in Figures 6.5, 6.7, 6.9 and 6.10. Figures 6.6 and 6.8 show complimentary numerical simulation data. Figure 6.5 shows the low sinuosity channel at a 2º slope with contours at bend 2, the following inflection and at bend 4. The flow is super-elevated towards the inner bank, with the high-velocity core also hugging the inner bank. A bifurcation in the secondary flow field is also present at the inner bank with the flow overspilling at both crests.

Figures 6.7 and 6.9 show the mid sinuosity channel at a 2º and 0.5º slope respectively with contours at bend 1, bend 2 and the inflection between. For both cases at both bends, the flow interface is super-elevated towards the outer bank. The 0.5º slope also exhibits evidence of elevation of the densest, inner region of the flow, i.e. radial cross-stream density gradients [Dorrell et al., 2013; Ezz and Imran, 2014]. The high-velocity core remains near the inner bank for both cases. There is also a clear ‘lag’ between the current and the channel, with the flow experiencing significant super-elevation up to the inflection point between the bends and significant net radial fluxes. The secondary flow fields are parallel with the channel profile and exhibit a singular cross-stream direction. No helical structure is observed due to the significant overspill at the outer bank. The maximum cross-stream velocity magnitudes coincide spatially with the streamwise

velocity maximum. Figure 6.10 shows contours at the first bend apex of the high sinuosity channel at a 2º slope. Here the super-elevation at the outer bend is the most pronounced of any case, with both the flow interface and inner stratified region shifted outwards. Additionally, in contrast with the lower sinuosity channels, the high-velocity core is also shifted to the outer bank. The secondary flow field exhibits similar characteristics to the mid-sinuosity cases, parallel to the channel profile and with large overspill levels at the outer bank.

Direct comparisons can be made between the numerical and laboratory data. Results from the numerical model for the low and mid sinuosity channel are shown in Figures 6.6 and 6.8 respectively and can be compared with the laboratory data in Figures 6.5 and 6.7. Qualitatively, both channel setups compare well. The levels of super-elevation and position of the velocity maximum agree well, with the cross-stream flow field pattern also captured well in a variety of locations.

Quantitively, the model has areas of strength and weakness. It accurately predicts both maximum streamwise velocity magnitudes and flow depths. However, while it predicts the correct cross-stream flow patterns, it fails to simulate the correct magnitudes for the mid sinuosity channel. This may be due to the lower magnitudes of cross-stream velocities in comparison to the streamwise component which makes them harder to model; cross-stream comparisons to laboratory results are often neglected [e.g. Imran et al., 2007; Giorgio Serchi et al., 2011]. For the low sinuosity channel, both cross-stream velocity and radial flux values remain closely matched.

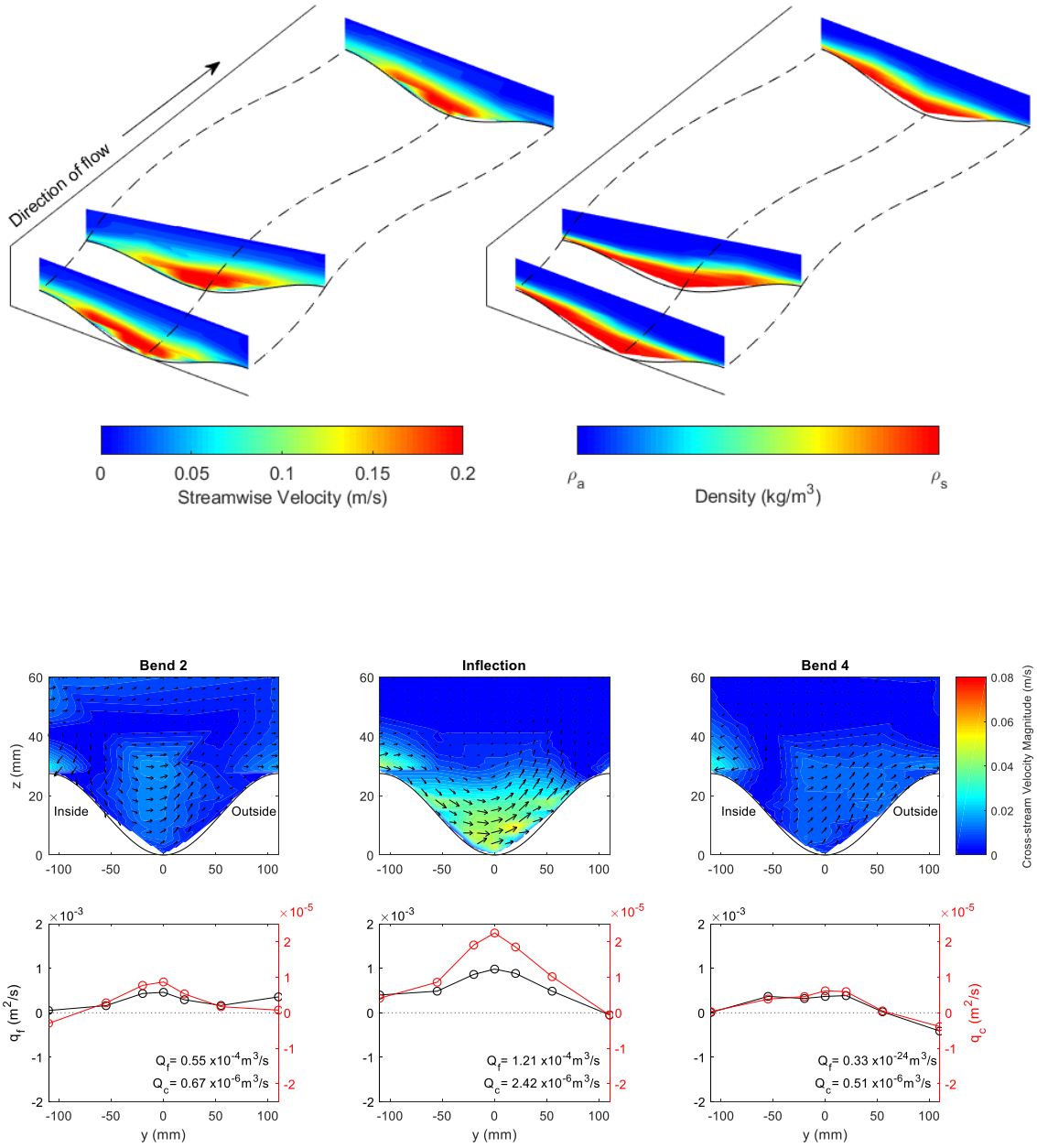

Figure 6.5 Streamwise velocity, density and cross-stream velocity cross-sectional contours alongside radial fluxes for the low-sinuosity channel at a 2º slope. Data are shown at the apex of bend 2, the following inflection point and the apex of bend 4. Views are taken looking downstream.

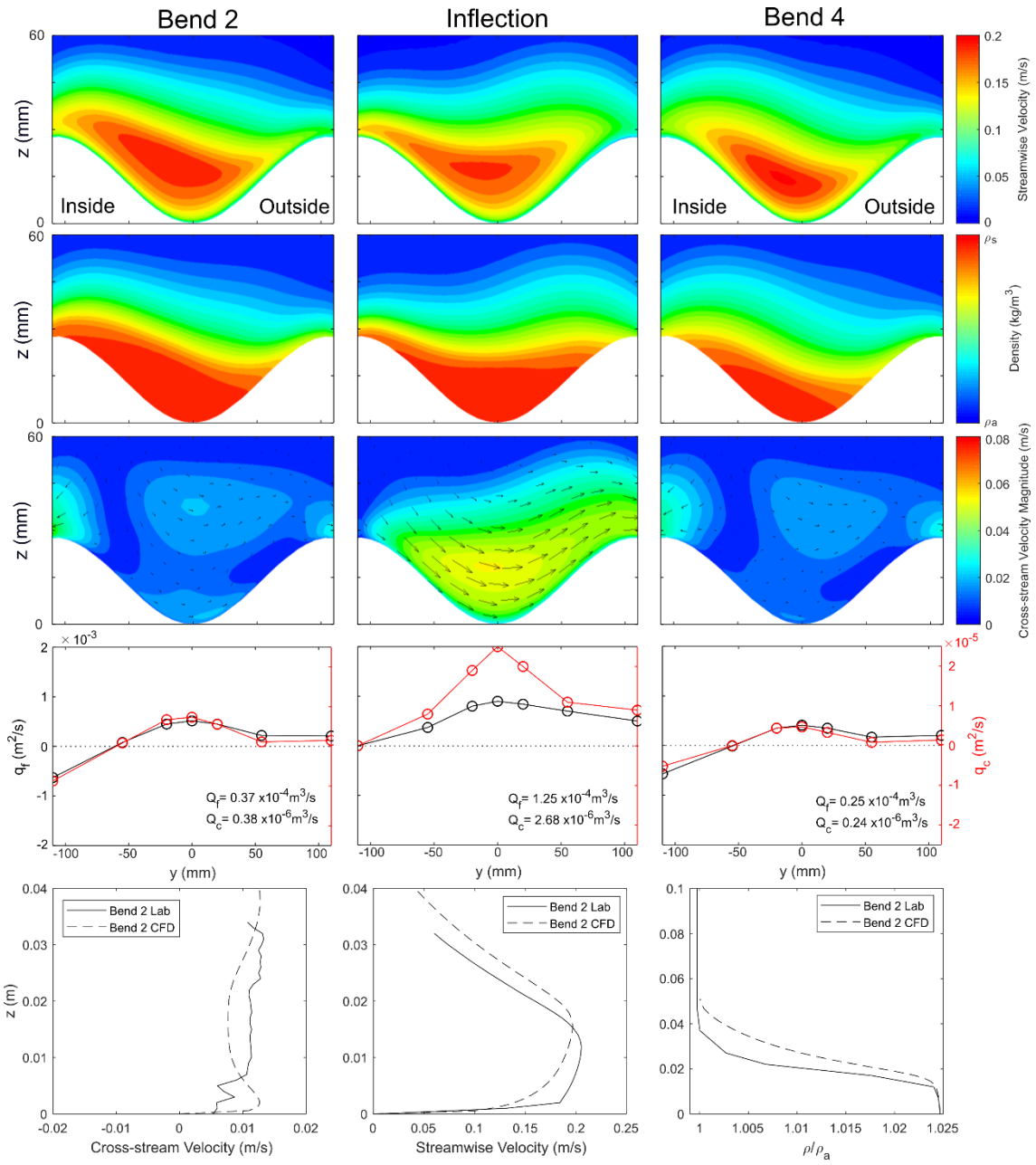

Figure 6.6 Numerical simulation data for the low-sinuosity channel at a 2º slope; (top) streamwise velocity, density and cross-stream velocity cross-sectional contours; (middle) radial fluxes; (bottom) thalweg profiles of cross-stream velocity, streamwise velocity and density compare well qualitatively to the laboratory data. Data is at the apex of bend 2, the following inflection and at the apex of bend 4. Views are taken looking downstream.

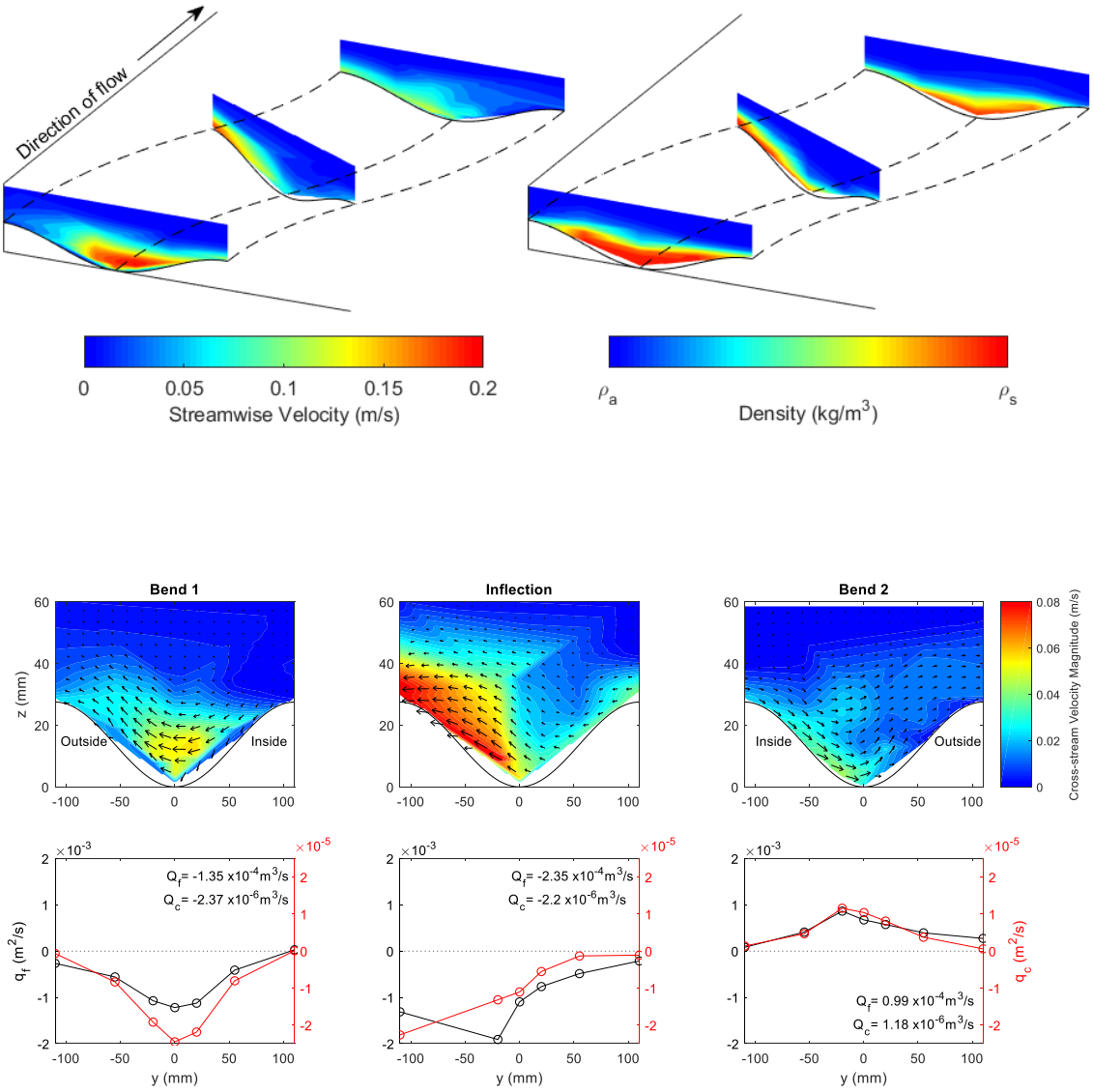

Figure 6.7 Streamwise velocity, density and cross-stream velocity cross-sectional contours alongside radial fluxes for the mid-sinuosity channel at a 2º slope. Data are shown at the apexes of bend 1, bend 2 and their inflection. Views are taken looking downstream.

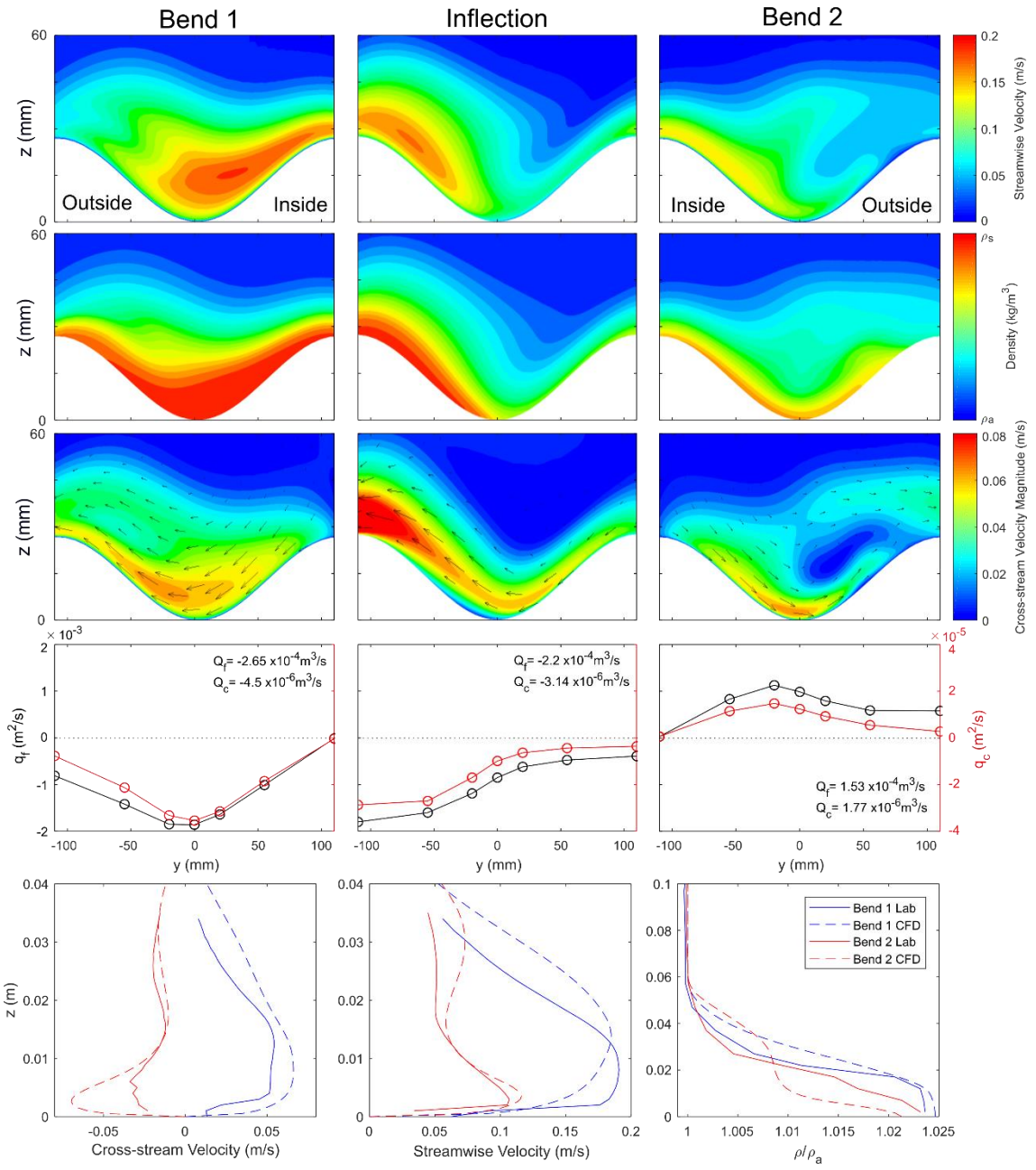

Figure 6.8 Numerical simulation data for the mid-sinuosity channel at a 2º slope; (top) streamwise velocity, density and cross-stream velocity cross-sectional contours; (middle) radial fluxes; (bottom) thalweg profiles of cross-stream velocity, streamwise velocity and density compare well qualitatively to the laboratory data. Data is shown at the apexes of bend 1, bend 2 and the inflection point between. Views are taken looking downstream.

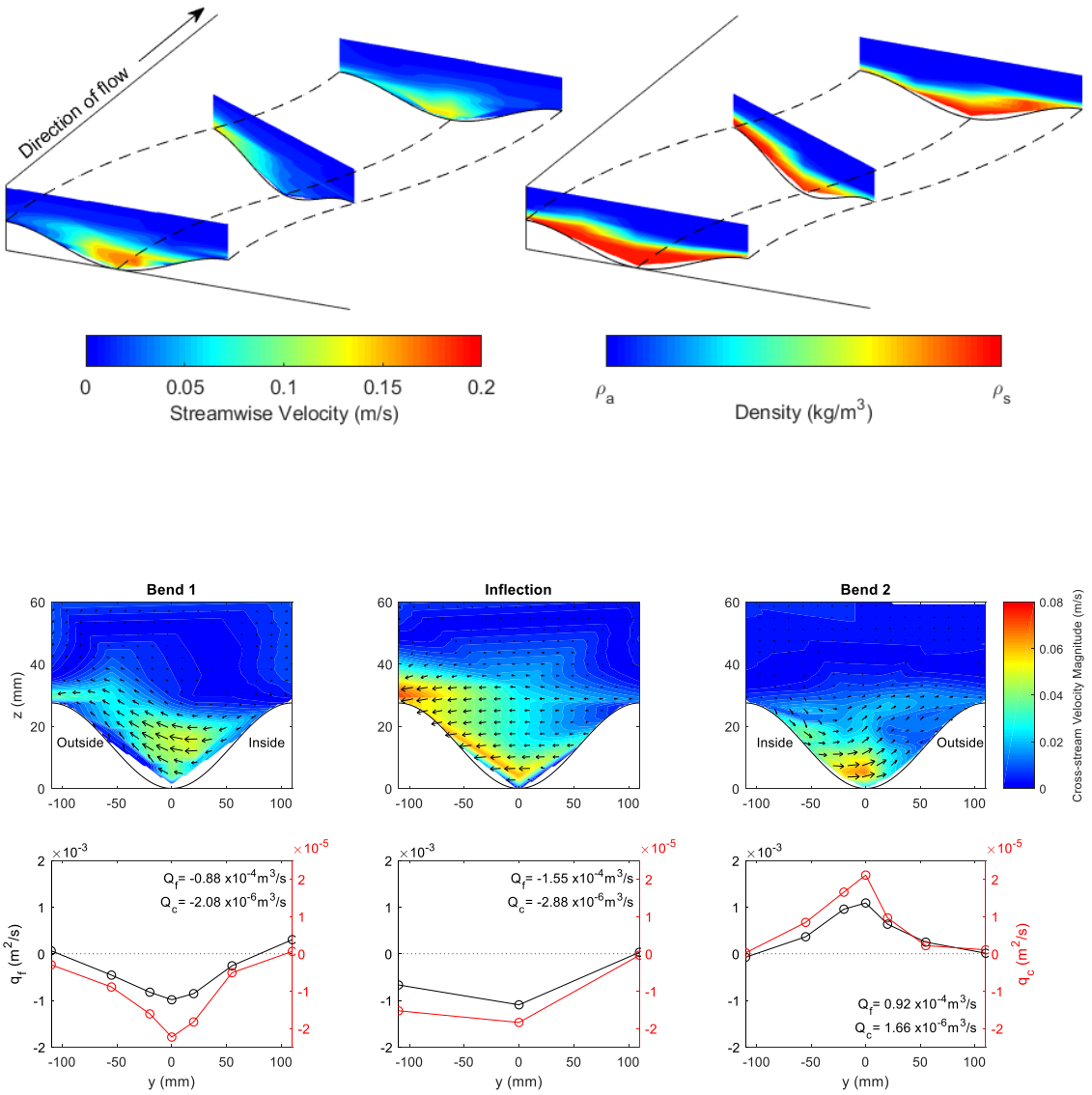

Figure 6.9 Streamwise velocity, density and cross-stream velocity cross-sectional contours alongside radial fluxes for the mid-sinuosity channel at a 0.5º slope. Data are shown at the apexes of bend 1, bend 2 and their inflection. Views are taken looking downstream.

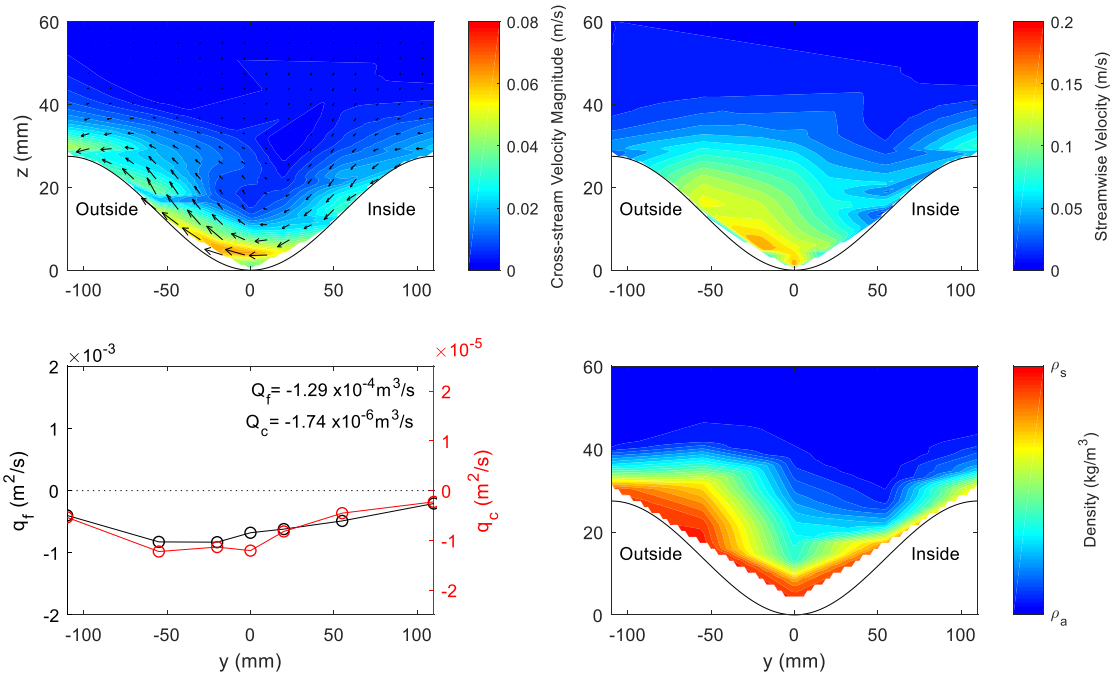

Figure 6.10 Cross-stream velocity, streamwise velocity and density cross-sectional contours with radial fluxes for the high-sinuosity channel at a 2º slope. Data are shown at the apex of bend 1. Views are taken looking downstream.

6.3.2 Development of a secondary flow rotational cell

In this work, no rotational cells were observed in the laboratory nor in the numerical simulations covering the same domain. However, the simulations enabled the study of downstream bends not modelled in the laboratory setting. Figure 6.11 shows cross-sectional contours of cross-stream velocity, streamwise velocity, density and radial pressure gradient at bend 2, 3 and 4 of the mid sinuosity channel at a slope of 0.5º. The development of a rotational cell can be observed. At bend 2 there is a weak river-reversed cell in the upper part of the flow; at bend 3 a small river-like cell has formed at the base of the outside bank; at bend 4 a larger river-like cell is present at the thalweg. This is a similar secondary flow field to the one observed by Islam et al. [2008] in a laboratory setting.

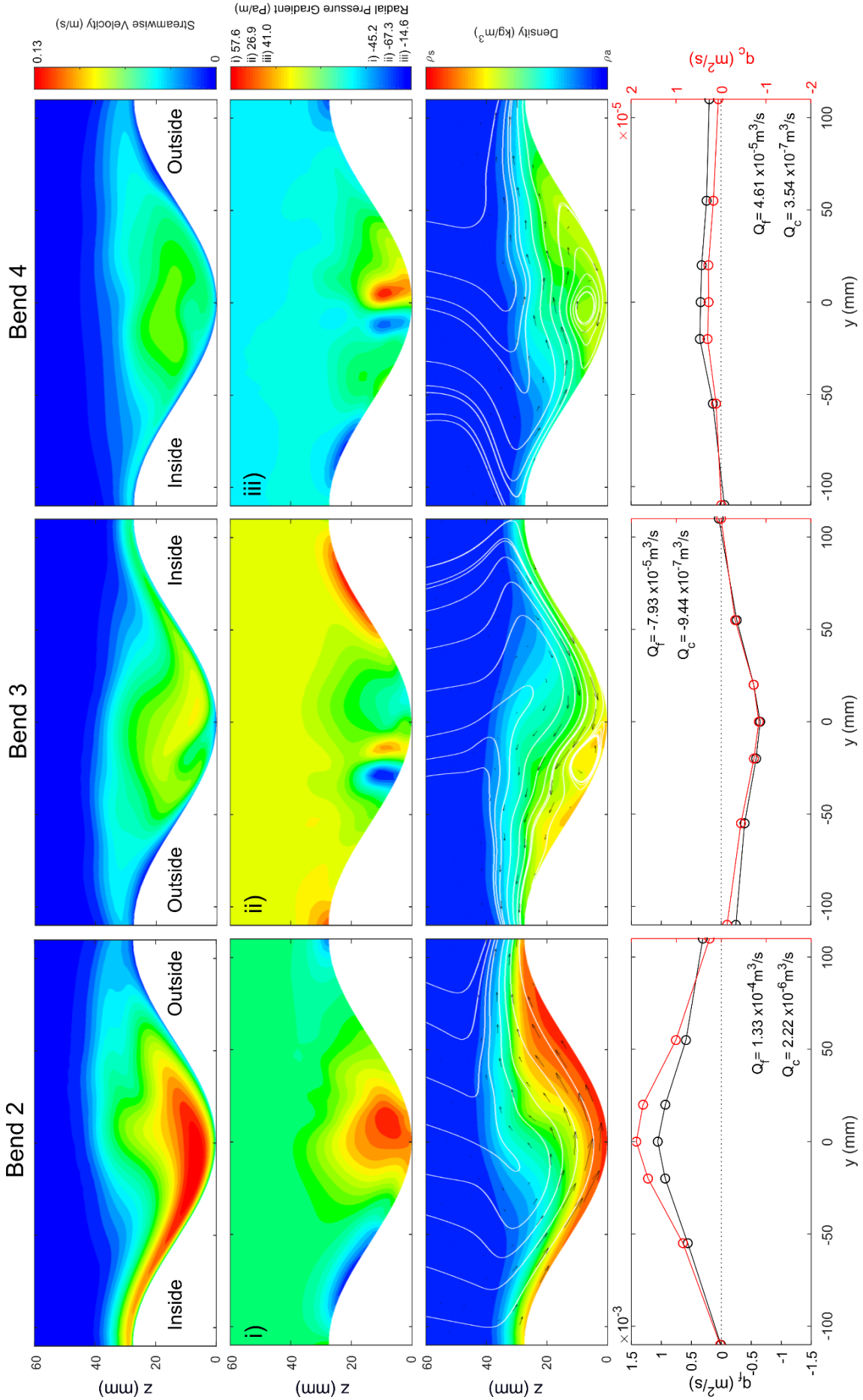
Bend 2
Bend 3
Bend 4
Inside
Outside
i)
ii)
iii)
z (mm)
y (mm)
Streamwise Velocity (m/s)
Radial Pressure Gradient (Pa/m)
Density (kg/m³)
i) 57.6
ii) 26.9
iii) 41.0
i) -45.2
ii) -67.3
iii) -14.6
q_f (m²/s)
q_c (m²/s)
Q_f= 1.33 x10⁻⁴m³/s
Q_c= 2.22 x10⁻⁶m³/s
Q_f= -7.93 x10⁻⁵m³/s
Q_c= -9.44 x10⁻⁷m³/s
Q_f= 4.61 x10⁻⁵m³/s
Q_c= 3.54 x10⁻⁷m³/s

Figure 6.11 (previous page) Numerical data for the mid-sinuosity channel at a 0.5º slope shows how a rotational cell develops over a series of three consecutive bends. Whilst the high-density region of the flow remains elevated on the outer bank, the high-velocity core shifts to the thalweg from the inner bank. The pattern of the radial pressure gradient field also changes significantly. The rotational cell is characterised by two regions of opposing gradient. This is the same for all rotational cells observed in this study.

The development of this cell coincides with a shift in the lateral position of the streamwise velocity maximum from the inner bank towards the thalweg. Moreover, there is a significant change in the radial pressure gradient field. The presence of a rotational cell is characterised by two adjacent regions of opposing radial pressure gradient. The same characteristic radial pressure gradient field is observed for every rotational cell observed in this set of simulations. For all the bends, the centrifugal forces cause the radial fluxes to remain towards the outer bank over the entire channel width.

Levels of overspill appear to be a key control on cell development. Figure 6.12 shows the downstream evolution of the ratio of overbank material flux at the outer bank to downstream material flux at the channel thalweg for several of the numerical simulations. The first bend for each case at which a rotational cell has formed at the channel base is circled. For some of the cases a small cell formed on the outer bank at the previous bend as in the example shown in Figure 6.11. For these simulations there is an apparent threshold ratio below which a rotational cell can form. It should be noted that, despite the significant reduction in overspill in the high sinuosity cases, no vertically stacked cells were observed.

The faster reduction in overbank to downstream material flux ratio for higher sinuosity channels shows their increased efficiency at flow stripping via overbank losses. In the low sinuosity case, even though the ratio of overbank to downstream material flux drops below this threshold, no rotational cells were observed. This indicates that in low sinuosity channels there may be insufficient centrifugal force to generate rotational cells,

indicated by the flows remaining super-elevated towards the inner bank, even after a series of many bends (Figure 6.13).

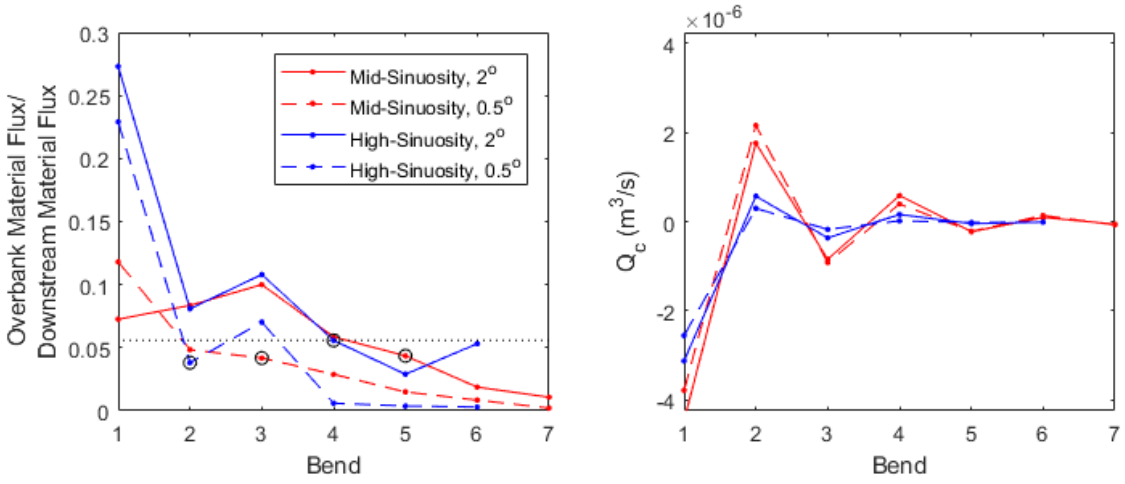

Figure 6.12 High levels of overspill at proximal bends dominate the flow field and prevent any helical structure. Reductions in overspill downstream lead to a reduction in the ratio of overbank material flux to downstream material flux (left). The first bend for each case at which a rotational cell develops is circled. This appears to show a threshold ratio value, below which a helical structure is triggered. Low sinuosity cases are omitted due to no curvature induced rotation. As the helical structure develops downstream, and overspill levels drop, net radial material flux tends to zero (right).

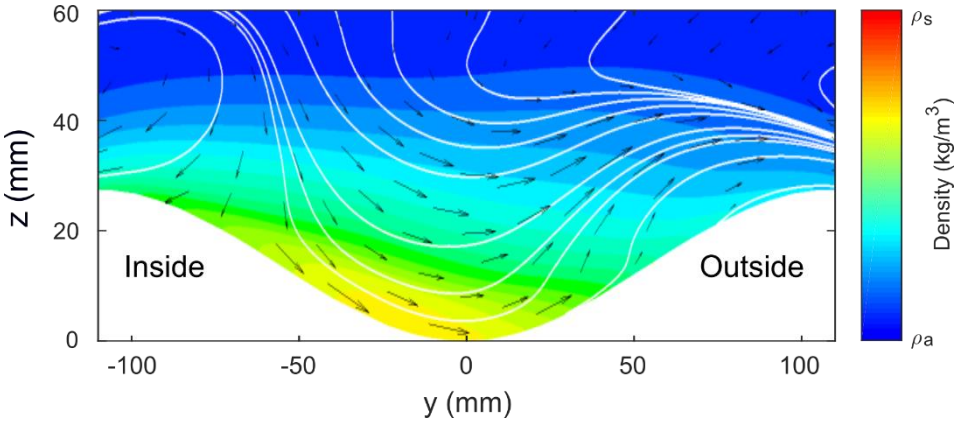

Figure 6.13 Cross-sectional density contour and secondary flow vectors/streamlines at bend 12 of the low sinuosity channel at a slope of 2º. Even after a succession of bends, the lack of curvature means the flow remains super-elevated on the inner bank with no complete rotational cells forming.

6.3.3 Effect of channel profile

Changing the cross-sectional profile of the channel, while keeping aspect ratio and input flow rate fixed generates significant differences in the lateral flow structure. Flows with identical input conditions (1 l/s flow rate and a 2° slope) were simulated in channels with the original, sine-curve profile and the flatter profile (Figure 6.4). Figure 6.14 shows cross-sectional density contours and secondary flow vectors and streamlines at the 6th bend of each channel. A river-like cell has developed in the original, cosine-curve channel. For the flatter profile, the dominant basal flow direction has switched, with the small river-like cell being pushed towards the outer bank. Both channels are river-reversed in that flow transports material from the inner to the outer bank, with a switching of flow direction around the ambient interface. The shape of the flatter profile results in a greater degree of confinement and, subsequently, a denser flow.

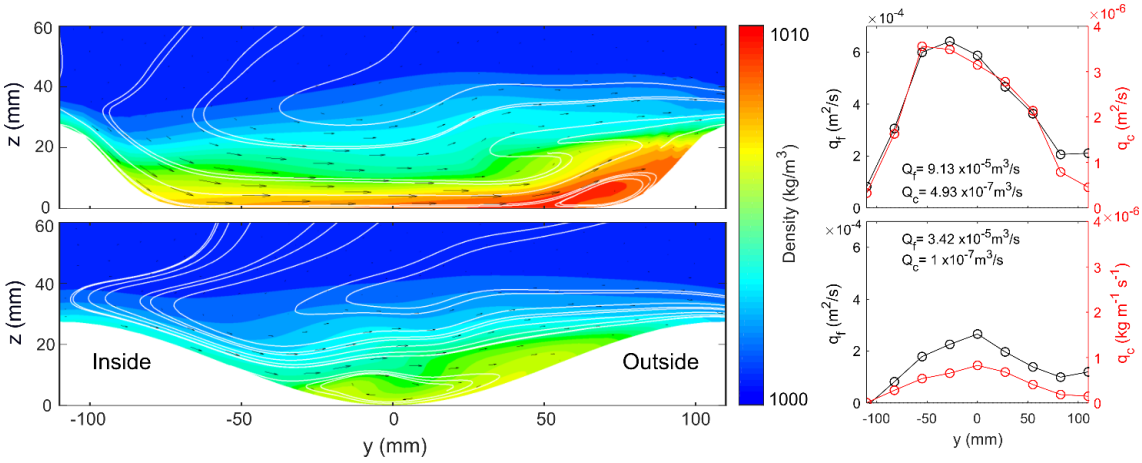

Figure 6.14 Cross-sectional density contours at bend 6 for both channel profiles, at mid-sinuosity and a slope of 2º. The vectors and streamlines overlaying the density contours show the secondary flow structure. Axes have not been stretched to show the true channel profiles. Radial fluxes show that material is transported to the outer bank for both channels.

6.3.4 Evolution of secondary flow between bends

Figure 6.15 shows how both the density and secondary flow fields progressively change between two successive bend apexes. The rotational cell appears to shift laterally towards the outer bank until a transition can be observed occurring at the inflection. Here, a new rotational cell of opposing direction has been created, with the two rotational cells of opposing rotation horizontally adjacent to each other. This transition is simultaneous to the dense core of the flow switching channel sides. The downstream change in net radial flux around the bend is also shown in Figure 6.15, with the cross-stream variations shown in Figure 6.16. The transition of the net fluxes is relatively uniform, albeit with a small lag evidenced by a slightly more rapid change after the inflection, where the majority of the flow switches direction.

The lag is more apparent in the material flux. At the inflection, there is a bifurcation in the radial fluid flux at the thalweg whereby fluid is directed away from the thalweg and overbank in both halves of the flow. In comparison, the radial material flux shows a greater degree of bias towards the direction of the previous bend's outer bank. While still present, this level of lag is far less significant than in more proximal bends. The inflection between bends 1 and 2 shows radial fluxes directed towards bend 1's outer bank across the entire channel width and of similar magnitudes to that at bend 1's apex (Figures 6.7 and 6.9). This suggests the development of a greater degree of equilibrium between current and channel in the downstream direction. As a result of the partially-confined, overspilling nature of the flow, there is still net flow towards the outer bank across nearly the whole channel at the bend apexes.

The thalweg cross-stream velocity profile at the inflection is shown in Figure 16. It shares similarities to the thalweg-inflection profile observed by Azpiroz-Zabala et al. [2017] in the Congo Canyon, attributed to the presence of vertically stacked cells. However, the analysis herein shows the same structure may also be generated by two horizontally stacked cells interacting near the thalweg.

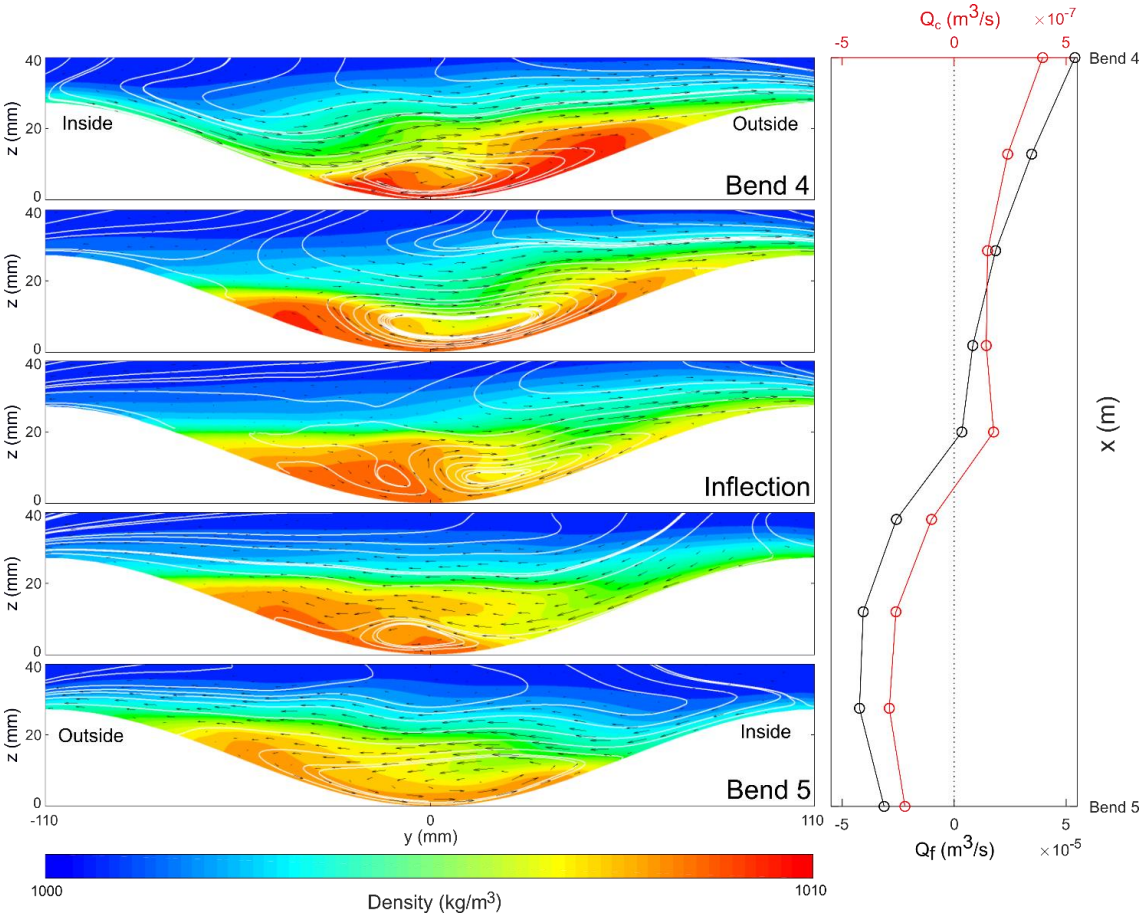

Figure 6.15 Numerical data of the mid-sinuosity channel at a 0.5º slope depict how a rotation cell switches direction between two bends. Cross-sectional planes (left) are taken at equal distances around the bend. Flow vectors and streamlines show secondary velocity on a cross-sectional density contour. The downstream evolution of the net radial fluid and material fluxes over the same bend is also shown (right).

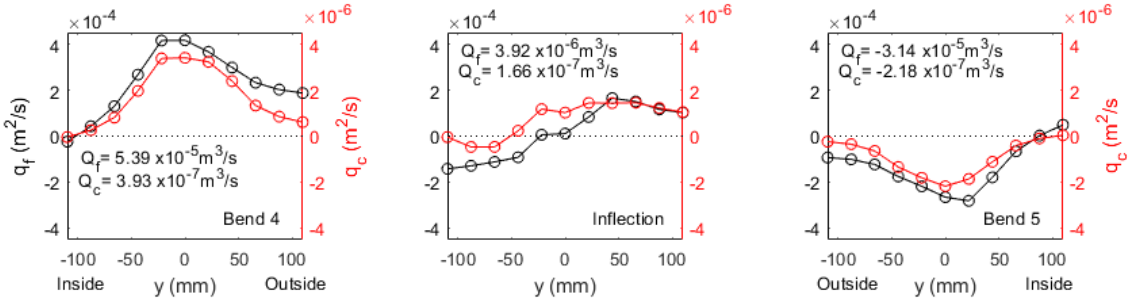

Figure 6.16 Lateral variation in radial flux for the numerical case shown in Figure 6.15. At both bend apexes there is net movement of fluid towards the outer bank across almost the whole channel, while at the inflection there is a bifurcation at the thalweg.

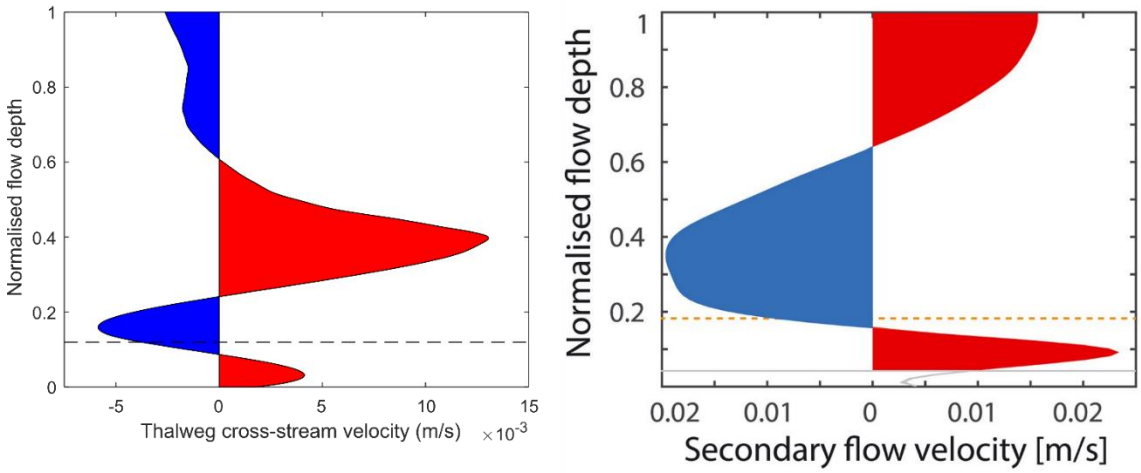

Figure 6.17 Cross-stream thalweg velocity profiles, normalised by flow depth, for the inflection shown in Figure 6.15 (left) and the Azpiroz-Zabala et al. [2017] study of the Congo Canyon (right). The horizontal dashed lines indicate the height of the streamwise velocity maximum.

6.4 Discussion

6.4.1 Numerical model performance and capability

Despite the ever-increasing viability of real-world data from field studies providing real-world data, at present only laboratory experiments and numerical simulations can provide data with high spatial and temporal resolution. Comparisons between the model output and laboratory data can be seen in Section 6.3.1; the qualitative prediction of the flow field patterns is good. As a result, this modelling approach has been widely used in previous studies [e.g. Imran et al., 2007; Giorgio Serchi et al., 2011; Ezz and Imran, 2014] and is a valuable tool in increasing our understanding of these complex flows.

In this study, the use of a numerical model alongside the laboratory enables a significant increase in both the spatial scope of possible analysis and in the spatial density of the data. Thus, study domains were extended beyond what was possible in the laboratory, allowing the examination of successions of bends further downstream, where the flow had a longer developmental distance to adapt to the channel geometry; only in these more distal areas

were rotational cells observed (see Section 6.4.2). The numerical simulations also enable direct analysis of the whole 3D flow-field view, rather than relying on interpolations between discrete data points. The examination of the switching in direction of a rotational cell between bends (Figure 6.15) is one example; to gather the equivalent laboratory data at this spatial density would not have been feasible within the scope of this study. Additionally, the numerical model can provide data that cannot be readily recorded in either the laboratory or the field, such as the pressure-gradient fields shown in Figure 6.11.

6.4.2 The onset and formation of a helical structure

Rotation is understood to be driven by the vertical imbalance between centrifugal forces and pressure gradients due to super-elevation [Rosovskii, 1957] and stratification [Dorrell et al., 2013]. As stated above, no rotational cells were observed in the laboratory experiments described. For the low sinuosity channel, low centrifugal forces allowed the flow to remain relatively evenly distributed across the channel (Figure 6.5). The numerical simulations showed this to remain the case even after a series of 12 bends (Figure 6.13). This suggests a threshold sinuosity must be surpassed to induce a change of near-bed flow direction from towards the inner banks to towards the outer bank (Figures 6.5 and 6.7). Change in near-bed flow orientation may help explain the ossification of meandering sinuous channels [Peakall et al., 2000; Dorrell et al., 2018a]. It is possible a channel increases in sinuosity until basal flow switches its dominant direction to the outer bank, upon which the net transport of material stabilises the channel's planform. Any transition would likely be highly transient, dependent on variations in the magnitudes of flows entering the system and temporal fluctuations in the flow [Dorrell et al., 2018a].

For the mid and high sinuosity channels, despite super-elevation on the outer bank, a helical flow structure remained suppressed in the laboratory setting. However, the numerical simulations showed river-like rotational cells developing in bends further

downstream. The lack of helical structure proximally is attributed to large levels of overspill as the current adjusts to the channel geometry. As overspill levels reduce, rotational cells begin to form (Figures 6.11 and 6.12). The ability of overspill to inhibit secondary rotation has been seen previously. Keevil et al. [2006] observed an absence of rotation at the first channel bend of their study which can be attributed to a greater level of overspill than at subsequent bends. Furthermore, Dorrell et al., [2013] and Aspiroz-Zabala et al. [2017] discuss how overspill may inhibit rotational cell development. Previously, the presence of vertically stacked cells has been discussed with these being seen in both numerical models [Imran et al., 2007] and the laboratory [Islam et al., 2008; Abad et al., 2011; Dorrell et al., 2018a]. However, all these cases featured high degrees of confinement, and when overspill was present the upper cell did not form. Such results, combined with those reported here, suggest vertically stacked cells are unlikely to develop in seafloor channels where significant overspill is present.

The presence of super-elevation and overspill results in a net radial flux towards the outer bank, which Dorrell et al. [2013] demonstrated as being a key control in setting the direction of any rotation. In the cases reported here, when no rotation occurred initially due to overspill, it would appear that the strong radial flux generated dominates the entire secondary flow field. While overspill is seemingly capable of inhibiting secondary rotation, this view must be balanced by noting that higher levels of overspill would be expected to produce a greater degree of channel asymmetry as sediment is deposited on the outer levee [Ezz et al., 2013]. Subsequently, a higher channel sinuosity would correlate with increased asymmetry. However, evaluation of this complex current-channel feedback system lies outside the scope of this study.

Radial pressure gradients are understood to be a key driver in secondary flow structure, caused by stratification in the flow. Single, and multiple horizontally stacked, rotational cells observed in this study are characterised by local reversals in the radial pressure gradient (Figure 6.11). This is associated with a small fluctuation in the density field,

although it is uncertain whether this is a cause or a by-product of advection initiated by the secondary flow.

6.4.3 Channel morphology, rotational cell position and bend transition

The direction of secondary flow rotation has received much attention over the years, not least because it determines the direction of basal flow, an important factor to consider when examining channel evolution and the nature and location of deposition. Numerical simulation results shown here (Figure 6.14) highlight how a change in channel geometry, while keeping flow conditions fixed, can results in a reversal in the basal flow direction. This is partly due to the lateral location of the rotational cells. In the case of the cosine-curve channel profile (Figure 6.2), river-like cells are positioned directly over the thalweg and, as a result, direction of basal flow is towards the inner bank (Figures 6.11, 6.14 and 6.15). Changing the profile of the channel to that shown in Figure 6.4 had a profound effect on the lateral flow structure (Figure 6.14). Although a small river-like cell can still be observed it is positioned on the outer bank, resulting in a strong basal flow towards the outer bank. The slope of the inner channel bank is therefore a key control on a current's secondary flow field. A steeper bank also increases the effective confinement, with a denser flow being observed at the same downstream location in the flatter channel in comparison to the flow traversing the cosine-curve channel, due to less overspill. This increased lateral stratification and more pronounced super-elevation is thought to contribute to the strong outwards basal flow.

The location and behaviour of a rotational cell was also analysed around the arc of a bend (Figure 6.15). There is very little data available concerning secondary flow at an inflection or anywhere between bend apexes. Keevil et al. [2006] observed a weak rotational cell at the inflection of the opposite direction to the previous apex. Sumner et al. [2014] show transects at various stages round the bend with complex, varying behaviour. Here, a transition occurring at the inflection with two horizontally adjacent cells of opposing

direction is observed. This transition occurs fairly abruptly, the net radial fluxes showing asudden change in direction just after the inflection. The point of transition would also appear to be dependent on the channel and flow conditions, with it seemingly occuring before the inflection in the experiments of Keevil et al. [2006].

The cross-stream velocity profile resulting from the two horizontally adjacent cells is shown in Figure 6.17 and is similar to the velocity profile recorded by Azpiroz-Zabala et al. [2017] in the Congo Canyon. This was understandably interpreted as resulting from the presence of two vertically stacked rotational cells. However, the measurement location of Azpiroz-Zabala et al. [2017] was close to the inflection point between two bends, and it is possible that a transition point could have been identified with cells stacked horizontally rather than vertically. From the given data it is not be possible to distinguish between these two possibilities, highlighting the difficulty of inferring the whole flow-field from thalweg data alone.

6.5 Conclusions

Results of both laboratory experiments and numerical simulations of gravity currents traversing sinuous channels have been reported. Both river-like and river-reversed secondary flow rotational cells were observed. However, secondary rotation is inhibited when channel sinuosities are low or levels of overspill are high. It is concluded that the development of multiple vertically stacked rotational cells in partially-confined settings is more unlikely than in a fully-confined, canyon-like setting. In this study, all rotational cells are associated with a local reversal in the radial pressure gradient, which is therefore inferred to be a key control on the development of secondary flow structure. The evolution of the secondary flow-field around a bend has been investigated, with the transition point being characterised by the development of two horizontally adjacent rotational cells. Numerical simulations show that changes in cross-sectional channel geometry are capable of inducing switches in the direction of cross-stream basal flow, indicating that channel morphology is a primary factor in both the position and sense of movement of rotational cells.

Chapter 7

Downstream evolution of partially-confined gravity currents and the identification of an equilibrium state

Key points

- Basal shear stress maps are used to analyse the downstream evolution of flows and their interactions with channels.
- An onset of flow response to channel curvature is identified; flows in straight and low sinuosity channels display similar evolution characteristics which are distinctly different to those in channels with higher sinuosities.
- Evidence is observed of flow tuning; the flux rates and flow field characteristics of flows of differing input conditions traversing the same channel become similar after a series of bends.
- An equilibrium state between current and channel is identified, with definitions for such a state discussed.

Abstract

Submarine channels are ubiquitous and critical features of the sea floor. They act as the main conduit for turbidity currents and as such can be vital sediment and nutrient pathways to the deep ocean. A complex system of feedback governs the interaction and subsequent development of a current and its confining channel. It operates at two timescales: at the scale of individual flows, the flow field is modulated due to flow through channel form; over longer timescales, the combined depositional and erosional impact of large numbers of successive flows modulates the channel morphology. This

chapter is concerned with the scale of individual currents and the control of the channel form on intrachannel flow structure and downstream flow evolution. Numerical simulations are conducted of saline gravity currents partially-confined within sinuous channels of a fixed cross-sectional profile, representative of real-world morphologies. The datasets are used to construct maps of basal shear stress and analyse the downstream evolution of fluid and material fluxes. The effect of changes in channel sinuosity, axial slope and input mass flow rate are investigated. Channels are shown to be capable of tuning a flow, whereby flows of differing magnitudes approach a stable set of conditions. This stable set of conditions is identified as a state of equilibrium; for the cases studied here it is characterised by a symmetrical cross-channel basal stress profile. Such a state could result in the previously observed phenomenon of a seafloor channel achieving planform stability.

7.1 Introduction

The interaction of turbidity currents and their confining channels is a key area of research in sedimentology [e.g. Mohrig and Buttles, 2007; Straub et al., 2008; De Leeuw et al., 2016]. The complex feedback system of channel inception and development by a flow, and the subsequent flow forcing by the channel (see Chapter 5), determines both the evolution of channel morphology and the dynamics and runout of a current.

In comparison to fluvial systems [e.g. Leopold and Wolman, 1957; Thorne et al. 1982], relatively little is known about the precise mechanisms governing seafloor channel development. Laboratory studies have examined the depositional patterns of small-scale flows [e.g. Kane et al., 2008; Straub et al., 2008; Ezz et al., 2013] and field studies have been used to examine the architecture and aggradational patterns of both ancient and active channels [e.g. Deptuck et al., 2007; Gee et al., 2007; Babonneau et al., 2010; Conway et al., 2012].

Peakall et al. [2000] outlined a process model for submarine channel development, showing significantly different behaviours to the typical fluvial model of progressive downstream migration, which is due to erosion at the outer bank and deposition at the inner bank. Analysis of individual submarine channels identified an equilibrium phase, during which the planform of the channel remains fixed (Figure 7.1). This is despite submarine channel systems often being subject to a wide range of input conditions and flow magnitudes [Xu et al., 2004; Vangriesham et al., 2009; Azpiroz-Zabala et al., 2017]. Although turbidity currents have been shown to have the ability to deposit sediment both at the inner and outer channel banks [Timbrell 1993; Peakall et al., 2007; Kane et al., 2008], the precise mechanisms governing development of a channel-current equilibrium are still not understood.

Numerical models of gravity currents are relatively widespread. Solutions of the Reynolds-averaged Navier-Stokes (RANS) equations were first found by Eidsvik and Brørs [1989] and similar models have been used in several studies since [e.g. Kassem and Imran, 2004; Huang et al., 2005, 2008; Giorgio Serchi et al., 2011; Ezz and Imran, 2014; Afraie et a., 2018]. Predominantly, these studies have focussed on the structure and dynamics of the flows, and not on the interaction with or the effect of any channel geometry. Here, numerical simulations are used to examine the downstream evolution patterns of gravity currents traversing a range of channel planforms. Additionally, maps

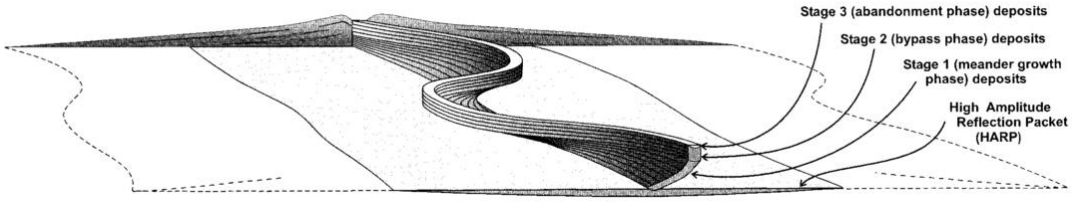

Figure 7.1 The process and evolution modelled outlined by Peakall et al. [2000]. After an initial development phase where the channel develops and increases in sinuosity (much like a fluvial channel) an equilibrium phase is reached, during which the channel aggrades upwards with relatively little change in planform.

of basal stress are produced to show explicitly the interaction between a current and its confining channel.

7.2 Methodology

Both laboratory experiments and numerical simulations were conducted of saline gravity currents traversing sinuous channels, with the aim of investigating the effects of partial-confinement on flow evolution. Three channel planforms were used with sinuosities of 1.01, 1.05 and 1.11. Hereafter, these are referred to as the low, mid and high sinuosity channels respectively.

In the Sorby Environmental Fluid Dynamics Laboratory, the velocity of continuous release saline gravity currents was recorded using acoustic Doppler velocimetry. This provided velocity profiles across the width of the channels at both bend apexes and inflections. Currents with a 1 l/s input flow rate traversed channels with the above sinuosities at a slope of 2°. Full details of the experiments and channel geometries can be found in Chapter 3.

The numerical simulations used a RANS model with a shear stress transport turbulence closure [Menter, 1994]. Simulations mimicked the laboratory channel geometry and flow conditions. However, flexibility of modelling allowed channels to be extended downstream from what was possible in the laboratory, tripling the number of modelled bends. Furthermore, the effect of both a shallower slope (0.5°) and different flow input rates (0.5, 0.25 and 0.125 l/s) were investigated. A single simulation was also conducted in an extended version of the mid sinuosity channel, comprising 16 bends, in order to investigate longer run-out distances and is shown in Figure 7.2.

These simulations provide data for the entire flow. Maps of basal shear stress are used to analyse the interaction between a current and a channel and to show the path of the flow.

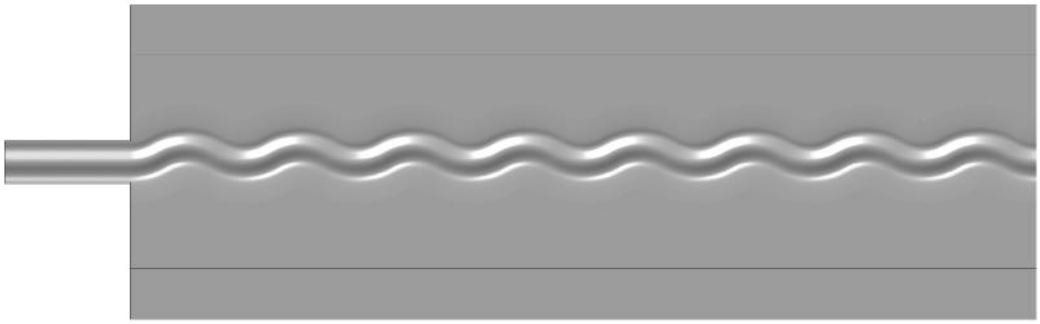

Figure 7.2 The extended version of the mid sinuosity channel, comprising 16 bends, used to investigate longer run-out distances.

Basal shear stress, or wall shear stress, is calculated from the basal velocity gradient and is defined as,

$$\tau_b = \mu \frac{\partial u}{\partial z}\bigg|_{z=0}. \tag{7.1}$$

In this scenario, it is a measure of the force exerted on the channel by the flow (and vice-versa). The basal stress maps can therefore indicate areas of the channel that are likely susceptible to erosion (high magnitudes of stress) or deposition (low magnitudes).

In addition, the downstream change in fluid and material fluxes are shown to analyse flow evolution. The streamwise fluid and material fluxes are, respectively, defined as,

$$Q_{df} = \int_L^R \int_0^\infty u \, dz dr, \qquad Q_{dc} = \int_L^R \int_0^\infty uc \, dz dr, \tag{7.2}$$

the overbank fluxes as,

$$q_{of} = \int_0^\infty v \, dz\bigg|_{r=out}, \qquad q_{oc} = \int_0^\infty vc \, dz\bigg|_{r=out}, \tag{7.3}$$

and the net radial fluxes as,

$$Q_{rf} = \int_L^R \int_0^\infty v \, dz dr, \qquad Q_{rc} = \int_L^R \int_0^\infty vc \, dz dr, \tag{7.4}$$

where $c = (\rho - \rho_a)/\rho_a$ is the effective concentration, r is the radial direction, L and R are the levee crests and $out = L$ or R is the bend-dependent outside crest.

7.3 Results

7.3.1 Laboratory Data

Laboratory velocity data was used to create diagrams of basal flow, shown in Figure 7.3. Data are shown for the three channel sinuosities at a slope of 2°. Vectors were calculated using data acquired 3 mm and 1mm above the channel floor. The 3mm data gives the best representation of the mean flow direction, while the 1mm data provides information on basal flow direction. Several key features of the flow can be identified.

The low sinuosity channel exhibits a significantly different flow pattern to the mid and high sinuosity channels. There is very little evidence of any curvature induced effects,

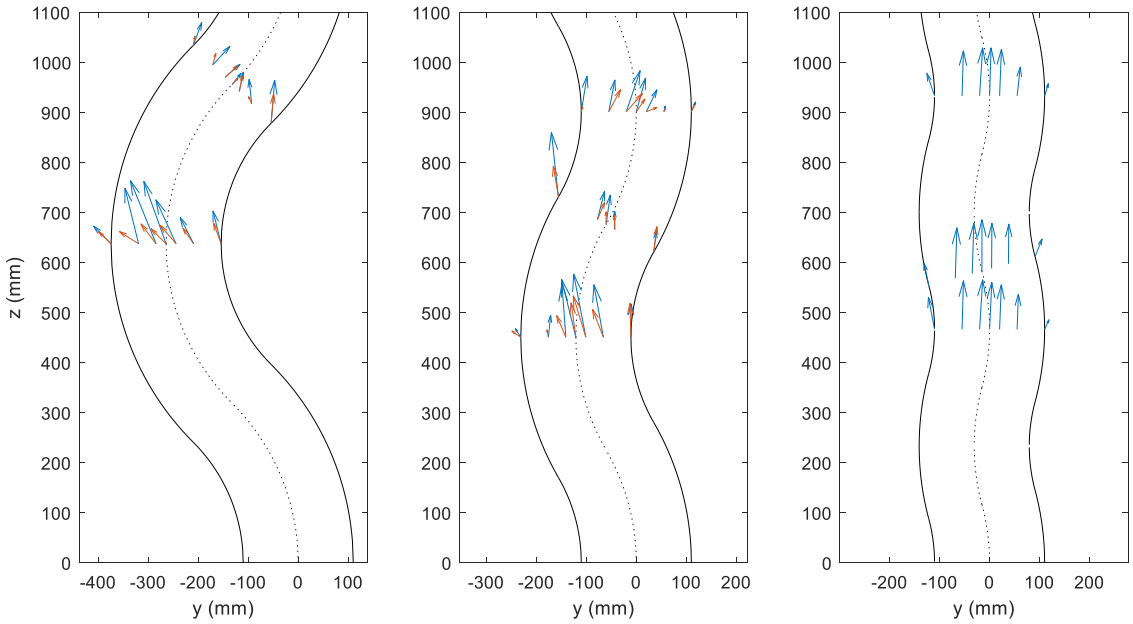

Figure 7.3 Basal flow vectors for the high (left), mid (centre) and low sinuosity (right) laboratory cases at a 2º slope. Vectors are calculated from flow velocities 3 mm (blue) and 1mm (red) above the channel base. 1mm data has been omitted from the low sinuosity channel for clarity; there is negligible difference in direction.

with the intrachannel flow remaining largely parallel with the axial slope at both the bend apexes and the inflection point, and with little lateral variation in velocity magnitudes. Overspill is apparent at both levee crests. There is also little difference between the cross-channel flow profiles at the second and fourth bend apexes, showing relatively little downstream evolution (1mm data has been omitted from the image for better legibility as there was negligible difference in direction).

In comparison, the mid and high sinuosity channels clearly display channel curvature effects in both velocity magnitudes and direction. This can also be seen in the cross-sectional contour data in Chapter 6 (Figures 6.5, 6.7, 6.9, 6.10), where levels of super-elevation are observed at the outer bank with clear radial density and velocity gradients. The vectors show flow directed towards the outer bank at bend apexes. This is evident to a greater degree in the high sinuosity channel due to the greater centrifugal forces present. The channel curvature also prevents any overspill at the inner bank, with overbank losses occurring exclusively at the outer bank.

The flow direction at the inflections reveals further features. The flow field shows a lag effect for the mid sinuosity channel, highlighted previously in Chapter 6. Thus, overbank losses are greater at an inflection than at the previous bend apex, with intrachannel flow not entirely parallel with the channel thalweg. Any lag is less obvious in the high sinuosity channel. This could be due to the longer wavelength of the channel, allowing a longer adaptation time for the current to conform to the channel geometry. Overbank loss is comparable to that at the previous bend apex. Although there is less lag effect at the inflection, the high sinuosity channel appears to be affected by re-entrainment of overspill, whereby flow previously lost overbank re-enters the channel. This is evidenced at the inflection by flow, at some near-bank data points, aligned with the axial slope rather than the channel. Channels with higher sinuosity would appear to me more susceptible to this.

For the mid and high sinuosity channels there is a clear difference between the basal and mean flow direction at the bend apexes. The basal flow is directed to a greater degree

towards the outer bank. At the inflection there is little to no difference in the flow directions. The magnitude of basal velocity is linearly related to basal stress, as this is what determines the basal velocity gradient (Equation 7.1). The size of the red arrows in Figure 7.3 could therefore also be indicative of the relative basal stress magnitudes. For the low sinuosity channel, the basal flow magnitudes are relatively evenly distributed (basal flow magnitudes were proportional to mean flow magnitudes in this case), with a decrease at the levee crests where the flow is slower. For the mid sinuosity channel data, the basal velocity magnitudes are still proportional with the mean flow but the distribution is not so uniform, with larger magnitudes prevalent at the inner banks of the apexes. For the high sinuosity channel data, there is the greatest disconnect between mean flow and basal flow; both direction and magnitude distribution are different. The mean flow is fastest towards the outer bank (also see Figure 6.10) whereas the basal flow magnitudes remain relatively evenly distributed across the channel.

The laboratory data reveals several interesting flow features. However, as is the nature of such data it is acquired at discrete points and is subject to limitations (see Section 7.4.1 for further discussion). The domain sizes in the laboratory are also restricted to a relatively low number of bends. The numerical simulations, however, enable analysis both of high-resolution, whole channel basal dynamics and of the continued downstream evolution of a current. These are described in the following sections.

7.3.2 Basal stress maps

The following sections in this chapter all make use of basal stress maps produced from the numerical simulation data. Figure 7.4 shows the basal stress map of a 1 l/s flow traversing the mid sinuosity channel at a 2° slope. Superimposed vectors show flow direction and magnitude 3 mm above the base; they are a representation of the mean flow. The basal stress map highlight areas where the flow places the most stress on the channel; regions of high stress magnitudes can be interpreted as regions where, in an erodible environment, erosion rates would be highest. If an assumption is made that deposition

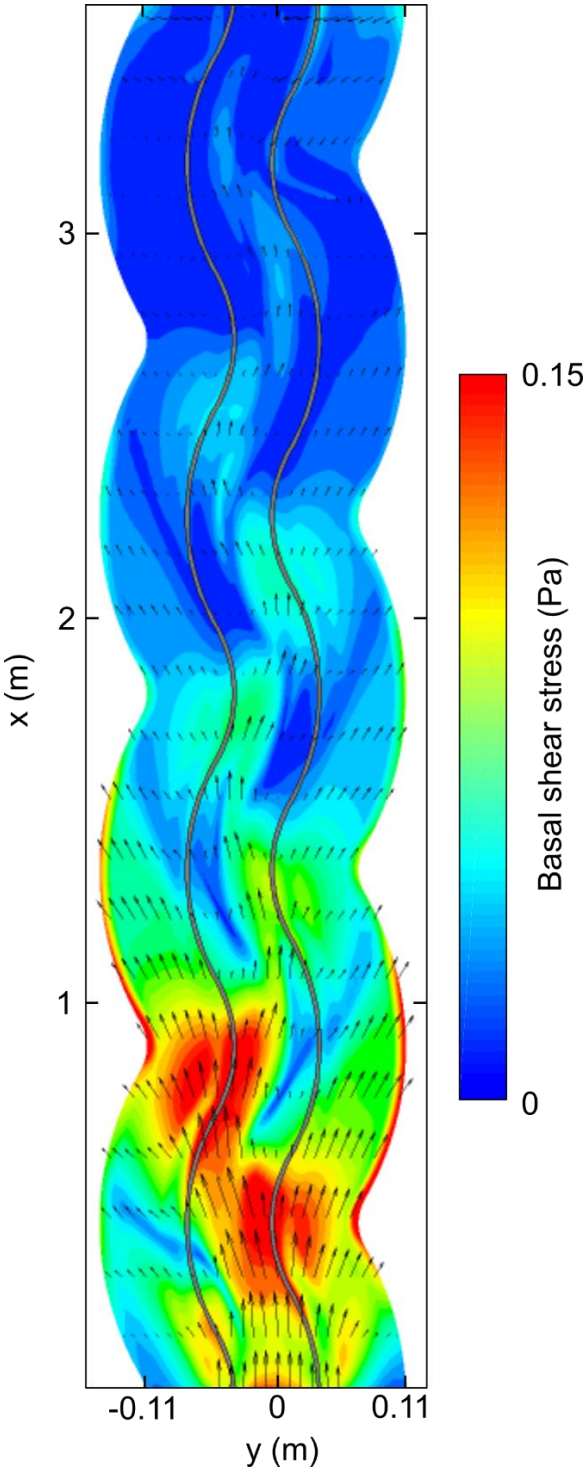

Figure 7.4 Basal stress map for the mid sinuosity channel at a 2° slope. Regions of high stress can be interpreted as areas where the flow exerts higher forcing on the channel which, in an erodible setting, would result in higher rates of erosion. Grey bands indicate the levee crests. Vectors show the velocity of flow taken 3 mm above the floor and are indicative of mean flow.

rates are uniform across the channel, regions of low stress magnitudes would represent regions of net aggradation. This is of course an idealised approach; in reality, deposition rates depend on many variables including particulate concentration and flow turbulence. On the far edges of the channel model, the step in the levee profile results in raised stress magnitudes which are an artefact of the model setup.

The stress map in Figure 7.4 show features common to many of the flows described in this chapter. Stress magnitudes are highest proximally, diminishing over the course of a few bends. Initially, peak stress magnitudes are similar both intrachannel and on the levees. Further downstream, the higher relative magnitudes are found intrachannel where the flow is faster and less fluid is lost overbank. In some places there is a disconnect between the mean flow and basal stress pattern. At the apex of the first bend for example, the highest velocities are centred on the thalweg, whereas the high stress region lies on the inner bank.

A high stress region at the inner bank can be observed for at least the first five bends. Additionally, low stresses are found at the outer bank, at direct odds with the well understood fluvial behaviour of high erosion rates at the outer bank [Thorne, 1982]. This river-reversed stress pattern is consistent with the deposition of outer bank deposits [Peakall et al., 2000].

The following sections explore the effects of changes in channel sinuosity, slope and input flow rate.

7.3.3 Effects of sinuosity

Figure 7.5 shows the basal stress maps for a 1 l/s flow traversing the low, mid and high sinuosity channels at a slope of 2°. Some clear differences can be seen not only in the basal stress patterns but also in the downstream evolution of the flow, illustrated by the fluxes presented in Figure 7.6. Definitions of these can be found in Section 7.2. The low sinuosity channel displays markedly different characteristics in comparison to the mid and high sinuosity channels. The decay of downstream flux is fairly linear in nature in the low sinuosity case and this is corroborated by a near constant overbank fluid flux. The mid and high sinuosity channels exhibit an exponential flux decay, caused by far higher overbank losses during the initial bends.

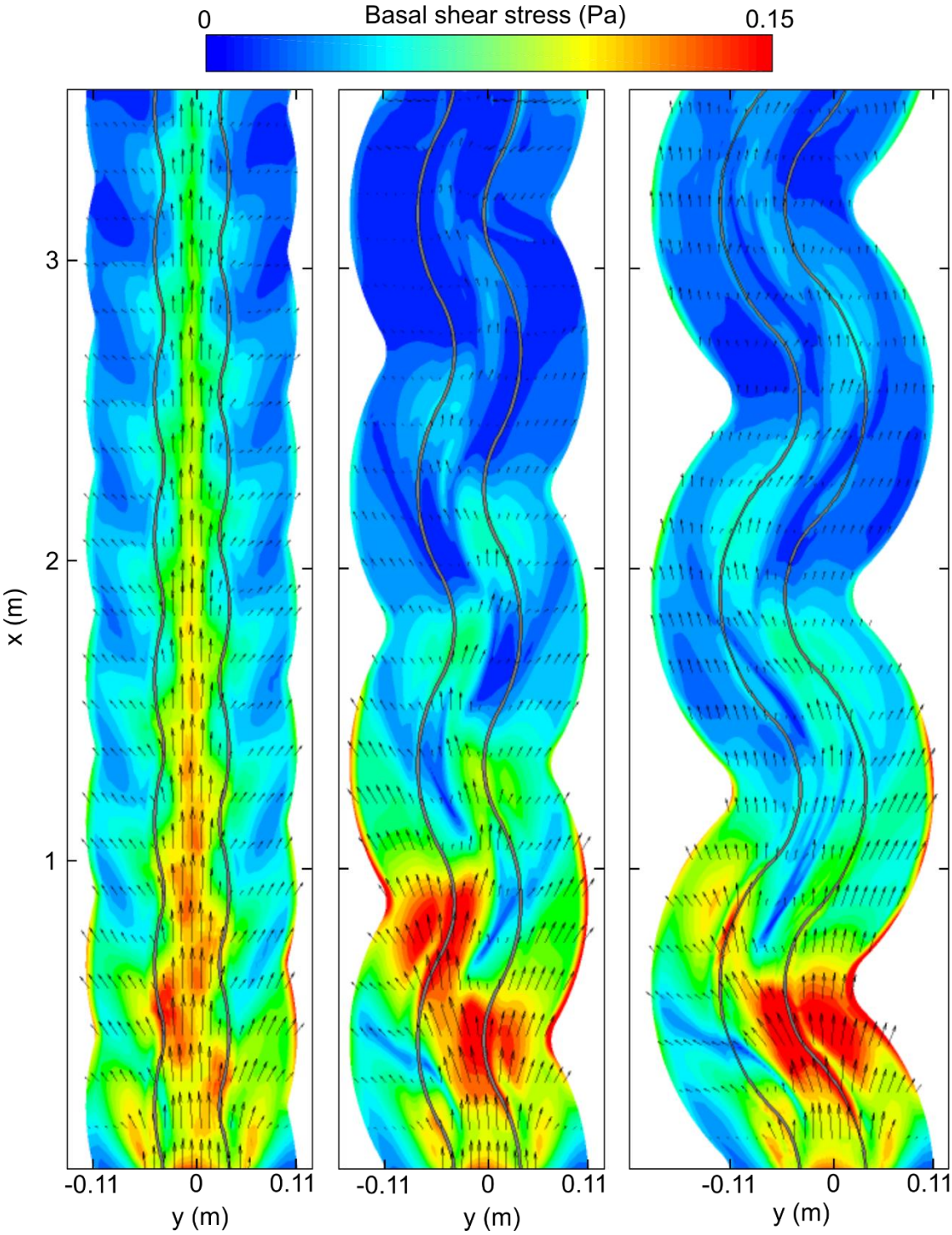

Figure 7.5 Basal stress maps for three channel sinuosities at a 2º slope. Low sinuosity (left); mid sinuosity (centre); high sinuosity (right). Grey bands indicate the levee crests. Vectors show the velocity of flow taken 3 mm above the floor and are indicative of mean flow.

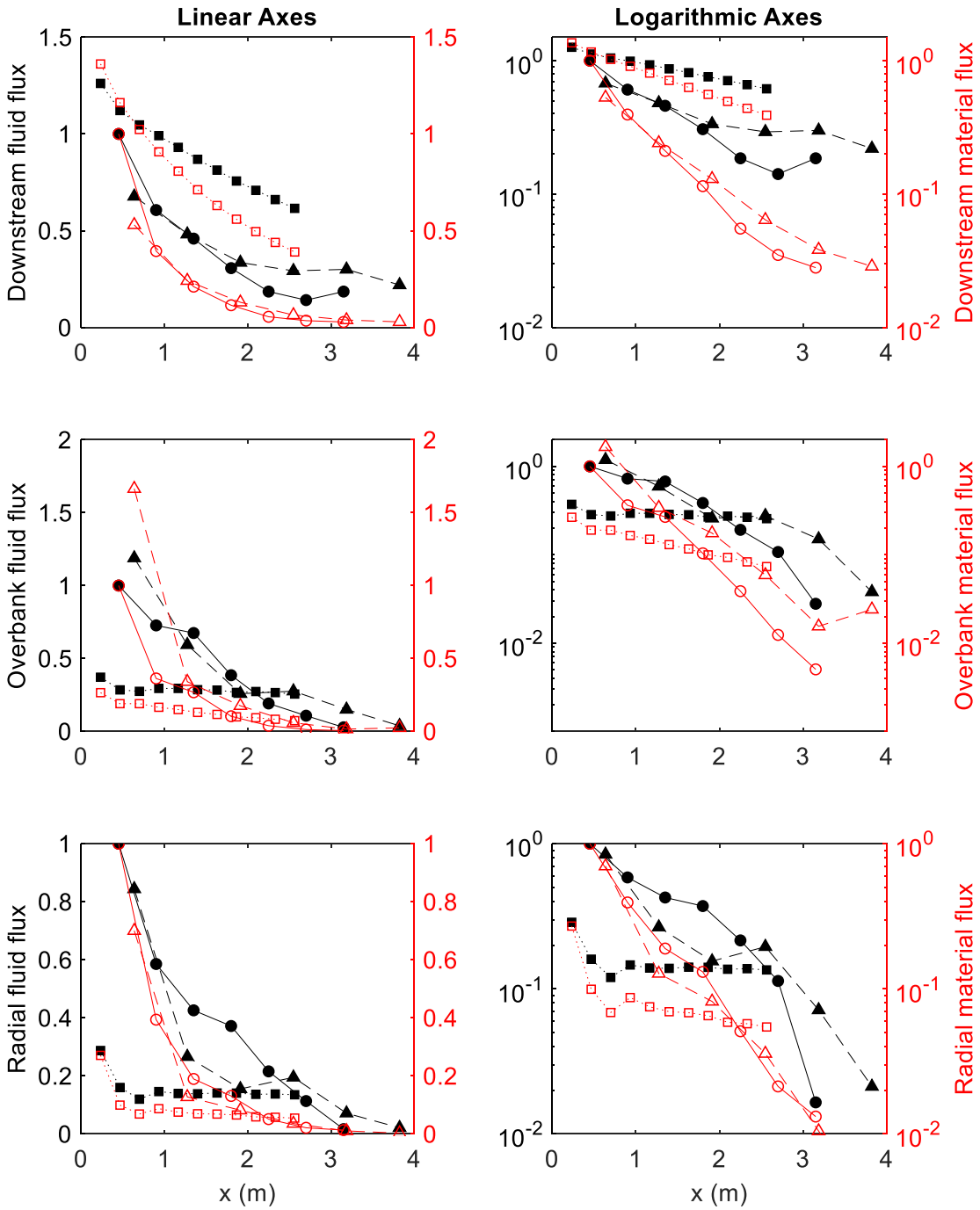

Figure 7.6 Comparison of fluxes for varying channel sinuosity. Downstream (top), overbank (centre) and radial (bottom) fluxes. Fluid fluxes are shown in black; material fluxes are shown in red. High sinuosity - dashed line and triangles; mid sinuosity - solid line and circles; low sinuosity – dotted line and squares. Plots in the left column use linear axes; plots in the right column use logarithmic axes. Fluxes have been normalised using the value at the first bend of the mid sinuosity channel.

These different flux evolution characteristics are directly reflected in the basal stress patterns. Both intrachannel and levee stress magnitudes decay more slowly for the low sinuosity channel. The large proximal overbank losses for the mid and high sinuosity channels lead to the high levels of basal stress that can be observed on the channel levees. Meanwhile, intrachannel stress magnitudes decay rapidly in comparison to the low sinuosity channel. The similarity in the collapse of the downstream fluxes for the mid and high sinuosity channels, especially the material flux, is a point of interest. Despite the differences in sinuosity there appears to be little difference in the channels' abilities to transport material downstream.

The mean flow vectors over the first bends (Figure 7.4) can be compared to those in the laboratory (Figure 7.3). Agreement is very good, with both direction and relative magnitudes predicted accurately. Corroborating the laboratory data, the mean flow data shows how the high sinuosity channel is affected by flow re-entrainment at the second bend. This flow feature is not present in the other channels. The mean flow in the low sinuosity channel displays little evidence of channel curvature, with the bulk of the flow remaining parallel to the axial slope. Finally, as with the laboratory data, there is some disconnect between the pattern of the mean flow and the basal stresses. While there is a broad correlation between the fastest parts of the flow and the high stress regions, there are local differences. For example, at the first bend of the high sinuosity channel the mean flow velocity maximum is towards the outside of the bend, whereas the peak stress magnitude occurs on the inside of the bend. The laboratory data also shows this (Figure 7.3).

7.3.4 Effects of slope

Figure 7.7 shows the basal stress maps for a 1 l/s flow traversing the mid sinuosity channel at slopes of 2° and 0.5°. Fluid and material fluxes are shown in Figure 7.8. As expected, the steeper slope results in, initially, a faster flow and the higher stress magnitudes that this leads to. Proximally, the steeper channel has higher stresses both intrachannel and on the levees. However, by the ends of the channel, this has changed. Due to lower levels of both overbank loss and ambient entrainment, the downstream material flux and the peak intrachannel stresses are both slightly higher distally in the shallower channel. Interestingly, whilst the downstream material fluxes differ at the end of the channel, both net radial and overbank material fluxes converge. This could suggest that a flow's radial dynamics are more dependent on channel sinuosity than slope. Figure 7.6 does show different overbank flux profiles for the three channel sinuosities, while the net radial flux is similar for the mid and high sinuosity channels.

The basal stress patterns are broadly similar for the two slopes. Peak stress magnitudes occur at the inside of the bends proximally, migrating towards a thalweg position as the flow travels downstream. For the shallower slope, a combination of lower stress magnitudes in proximal regions, combined with the higher depositional rates of a slower flow, would suggest a more depositional environment. If the flow dropped below the zero net entrainment and deposition threshold [Dorrell et al., 2018b], this would have a significant effect on the evolution of the channel morphology.

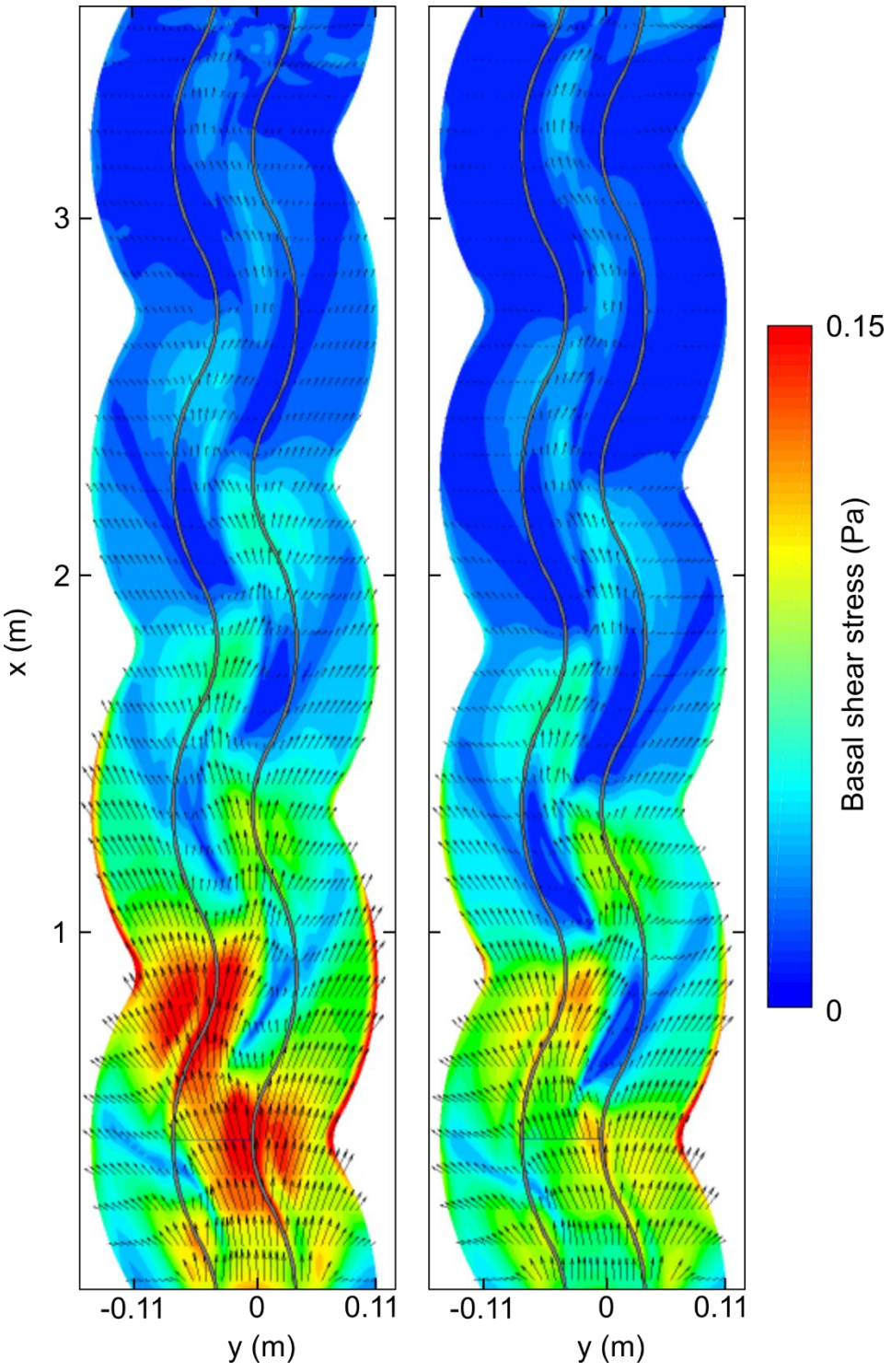

Figure 7.7 Basal stress maps for the mid sinuosity channel at a 2º (left) and 0.5º (right) slope. Grey bands indicate the levee crests. Vectors show the velocity of flow taken 3 mm above the floor and are indicative of mean flow.

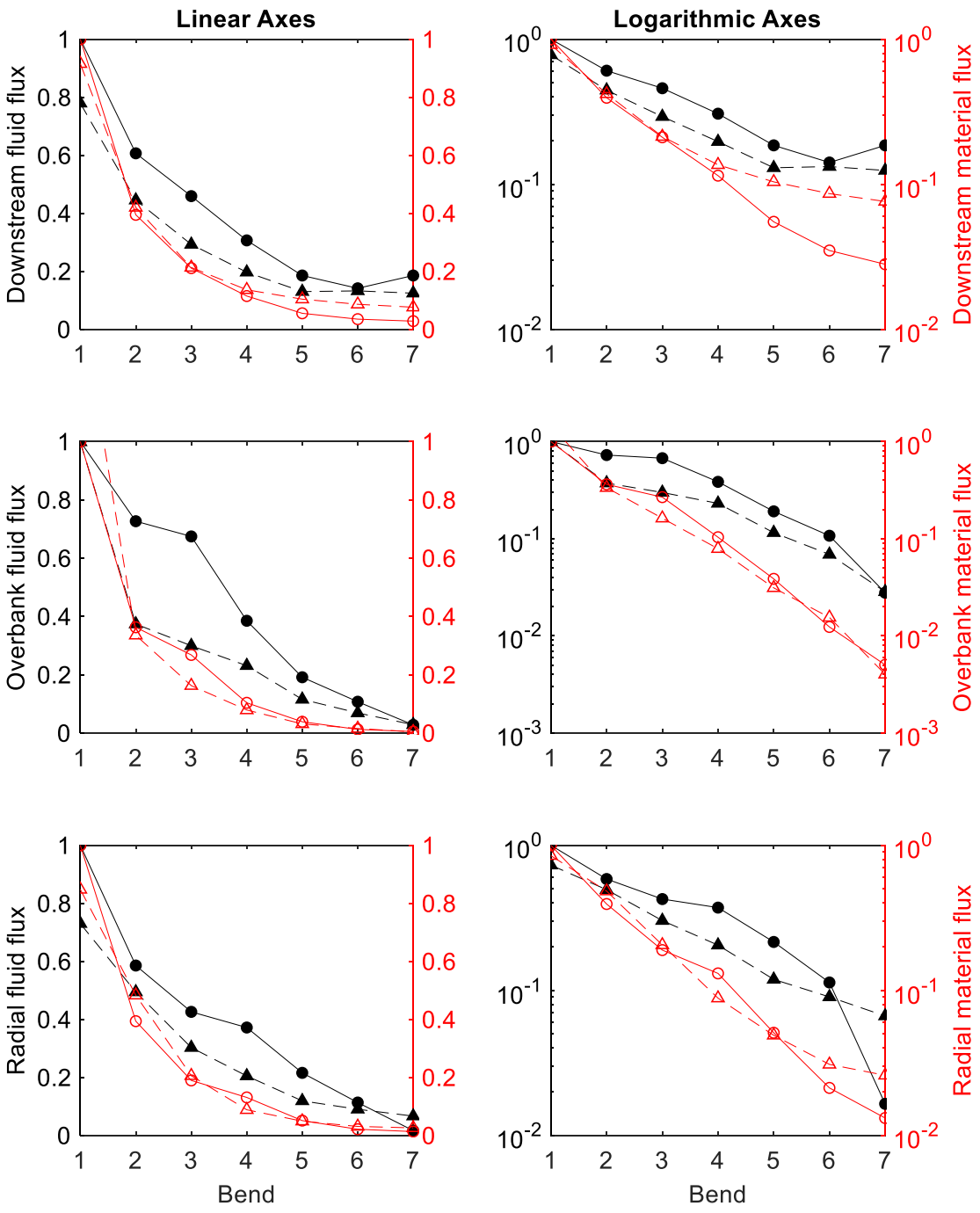

Figure 7.8 Comparison of fluxes for different slopes. Downstream (top), overbank (centre) and radial (bottom) fluxes for the mid-sinuosity channel. Fluid fluxes are shown in black; material fluxes are shown in red. 2º slope – solid line and circles; 0.5º slope – dashed line and triangles. Plots in the left column use linear axes; plots in the right column use logarithmic axes. Fluxes have been normalised using the value at the first bend of the 2º slope.

7.3.5 Flow tuning

Flow tuning, as has been described in previous chapters, is the process of channel morphology reducing downstream flow variability, i.e. 'tuning' a flow to a certain set of conditions. Figure 7.9 shows the basal stress maps for 1 l/s, 0.5 l/s, 0.25 l/s and 0.125 l/s flows traversing the mid sinuosity channel at a slope of 2°. Fluid and material fluxes are shown in Figure 7.10. The salient feature is the marked degree of flux convergence shown between the flows. Both downstream, overbank and net radial fluxes approach the same values despite distinctly different initial conditions. When examined closely, the fluxes of the 0.25 and 0.125 l/s flows approach an equilibrium state at a quicker rate and are decaying at a slower rate than the larger flows.

These features are mirrored in the basal stress maps, with all flows achieving similar distal stress patterns. However, there is a subtle inverse relationship between the peak stress magnitude at the distal bends and the input flow rate. The smaller initial flows result in the larger stress magnitudes after a series of bends and, correspondingly, the larger downstream material fluxes. This is, in part, due to flow stripping, whereby the larger currents lose more fluid overbank at the initial bends. As previously described, this results in the high stress levels seen on the proximal levees of the larger flows. Here, the smaller flows differ, in that peak intrachannel stress magnitudes are larger than those on the levee.

There is evidence of the two possible flow tuning approaches here that are described in Chapter 5, inflation and deflation. Unlike other flows, the overbank losses of the smallest flow (0.125 l/s) increase over the first few bends. This is because of the smaller flow magnitude and height, meaning that proximal overbank losses are smaller than the levels of ambient entrainment and indicates that flow inflation, rather than deflation, predominates in this case.

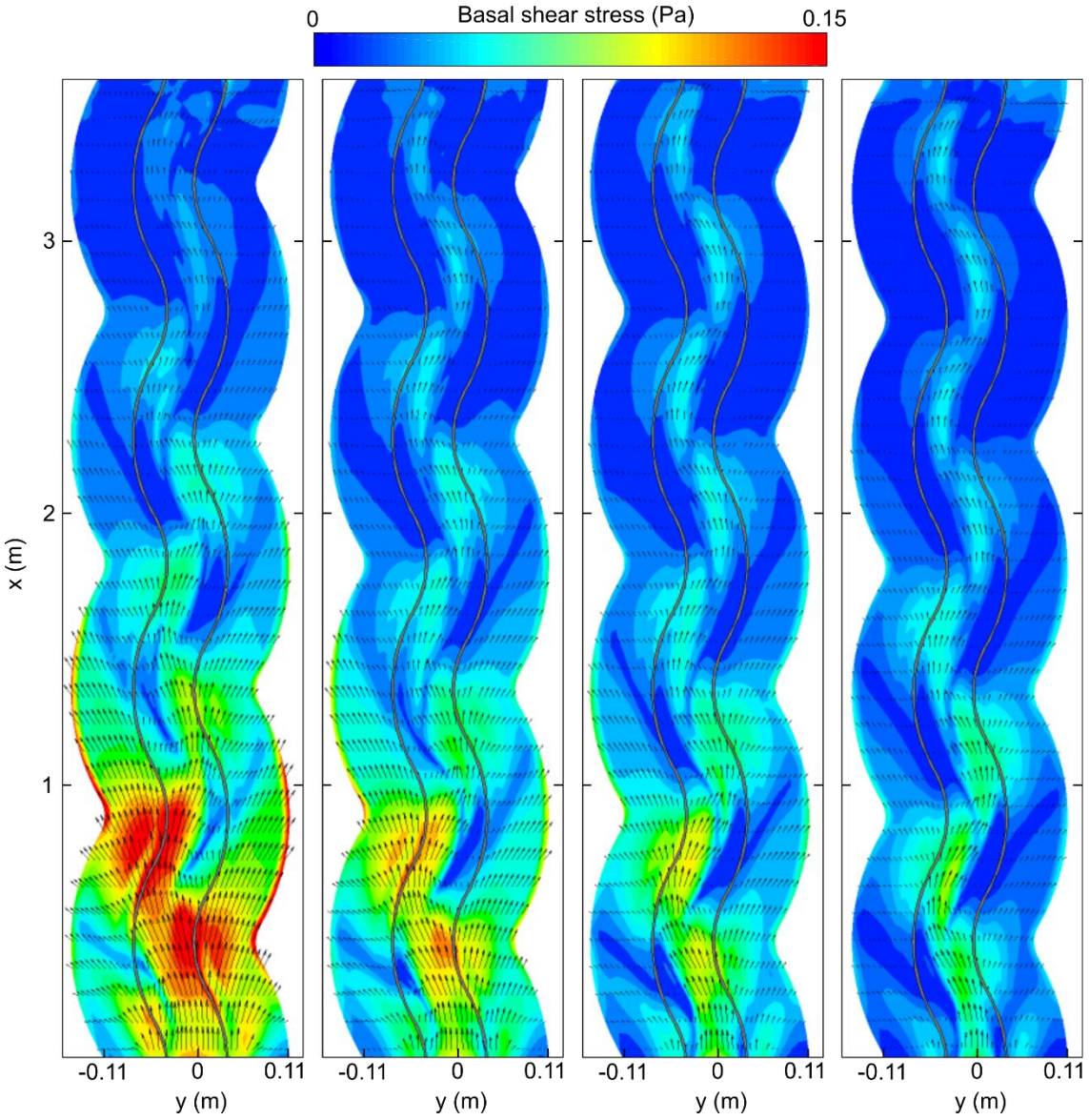

Figure 7.9 Basal stress maps for the mid sinuosity channel at a 2º slope. The four illustrated channels have differing input flow rates. From left to right: 1 l/s, 0.5 l/s, 0.25 l/s and 0.125 l/s. Grey bands indicate the levee crests. Vectors show the velocity of flow taken 3 mm above the floor and are indicative of mean flow.

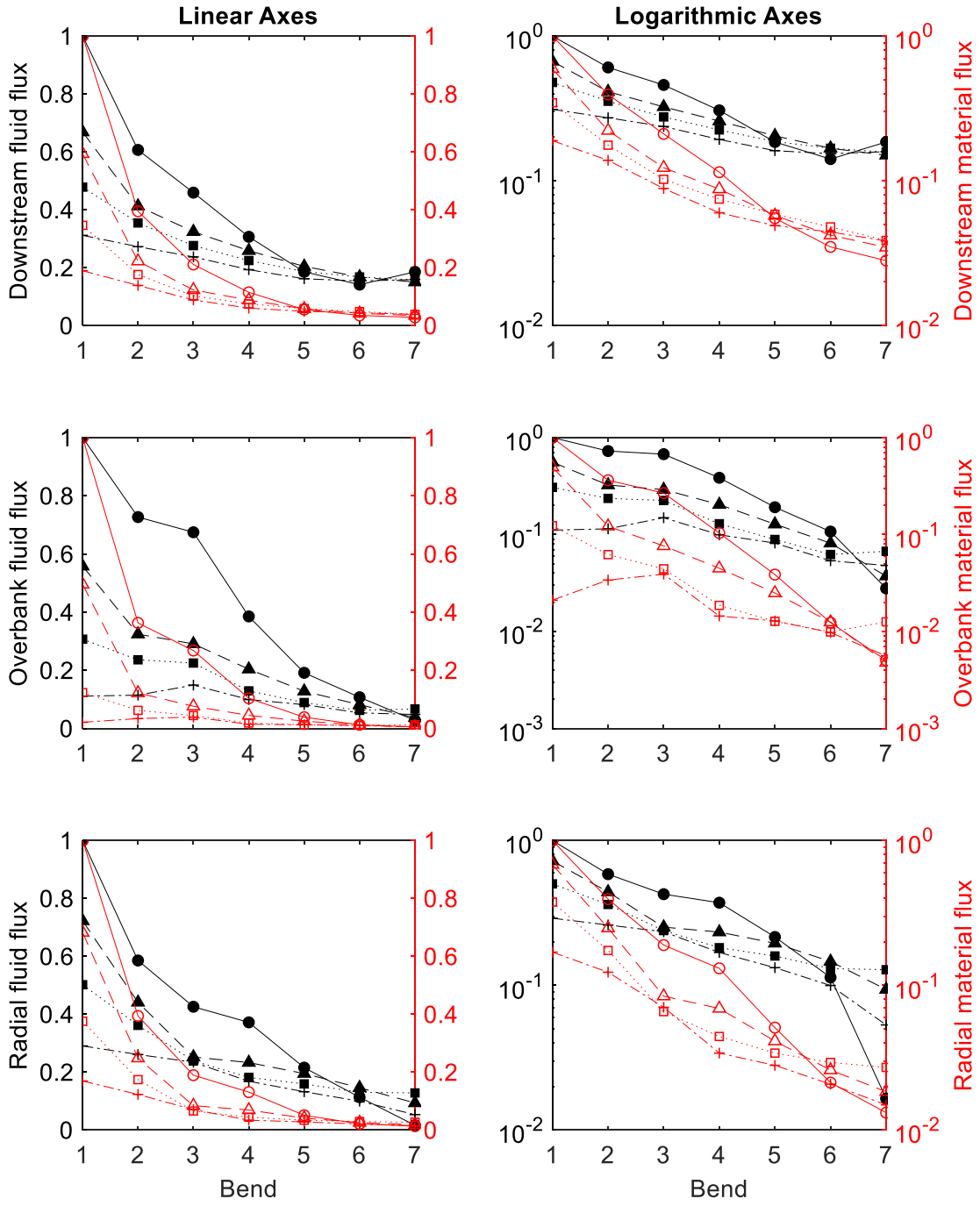

Figure 7.10 Comparison of fluxes for varying input flow rates. Downstream (top), overbank (centre) and radial (bottom) fluxes for the mid sinuosity channel at a 2º slope. Fluid fluxes are shown in black; material fluxes are shown in red. 1 l/s – solid line and circles; 0.5 l/s - dashed line and triangles; 0.25 l/s – dotted line and squares; 0.125 l/s – dash dot line and pluses. Plots in the left column use linear axes; plots in the right column use logarithmic axes. Fluxes have been normalised using the value at the first bend of the 1 l/s case.

7.3.6 Longer runout distances and current-channel equilibrium

To investigate flow behaviour over longer runout distances, a 1 l/s flow at a 0.5° slope was simulated over an extended version of the mid sinuosity channel (Figure 7.2). Figure 7.11 shows the basal stress map of this flow, with the fluxes displayed in Figure 7.12. Two phases of the flow can be identified:

i) an initial development period covering approximately the first 6 bends, during which the flow adjusts to the channel geometry via overbank losses and ambient entrainment (see Chapter 5 for further discussion of these mechanisms);

ii) a quasi-equilibrium period from bend 7 onwards, during which the basal stress pattern remains relatively unchanged from bend to bend and both downstream fluxes, overbank fluxes and lag approach a constant value.

The idea of flow tuning is discussed in Chapter 5, where a current conforms to a given channel geometry via overbank losses and ambient entrainment. The resultant ratio of fluid gains to fluid losses determines whether flow magnitude decreases (if overbank losses dominate), increases (if ambient entrainment dominates) or approaches a stable condition, where gains and losses balance. The relatively uniform basal stress distribution over successive bends in the distal reached of the modelled channel is here interpreted as an example of how a gravity current is capable of achieving a state of quasi-equilibrium with its confining channel via flow tuning. An abrupt decrease in the rate of downstream fluid flux adjustment is observed at bend 5, after which it decreases at a very slow rate. A similar abrupt decrease in the rate of overbank flux adjustment is seen at bend 7, with a quasi-constant value of flux seen thereafter. Although the decay rate of the downstream material flux reduces in the equilibrium phase, it still decreases quicker than the fluid flux. This is to be expected, as if a constant fluid flux is achieved via a balance between overbank losses and ambient entrainment, the current will still be diluted by the ambient fluid and lead to a subsequent reduction in material flux.

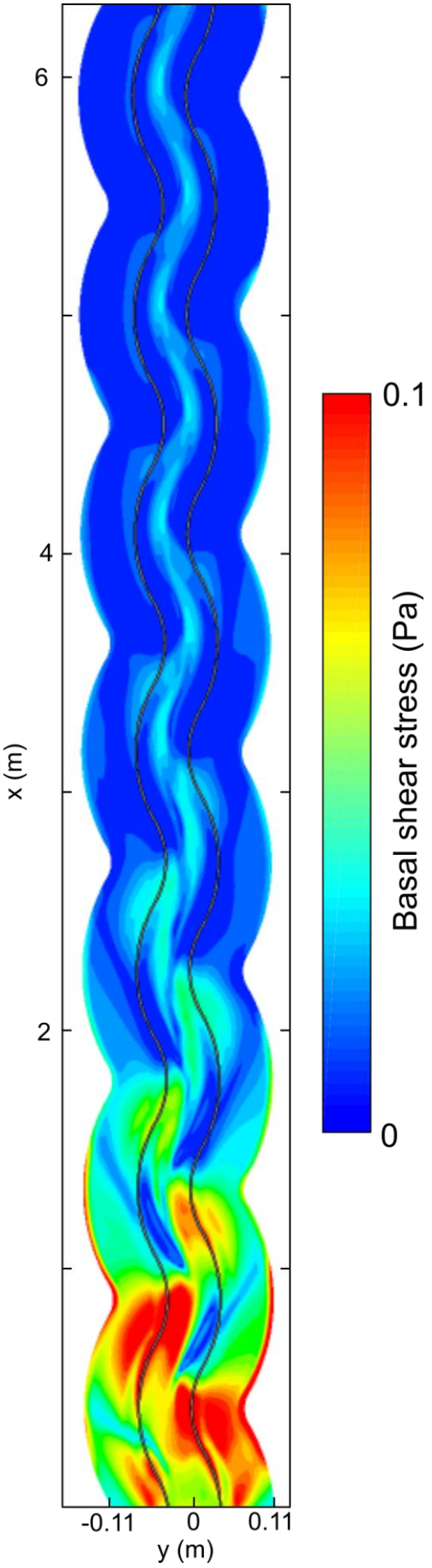

Figure 7.11 Basal stress map for the mid sinuosity channel at a 0.5º slope. A longer simulation domain was used to show how a current can achieve a state of quasi-equilibrium with a channel, illustrated here by a consistent basal stress pattern. Grey bands indicate the levee crests.

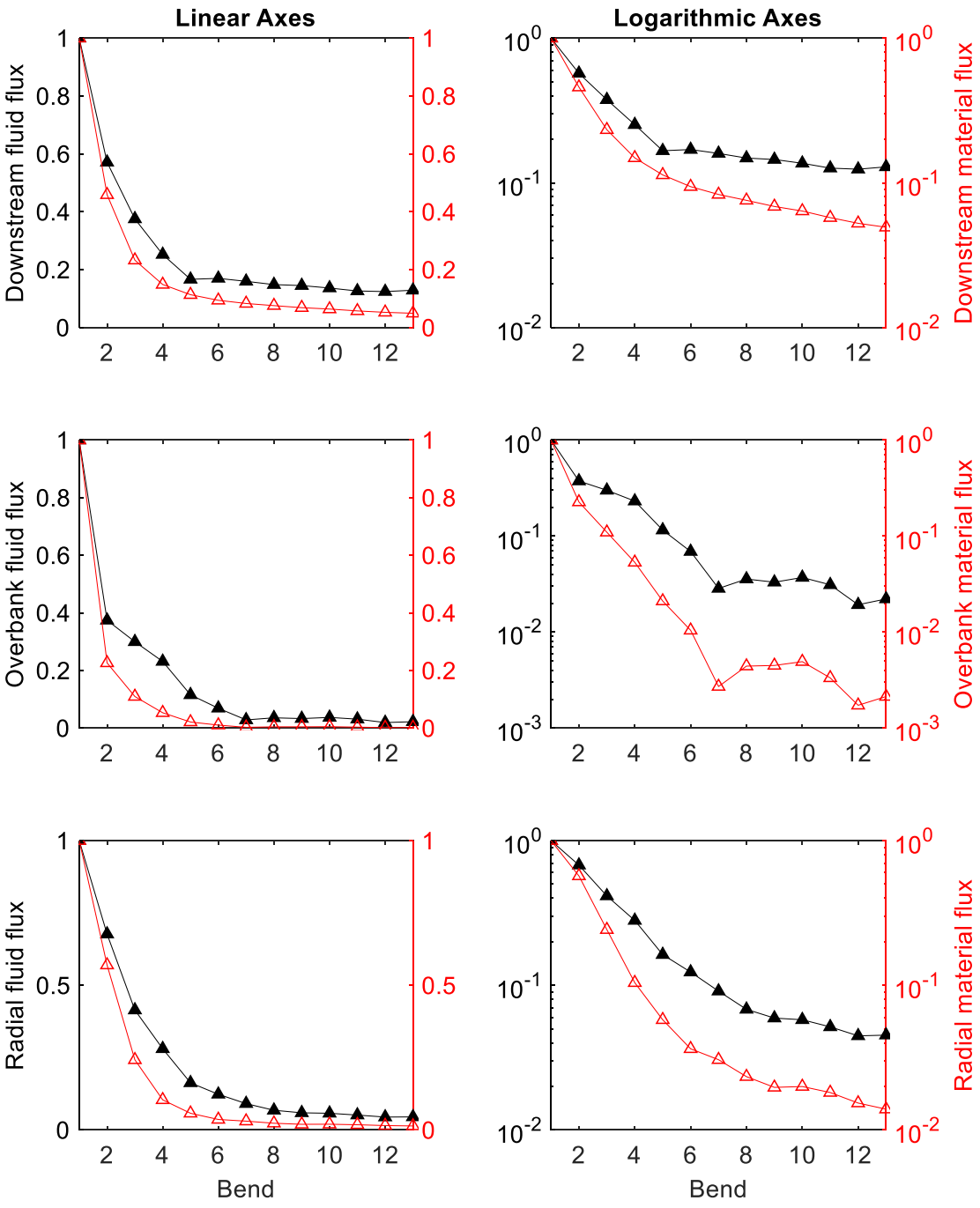

Figure 7.12 Downstream (top), overbank (centre) and radial (bottom) fluxes for the mid-sinuosity long channel at a 0.5º slope. Fluid fluxes are shown in black; material fluxes are shown in red. Plots in the left column use linear axes; plots in the right column use logarithmic axes. Fluxes have been normalised using the value at the first bend.

For this simulation, entrainment fluxes are shown in Figure 7.13. These have been calculated with two different methods (referred to as A and B hereafter), outlined below.

Method A: the method used in Chapter 5 and best suited to discrete laboratory data. This uses the equation,

$$2\hat{e}_W|\widehat{U}|Y = \frac{\partial \widehat{U}A}{\partial x} + |V(Y)h(Y)| + |V(-Y)h(-Y)|, \tag{7.5}$$

where the first term, $2\hat{e}_W|\widehat{U}|Y$, is the entrainment flux. This is almost the same as the equation (5.9) used in Chapter 5, except the flow can now no longer be assumed to be symmetrical. Overbank losses must therefore be calculated at both banks and the area of the flow is now defined as $A = \int_{-Y}^{Y} h \; dy$, with Y still defined as half the channel width. Similarly, the velocity must be integrated across the whole channel, so $|\widehat{U}| = \left(\int_{-Y}^{Y}\int_{0}^{h}|u| \; dz \; dy\right)/A$.

Method B: here, the vertical velocity component is integrated across the width of the channel at the top of the flow to calculate the 'true' amount of ambient fluid entering the flow from above,

$$\text{entrainment} = \int_{-Y}^{Y} v(h)dy\,. \tag{7.6}$$

The 'true' entrainment flux (method B) is shown with the dashed line. The downstream evolution pattern is very similar to that of the overbank losses. There is a rapid decrease over the first few bends as the flow magnitude reduces. After bend 8, an approximately constant value is reached. This balance between entrainment and overbank coincides with the equilibrium phase. There are significant differences between the values from the two calculation methods. While the two methods output similar values at the distal bends, method A under-predicts the amount of fluid entrained at the upper interface proximally. This is attributed to the larger downstream velocity gradients during the development phase, and the greater fluctuation of overbank losses over the course of a proximal bend,

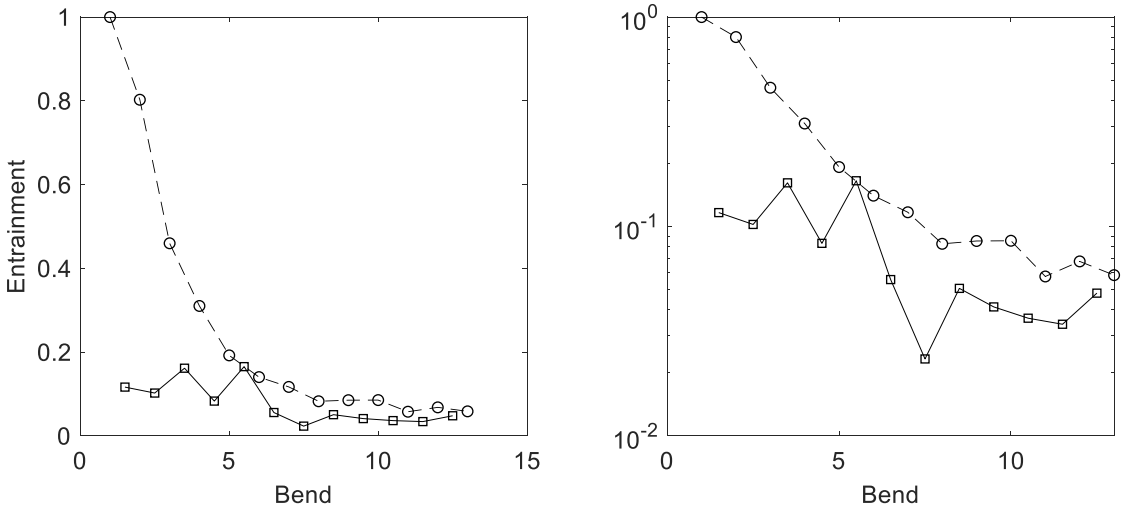

Figure 7.13 Entrainment fluxes for the mid-sinuosity long channel at a 0.5º slope, displayed on linear (left) and logarithmic (right) axes. Two different calculation methods were used (see text). Solid line – method A (7.5); dashed line – method B (7.6).

which are not resolved by method A. Method A is therefore best used in straight channel environments or where data is available at multiple locations around a bend.

The cross-channel basal stress profiles at each bend apex are shown in Figure 7.14. The two flow phases described above are also evident here. As the flow is progressively 'tuned' into conformance with the channel form, the peak intrachannel stress magnitudes migrate from the inner bank to the channel thalweg. From bend 7 onwards the stress profiles remain fairly constant, both in magnitude and shape, with a normal distribution across the channel width. As well as migrating towards the channel thalweg, due to a reduction in lag the peak stress values also migrate upstream from the inflection to the previous bend apex. This is shown in Figure 7.15, where lag is defined as the x coordinate of a bend subtracted from the x coordinate of the respective peak basal stress location, i.e. the further around the bend at which the peak stress occurs, the greater the lag.

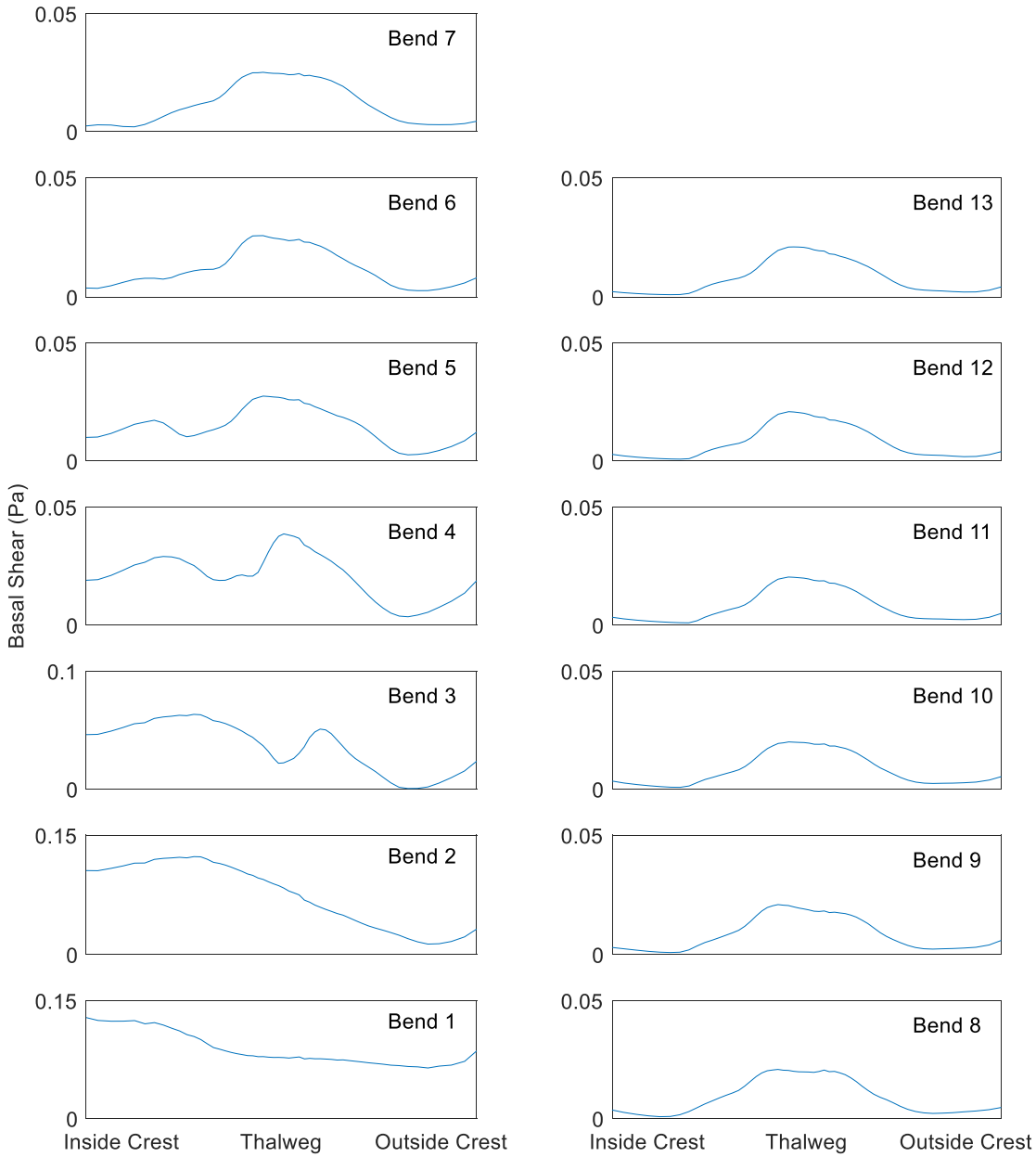

Figure 7.14 Cross-channel profiles of basal shear stress at the bend apexes of the mid-sinuosity channel at a slope of 0.5º. A normal distribution is approached as the current achieves a greater degree of equilibrium with the channel, with the peak stress magnitude migrating from the inner bank to the channel thalweg. Alternate bends are flipped so that the inside bend is always plotted on the left.

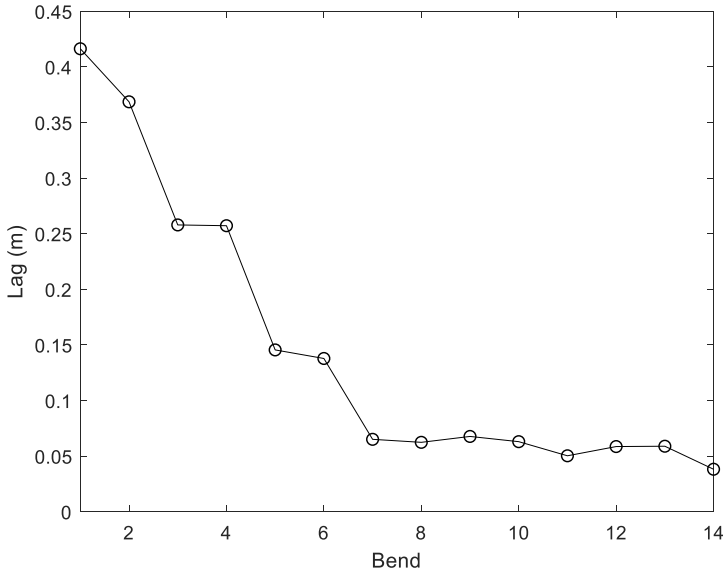

Figure 7.15 The lag of the flow simulated within the extended channel. Lag reduces as the flow is tuned, reaching a quasi-equilibrium after bend 7. Lag is defined as the x coordinate of a bend subtracted from the x coordinate of the respective peak basal stress location, i.e. the further around the bend at which the peak stress occurs, the greater the lag.

7.4 Discussion

7.4.1 Basal stress maps as a tool for flow analysis

The laboratory data described above gives useful insight into flow dynamics and behaviour and have been used extensively throughout this study. However, there are some clear limitations in relying on such data alone. Many person-hours are needed to build up flow datasets of only moderate spatial resolution; the resultant data are necessarily discrete, giving only patchy coverage.

Additionally, for the purposes of basal stress analysis, accurate measurements of near-bed velocities ($z \leq 1$ mm) are challenging to achieve with ADV technology around complex model forms. Whilst the ADV is not affected by basal effects, the difficulty arises in determining the precise position of the probe. Small changes in height (even of

the order of 0.1 mm) can have a large effect on the resultant apparent velocity gradient. This constraint is discussed by Cossu and Wells [2012] in a study of dynamics in the bottom boundary layer of gravity and turbidity currents. When trying to calculate drag coefficients, they found resolution and accuracy of the data was key and calculated values were often far larger or smaller than expected, depending on method of calculation.

The numerical data do not suffer from the issues described above and, if satisfactorily validated, can provide whole flow-field datasets; the advantages of this approach have been previously discussed in Chapter 6. The basal stress maps used throughout this chapter are one such approach that can be pursued using a numerical dataset. They immediately provide both quantitative and qualitative data regarding the interaction between a current and a channel, showing the path of the flow and giving an idea of areas that are likely susceptible to erosion or deposition. Additionally, they can be used to characterise the downstream evolution of a current, highlighting zones where the stress pattern achieves stability from bend to bend. This quasi-equilibrium channel-current interaction state, and how to define it, is discussed further in Section 7.4.4.

Channel morphology evolution has been studied previously in the laboratory by analysing the differences in the initial and final profiles of erodible channels after a series of flows [e.g. Straub et al., 2008; De Leeuw et al., 2016]. Although the channel forms remained fixed in the simulations described here, the use of numerical models to investigate basal stress patterns and create a whole-flow field picture of current-channel interaction represents a significant development and an important new research tool; in principle, this approach could be extended to simulate deposition and erosion, and thus channel morphology evolution (see below).

7.4.2 Model limitations and possible further developments

While describing the advantages of numerical modelling approaches, it is important to be aware of their limitations. For this study, saline gravity currents were used as turbidity

currents proxies for both the laboratory and numerical modelling efforts. The pros and cons of such an approach have been discussed in Chapter 2. The biggest difference is the absence of both particulate deposition and basal sediment entrainment. The modelled flows can therefore be thought of as equivalent to bypassing depositional flow, where the net basal material exchange is zero. With such a condition imposed, it becomes impossible for a flow to attain a true state of equilibrium and by definition it must have a finite lifetime and runout distance. Entrainment of ambient fluid at the flow interface is a continual process and reduces the density of the current. With no method of increasing its density (i.e. basal entrainment), the current will continue to decelerate. Over the length-scales studied here, however, this imbalance does not have a significant effect and the currents can self-maintain.

With sufficient laboratory validation, a future model may be able to include a basal entrainment parameterisation and be able to predict depositional patterns. Furthermore, developing a fully validated model that could directly predict channel evolution (e.g. using active mesh adaptation) would represent a significant development in the field, but currently this is restricted to simple geometries in 2D [e.g. Arfaie, 2015].

7.4.3 Flow tuning and channel sinuosity

Flow tuning is discussed in detail in Chapter 5, with a model presented that shows how a gravity current is capable of adapting to a given channel geometry via two mechanisms: overbank losses (decreasing current magnitude) and ambient entrainment (increasing current magnitude). In this chapter, further evidence of this phenomenon is seen. For the 1 l/s flows, there are rapid changes in both downstream and overbank fluxes over the first few bends of the channel (e.g. Figure 7.6). This is more evident in the high and mid sinuosity channels. There is also evidence for tuning towards an equilibrium state, with convergence of fluxes seen in flows of different magnitudes (Figure 7.10) and the reduction in downstream decay rates in the long channel simulation (Figure 7.12).

A notable feature is the different downstream flux decay rates for the low sinuosity channel compared to the mid and high sinuosity channel (Figure 7.6). This raises the idea of tuning efficiency, or how quickly a channel can tune a flow to an equilibrium state. The low sinuosity downstream fluxes decay at a much slower rate than at higher sinuosities, with the overbank losses remaining constant down the length of the channel. The decay pattern of the downstream fluxes is more linear than the higher sinuosity channels and is more comparable to the flow evolution behaviour of the straight channels in Chapter 5. A channel's tuning efficiency would therefore appear to increase with sinuosity due to larger proximal overbank losses. These observations raise several linked questions:

i. Is flow tuning a continuous function of sinuosity or can different regimes be identified? If the latter:

ii. Is there a threshold sinuosity at which sinuous effects begin or are measurable?

iii. Can a channel's tuning efficiency be too high and does this set an upper limit on sinuosity?

iv. Is channel sinuosity the dominant variable in the flow tuning mechanism?

i) In answering the first, we can examine the fluxes of the different channel sinuosities (Figure 7.6). Overbank losses at the initial bends should increase with the channel sinuosity due to the increase in centrifugal forces and indeed this is observed. However, the differences in the flows traversing the mid and high sinuosity channel are relatively small, leading us to the second question.

ii) The difference in sinuosity between the mid and low sinuosity channels (1.05 compared to 1.01) is smaller than that between the mid and high sinuosity channel (1.05 compared to 1.11), yet the difference in flow evolution character is much more pronounced. The onset of the pronounced effects of curvature must therefore occur over a relatively small sinuosity range. It could be argued that two regimes could be identified based on tuning efficiency: one of straight and low sinuosity channels where the decay of

downstream fluxes is relatively linear, and one of higher sinuosity channels where the effects of curvature actively increase overbank losses leading to an exponential decay. If there is a transitional sinuosity between the two regimes, this leads us to the third question of whether a channel's tuning efficiency can be too high.

iii) If overbank losses are too large, the intrachannel current effectively become extinguished within the first few channel bends if it loses too much of the material that is driving the flow, providing an upper limit on sinuosity. As well as having the effect of destroying a flow, large overbank losses could have significant implications for channel evolution. High shear stress levels are observed overbank for the mid and high sinuosity at the initial bends, which, under the right conditions, could lead to erosion and then channel avulsion, during which the flow breaks through the confines of the levees, ultimately creating a new channel. Avulsions lead to the 'arteries and vein' type structures seen in submarine fans (outlined in Chapter 2). The Congo fan [Savoye et al., 2009] is an example (Figure 7.16). The avulsion nodes, where two channels join, appear to occur more commonly towards the canyon source [Picot et al., 2016]. The combination of both flow and levee destruction (due to excessive flow stripping and high overbank basal stresses in high sinuosity channels) may therefore impose the sinuosity restriction described above. While sinuosity is clearly a primary factor in the linked development of

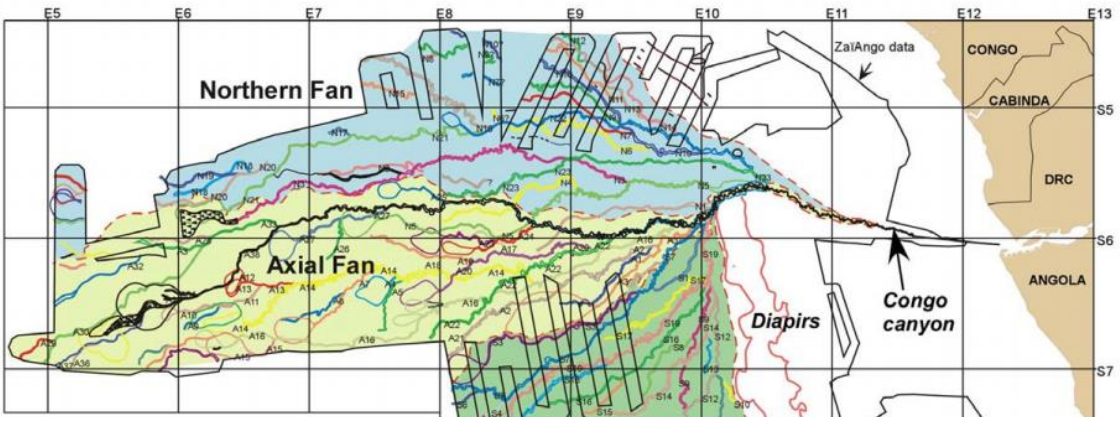

Figure 7.16 Map of the Congo fan off the coast of West Africa from Savoye et al. [2009]. The current active channel is shown in black. Historical channels are shown in other colours, with an apparent bias in the avulsion history towards proximal settings.

channel morphology and flow, it does not appear to be independent of setting, leading us to the fourth and final question posed above.

iv) The evolution of both systems and individual channels is evidently a complex process controlled by a set of variables, including, but not restricted to, the axial slope and system input conditions (e.g. input flow rate and regularity). The effect of both of these has been investigated above, with both having an impact to some degree on flow development while the channel sinuosity remained fixed. An example of this control is the change in proximal behaviour when slope is varied. The high overbank losses and levee basal stresses described above are both significantly lowered when a shallower slope is imposed (Figures 7.7 and 7.8). This could be interpreted as, given a fixed input flow condition, shallower slopes being able to sustain a higher channel sinuosity without flow destruction or channel avulsion. In the field, the link between axial slope and channel sinuosity is a weakly inverse (Figure 7.17), though not universal; Deptuck et al. [2007] observed the opposite on the western Niger Delta slope, with a decrease in sinuosity as the slope increased. As such, channel sinuosity should be seen as a crucial determinant in a turbidity current's dynamics, albeit one that is part of a complex system which ultimately governs a current's flow pattern and the resultant effects on channel evolution.

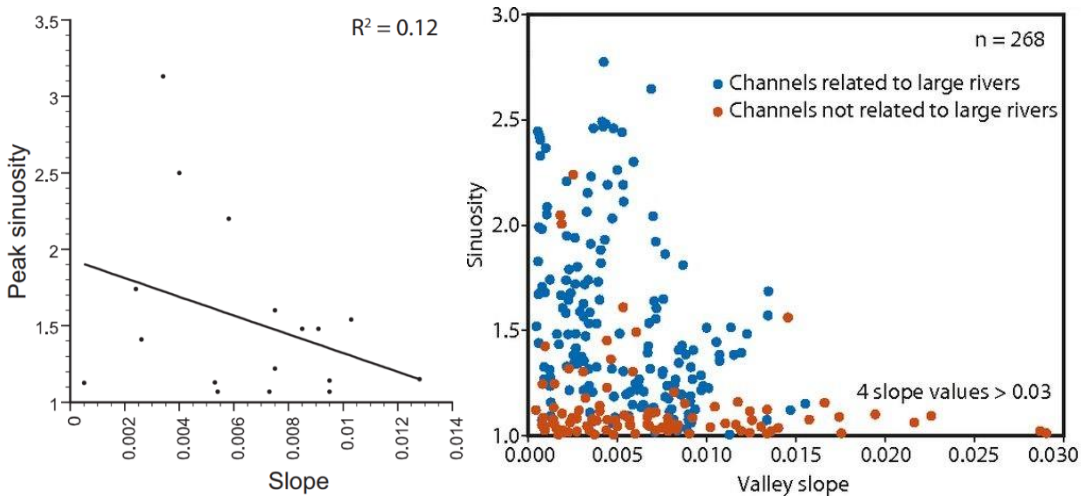

Figure 7.17 Field data from Peakall et al. [2012] and Sylvester et al. [2013]. There is a very weak inverse correlation between channel sinuosity and axial slope.

7.4.4 Current-channel equilibrium

The idea of an equilibrium phase in a submarine channel's development, based upon field observations, is outlined by Peakall et al. [2000] (Figure 7.1). During an equilibrium phase, a channel evolves with relatively little change in its planform and sinuosity. In the previous section a channel's ability to tune a flow to a certain condition was analysed. This process is also discussed in Chapter 5, where a model was proposed that a flow decreases or increases in size, depending on the balance between overbank losses and ambient entrainment, towards an 'equilibrium zone'. As previously noted, it is unlikely that each successive current traversing a channel achieve identical forms. As such, it is probably equally unlikely that an environment as dynamic as a submarine channel achieves a true equilibrium with a completely fixed morphology. In reality, a channel's sinuosity evolution rate may simply stall, decrease, or oscillate around a fixed point. However, such combinations of processes are likely still to result in a deposit history in which channels aggrade with the same overall form, building significant, cumulative thicknesses of thalweg deposits (as noted in Peakall et al. [2000]).

A complex set of variables contributes to channel evolution and determines a channel's equilibrium planform. For example, Peakall et al. [2012] proposed a link between sinuosity and latitude. A trend was identified between a channel's peak sinuosity and its latitudinal position, whereby straighter channels were observed away from the equator. This was attributed to Coriolis forcing, which is more pronounced at higher latitudes. This association was criticised by Sylvester et al. [2013], partly for the use of peak sinuosity, and also by showing firstly that the relationship was arguably not as clear as had been suggested and secondly that Coriolis effects would only impact the largest flows.

Tied to the concept of an equilibrium or quasi-equilibrium stage of channel development is the concept of an equilibrium current. However, defining such a flow type is not straightforward. Nevertheless, in this work we have observed several flows adjusting to an imposed channel geometry and we can attempt to define and identify states of equilibrium. When doing so, there are several attributes to consider:

i) the total downstream flux of a current. The decay rate of the downstream fluxes decreases for the currents simulated here as an equilibrium state is approached. An equilibrium current would be presumed to have a uniform downstream flux. However, for a saline or bypassing current, this is not a possibility as there is no mechanism via which material lost overbank can be replaced. As such, the downstream material flux continually decays for all the currents here; the development of the downstream flux for an equilibrium current is therefore dependent on its erosional vs. depositional nature.

ii) the overbank losses or fluxes of a current. After proximally high overbank losses, some of the currents here achieve constant levels of overspill, namely the flow within the low sinuosity channel (Figure 7.6) and the flow within the long mid sinuosity channel (Figure 7.12). The entrainment flux of the latter flow also reaches an equilibrium (Figure 7.13). This is arguably a reasonable example of the process model outlined in Chapter 5 and described above, whereby a current balances its overbank fluid losses with ambient entrainment and show that at least a quasi-equilibrium has been reached.

iii) the net radial flux of a current. For a partially-confined, overspilling flow in a sinuous channel, this will always be non-zero due to a net loss of fluid over the outer bank. However, for all the currents here, other than that in the low sinuosity channel, the net radial flux continues to decay over the entire length of the channels. It is unclear whether an equilibrium value can be reached, or if it continues to decay due to the continual energy dissipation of the current.

iv) the basal stress patterns. The basal stress maps in this chapter are a key tool in quickly identifying phases of equilibrium. If an equilibrium current is one which maintains the channel planform geometry, then by definition a basal stress pattern which remains unchanged from bend to bend must be a signature of such a flow. Indeed, this is achieved by several of the simulated flows here. Most clearly, it is displayed in the maps for the 0.25 and 0.125 l/s flows (Figure 7.9) and the long channel simulation (Figure 7.11).

The exact definition of an equilibrium current will be dependent on the make-up and deposition characteristics of a flow. Here, an equilibrium phase is most easily identified

in the long channel simulation (Figure 7.11). It is characterised by a repetitive basal stress pattern, a reduction in the decay rate of the downstream fluxes and continual levels of overbank loss and ambient entrainment. Crucially, the cross-channel basal stress profile also approaches a symmetrical, normal distribution, with the peak stress magnitudes focussed on the thalweg at the bend apexes. This combination of attributes can be interpreted as the flow acting neither to increase nor to decrease the channel's sinuosity and would be equivalent to the equilibrium phase described by Peakall et al. [2000]. An illustration of the process of a flow approaching an equilibrium is shown in Figure 7.18. This could happen over two timescales. Over short timescales, individual currents can be

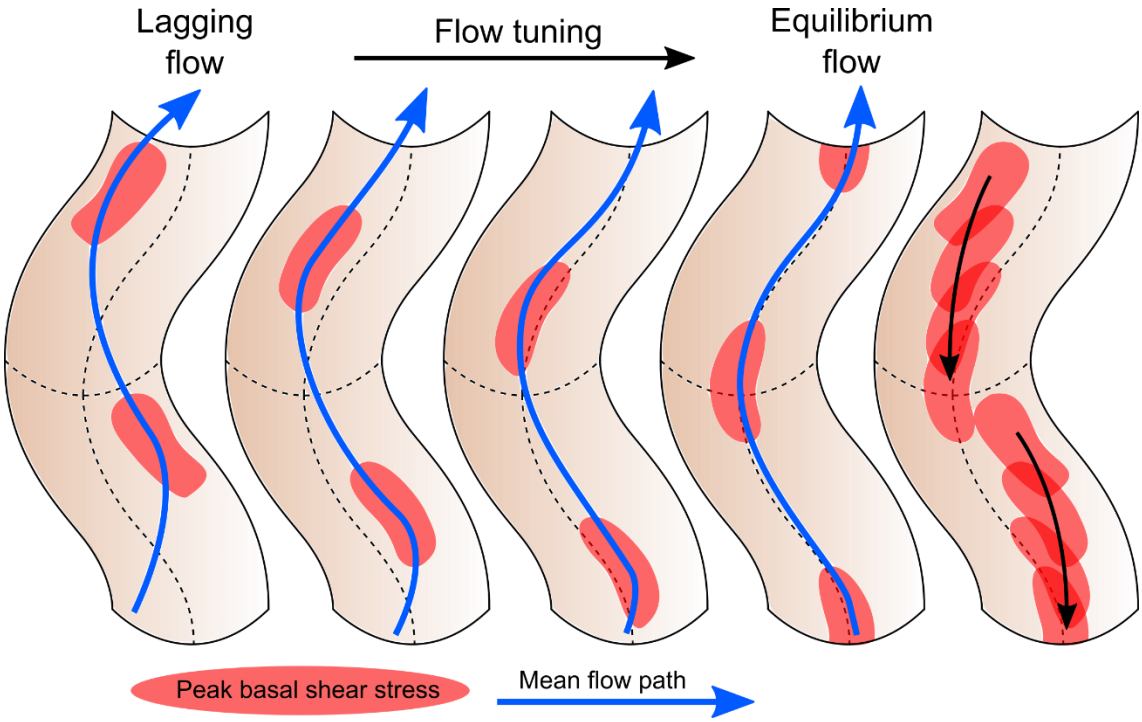

Figure 7.18 A model showing the transition to an equilibrium flow. As a flow is tuned, lag reduces and the position of the peak basal stresses migrates upstream and towards the bend apex. An equilibrium flow has been shown to have a symmetrical cross-channel stress distribution, providing an explanation for how a seafloor channel can achieve a degree of planform stability. Over short timescales, individual currents can be tuned to such an equilibrium state. Over long timescales, successive flows could cause the channel morphology to evolve to a form that allows a flow, with a mean input condition for that system, to be in equilibrium for the entire channel length.

tuned to such an equilibrium state as discussed above. Additionally, over long timescales, successive flows could cause the channel morphology to evolve to a form that allows a flow, with a mean input condition for that system, to be in equilibrium for the entire channel length. For example, proximal levee growth (in the absence of avulsion) could eventually reduce extreme overbank fluid and sediment losses.

An equilibrium current will likely be different for every channel geometry. As previously discussed (Chapter 5), there could also be an 'equilibrium zone' which covers a range of flow magnitudes. There is certainly evidence of different flow evolution behaviours for the different channel sinuosities (Figure 7.6) with the downstream fluxes converging on different values, whereas flows of different initial sizes converge on the same value for a set channel sinuosity (Figure 7.10).

7.4.5 Implications for sedimentary deposits

If they occur in turbidity currents, the processes of flows conforming to channel morphology discussed above would likely have significant implications for the deposits in prototype settings. Firstly, sediments are deposited through the basal flow of a current and thus record conditions there. Anisotropic erosional features and sediment grain fabrics have been used to infer flow orientations from the rock record; such data are commonly used to gain an understanding of ancient systems [e.g. Hiscott et al., 1997; Kane et al., 2010]. Here though, both laboratory and numerical data show how there can be a discrepancy between basal and mean flow directions. In the laboratory there are angular differences of up to 45° between flow 1 and 3 mm above the channel base (Figure 7.3); further, the numerical data show how the pattern of the mean flow magnitude does not always correspond to pattern of basal stresses (see basal stress maps and Section 7.3.2). Care should therefore be taken when interpreting paleoflow data as they may not be a true representation of the mean flow direction, especially at bend apexes where inertial effects dominate

Another interesting outcome of this work is the behaviour of flows with differing input flow rates (Figure 7.10). While the 1, 0.5 and 0.25 l/s flows all converge approximately due to flow tuning, the downstream flux and the peak intrachannel stress magnitudes at the final bend are larger under the smaller 0.25 and 0.125 l/s flows. It follows that the deposition records at the distal channel reaches and terminal lobes may not reflect the input conditions and proximal flow of a system. Smaller initial flows may even be responsible for the majority of sediment deposited within the channel confines and transported to the channel terminals, although this may depend in part on their suspension capacity, which was not modelled in this work. Additionally, the occurence of flow tuning implies that homogeneity of deposits should increase downstream, with far greater variations in grain size and sequence thicknesses in proximal settings. The large variations in levee stress pattern also suggest degrees of heterogeneity in overbank deposits, with most material lost and therefore on the outside levees of bends.

As is the case for smaller initial inputs, flows in channels with a shallower axial slope appear able to maintain a higher downstream flux (Figure 7.10). However, this must be balanced with such a flow having a lesser capacity for suspension (Section 2.1.1) which is not reflected in these simulations. It has been previously proposed that channels may evolve to maintain an equilibrium gradient [Pirmez et al., 2000; Kneller, 2003]. As has been discussed above, however, the commonly cited correlation between slope and sinuosity is actually weak [Peakall et al., 2012; Sylvester et al., 2013] and the opposite correlation has also been observed [Deptuck et al., 2007; Gee et al., 2007]. It remains unclear as to what precisely drives a channel's initial sinuosity development phase and whether slope is a determining factor. Channel inception following the passage of initially unconfined turbidity currents has been recently been successfully demonstrated in the laboratory [De Leeuw et al., 2016], resulting in the creation of straight channels. It is possible that some initial perturbation to the system is required to initially trigger meander development, such as topographic irregularities that are not present on a smooth laboratory slope. Whether the steepness of such a slope determines the final sinuosity is

debateable. The basal stress patterns of differing slopes presented here (Figure 7.7) certainly differ in magnitude, but the path of the flow within the channel and the areas of high and low stresses are essentially similar. It may be that channels on differing slopes evolve in similar ways but at varying rates.

One noticeable difference between the flows on differing slopes is the distribution of outer bank basal stress; more pronounced areas of lower stresses were observed at the outer banks on a 0.5° slope than on a 2° slope (Figure 7.7). In the results section the link was drawn between these and the outer bank deposits, or nested mounds, that are unique to submarine channels. Kane et al. [2008] observe that preference for inner vs. outer bank deposition is dependent on the level of flow bypass. The data presented here suggests that a combination of bypass, slope and degree of flow adaptation to channel form could determine depositional locations. As noted above, an equilibrium phase can be identified by a normal cross-channel stress distribution. Therefore, as Kane et al. [2008] hypothesised, flows with varying capacities could fluctuate between inner and outer bank deposition, with erosion centred on the thalweg, leading to increased channel stability. This variation in deposition location is markedly different to the processes seen in fluvial systems, where deposition continually occurs on the inner bank and erosion on the outer bank.

7.5 Conclusions

A variety of approaches has been used to examine the downstream evolution patterns of gravity currents partially-confined within a submarine channel. The effects of changes in slope, channel sinuosity and input flow rate have been investigated.

Numerical simulations have been used to create maps of basal stress for a range of flows. Such maps are a previously unused tool in this field and give a clear picture of a current's interaction with its containing channel. In combination with downstream, overbank and radial flux analysis, the maps have enabled the identification of two principal phases of

flow. Initially, flow tuning occurs, whereby a current undergoes a transformation towards a more stable flow state. This transformation process can occur via overbank losses and ambient entrainment. The stable flow state represents the equilibrium phase. This is characterised by constant levels of overspill and entrainment and a reduction in the decay rate of the downstream flux. Furthermore, the basal stress pattern becomes relatively invariant from bend to bend, with cross-channel stress profiles showing a normal distribution and peak stresses occurring at the bend apexes.

These processes have important implications for the sedimentary deposits of a turbidity currents. The equilibrium phase of a flow reveals how, unlike in fluvial settings, a seafloor channel is capable of maintaining a constant planform, with thalweg centred erosion and deposition possible at both inner and outer banks. Additionally, differences in the basal and mean flow directions, seen both in the laboratory and simulations, mean flow analysis using paleocurrent data should be interpreted with caution. Finally, distal and lobe deposits may not truly reflect the full flow history or input conditions of a system, with increased homogeneity downstream due to flow tuning.

Chapter 8

Conclusions

This thesis has focussed on the fluid dynamics of density driven flows, partially-confined within submarine channels. The interaction between current and channel is dominated by a complex feedback system. As described in Chapter 1 this feedback operates at two timescales: at the scale of individual flows, the flow field is modulated due to flow through the channel form; over longer timescales, the combined depositional and erosional impact of large numbers of successive flows modulates the channel morphology. The primary aim of this work was to characterise the control of the submarine channel form on the flow field of turbidity currents, with focus on the development of intrachannel flow structure and on downstream flow evolution. A combined laboratory and numerical approach was employed. The findings are summarised in the following sections.

8.1 Intrachannel flow structure

A turbidity current's confining channel is a primary control on the structure of the flow [Kassem and Imran, 2004; Keevil et al., 2006; Islam et al., 2008; Ezz and Imran 2014]. However, previous studies focussing on flow dynamics have used channel with unrealistic geometries. In this work, the aim was to investigate the effect of a partially-confining channel, with both internal and external profiles representative of natural morphology, on the dynamics of a continuous gravity current. Experiments conducted in the Sorby Environmental Fluid Dynamics Laboratory measured the velocity and density of such flows. Numerical simulations employing a Reynolds-averaged Navier-Stokes (RANS) based approach were used to extend the domain space and to analyse variables such as pressure and basal stress that are not easily measurable in the laboratory.

Several flow controls were identified that have previously not been recognised. Firstly, in Chapter 5, it was shown that channel form is a principal factor in determining a flow's vertical structure and in particular that it can dictate the height of the velocity maximum. In the experiments conducted here, the channel half-depth acted as an upper limit on this height; an increase of an order of magnitude of input flow rate, and a resultant 70% increase in the flow height, did not lead to any significant change in the velocity maximum height. Numerical simulations enabled the study of larger flows than are feasible in the laboratory. The same upper limit was identified, even for these larger flows, suggesting channel is the principal control on vertical structure (cf. the current preferred interpretation that this is controlled by Froude number [e.g. Sequeiros et al., 2010] or Reynolds number [Stagnaro and Pittaluga, 2014]). The ability of a channel to limit the height of a flow's velocity maximum enables it to maintain a confined high-velocity core, perhaps providing an explanation for the long runout distances documented for turbidity currents [Klaucke et al., 1998; Talling et al., 2013].

Secondly, in addition to having a control on vertical structure, the geometry of a channel is capable of determining a flow's lateral structure and dynamics. Chapter 6 analysed secondary flow fields in sinuous channels. Turbidity currents traversing such channels can form a helical structure [e.g. Kassem and Imran, 2004; Keevil et al., 2006; Sumner et al., 2014], which may have significant implications for both channel and flow development [Pirmez and Imran, 2003; Keevil et al., 2006; Dorrell et al., 2013]. It has been shown previously that a partially-confined environment can alter this structure in comparison to a fully-confined environment [Kassem and Imran, 2004; Islam et al., 2008; Ezz and Imran 2014]. Furthermore, there has been much debate over the mechanisms governing the sense of rotation of the helical structure with respect to the channel bend morphology [e.g. Keevil et al., 2006; Abad et al., 2011; Dorrell et al., 2013; Bolla Pittaluga 2014a,b; Peakall et al., 2014]. Here, the channel geometry is shown to be a first order control on secondary flow; a change in the cross-sectional profile is capable of effectively switching the dominant basal flow direction and thus the sense of rotation.

Further findings concerning the helical structure of a turbidity current were made. Both large levels of overbank fluid losses and low channel sinuosities inhibited the formation of such structures altogether. It has been hypothesised that secondary flow rotation is an important mechanism in the suspension of sediment and maintaining autosuspension [Keevil et al., 2006; Straub et al., 2008]. However, the existence of long, low sinuosity channels, such as the North Atlantic Mid Ocean Channel, where helical flow may be suppressed, suggests that other factors are involved. A channel's ability to maintain a high-velocity core, as described above, could be one such factor.

In higher sinuosity channels, as described above, helical structures and secondary rotational cells of both orientations (i.e. river-like, with basal flow directed towards the inner bend, and river-reversed) were observed, depending on channel geometry. It has been postulated that this rotation is driven by the balance of centrifugal forces and pressure gradients of the intrachannel flow [Abad et al., 2011; Dorrell et al., 2013]. In this study, secondary rotational cells are confirmed to be characterised by a local reversal in the radial pressure gradient. Furthermore, while vertically stacked cells have been previously recognised [Imran et al., 2007], here horizontally stacked cells have also been observed in the transition between bends; both cases can result in a similar vertical cross-stream velocity profile at the thalweg, which has implications for the interpretation of field data.

In summary, it has been shown that the morphometric attributes of submarine channels play a critical role in determining the dynamics and structure of turbidity currents. In particular, channel depth and cross-sectional profiles are key controls on the vertical structure and secondary dynamics of a flow, respectively.

8.2 Downstream flow evolution

The evolution of a turbidity current as it traverses a channel has both short-term implications for individual deposits and flow runout and long-term implications for the

development of the channel system itself. The passage of successive flows determines individual channel evolution patterns and eventually leads to avulsion and the evolution of the system. By analysing downstream changes in both flow fluxes and basal shear stress patterns the evolution of saline gravity currents in channels of different sinuosities has been investigated. A simplified model has been proposed of the processes by which flow magnitude is 'tuned' to a channel's specific geometry, the subsequent adjustments in flow characteristics and the implications this has for a channel's development.

Two mechanisms underly a gravity current's downstream evolution in a partially-confined setting, overbank losses (or overspill) and the entrainment of ambient fluid. Figure 8.1, a model proposed in Chapter 5, shows how differences in the ratios of these mechanisms means a flow may approach an equilibrium condition whereby fluid gains and losses are balanced. This phenomenon was examined in greater detail in Chapter 7, where it was confirmed that a channel has the ability to tune a flow to a stable set of conditions, or a quasi-equilibrium state. Figure 8.2 shows a model of a proposed

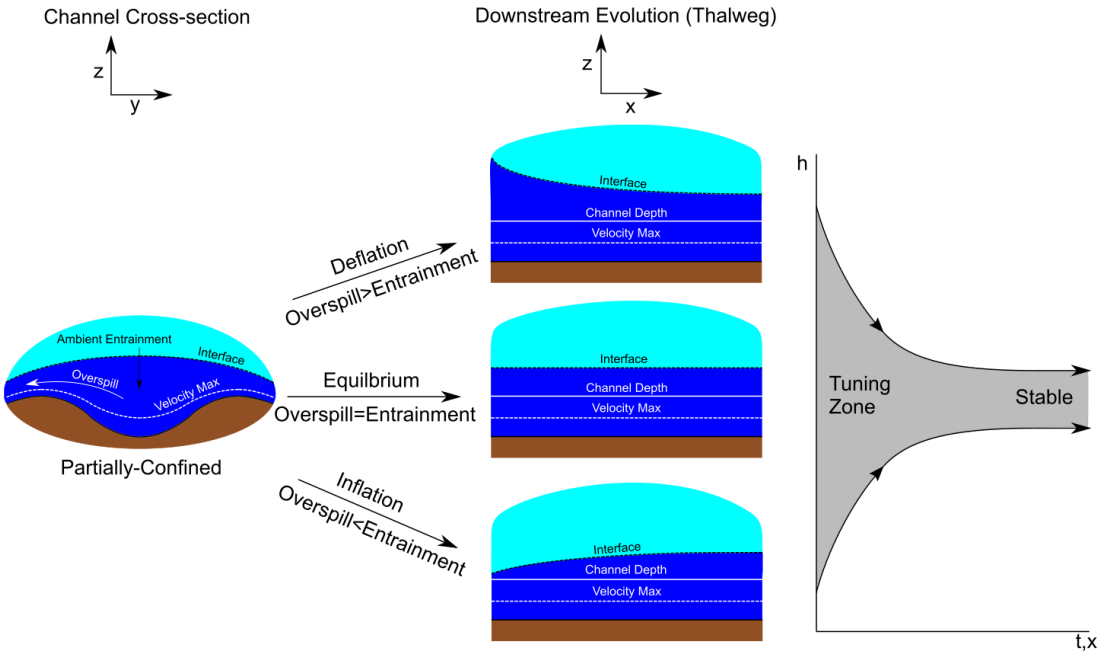

Figure 8.1 A model of the possible downstream evolution patterns of a partially-confined gravity current, originally proposed in Chapter 5. A combination of overbank losses and ambient entrainment can result in a current 'tuning' towards a stable, quasi-equilibrium state.

developmental sequence via which a flow in a sinuous channel can approach equilibrium, with the mean flow path mirroring that of the channel thalweg and peak basal stresses occurring at the bend apexes.

The quasi-equilibrium states identified were characterised by a reduction in the decay rates of downstream, overbank and entrainment fluxes. Additionally, the basal stress pattern of a flow becomes relatively invariant from bend to bend and, significantly, the cross-channel basal stress profile approaches a symmetrical, normal distribution. The implications for channel development are significant. This state of interaction between current and channel supports the theory that a submarine channel can undergo a period of relative stability, during which there is no substantial change in its planform [Peakall et al., 2000].

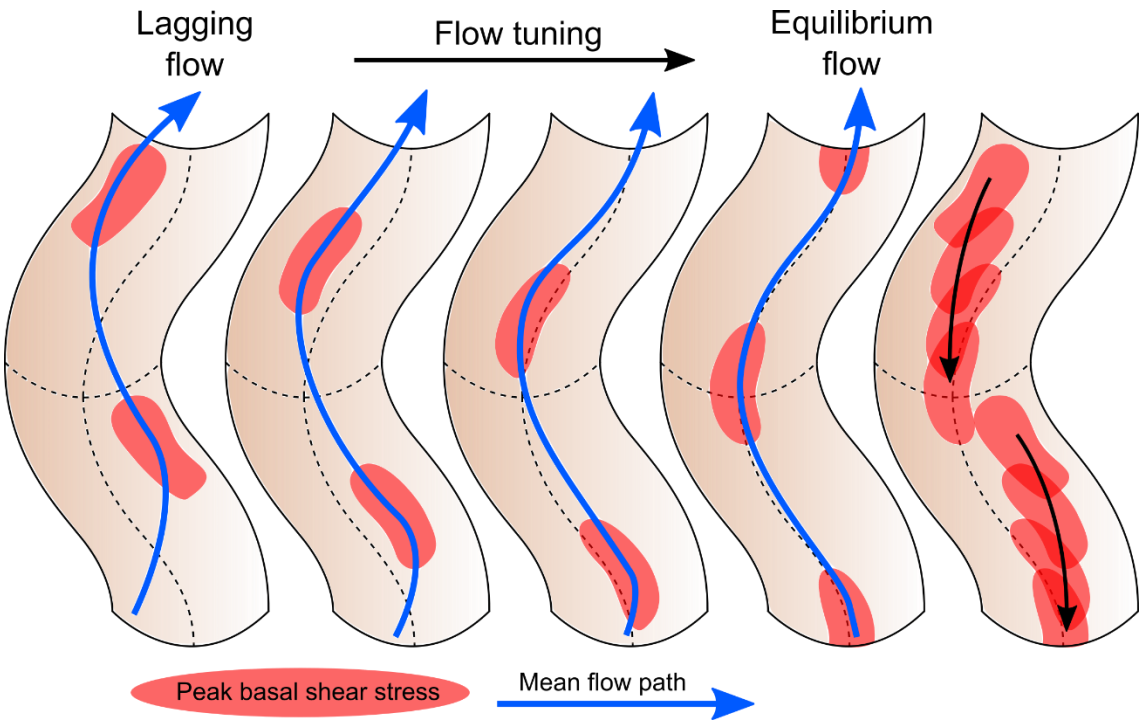

Figure 8.2 A model of a partially-confined gravity current transitioning towards a quasi-equilibrium state, originally proposed in Chapter 7. In this study, this state is characterised by symmetrical cross-channel basal stress profiles at the bend apexes and a mean flow path mirroring the channel thalweg.

There are still questions over the long time-scale consequences of large numbers of successive flows for the evolution of the channel form. While an ‘equilibrium pattern’ of basal stress could theoretically maintain a certain channel sinuosity or planform, a differential intra- to extra-channel distribution of deposition must have implications for the long-term channel stability. Dorrell et al. [2015] modelled this stability problem, concluding that channels, under aggradational conditions, are inherently unstable and will at some point avulse due to autogenic (internal-forced) channel narrowing. However, their 2D analysis did not account for streamwise variations in net aggradational rates, which here are shown to be present, and likely important, in channel development.

Additionally, a difference is observed in the evolution characteristics of flows in straight and low sinuosity channels and flows in more sinuous channels. The effects of channel curvature on the lateral flow field and levels of overbank loss result in an exponential rather than linear downstream decay rate of streamwise fluxes. However, the processes governing the initial sinuosity growth and expansion of these straighter channels are still not fully understood.

8.3 Summary

A flow’s intrachannel dynamics and structure and its downstream evolution patterns are inextricably linked; this study has shown that the morphology of the confining channel exerts a significant control on both. Providing a conduit for flow, partial-confinement within a seafloor channel helps facilitate the long runout distances that turbidity currents are capable of. Through the tuning of flow magnitudes and intrachannel velocity distributions, a turbidity current will experience limited inflation, maintaining a high-velocity core. A degree of flow conformity with the channel is also a requirement for the development of the helical flow structures that have been observed both in the laboratory and in the field. The sense of rotation of these structures is shown to be dependent on channel morphology. Finally, the flow tuning process has been shown to result in the

development of flows whose character could help stabilise and maintain a channel's planform geometry.

8.4 Topics for future research

This study has provided new insights into flow dynamics within seafloor channels but also indicated areas where insight is lacking. Below, further areas of research are highlighted which could build upon the findings here.

The experiments and simulations conducted for this work used a channel model with a profile more representative of field morphology than previous studies. However, further improvements could still be made in this area. Large levels of proximal overspill were observed for many of the modelled flows. While this illustrates the flow stripping and tuning mechanisms well, such processes may lead to levee erosion and subsequent channel avulsion. Alternatively, successions of overspilling sediment-laden flows could lead to levee build up and channel asymmetry with a larger confining levee on the outer banks of bends. To study the latter effect, cross-channel imbalances in channel depth and levee height could be paired with a downstream decay profile, with the channel getting shallower downstream as the flows streamwise fluxes decrease. The main challenge posed by this approach would be scaling such a model. Furthermore, the scope of the experiments here was limited by flume size. The ability to measure data at more distal bends could give further insights into broader patterns of flow development and the long-term evolution of channel morphology.

There is an opportunity to build upon and improve the numerical model used here. Incorporating sediment transport would allow the prediction of flows' depositional patterns. This would require the modelling of not only particulate suspension but also basal entrainment, perhaps via the use of a shear-dependent boundary source term. It would also require further validation against depositional laboratory flows in order to evaluate model accuracy. Incorporation of sediment transport, deposition and erosion into

the numerical modelling approach would overcome the limitation of this study in relying exclusively on basal stress to interpret current-channel interaction.

Development of a sediment transport model as described above would be a logical step in progression towards a model with a deforming bottom boundary, capable of explicitly predicting channel evolution. This would be a valuable tool in the study of seafloor channel development. Such models have been developed in two dimensions [e.g. Arfaie, 2015] but even these simplified cases suffer from technical limitations. Perhaps the most significant outstanding challenge is to develop a three-dimensional numerical model capable of accurately predicting changes in substrate morphology, whether that be at the larger scales of channel form or the smaller scale of bedforms and scours.

References

Abad, J.D., Sequeiros, O.E., Spinewine, B., Pirmez, C., Garcia, M.H. and Parker, G., 2011. Secondary current of saline underflow in a highly meandering channel: experiments and theory. *Journal of Sedimentary Research*, *81*(11), pp.787-813.

Abd El-Gawad, S., Cantelli, A., Pirmez, C., Minisini, D., Sylvester, Z. and Imran, J., 2012. Three-dimensional numerical simulation of turbidity currents in a submarine channel on the seafloor of the Niger Delta slope. *Journal of Geophysical Research: Oceans*, *117*(C5).

Altinakar, M.S., Graf, W.H. and Hopfinger, E.J., 1996. Flow structure in turbidity currents. *Journal of Hydraulic Research*, *34*(5), pp.713-718.

Amos, K.J. and Peakall, J., 2006. Down by the river. *Planet Earth*.

Anka, Z., Seranne, M., Lopez, M., Scheck-Wenderoth, M. and Savoye, B., 2009. The long-term evolution of the Congo deep-sea fan: A basin-wide view of the interaction between a giant submarine fan and a mature passive margin (ZaiAngo project). *Tectonophysics*, *470*(1-2), pp.42-56.

Aoki, I., Kurosaki, Y., Osada, R., Sato, T. and Kimura, F., 2005. Dust storms generated by mesoscale cold fronts in the Tarim Basin, Northwest China. *Geophysical Research Letters*, *32*(6).

Arfaie, A., 2015. Numerical Modelling of the Influence of Lower Boundary Roughness on Turbulent Sedimentary Flows (Doctoral dissertation, University of Leeds).

Ashida, K. and Egashira, S., 1975, May. Basic study on turbidity currents. *Proceedings of the Japan Society of Civil Engineers*, 237, pp. 37-50.

Azpiroz-Zabala, M., Cartigny, M.J., Sumner, E.J., Clare, M.A., Talling, P.J., Parsons, D.R. and Cooper, C., 2017. A general model for the helical structure of geophysical flows in channel bends. *Geophysical research letters*, *44*(23).

Azpiroz-Zabala, M., Cartigny, M.J., Talling, P.J., Parsons, D.R., Sumner, E.J., Clare, M.A., Simmons, S.M., Cooper, C. and Pope, E.L., 2018. Newly recognized turbidity current structure can explain prolonged flushing of submarine canyons. *Science advances*, *3*(10), pp. 170-200.

Babonneau, N., Savoye, B., Cremer, M. and Bez, M., 2010. Sedimentary architecture in meanders of a submarine channel: detailed study of the present Congo turbidite channel (Zaiango project). *Journal of Sedimentary Research*, *80*(10), pp.852-866.

Bagnold, R.A., 1962. Auto-suspension of transported sediment; turbidity currents. *Proc. R. Soc. Lond. A*, *265*(1322), pp.315-319.

Benjamin, T.B., 1968. Gravity currents and related phenomena. *Journal of Fluid Mechanics*, *31*(2), pp.209-248.

Birman, V.K., Meiburg, E. and Kneller, B., 2009. The shape of submarine levees: exponential or power law? *Journal of Fluid Mechanics*, *619*, pp.367-376.

Blanchette, F., Piche, V., Meiburg, E. and Strauss, M., 2006. Evaluation of a simplified approach for simulating gravity currents over slopes of varying angles. *Computers & Fluids*, *35*(5), pp.492-500.

Bolla Pittaluga, M. and Imran, J., 2014a. A simple model for vertical profiles of velocity and suspended sediment concentration in straight and curved submarine channels. *Journal of Geophysical Research: Earth Surface*, *119*(3), pp.483-503.

Bolla Pittaluga, M., Imran, J. and Parker, G., 2014b. Reply to comment by J. Peakall et al. on “A simple model for vertical profiles of velocity and suspended sediment concentration in straight and curved submarine channels”. *Journal of Geophysical Research: Earth Surface*, *119*(9), pp.2074-2078.

Bonnecaze, R.T., Huppert, H.E. and Lister, J.R., 1993. Particle-driven gravity currents. *Journal of Fluid Mechanics*, *250*, pp.339-369.

Bouma, Arnold H., William R. Normark, and Neal E. Barnes. *Submarine fans and related turbidite systems*. Springer Science & Business Media, 2012.

Bournet, P.E., Dartus, D., Tassin, B. and Vincon-Leite, B., 1999. Numerical investigation of plunging density current. *Journal of Hydraulic Engineering*, *125*(6), pp.584-594.

Boussinesq, J., 1877. *Essai sur la théorie des eaux courantes*. Impr. nationale.

Breard, E.C., Lube, G., Jones, J.R., Dufek, J., Cronin, S.J., Valentine, G.A. and Moebis, A., 2016. Coupling of turbulent and non-turbulent flow regimes within pyroclastic density currents. *Nature Geoscience*, *9*(10), p.767.

Brørs, B. and Eidsvik, K.J., 1992. Dynamic Reynolds stress modeling of turbidity currents. *Journal of Geophysical Research: Oceans*, *97*(C6), pp.9645-9652.

Buckee, C., Kneller, B. and Peakall, J., 2001. Turbulence structure in steady, solute-driven gravity currents. *Particulate Gravity Currents, IAS Spec. Publ., 31*, pp.173–187.

Cantero, M.I., Lee, J.R., Balachandar, S. and Garcia, M.H., 2007. On the front velocity of gravity currents. *Journal of Fluid Mechanics*, *586*, pp.1-39.

Cantero, M.I., Balachandar, S., García, M.H. and Bock, D., 2008. Turbulent structures in planar gravity currents and their influence on the flow dynamics. *Journal of Geophysical Research: Oceans*, *113*(C8).

Cantero, M.I., Balachandar, S., Cantelli, A., Pirmez, C. and Parker, G., 2009. Turbidity current with a roof: Direct numerical simulation of self-stratified turbulent channel flow driven by suspended sediment. *Journal of Geophysical Research: Oceans*, *114*(C3).

Charba, J., 1974. Application of gravity current model to analysis of squall-line gust front. *Monthly Weather Review*, *102*(2), pp.140-156.

Chen, G.Q. and Lee, J.H.W., 1999. Turbulent gravity current of lock release type: A numerical study. *Communications in Nonlinear Science and Numerical Simulation*, *4*(1), pp.20-24.

Choi, S.U. and Garcia, M.H., 2002. k-ε turbulence modeling of density currents developing two dimensionally on a slope. *Journal of Hydraulic Engineering*, *128*(1), pp.55-63.

Clark, J.D., Kenyon, N.H. and Pickering, K.T., 1992. Quantitative analysis of the geometry of submarine channels: implications for the classification of submarine fans. *Geology*, *20*(7), pp.633-636.

Conway, K.W., Barrie, J.V., Picard, K. and Bornhold, B.D., 2012. Submarine channel evolution: active channels in fjords, British Columbia, Canada. *Geo-Marine Letters*, *32*(4), pp.301-312.

Cossu, R. and Wells, M.G., 2010. Coriolis forces influence the secondary circulation of gravity currents flowing in large-scale sinuous submarine channel systems. *Geophysical Research Letters*, *37*(17).

Cossu, R. and Wells, M.G., 2012. A comparison of the shear stress distribution in the bottom boundary layer of experimental density and turbidity currents. *European Journal of Mechanics-B/Fluids*, *32*, pp.70-79.

Cossu, R., Wells, M.G. and Peakall, J., 2015. Latitudinal variations in submarine channel sedimentation patterns: the role of Coriolis forces. *Journal of the Geological Society*, *172*(2), pp.161-174.

Covault, J.A., Fildani, A., Romans, B.W. and McHargue, T., 2011. The natural range of submarine canyon-and-channel longitudinal profiles. *Geosphere*, *7*(2), pp.313-332.

Curray, J.R., Emmel, F.J. and Moore, D.G., 2002. The Bengal Fan: morphology, geometry, stratigraphy, history and processes. *Marine and Petroleum Geology*, *19*(10), pp.1191-1223.

Cuthbertson, A.J.S., Lundberg, P., Davies, P.A. and Laanearu, J., 2014. Gravity currents in rotating, wedge-shaped, adverse channels. *Environmental Fluid Mechanics*, *14*(5), pp.1251-1273.

Cuthbertson, A., Laanearu, J., Carr, M., Sommeria, J. and Viboud, S., 2018. Blockage of saline intrusions in restricted, two-layer exchange flows across a submerged sill obstruction. *Environmental Fluid Mechanics*, *18*(1), pp.27-57.

Daly, R.A., 1936. Origin of submarine canyons. *American Journal of Science*, (186), pp.401-420.

Daly, B.J. and Pracht, W.E., 1968. Numerical study of density-current surges. *The Physics of Fluids*, *11*(1), pp.15-30.

Das, H.S., Imran, J., Pirmez, C. and Mohrig, D., 2004. Numerical modeling of flow and bed evolution in meandering submarine channels. *Journal of Geophysical Research: Oceans*, *109*(C10).

De Leeuw, J., Eggenhuisen, J.T. and Cartigny, M.J., 2016. Morphodynamics of submarine channel inception revealed by new experimental approach. *Nature communications*.

De Rooij, F. and Dalziel, S., 2001. Time-and space-resolved measurements of deposition under turbidity currents. *Particulate Gravity Currents, Wiley, New York*, pp.207-215.

Deptuck, M.E., Sylvester, Z., Pirmez, C. and O'Byrne, C., 2007. Migration–aggradation history and 3-D seismic geomorphology of submarine channels in the Pleistocene Benin-major Canyon, western Niger Delta slope. *Marine and Petroleum Geology*, *24*(6-9), pp.406-433.

Doronzo, D.M., 2013. Aeromechanic analysis of pyroclastic density currents past a building. *Bulletin of volcanology*, *75*(1), p.684.

Dorrell, R.M., Darby, S.E., Peakall, J., Sumner, E.J., Parsons, D.R. and Wynn, R.B., 2013. Superelevation and overspill control secondary flow dynamics in submarine channels. *Journal of Geophysical Research: Oceans*, *118*(8), pp.3895-3915.

Dorrell, R.M., Darby, S.E., Peakall, J., Sumner, E.J., Parsons, D.R. and Wynn, R.B., 2014. The critical role of stratification in submarine channels: Implications for

channelization and long runout of flows. *Journal of Geophysical Research: Oceans*, *119*(4), pp.2620-2641.

Dorrell, R.M., Burns, A.D. and McCaffrey, W.D., 2015. The inherent instability of leveed seafloor channels. *Geophysical Research Letters*, *42*(10), pp.4023-4031.

Dorrell, R.M., Peakall, J., Sumner, E.J., Parsons, D.R., Darby, S.E., Wynn, R.B., Özsoy, E. and Tezcan, D., 2016. Flow dynamics and mixing processes in hydraulic jump arrays: Implications for channel-lobe transition zones. *Marine Geology*, *381*, pp.181-193.

Dorrell, R.M., Peakall, J., Burns, C. and Keevil, G.M., 2018a. A novel mixing mechanism in sinuous seafloor channels: Implications for submarine channel evolution. *Geomorphology*, *303*, pp.1-12.

Dorrell, R.M., Amy, L.A., Peakall, J. and McCaffrey, W.D., 2018b. Particle size distribution controls the threshold between net sediment erosion and deposition in suspended load dominated flows. *Geophysical Research Letters*, *45*(3), pp.1443-1452.

Dufek, J., 2016. The fluid mechanics of pyroclastic density currents. *Annual Review of Fluid Mechanics*, *48*, pp.459-485.

Eggenhuisen, J.T. and McCaffrey, W.D., 2012. The vertical turbulence structure of experimental turbidity currents encountering basal obstructions: implications for vertical suspended sediment distribution in non-equilibrium currents. *Sedimentology*, *59*(3), pp.1101-1120.

Eidsvik, K.J. and Brørs, B., 1989. Self-accelerated turbidity current prediction based upon (k-ε) turbulence. *Continental Shelf Research*, *9*(7), pp.617-627.

Ellison, T.H. and Turner, J.S., 1959. Turbulent entrainment in stratified flows. *Journal of Fluid Mechanics*, *6*(3), pp.423-448.

Ezz, H., Cantelli, A. and Imran, J., 2013. Experimental modeling of depositional turbidity currents in a sinuous submarine channel. *Sedimentary Geology*, *290*, pp.175-187.

Ezz, H. and Imran, J., 2014. Curvature-induced secondary flow in submarine channels. *Environmental Fluid Mechanics*, *14*(2), pp.343-370.

Felix, M., Sturton, S. and Peakall, J., 2005. Combined measurements of velocity and concentration in experimental turbidity currents. *Sedimentary Geology*, *179*(1-2), pp.31-47.

Felix, M. and Peakall, J., 2006. Transformation of debris flows into turbidity currents: mechanisms inferred from laboratory experiments. *Sedimentology*, *53*(1), pp.107-123.

Foreman, B.Z., Lai, S.Y., Komatsu, Y. and Paola, C., 2015. Braiding of submarine channels controlled by aspect ratio similar to rivers. *Nature Geoscience*, *8*(9), p.700.

Galy, V., France-Lanord, C., Beyssac, O., Faure, P., Kudrass, H. and Palhol, F., 2007. Efficient organic carbon burial in the Bengal fan sustained by the Himalayan erosional system. *Nature*, *450*(7168), p.407.

García, M.H., 1993. Hydraulic jumps in sediment-driven bottom currents. *Journal of Hydraulic Engineering*, *119*(10), pp.1094-1117.

Garcia, M. and Parker, G., 1993. Experiments on the entrainment of sediment into suspension by a dense bottom current. *Journal of Geophysical Research: Oceans*, *98*(C3), pp.4793-4807.

Garcia, M.H., 1994. Depositional turbidity currents laden with poorly sorted sediment. *Journal of hydraulic engineering*, *120*(11), pp.1240-1263.

Gardner, J.V., 2010. The West Mariana Ridge, western Pacific Ocean: Geomorphology and processes from new multibeam data. *Bulletin*, *122*(9-10), pp.1378-1388.

Gauer, P., Kvalstad, T.J., Forsberg, C.F., Bryn, P. and Berg, K., 2005. The last phase of the Storegga Slide: simulation of retrogressive slide dynamics and comparison with slide-scar morphology. In *Ormen Lange–an Integrated Study for Safe Field Development in the Storegga Submarine Area* (pp. 171-178).

Gee, M.J.R., Gawthorpe, R.L., Bakke, K. and Friedmann, S.J., 2007. Seismic geomorphology and evolution of submarine channels from the Angolan continental margin. *Journal of Sedimentary Research*, *77*(5), pp.433-446.

Giorgio Serchi, F., Peakall, J., Ingham, D.B. and Burns, A.D., 2011. A unifying computational fluid dynamics investigation on the river-like to river-reversed secondary circulation in submarine channel bends. *Journal of Geophysical Research: Oceans*, *116*(C6).

Gray, T.E., Alexander, J. and Leeder, M.R., 2005. Quantifying velocity and turbulence structure in depositing sustained turbidity currents across breaks in slope. *Sedimentology*, *52*(3), pp.467-488.

Guo, Y., Zhang, Z. and Shi, B., 2014. Numerical simulation of gravity current descending a slope into a linearly stratified environment. *Journal of Hydraulic Engineering*, *140*(12), p.04014061.

Hacker, J., Linden, P.F. and Dalziel, S.B., 1996. Mixing in lock-release gravity currents. *Dynamics of Atmospheres and Oceans*, *24*(1-4), pp.183-195.

Härtel, C., Meiburg, E. and Necker, F., 2000a. Analysis and direct numerical simulation of the flow at a gravity-current head. Part 1. Flow topology and front speed for slip and no-slip boundaries. *Journal of Fluid Mechanics*, *418*, pp.189-212.

Härtel, C., Carlsson, F. and Thunblom, M., 2000b. Analysis and direct numerical simulation of the flow at a gravity-current head. Part 2. The lobe-and-cleft instability. *Journal of Fluid Mechanics*, *418*, pp.213-229.

Heezen, B.C. and Ewing, M., 1952. Turbidity currents and submarine slumps, and the 1929 Grand Banks earthquake. *American journal of Science*, *250*(12), pp.849-873.

Hiscott, R.N., Hall, F.R. and Pirmez, C., 1997. Turbidity-current overspill from the Amazon Channel: texture of the silt/sand load, paleoflow from anisotropy of magnetic

susceptibility, and implications for flow processes. In *Proceedings-Ocean Drilling Program Scientific Results* (pp. 53-78).

Ho, V.L., Dorrell, R.M., Keevil, G.M., Burns, A.D. and McCaffrey, W.D., 2018. Pulse propagation in turbidity currents. *Sedimentology*, *65*(2), pp.620-637.

Hogg, A.J. and Huppert, H.E., 2001. Two-dimensional and axisymmetric models for compositional and particle-driven gravity currents in uniform ambient flows. *Particulate Gravity Currents*, pp.121-134.

Hogg, A.J., Nasr-Azadani, M.M., Ungarish, M. and Meiburg, E., 2016. Sustained gravity currents in a channel. *Journal of Fluid Mechanics*, *798*, pp.853-888.

Holeman, J.N., 1968. The sediment yield of major rivers of the world. *Water resources research*, *4*(4), pp.737-747.

Holyer, J.Y. and Huppert, H.E., 1980. Gravity currents entering a two-layer fluid. *Journal of Fluid Mechanics*, *100*(4), pp.739-767.

Hopfinger, E.J., 1983. Snow avalanche motion and related phenomena. *Annual review of fluid mechanics*, *15*(1), pp.47-76.

Huang, H., Imran, J. and Pirmez, C., 2005. Numerical model of turbidity currents with a deforming bottom boundary. *Journal of Hydraulic Engineering*, *131*(4), pp.283-293.

Huang, H., Imran, J. and Pirmez, C., 2008. Numerical study of turbidity currents with sudden-release and sustained-inflow mechanisms. *Journal of Hydraulic Engineering*, *134*(9), pp.1199-1209.

Huang, H., Imran, J., Pirmez, C., Zhang, Q. and Chen, G., 2009. The critical densimetric Froude number of subaqueous gravity currents can be non-unity or non-existent. *Journal of Sedimentary Research*, *79*(7), pp.479-485.

Huppert, H.E. and Simpson, J.E., 1980. The slumping of gravity currents. *Journal of Fluid Mechanics*, *99*(4), pp.785-799.

Imran, J., Kassem, A. and Khan, S.M., 2004. Three-dimensional modeling of density current. I. Flow in straight confined and unconfined channels. *Journal of Hydraulic Research*, *42*(6), pp.578-590.

Imran, J., Islam, M.A., Huang, H., Kassem, A., Dickerson, J., Pirmez, C. and Parker, G., 2007. Helical flow couplets in submarine gravity underflows. *Geology*, *35*(7), pp.659-662.

Imran, J., Khan, S.M., Pirmez, C. and Parker, G., 2016. Froude scaling limitations in modeling of turbidity currents. *Environmental Fluid Mechanics*, *1*(17), pp.159-186.

Islam, M.A. and Imran, J., 2008. Experimental modeling of gravity underflow in a sinuous submerged channel. *Journal of Geophysical Research: Oceans*, *113*(C7).

Islam, M.A., Imran, J., Pirmez, C. and Cantelli, A., 2008. Flow splitting modifies the helical motion in submarine channels. *Geophysical Research Letters*, *35*(22).

Islam, M.A. and Imran, J., 2010. Vertical structure of continuous release saline and turbidity currents. *Journal of Geophysical Research: Oceans*, *115*(C8).

Jobe, Z.R., Sylvester, Z., Parker, A.O., Howes, N., Slowey, N. and Pirmez, C., 2015. Rapid Adjustment of Submarine Channel Architecture To Changes In Sediment Supply. *Journal of Sedimentary Research*, *85*(6), pp.729-753.

Jones, W.P. and Launder, B.E., 1972. The prediction of laminarization with a two-equation model of turbulence. *International journal of heat and mass transfer*, *15*(2), pp.301-314.

Kane, I.A., Kneller, B.C., Dykstra, M., Kassem, A. and McCaffrey, W.D., 2007. Anatomy of a submarine channel–levee: an example from Upper Cretaceous slope sediments, Rosario Formation, Baja California, Mexico. *Marine and Petroleum Geology*, *24*(6-9), pp.540-563.

Kane, I.A., McCaffrey, W.D. and Peakall, J., 2008. Controls on sinuosity evolution within submarine channels. *Geology*, *36*(4), pp.287-290.

Kassem, A. and Imran, J., 2004. Three-dimensional modeling of density current. II. Flow in sinuous confined and uncontined channels. *Journal of Hydraulic Research*, *42*(6), pp.591-602.

Keevil, G.M., Peakall, J., Best, J.L. and Amos, K.J., 2006. Flow structure in sinuous submarine channels: velocity and turbulence structure of an experimental submarine channel. *Marine Geology*, *229*(3), pp.241-257.

Kelly, R.W., 2015. Computational analysis of experimental gravity currents (unpublished master's thesis). *University of Leeds.*

Kenyon, N.H., Amir, A. and Cramp, A., 1995. Geometry of the younger sediment bodies of the Indus Fan. In *Atlas of Deep Water Environments* (pp. 89-93). Springer Netherlands.

Keulegan, G.H., 1957. An experimental study of the motion of saline water from locks into fresh water channels. *Nat. Bur. Stand. Rept. Technical Report*, *5168*.

Khripounoff, A., Vangriesheim, A., Babonneau, N., Crassous, P., Dennielou, B. and Savoye, B., 2003. Direct observation of intense turbidity current activity in the Zaire submarine valley at 4000 m water depth. *Marine Geology*, *194*(3), pp.151-158.

Khripounoff, A., Vangriesheim, A., Crassous, P. and Etoubleau, J., 2009. High frequency of sediment gravity flow events in the Var submarine canyon (Mediterranean Sea). *Marine Geology*, *263*(1-4), pp.1-6.

Khripounoff, A., Crassous, P., Bue, N.L., Dennielou, B. and Jacinto, R.S., 2012. Different types of sediment gravity flows detected in the Var submarine canyon (northwestern Mediterranean Sea). *Progress in Oceanography*, *106*, pp.138-153.

Klaucke, I. and Hesse, R., 1996. Fluvial features in the deep-sea: new insights from the glacigenic submarine drainage system of the Northwest Atlantic Mid-Ocean Channel in the Labrador Sea. *Sedimentary Geology*, *106*(3-4), pp.223-234.

Klaucke, I., Hesse, R., and Ryan, W., 1998. Morphology and structure of a distal submarine trunk channel: the Northwest Atlantic Mid-Ocean Channel between lat 53 N and 44 30′ N. *Geological Society of America Bulletin* 110.1.

Kneller, B.C., Bennett, S.J. and McCaffrey, W.D., 1997. Velocity and turbulence structure of density currents and internal solitary waves: potential sediment transport and the formation of wave ripples in deep water. *Sedimentary Geology*, *112*(3-4), pp.235-250.

Kneller, B.C., Bennett, S.J. and McCaffrey, W.D., 1999. Velocity structure, turbulence and fluid stresses in experimental gravity currents. *Journal of Geophysical Research: Oceans*, *104*(C3), pp.5381-5391.

Kneller, B. and Buckee, C., 2000. The structure and fluid mechanics of turbidity currents: a review of some recent studies and their geological implications. *Sedimentology*, *47*(s1), pp.62-94.

Kneller, B., 2003. The influence of flow parameters on turbidite slope channel architecture. *Marine and Petroleum Geology*, *20*(6-8), pp.901-910.

Kneller, B., Nasr-Azadani, M.M., Radhakrishnan, S. and Meiburg, E., 2016. Long-range sediment transport in the world's oceans by stably stratified turbidity currents. *Journal of Geophysical Research: Oceans*.

Kolla, V., Posamentier, H.W. and Wood, L.J., 2007. Deep-water and fluvial sinuous channels—Characteristics, similarities and dissimilarities, and modes of formation. *Marine and Petroleum Geology*, *24*(6-9), pp.388-405.

Kolmogorov, A.N., 1941, February. The local structure of turbulence in incompressible viscous fluid for very large Reynolds numbers. In *Dokl. Akad. Nauk SSSR* (Vol. 30, No. 4, pp. 299-303).

Krause, D.C., White, W.C., Piper, D.J.W. and Heezen, B.C., 1970. Turbidity currents and cable breaks in the western New Britain Trench. *Geological Society of America Bulletin*, *81*(7), pp.2153-2160.

Kuenen, P.H. and Migliorini, C.I., 1950. Turbidity currents as a cause of graded bedding. *The Journal of Geology*, *58*(2), pp.91-127.

Kuenen, P.H., 1966. Matrix of turbidites: experimental approach. *Sedimentology*, *7*(4), pp.267-297.

Launder, B.E., Reece, G.J. and Rodi, W., 1975. Progress in the development of a Reynolds-stress turbulence closure. *Journal of Fluid Mechanics*, *68*(3), pp.537-566.

Launder, B.E. and Rodi, W., 1983. The turbulent wall jet measurements and modeling. *Annual Review of Fluid Mechanics*, *15*(1), pp.429-459.

Liu, J.T., Wang, Y.H., Yang, R.J., Hsu, R.T., Kao, S.J., Lin, H.L. and Kuo, F.H., 2012. Cyclone-induced hyperpycnal turbidity currents in a submarine canyon. *Journal of Geophysical Research: Oceans*, *117*(C4).

Lofquist, K., 1960. Flow and stress near an interface between stratified liquids. *The Physics of Fluids*, *3*(2), pp.158-175.

Luchi, R., Balachandar, S., Seminara, G. and Parker, G., 2018. Turbidity currents with equilibrium basal driving layers: A mechanism for long runout. *Geophysical Research Letters*, *45*(3), pp.1518-1526.

Mahdinia, M., Firoozabadi, B., Farshchi, M., Varnamkhasti, A.G. and Afshin, H., 2011. Large eddy simulation of Lock-Exchange flow in a curved channel. *Journal of Hydraulic Engineering*, *138*(1), pp.57-70.

Masson, D.G., Kenyon, N.H. and Weaver, P.P.E., 1996. Slides, debris flows, and turbidity currents. *Oceanography: an illustrated guide*, pp.136-51.

Mayall, M., Jones, E. and Casey, M., 2006. Turbidite channel reservoirs—Key elements in facies prediction and effective development. *Marine and Petroleum Geology*, *23*(8), pp.821-841.

Meiburg, E. and Kneller, B., 2010. Turbidity currents and their deposits. *Annual Review of Fluid Mechanics*, *42*, pp.135-156.

Menter, F.R., 1994. Two-equation eddy-viscosity turbulence models for engineering applications. *AIAA journal*, *32*(8), pp.1598-1605.

Menter, F.R., 2009. Review of the shear-stress transport turbulence model experience from an industrial perspective. *International Journal of Computational Fluid Dynamics*, *23*(4), pp.305-316.

Middleton, G.V., 1966. Experiments on density and turbidity currents: I. Motion of the head. *Canadian Journal of Earth Sciences*, *3*(4), pp.523-546.

Middleton, G.V., 1993. Sediment deposition from turbidity currents. *Annual Review of Earth and Planetary Sciences*, *21*(1), pp.89-114.

Mohrig, D. and Buttles, J., 2007. Deep turbidity currents in shallow channels. *Geology*, *35*(2), pp.155-158.

Mulder, T. and Alexander, J., 2001. The physical character of subaqueous sedimentary density flows and their deposits. *Sedimentology*, *48*(2), pp.269-299.

Nakajima, T. and Kneller, B.C., 2013. Quantitative analysis of the geometry of submarine external levees. *Sedimentology*, *60*(4), pp.877-910.

Nasr-Azadani, M.M. and Meiburg, E., 2011. TURBINS: an immersed boundary, Navier–Stokes code for the simulation of gravity and turbidity currents interacting with complex topographies. *Computers & Fluids*, *45*(1), pp.14-28.

Nasr-Azadani, M.M. and Meiburg, E., 2015. Gravity currents propagating into shear. *Journal of Fluid Mechanics*, *778*, pp.552-585.

Necker, F., Härtel, C., Kleiser, L. and Meiburg, E., 2002. High-resolution simulations of particle-driven gravity currents. *International Journal of Multiphase Flow*, *28*(2), pp.279-300.

Normark, W.R. and Damuth, J.E., 1997. Sedimentary facies and associated depositional elements of the Amazon Fan. In *Proceedings of the Ocean Drilling Program. Scientific Results* (Vol. 155, pp. 611-651). Ocean Drilling Program.

Paik, J., Eghbalzadeh, A. and Sotiropoulos, F., 2009. Three-Dimensional unsteady RANS modeling of discontinuous gravity currents in rectangular domains. *Journal of Hydraulic Engineering*, *135*(6), pp.505-521.

Pantin, H.M., 1979. Interaction between velocity and effective density in turbidity flow: phase-plane analysis, with criteria for autosuspension. *Marine Geology*, *31*(1-2), pp.59-99.

Pantin, H.M., 2001. Experimental evidence for autosuspension. *Particulate gravity currents*, *31*, pp.189-205.

Parker, G., Fukushima, Y. and Pantin, H.M., 1986. Self-accelerating turbidity currents. *Journal of Fluid Mechanics*, *171*, pp.145-181.

Parker, G., Garcia, M., Fukushima, Y. and Yu, W., 1987. Experiments on turbidity currents over an erodible bed. *Journal of Hydraulic Research*, *25*(1), pp.123-147.

Parsons, D.R., Peakall, J., Aksu, A.E., Flood, R.D., Hiscott, R.N., Beşiktepe, Ş. and Mouland, D., 2010. Gravity-driven flow in a submarine channel bend: direct field evidence of helical flow reversal. *Geology*, *38*(12), pp.1063-1066.

Paull, C.K., Ussler, W.I.I.I., Greene, H.G., Keaten, R., Mitts, P. and Barry, J., 2002. Caught in the act: the 20 December 2001 gravity flow event in Monterey Canyon. *Geo-Marine Letters*, *22*(4), pp.227-232.

Peakall, J., McCaffrey, B. and Kneller, B., 2000. A process model for the evolution, morphology, and architecture of sinuous submarine channels. *Journal of Sedimentary Research*, *70*(3), pp.434-448.

Peakall, J., Felix, M., McCaffrey, B. and Kneller, B., 2001. Particulate gravity currents: Perspectives. *Particulate gravity currents*, *16*, pp.1-8.

Peakall, J., Amos, K.J., Keevil, G.M., Bradbury, P.W. and Gupta, S., 2007. Flow processes and sedimentation in submarine channel bends. *Marine and Petroleum Geology*, *24*(6-9), pp.470-486.

Peakall, J., Kane, I.A., Masson, D.G., Keevil, G., McCaffrey, W. and Corney, R., 2012. Global (latitudinal) variation in submarine channel sinuosity. *Geology*, *40*(1), pp.11-14.

Peakall, J., Darby, S.E., Dorrell, R.M., Parsons, D.R., Sumner, E.J. and Wynn, R.B., 2014. Comment on "A simple model for vertical profiles of velocity and suspended sediment concentration in straight and curved submarine channels" by M. Bolla Pittaluga and J. Imran. *Journal of Geophysical Research: Earth Surface*, *119*(9), pp.2070-2073.

Peakall, J. and Sumner, E.J., 2015. Submarine channel flow processes and deposits: A process-product perspective. *Geomorphology*, *244*, pp.95-120.

Pierson, T.C. and Scott, K.M., 1985. Downstream dilution of a lahar: transition from debris flow to hyperconcentrated streamflow. *Water resources research*, *21*(10), pp.1511-1524.

Piper, D.J., Cochonat, P. and Morrison, M.L., 1999. The sequence of events around the epicentre of the 1929 Grand Banks earthquake: initiation of debris flows and turbidity current inferred from sidescan sonar. *Sedimentology*, *46*(1), pp.79-97.

Piper, D.J. and Normark, W.R., 2009. Processes that initiate turbidity currents and their influence on turbidites: a marine geology perspective. *Journal of Sedimentary Research*, *79*(6), pp.347-362.

Pirmez, C., Beaubouef, R.T., Friedmann, S.J. and Mohrig, D.C., 2000, December. Equilibrium profile and baselevel in submarine channels: examples from Late Pleistocene systems and implications for the architecture of deepwater reservoirs. In *Global deep-water reservoirs: Gulf Coast Section SEPM Foundation 20th Annual Bob F. Perkins Research Conference* (pp. 782-805).

Pirmez, C. and Imran, J., 2003. Reconstruction of turbidity currents in Amazon Channel. *Marine and petroleum geology*, *20*(6-8), pp.823-849.

Posamentier, H.W. and Kolla, V., 2003. Seismic geomorphology and stratigraphy of depositional elements in deep-water settings. *Journal of sedimentary research*, *73*(3), pp.367-388.

Rottman, J.W. and Simpson, J.E., 1983. Gravity currents produced by instantaneous releases of a heavy fluid in a rectangular channel. *Journal of Fluid Mechanics*, *135*, pp.95-110.

Rozovskiĭ, I.L., 1957. *Flow of water in bends of open channels*. Academy of Sciences of the Ukrainian SSR.

Samuel, A., Kneller, B., Raslan, S., Sharp, A. and Parsons, C., 2003. Prolific deep-marine slope channels of the Nile Delta, Egypt. *AAPG bulletin*, *87*(4), pp.541-560.

Savoye, B., Babonneau, N., Dennielou, B. and Bez, M., 2009. Geological overview of the Angola–Congo margin, the Congo deep-sea fan and its submarine valleys. *Deep Sea Research Part II: Topical Studies in Oceanography*, *56*(23), pp.2169-2182.

Sequeiros, O.E., Naruse, H., Endo, N., Garcia, M.H. and Parker, G., 2009. Experimental study on self-accelerating turbidity currents. *Journal of Geophysical Research: Oceans*, *114*(C5).

Sequeiros, O.E., Spinewine, B., Beaubouef, R.T., Sun, T., García, M.H. and Parker, G., 2010. Characteristics of velocity and excess density profiles of saline underflows and turbidity currents flowing over a mobile bed. *Journal of Hydraulic Engineering*, *136*(7), pp.412-433.

Sequeiros, O.E., 2012. Estimating turbidity current conditions from channel morphology: A Froude number approach. *Journal of Geophysical Research: Oceans*, *117*(C4).

Shepard, F.P. and Buffington, E.C., 1968. La Jolla submarine fan-valley. *Marine Geology*, *6*(2), pp.107-143.

Shin, J.O., Dalziel, S.B. and Linden, P.F., 2004. Gravity currents produced by lock exchange. *Journal of Fluid Mechanics*, *521*, pp.1-34.

Simpson, J.E., 1999. *Gravity currents: In the environment and the laboratory*. Cambridge university press.

Simpson, J.E. and Britter, R.E., 1980. A laboratory model of an atmospheric mesofront. *Quarterly Journal of the Royal Meteorological Society*, *106*(449), pp.485-500.

Skene, K.I., Piper, D.J. and Hill, P.S., 2002. Quantitative analysis of variations in depositional sequence thickness from submarine channel levees. *Sedimentology*, *49*(6), pp.1411-1430.

Stacey, M.W. and Bowen, A.J., 1988. The vertical structure of density and turbidity currents: theory and observations. *Journal of Geophysical Research: Oceans*, *93*(C4), pp.3528-3542.

Stagnaro, M. and Pittaluga, M.B., 2014. Velocity and concentration profiles of saline and turbidity currents flowing in a straight channel under quasi-uniform conditions. *Earth Surface Dynamics*, *2*(1), p.167.

Stevenson, C.J., Talling, P.J., Wynn, R.B., Masson, D.G., Hunt, J.E., Frenz, M., Akhmetzhanhov, A. and Cronin, B.T., 2013. The flows that left no trace: Very large-volume turbidity currents that bypassed sediment through submarine channels without eroding the sea floor. *Marine and Petroleum Geology*, *41*, pp.186-205.

Straub, K.M., Mohrig, D., McElroy, B., Buttles, J. and Pirmez, C., 2008a. Interactions between turbidity currents and topography in aggrading sinuous submarine channels: A laboratory study. Geological Society of America Bulletin, 120(3-4), pp.368-385.

Straub, K.M. and Mohrig, D., 2008. Quantifying the morphology and growth of levees in aggrading submarine channels. *Journal of Geophysical Research: Earth Surface*, *113*(F3).

Sumner, E.J., Peakall, J., Parsons, D.R., Wynn, R.B., Darby, S.E., Dorrell, R.M., McPhail, S.D., Perrett, J., Webb, A. and White, D., 2013. First direct measurements of

hydraulic jumps in an active submarine density current. *Geophysical Research Letters*, *40*(22), pp.5904-5908.

Sumner, E.J. and Paull, C.K., 2014. Swept away by a turbidity current in Mendocino submarine canyon, California. *Geophysical Research Letters*, *41*(21), pp.7611-7618.

Sumner, E. J., J. Peakall, R. M. Dorrell, D. R. Parsons, S. E. Darby, R. B. Wynn, S. D. McPhail, J. Perrett, A. Webb, and D. White, 2014. Driven around the bend: Spatial evolution and controls on the orientation of helical bend flow in a natural submarine gravity current. *Journal of Geophysical Research: Oceans*119, no. 2 (2014): 898-913.

Sylvester, Z., Pirmez, C., Cantelli, A. and Jobe, Z.R., 2013. Global (latitudinal) variation in submarine channel sinuosity: Comment. *Geology*, *41*(5), pp.e287-e287.

Symons, W.O., Sumner, E.J., Paull, C.K., Cartigny, M.J., Xu, J.P., Maier, K.L., Lorenson, T.D. and Talling, P.J., 2017. A new model for turbidity current behavior based on integration of flow monitoring and precision coring in a submarine canyon. *Geology*, *45*(4), pp.367-370.

Talling, P.J., Amy, L.A. and Wynn, R.B., 2007. New insight into the evolution of large-volume turbidity currents: comparison of turbidite shape and previous modelling results. *Sedimentology*, *54*(4), pp.737-769.

Talling, P.J., Paull, C.K. and Piper, D.J., 2013. How are subaqueous sediment density flows triggered, what is their internal structure and how does it evolve? Direct observations from monitoring of active flows. *Earth-Science Reviews*, *125*, pp.244-287.

Talling, P.J., Allin, J., Armitage, D.A., Arnott, R.W., Cartigny, M.J., Clare, M.A., Felletti, F., Covault, J.A., Girardclos, S., Hansen, E. and Hill, P.R., 2015. Key Future Directions For Research On Turbidity Currents and Their Deposits. *Journal of Sedimentary Research*, *85*(2), pp.153-169.

Timbrell, G., 1993, January. Sandstone architecture of the Balder Formation depositional system, UK Quadrant 9 and adjacent areas. In *Geological Society, London, Petroleum Geology Conference series* (Vol. 4, No. 1, pp. 107-121). Geological Society of London.

Te Chow, V., 1959. *Open-channel hydraulics* (Vol. 1). New York: McGraw-Hill.

Thornburg, T.M. and Kulm, L.D., 1987. Sedimentation in the Chile Trench: Depositional morphologies, lithofacies, and stratigraphy. *Geological Society of America Bulletin*, *98*(1), pp.33-52.

Thorne, C. R. (1982). Processes and mechanisms of river bank erosion. *Gravel-bed rivers*, 227-271.

Tominaga, Y. and Stathopoulos, T., 2007. Turbulent Schmidt numbers for CFD analysis with various types of flowfield. *Atmospheric Environment*, *41*(37), pp.8091-8099.

Turner, J.S., 1979. *Buoyancy effects in fluids*. Cambridge University Press.

Vangriesheim, A., Khripounoff, A. and Crassous, P., 2009. Turbidity events observed in situ along the Congo submarine channel. *Deep Sea Research Part II: Topical Studies in Oceanography*, *56*(23), pp.2208-2222.

Von Karman, T., 1940. The engineer grapples with nonlinear problems. *Bulletin of the American Mathematical Society*, *46*(8), pp.615-683.

Voulgaris, G. and Trowbridge, J.H., 1998. Evaluation of the acoustic Doppler velocimeter (ADV) for turbulence measurements. *Journal of atmospheric and oceanic technology*, *15*(1), pp.272-289.

Wynn, R.B., Cronin, B.T. and Peakall, J., 2007. Sinuous deep-water channels: Genesis, geometry and architecture. *Marine and Petroleum Geology*, *24*(6-9), pp.341-387.

Xu, J.P., Noble, M.A. and Rosenfeld, L.K., 2004. In-situ measurements of velocity structure within turbidity currents. *Geophysical Research Letters*, *31*(9).

Xu, J.P., 2010. Normalized velocity profiles of field-measured turbidity currents. *Geology*, *38*(6), pp.563-566.

Xu, J.P., Barry, J.P. and Paull, C.K., 2013. Small-scale turbidity currents in a big submarine canyon. *Geology*, *41*(2), pp.143-146.

Xu, J.P., Sequeiros, O.E. and Noble, M.A., 2014. Sediment concentrations, flow conditions, and downstream evolution of two turbidity currents, Monterey Canyon, USA. *Deep Sea Research Part I: Oceanographic Research Papers*, *89*, pp.11-34.